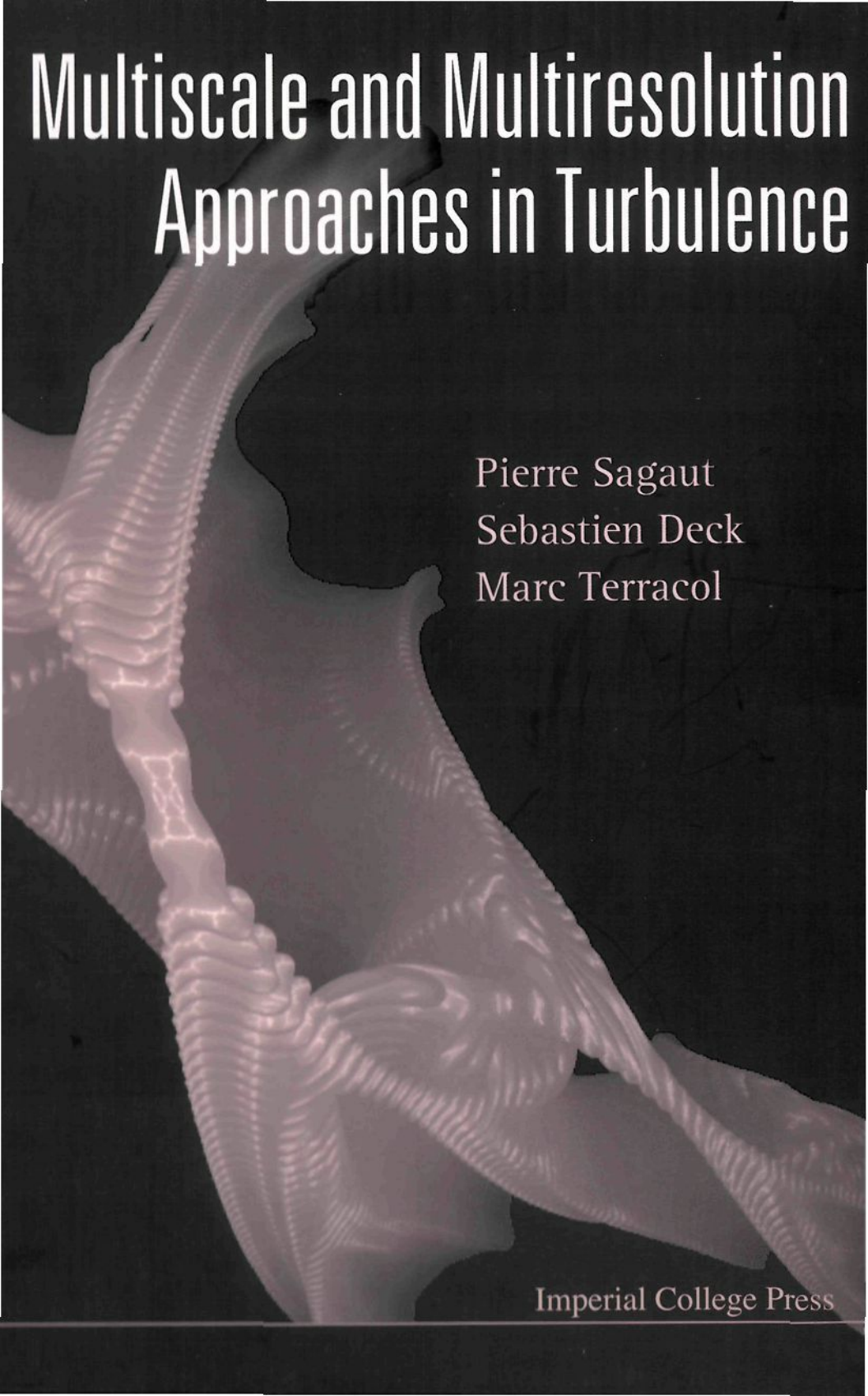


# Multiscale and Multiresolution Approaches in Turbulence



Pierre Sagaut  
Sebastien Deck  
Marc Terracol

Imperial College Press



**Multiscale and Multiresolution  
Approaches in Turbulence**

This page is intentionally left blank

# Multiscale and Multiresolution Approaches in Turbulence

Pierre Sagaut

Universite Pierre et Marie Curie, France

Sebastien Deck

ONERA, France

Marc Terracol

ONERA, France

*Published by*

Imperial College Press  
57 Shelton Street  
Covent Garden  
London WC2H 9HE

*Distributed by*

World Scientific Publishing Co. Pte. Ltd.  
5 Toh Tuck Link, Singapore 596224  
*USA office:* 27 Warren Street, Suite 401-402, Hackensack, NJ 07601  
*UK office:* 57 Shelton Street, Covent Garden, London WC2H 9HE

**British Library Cataloguing-in-Publication Data**

A catalogue record for this book is available from the British Library.

**MULTISCALE AND MULTIREOLUTION APPROACHES IN TURBULENCE**

Copyright © 2006 by Imperial College Press

*All rights reserved. This book, or parts thereof, may not be reproduced in any form or by any means, electronic or mechanical, including photocopying, recording or any information storage and retrieval system now known or to be invented, without written permission from the Publisher.*

For photocopying of material in this volume, please pay a copying fee through the Copyright Clearance Center, Inc., 222 Rosewood Drive, Danvers, MA 01923, USA. In this case permission to photocopy is not required from the publisher.

ISBN 1-86094-650-X

“... the answer, my friend, is blowin’ the wind ...”

Bob Dylan

This page is intentionally left blank

# Preface

Turbulence modeling is a complex subject and methods developed to deal with it are numerous and diverse. Many schools of thought exist and communication and understanding among them is often lacking. Comparisons may be odious but they need to be made and explored if a scientific discipline is to progress. This is why *Multiscale and Multiresolution Approaches in Turbulence* is so timely. It brings together many topics not found in one place before. A number have appeared only in very recent research papers and here grace the pages of a book for the first time. The proximity invites comparisons and suggests a greater unification of turbulence methodology than is at first apparent. The subject of the work is modeling, but the dual themes, expressed in the title, are multiscale and multiresolution approaches. These words conjure up fundamental and computational concepts, and, indeed, the text presents both in an integrated way. Multiscale and multiresolution methods have attracted enormous recent interest in a variety of scientific disciplines, and they seem to provide the ideal framework for organizing much, if not all, contemporary turbulence research.

The treatment begins in Chapter 1 with a brief introduction to turbulence ideas, including randomness, coherent structures, turbulent length and time scales, the Kolmogorov energy cascade, and transfers of energy between scales. In Chapter 2, the enormous cost of direct numerical solution of the Navier–Stokes equations is used to motivate the practical need for modeling. This amounts to approximating the effects of unrepresented scales and the basic strategies are described next, namely, Reynolds Averaged Numerical Simulation (RANS) and Large Eddy Simulation (LES), and are followed by a discussion of multilevel methods. Chapter 3 deals with statistical multiscale concepts and various RANS models are presented, including eddy-viscosity and Reynolds-stress models. Chapter 4

is concerned with multiscale subgrid models and self-adaptivity in LES. Fundamental ideas are introduced, along with the Germano identity, dynamic models, self-similarity, and variational multiscale (VMS) methods. Chapter 5 presents structured multiscale subgrid models for LES based on the estimation of small scales. Various reconstruction techniques are described, including deconvolution, multifractal, and multigrid, in addition to zonal multigrid/multidomain methods. Unsteady turbulence simulations on self-adaptive grids are discussed in Chapter 6, covering dynamic multi-level and adaptive wavelet methods, and DNS and LES with adaptive mesh refinement (AMR). Global hybrid RANS/LES approaches are presented in Chapter 7, including unsteady statistical modeling, blending, and Detached Eddy Simulation (DES). The theoretical basis of zonal RANS/LES methods commences Chapter 8 and is followed by a discussion of inlet data generation and turbulence reconstruction techniques.

This text is a very important addition to the literature on turbulence. It provides an excellent introduction to many areas of contemporary research and it systematically organizes many seemingly disparate approaches within its dual themes of multiscale and multiresolution methodology. Researchers will find it useful as a guide to the strengths and weaknesses of current technology, a classification system within which new developments will likely fit, and a hierarchy for locating methods to compare with. Student and expert alike will benefit greatly by reading it from cover to cover, and will also find it a reference work of lasting value.

Thomas J.R. Hughes,  
University of Texas, Austin,  
November 2005.

# Contents

<i>Preface</i>	vii
1. A Brief Introduction to Turbulence	1
1.1 Common Features of Turbulent Flows . . . . .	1
1.1.1 Introductory concepts . . . . .	1
1.1.2 Randomness and coherent structure in turbulent flows . . . . .	3
1.2 Turbulent Scales and Complexity of a Turbulent Field . . .	5
1.2.1 Basic equations of turbulent flow . . . . .	5
1.2.2 Defining turbulent scales . . . . .	8
1.2.3 A glimpse at numerical simulations of turbulent flows	13
1.3 Inter-scale Coupling in Turbulent Flows . . . . .	14
1.3.1 The energy cascade . . . . .	14
1.3.2 Inter-scale interactions . . . . .	16
2. Turbulence Simulation and Scale Separation	21
2.1 Numerical Simulation of Turbulent Flows . . . . .	21
2.2 Reducing the Cost of the Simulations . . . . .	23
2.2.1 Scale separation . . . . .	24
2.2.2 Navier–Stokes-based equations for the resolved quantities . . . . .	24
2.2.3 Navier–Stokes-based equations for the unresolved quantities . . . . .	26
2.3 The Averaging Approach: Reynolds-Averaged Numerical Simulation (RANS) . . . . .	26
2.3.1 Statistical average . . . . .	26
2.3.2 Reynolds-Averaged Navier–Stokes equations . . . . .	28

2.3.3	Phase-Averaged Navier Stokes equations . . . . .	29
2.4	The Large Eddy Simulation Approach (LES) . . . . .	31
2.4.1	Large and small scales separation . . . . .	31
2.4.2	Filtered Navier–Stokes equations . . . . .	33
2.5	Multilevel/Multiresolution Methods . . . . .	35
2.5.1	Hierarchical multilevel decomposition . . . . .	36
2.5.2	Practical example: the multiscale/multilevel LES decomposition . . . . .	38
2.5.3	Associated Navier–Stokes-based equations . . . . .	39
2.5.4	Classification of existing multilevel methods . . . . .	41
2.5.4.1	Multilevel methods based on resolved-only wavenumbers . . . . .	41
2.5.4.2	Multilevel methods based on higher wavenumbers . . . . .	42
2.5.4.3	Adaptive multilevel methods . . . . .	43
2.6	Summary . . . . .	44
3.	Statistical Multiscale Modelling . . . . .	51
3.1	General . . . . .	51
3.2	Exact Governing Equations for the Multiscale Problem . . . . .	54
3.2.1	Basic equations in physical and spectral space . . . . .	54
3.2.2	The multiscale splitting . . . . .	59
3.2.3	Governing equations for band-integrated approaches . . . . .	60
3.3	Spectral Closures for Band-integrated Approaches . . . . .	62
3.3.1	Local versus non-local transfers . . . . .	62
3.3.2	Expression for the spectral fluxes . . . . .	64
3.3.3	Dynamic spectral splitting . . . . .	67
3.3.4	Turbulent diffusion terms . . . . .	68
3.3.5	Viscous dissipation term . . . . .	68
3.3.6	Pressure term . . . . .	69
3.4	A Few Multiscale Models for Band-integrated Approaches . . . . .	69
3.4.1	Multiscale Reynolds stress models . . . . .	69
3.4.2	Multiscale eddy-viscosity models . . . . .	70
3.5	Spectral Closures for Local Approaches . . . . .	71
3.5.1	Local multiscale Reynolds stress models . . . . .	71
3.5.1.1	Closures for the linear transfer term . . . . .	72
3.5.1.2	Closures for the linear pressure term . . . . .	73

3.5.1.3	Closures for the non-linear homogeneous transfer term . . . . .	74
3.5.1.4	Closures for the non-linear non-homogeneous transfer term . . . . .	76
3.5.2	Local multiscale eddy-viscosity models . . . . .	77
3.6	Achievements and Open Issues . . . . .	78
4.	Multiscale Subgrid Models: Self-adaptivity . . . . .	87
4.1	Fundamentals of Subgrid Modelling . . . . .	87
4.1.1	Functional and structural subgrid models . . . . .	87
4.1.2	The Gabor-Heisenberg curse . . . . .	88
4.2	Germano-type Dynamic Subgrid Models . . . . .	93
4.2.1	Germano identity . . . . .	93
4.2.1.1	Two-level multiplicative Germano Identity . . . . .	93
4.2.1.2	Multilevel Germano Identity . . . . .	95
4.2.1.3	Generalized Germano Identity . . . . .	96
4.2.2	Derivation of dynamic subgrid models . . . . .	96
4.2.3	Dynamic models and self-similarity . . . . .	99
4.2.3.1	Turbulence self-similarity . . . . .	99
4.2.3.2	Scale-separation operator self-similarity . . . . .	106
4.3	Self-Similarity Based Dynamic Subgrid Models . . . . .	108
4.3.1	Terracol–Sagaut procedure . . . . .	109
4.3.2	Shao procedure . . . . .	111
4.4	Variational Multiscale Methods and Related Subgrid Viscosity Models . . . . .	114
4.4.1	Hughes VMS approach and extended formulations . . . . .	115
4.4.2	Implementation of the scale separation operator . . . . .	119
4.4.3	Bridging with hyperviscosity and filtered models . . . . .	123
5.	Structural Multiscale Subgrid Models: Small Scales Estimations . . . . .	125
5.1	Small-scale Reconstruction Methods: Deconvolution . . . . .	126
5.1.1	The velocity estimation model . . . . .	128
5.1.2	The Approximate Deconvolution Model (ADM) . . . . .	134
5.2	Small Scales Reconstruction: Multifractal Subgrid-scale Modelling . . . . .	141
5.2.1	General idea of the method . . . . .	141
5.2.2	Multifractal reconstruction of subgrid vorticity . . . . .	142
5.2.2.1	Vorticity magnitude cascade . . . . .	142

5.2.2.2	Vorticity orientation cascade . . . . .	144
5.2.2.3	Reconstruction of the subgrid velocity field . . . . .	146
5.3	Multigrid-based Decomposition . . . . .	146
5.4	Global Multigrid Approaches: Cycling Methods . . . . .	151
5.4.1	The multimesh method of Voke . . . . .	152
5.4.2	The multilevel LES method of Terracol <i>et al.</i> . . . . .	153
5.4.2.1	Cycling procedure . . . . .	154
5.4.2.2	Multilevel subgrid closures . . . . .	156
(a)	Dynamic mixed multilevel closure . . . . .	157
(b)	Generalized multilevel closure . . . . .	161
5.4.2.3	Examples of application . . . . .	162
5.5	Zonal Multigrid/Multidomain Methods . . . . .	163
6.	Unsteady Turbulence Simulation on Self-adaptive Grids . . . . .	173
6.1	Turbulence and Self-adaptivity: Expectations and Issues . . . . .	173
6.2	Adaptive Multilevel DNS and LES . . . . .	178
6.2.1	Dynamic Local Multilevel LES . . . . .	179
6.2.2	The Dynamic MultiLevel (DML) method of Dubois, Jauberteau and Temam . . . . .	183
6.2.2.1	Spectral multilevel decomposition . . . . .	184
6.2.2.2	Associated Navier–Stokes-based equations . . . . .	185
6.2.2.3	Quasi-static approximation . . . . .	187
6.2.2.4	General description of the spectral multilevel method . . . . .	188
6.2.2.5	Dynamic estimation of the parameters $i_1$ , $i_2$ and $n_V$ . . . . .	189
6.2.3	Dynamic Global Multilevel LES . . . . .	191
6.3	Adaptive Wavelet-based Methods: CVS, SCALES . . . . .	195
6.3.1	Wavelet decomposition: brief reminder . . . . .	196
6.3.2	Coherency diagram of a turbulent field . . . . .	198
6.3.2.1	Introduction to the coherency diagram . . . . .	198
6.3.2.2	Threshold value and error control . . . . .	201
6.3.3	Adaptive Wavelet based Direct Numerical Simulation . . . . .	203
6.3.4	Coherent Vortex Capturing method . . . . .	204
6.3.5	Stochastic Coherent Adaptive Large Eddy Simulation . . . . .	205
6.4	DNS and LES with Optimal AMR . . . . .	207
6.4.1	Error definition: surfacic versus volumic formulation . . . . .	207
6.4.2	A posteriori error estimation and optimization loop . . . . .	209

6.4.3	Numerical results . . . . .	211
7.	Global Hybrid RANS/LES Methods . . . . .	219
7.1	Bridging between Hybrid RANS/LES Methods and Multiscale Methods . . . . .	219
7.1.1	Concept: the effective filter . . . . .	219
7.1.2	Eddy viscosity effective filter . . . . .	221
7.1.3	Global hybrid RANS/LES methods as multiscale methods . . . . .	223
7.2	Motivation and Classification of RANS/LES Methods . . . . .	224
7.3	Unsteady Statistical Modelling Approaches . . . . .	228
7.3.1	Unsteady RANS approach . . . . .	228
7.3.2	The Semi-Deterministic Method of Ha Minh . . . . .	231
7.3.3	The Scale Adaptive Simulation . . . . .	237
7.3.4	The Turbulence-Resolving RANS approach of Travin <i>et al.</i> . . . . .	241
7.4	Global Hybrid Approaches . . . . .	243
7.4.1	The Approach of Speziale . . . . .	244
7.4.2	Limited Numerical Scales (LNS) . . . . .	247
7.4.2.1	General idea of LNS . . . . .	247
7.4.2.2	Example of application . . . . .	248
7.4.3	Blending methods . . . . .	249
7.4.3.1	General idea of blending methods . . . . .	249
7.4.3.2	Applications . . . . .	251
7.4.4	Detached-Eddy Simulation . . . . .	254
7.4.4.1	General idea . . . . .	254
7.4.4.2	DES based on the SA model . . . . .	256
7.4.4.3	Possible extensions of standard SA-DES . . . . .	259
7.4.4.4	Examples . . . . .	261
7.4.4.5	DES based on the $k - \omega$ model . . . . .	261
7.4.4.6	Extra-Large Eddy Simulation (XLES) . . . . .	265
7.4.5	Grey Area-Grid Induced Separation (GIS) . . . . .	267
7.4.6	Solutions against GIS . . . . .	270
7.4.6.1	Modifying the length scale . . . . .	270
7.4.6.2	Zonal-DES . . . . .	271
7.4.6.3	Shielding the boundary layer-Delayed Detached Eddy Simulation . . . . .	273
7.5	Summary . . . . .	276

8. Zonal RANS/LES Methods	283
8.1 Theoretical Setting of RANS/LES Coupling . . . . .	285
8.1.1 Full-variables approach . . . . .	285
8.1.1.1 Enrichment procedure from RANS to LES .	287
8.1.1.2 Restriction procedure from LES to RANS .	289
8.1.2 Perturbation approach: NLDE . . . . .	290
8.2 Inlet Data Generation – Mapping Techniques . . . . .	294
8.2.1 Precursor calculation . . . . .	295
8.2.2 Recycling methods . . . . .	298
8.2.3 Forcing conditions . . . . .	303
8.3 Turbulence Reconstruction for Inflow Conditions . . . . .	306
8.3.1 Random fluctuations . . . . .	307
8.3.2 Inverse Fourier transform technique . . . . .	307
8.3.3 Random Fourier modes synthesization . . . . .	309
8.3.4 Synthetic turbulence . . . . .	315
<i>Bibliography</i>	321
<i>Index</i>	339

## Chapter 1

# A Brief Introduction to Turbulence

The scope of this chapter is to recall some of the bases of the turbulence theory and its statistical analysis. The emphasis is put on turbulent flow features that are of primary interest for turbulent flow prediction and modelling: turbulent scales, Kolmogorov cascade, coherent structures in shear flows, turbulence production and dissipation. The reader interested in more in-depth discussions of the subject is referred to several reference textbooks: [Chassaing, 2000; Davidson, 2004; Hinze, 1959; Lesieur, 1990; Piquet, 1999; Tennekes and Lumley, 1974].

### 1.1 Common Features of Turbulent Flows

#### 1.1.1 *Introductory concepts*

Most fluid flows occurring in nature as well as in engineering applications are turbulent. Consequently, it does not take any further comment to emphasize that numerical simulations of turbulent flows are of outstanding importance for the scientific as well as for the engineering community. Even though many turbulent flows can be easily observed, it is very difficult to give an accurate and accepted definition of turbulence. However, researchers and engineers generally agree on some characteristics of turbulent flows. For this purpose, let us observe what happens in the turbulent flow past a sphere (see Fig. 1.1) and list the most generally agreed features.

#### •Unpredictability

The irregularity of the flow downstream separation makes a deterministic description of the motion detailed as a function of time and space coordinates impossible. Randomness is clearly shown in the above figure and is a

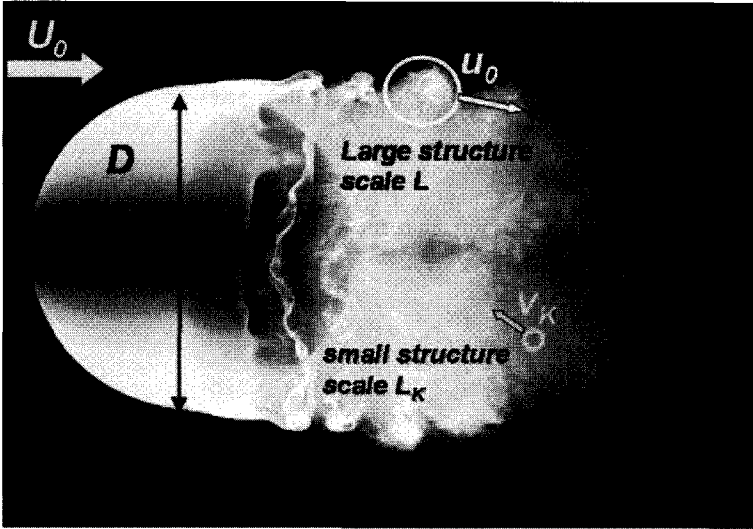


Fig. 1.1 Flow past at sphere at  $Re_D = \frac{U_0 D}{\nu} = 2.10^4$ . Note its continuum of scales from large to small ones which is one of the most fundamental aspects of turbulent fluid flows. Photograph by H. Werlé. Courtesy of J. Délyry, ONERA, France.

characteristic of all turbulent flows. This explains why statistical methods are often considered.

• Three-dimensionality of the vorticity fluctuations

The flow past the sphere is obviously three-dimensional and highly unsteady. Note that the shear layer emanating from the separation line on the cylinder is a region of strong coherent vorticity. In general, vorticity dynamics plays an important role in the analysis of turbulent flows.

• Diffusivity

Spreading of velocity fluctuations becomes stronger as the distance from separation increases. The diffusivity of turbulence is one of the most important properties as far as engineering applications are concerned (mixing enhancement, heat and mass transfer).

### •Broad spectrum

Turbulent fluctuations occur over a wide range of excited length and time scales in physical space leading to broadband spectra in wave number space.

In his book, Hinze [Hinze, 1959] suggests that:

*to describe a turbulent motion quantitatively, it is necessary to introduce the notion of scale of turbulence: a certain scale in time and a certain scale in space.*

In other words, Turbulence is a multi-scale problem with a highly non-linear coupling between these scales. This picture illustrates why the accurate prediction of turbulent flows is such a difficult problem.

#### 1.1.2 *Randomness and coherent structure in turbulent flows*

Though turbulent flows exhibit broad-band spectra, there is evidence from Fig. 1.1 that high-Reynolds number turbulent flows are far from being totally disorganized. What strikes us when looking at the shear layer downstream separation is the roll-up of eddies which can be found downstream with approximatively the same shape. Such eddies preserving a certain spatial organization are called coherent structures and retain their identity for much longer times than the eddy turn-over time characteristic of the turbulent fluctuation.

There are still controversies regarding the definition of coherent structures (see [Haller, 2005]) but there is general agreement on their existence and importance in the transport and mixing phenomena. Therefore the identification of coherent vortices plays an important role in the analysis of turbulent flows. Most common definitions are associated with vortical motion (see [Dubief, 2000] for a review) and turbulent structures are often exhibited by showing a positive iso-value of the criterion  $\mathcal{Q}$  ([Hunt *et al.*, 1988]). Vortex tubes are defined as the regions where the velocity gradient tensor  $\nabla \mathbf{u}$  is positive:

$$\mathcal{Q} = \frac{1}{2} (\boldsymbol{\Omega} : \boldsymbol{\Omega} - \mathbf{S} : \mathbf{S}) \quad (1.1)$$

where  $\boldsymbol{\Omega} = \frac{1}{2} (\nabla \mathbf{u} - {}^t \nabla \mathbf{u})$  is the vorticity tensor and  $\mathbf{S} = \frac{1}{2} (\nabla \mathbf{u} + {}^t \nabla \mathbf{u})$  is the rate of strain tensor.

Examples of coherent structures include for instance the horseshoe vortices observed in turbulent boundary layers (see Fig. 1.2) and mixing layers (see Fig. 1.3), and the vorticity tubes (often called filaments or worms) observed in statistically homogeneous flows (see Fig. 1.4).



Fig. 1.2 Wind-tunnel visualization of large-scale structures in the outer layer of a turbulent boundary layer. Courtesy of M. Stanislas, IMFL, France.

Turbulent flows are neither deterministic nor fully random since the occurrence of coherent structures reflects the existence of finite characteristic scales of spatial correlation as discussed in the next section.

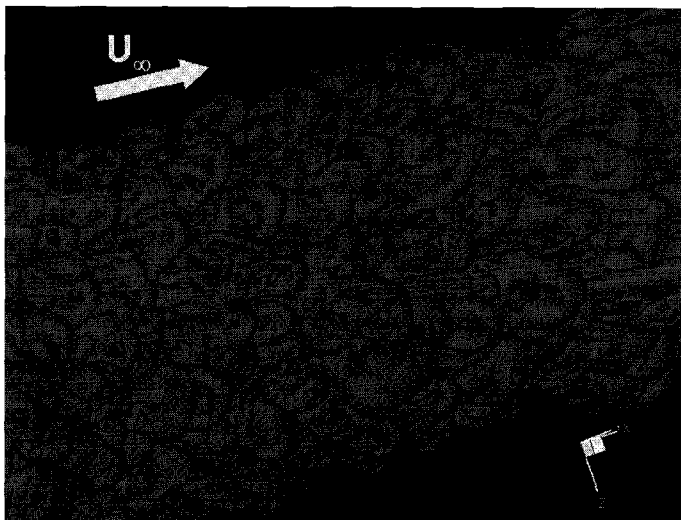


Fig. 1.3 Snapshot of the  $Q$  criterion highlighting turbulent structures in an axisymmetric supersonic wake (Zonal Detached-Eddy-Simulation on a  $20.10^6$  points grid). Note the streamwise array of hairpin vortices, one hairpin triggering another. Courtesy of F. Simon, ONERA, France.

## 1.2 Turbulent Scales and Complexity of a Turbulent Field

### 1.2.1 Basic equations of turbulent flow

The starting point is the Navier–Stokes model for a Newtonian<sup>1</sup> incompressible fluid with dynamic viscosity  $\mu$ , in the absence of body forces:

$$\nabla \cdot \mathbf{u} = 0 \quad (1.2)$$

$$\rho \left( \frac{\partial \mathbf{u}}{\partial t} + \mathbf{u} \cdot \nabla \mathbf{u} \right) = -\nabla P + \mu \nabla^2 \mathbf{u} \quad (1.3)$$

where  $\mathbf{u}$  denotes the velocity field,  $\rho$  the density and  $P$  the pressure field. Note also that we have to add initial and boundary conditions to get a well-posed problem. The non-linear term appearing in the Left-Hand Side

<sup>1</sup>Most of fluids of interest for aerodynamic-oriented studies obey Newton's law of viscosity which relates the viscous stress tensor  $\tau_v$  to the velocity strain:

$$\tau_v = 2\rho\nu\mathbf{S} \quad \text{where} \quad \mathbf{S} = \frac{1}{2} (\nabla\mathbf{u} + {}^t\nabla\mathbf{u}).$$

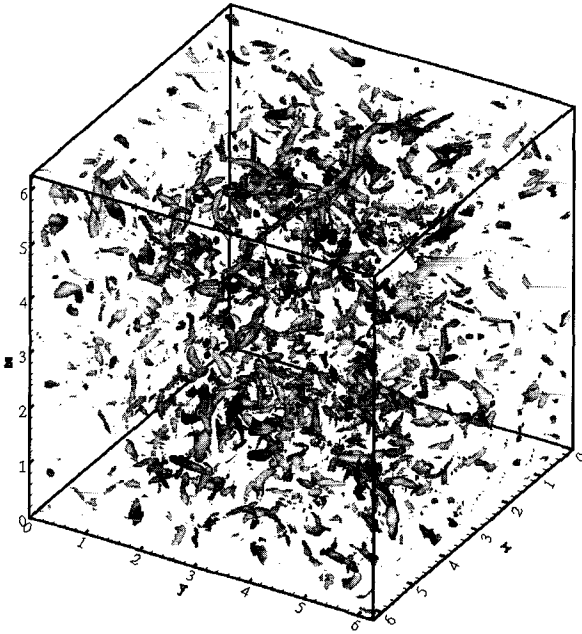


Fig. 1.4 Instantaneous vorticity contours in isotropic turbulence (Large-Eddy Simulation in a periodic cube on a  $128^3$  points grid). Note the worm-like structure of the vorticity field. Courtesy of E. Garnier, ONERA, France.

(LHS) of Eq. 1.3 leads to most of the complex and rich phenomena of fluid mechanics. In particular, this quadratic term is the reason why fluids become turbulent. When this term gets much larger than the diffusive term<sup>2</sup>, the flow becomes unstable and large flow structures break up in smaller and smaller eddies until these are diffused into heat by viscous effects. This important process is called energy cascade and is briefly introduced in § 1.3.

<sup>2</sup>The ratio of the convective and diffusive term is called Reynolds number. Let us consider a flow characterized by a mean velocity  $U_0$  and a typical length scale  $D$  (e.g. comparable to the geometry of surrounding flow, like the diameter of the sphere in Fig. 1.1), the non-linear term in Eq. 1.3 can be estimated as  $U_0^2/D$  and the viscous term as  $\nu U_0/D^2$ . This ratio is then:

$$Re_D = \frac{U_0 D}{\nu}$$

There exists a critical value  $Re_D^*$  of  $Re_D$  above which the flow becomes turbulent while remaining laminar for  $Re_D < Re_D^*$ . The value of  $Re_D^*$  is case-dependent and highly influenced by the level of turbulence of the incoming flow.

It is now worth looking at the energy relation that occurs in turbulent flows of an incompressible fluid. By taking the product of Eq. 1.3 with  $\mathbf{u}$  (by noting  $u^2 = \mathbf{u} \cdot \mathbf{u}$ ) and after some algebraic manipulations, we get:

$$\frac{\partial(u^2/2)}{\partial t} = \underbrace{-\nabla \cdot \left[ \left( \frac{u^2}{2} \right) \mathbf{u} \right]}_{\text{(I) advection}} \quad \underbrace{-\nabla \cdot \left[ \left( \frac{P}{\rho} \right) \mathbf{u} \right]}_{\text{(II) work by pressure forces}} \quad + \quad \underbrace{\nabla \cdot \left[ \frac{1}{\rho} \mathbf{u} \cdot \boldsymbol{\tau}_v \right]}_{\text{(III) work by viscous stresses}} - \underbrace{2\nu \mathbf{S} : \mathbf{S}}_{\text{(IV) } \geq 0}. \tag{1.4}$$

The LHS represents the local change of kinetic energy per unit mass and time. The term (I)+(II) may be interpreted either as the work due to the total pressure  $P + \frac{1}{2}\rho u^2$  (per unit mass and time) or as the change in transport of the total energy  $E = \frac{P}{\rho} + \frac{1}{2}u^2$  (per unit mass) through advection by the velocity  $\mathbf{u}$ . Term (III) represents the work done per unit mass and time by the viscous shear stresses of the turbulent motion. Furthermore, this equation tells us that the last term (IV) on the RHS represents the rate of dissipation of mechanical energy per unit mass to heat:

$$\varepsilon = 2\nu \mathbf{S} : \mathbf{S}. \tag{1.5}$$

By noting  $\boldsymbol{\omega} = \nabla \times \mathbf{u}$ , the vorticity field,  $\varepsilon$  can also be expressed as<sup>3</sup>:

$$\varepsilon = \nu \boldsymbol{\omega}^2 \tag{1.7}$$

$\Omega = \boldsymbol{\omega}^2/2$  is called the enstrophy.

Note that Eqs. 1.5 and 1.7 indicate firstly that turbulence produces gradients and vorticity and secondly that the rate at which energy is dissipated is particularly pronounced in regions where the instantaneous velocity gradients are large e.g. in the smallest eddies. This important feature of turbulent flows is briefly introduced in § 1.3.

---

<sup>3</sup>Noting that  $\nu \mathbf{u} \cdot (\nabla^2 \mathbf{u}) = -\nu (\nabla \times \mathbf{u})^2 + \nabla \cdot [\nu \mathbf{u} \times (\nabla \times \mathbf{u})]$ , Eq. 1.4 can be rewritten as:

$$\frac{\partial(u^2/2)}{\partial t} = -\nabla \cdot \left[ \left( \frac{u^2}{2} + \frac{P}{\rho} \right) \mathbf{u} + \nu (\nabla \times \mathbf{u}) \times \mathbf{u} \right] - \underbrace{\nu (\nabla \times \mathbf{u})^2}_{\text{dissipation}}. \tag{1.6}$$

### 1.2.2 Defining turbulent scales

Although the instantaneous velocity field  $\mathbf{u}(\mathbf{x}, t)$  exhibits a random and unpredictable character, it is fortunately possible to discern distinct statistical quantities such as averaged values. This important feature of the velocity fluctuations (both in time and space) reflect the existence of characteristic scales of statistical correlation. Therefore, we need to introduce some useful measures of the different scales describing the state of turbulent flows. To this end, there exist two quantities commonly used:

- the velocity correlation function
- the energy spectrum

In order to extract some statistical information of the flow, the instantaneous velocity  $\mathbf{u}$  is split into a mean value  $\bar{\mathbf{u}}$  and a fluctuating value as follows:

$$\mathbf{u} = \bar{\mathbf{u}} + \mathbf{u}' \quad (1.8)$$

where  $\mathbf{u}'$  is the random component of motion and consists at any instant of random collection of vortices. The above operation may be seen as a scale separation between the mean and the fluctuating field and this scale separation will be fully discussed in the next chapter.

For ease of explanation, we consider only the one-dimensional fluctuation of the velocity vector  $\mathbf{u}(\mathbf{x}, t)$ . The spatio-temporal correlation function is given by:

$$R(x, x', t, t') = \frac{\overline{u'(x, t) u'(x', t')}}{\overline{u'(x, t) u'(x, t)}}. \quad (1.9)$$

In case of an homogeneous statistically stationary flow, the auto-correlation functions (either in space or time) can be expressed as:

$$\begin{aligned} R(\xi, t_0) &= \frac{\overline{u'(x, t_0) u'(x + \xi, t_0)}}{\overline{u'(x, t_0) u'(x, t_0)}} \\ R(x_0, \tau) &= \frac{\overline{u'(x_0, t) u'(x_0, t + \tau)}}{\overline{u'(x_0, t) u'(x_0, t)}} \end{aligned} \quad (1.10)$$

where  $\xi = x' - x$ ,  $\tau = t' - t$  and  $x_0$  (respectively  $t_0$ ) denote a given location (respectively a given instant). The typical shape of these correlation functions is given in Fig. 1.5.

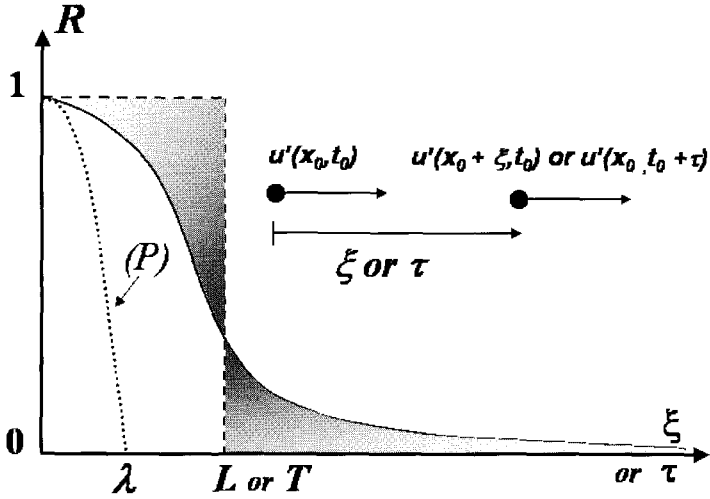


Fig. 1.5 Shape of the correlation function for a turbulent flow and Taylor's scales. The two filled surfaces are equal.

The integral spatial and temporal scales (referred sometimes as *Taylor's macro-scales*) are defined as:

$$L = \int_0^\infty R(x, \tau) d\tau \tag{1.11}$$

$$T = \int_0^\infty R(\xi, t) d\xi. \tag{1.12}$$

The integral scale of turbulence  $L$  provides a measure of the extent of the region over which velocities are appreciably correlated, e.g. the size of the large eddies carrying the energy of the turbulent motion. Similarly  $T$  provides a measure of the duration over which velocities are correlated, e.g. the duration of an eddy turn-over. For obvious reasons,  $T$  is sometimes called Eulerian integral time scale.

As outlined in the beginning of this section, one can also define the length scale of the energy-containing eddies thanks to the energy spectrum in wave number domain which indicates how the energy  $k = \frac{1}{2} u'_i u'_i$  is distributed over length scales (or inverse wave number). A typical shape of this energy spectrum is given in Fig. 1.6.

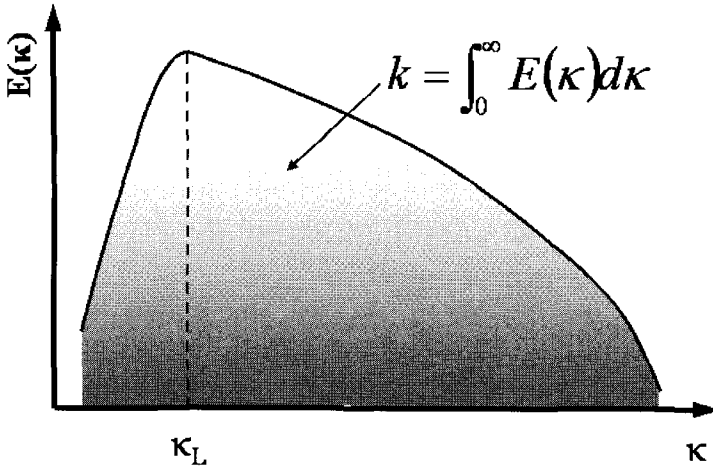


Fig. 1.6 Typical shape of the energy spectrum (e.g. energy spectral density function) in wave number space for a fully turbulent flow. A flow is called fully turbulent when it has reached a state in which the statistical quantities change slowly with respect to time or downstream distance. Both scales are logarithmic.

The wave number  $\kappa_L$  corresponding to the peak in the spectrum defines approximately the length scale of the energy-containing eddies:

$$L \equiv \frac{1}{\kappa_L}. \quad (1.13)$$

Note that the energy spectrum decreases with increasing wave numbers. In other words, most of the energy is at low wave numbers or at large scales in physical space. Therefore the velocity scale of the largest eddies can be characterized by the total kinetic energy as follows:

$$u_0 \equiv \sqrt{2k} \quad (1.14)$$

and the average size of the energy-containing eddies as follows:

$$L \equiv \frac{\int_0^{\infty} \frac{E(\kappa)}{\kappa} d\kappa}{\int_0^{\infty} E(\kappa) d\kappa}. \quad (1.15)$$

Another important length scale can be formed from the correlation function. Indeed, one can show that the correlation function admits the osculation parabola ( $P$ ) defined by  $\mathcal{R} = 1 - \frac{\xi^2}{\lambda^2}$  in the limit as  $\xi \rightarrow 0$ . Therefore, one can also define from the correlation functions, Taylor's micro-scales:

$$\left( \frac{\partial^2 R(\xi, t)}{\partial \xi^2} \right)_{\tau=0} = -\frac{2}{\lambda^2(t)}. \quad (1.16)$$

$\lambda$  is called micro-scale because it is defined by the curvature at the origin of the velocity correlation function, thus depending on the smallest eddies<sup>4</sup>. Note that the Taylor microscale is the characteristic spatial scale of the velocity gradients.

We can also define a micro time-scale in the same way as Taylor's micro-scale was introduced:

$$\left( \frac{\partial^2 R(x, \tau)}{\partial \tau^2} \right)_{x=0} = -\frac{2}{\lambda^2(x)}. \quad (1.19)$$

Nevertheless, the size of the smallest eddies populating a turbulent flow is not equal to  $\lambda$ . Indeed, let us denote as  $v_K$ ,  $L_K$  and  $\tau_K$  the velocity, length and time scales of the smallest turbulent structures. To obtain an expression for  $L_K$ , let us assume that at smallest scales, the convection and the viscous term in Eq. 1.3 are balanced. Assuming respectively  $\mathbf{u} \cdot \nabla \mathbf{u} \approx v_K^2/L_K$  and  $\nu \nabla^2 \mathbf{u} \approx \nu v_K/L_K^2$  we get:

$$Re_K = \frac{v_K L_K}{\nu} = 1. \quad (1.20)$$

Combining Eq. 1.5 and a dimensional analysis, the rate of dissipation of

---

<sup>4</sup>In the framework of isotropic and homogeneous turbulence studies, it is common to express the dissipation rate  $\varepsilon$  as a function of Taylor's micro-scale considering that the rate of strain of the dissipative scales can be evaluated by  $S' \approx u'/\lambda$ . Taylor's microscale can thus be defined as:

$$\lambda^2 = \frac{\overline{u'^2}}{\left( \frac{\partial u'}{\partial \xi} \right)^2} \quad (1.17)$$

and assuming  $\varepsilon = 2\nu \left( \overline{\frac{\partial u'}{\partial \xi}} \right)^2$ , we get:

$$\varepsilon = 2\nu \frac{\overline{u'^2}}{\lambda^2}. \quad (1.18)$$

This relation shows that the Taylor microscale characterizes the dissipative phenomena.

kinetic energy can be expressed as:

$$\varepsilon \approx \frac{\nu}{\tau_K^2} \quad (1.21)$$

combining these expressions with the additional relation  $v_K = \frac{L_K}{\tau_K}$  we find:

$$\tau_K = \left(\frac{\nu}{\varepsilon}\right)^{\frac{1}{2}} \quad L_K = \frac{\nu^{\frac{3}{4}}}{\varepsilon^{\frac{1}{4}}} \quad v_K = (\nu\varepsilon)^{\frac{1}{4}} \quad (1.22)$$

The scales  $L_K$  and  $v_K$  are called the *Kolmogorov micro-scales* of turbulence and characterize the energy-dissipating eddies.

It is now worth giving the relationships between the integral, Taylor and Kolmogorov length scales. For this purpose, let us consider the Reynolds number characterizing the largest scale of the turbulent motion:

$$Re_L = \frac{u_0 L}{\nu}. \quad (1.23)$$

The rate of dissipation of kinetic energy can also be expressed (see 1.3.1) with  $u_0$  and  $L$  as follows:

$$\varepsilon \approx \frac{u_0^3}{L}. \quad (1.24)$$

Combining Eqs. 1.24 with 1.23 and 1.18 yields:

$$\frac{L_K}{L} \approx Re_L^{-\frac{3}{4}} \quad (1.25)$$

$$\frac{\lambda}{L} \approx Re_L^{-\frac{1}{2}} \quad (1.26)$$

$$\frac{L_K}{\lambda} \approx Re_L^{-\frac{1}{4}}. \quad (1.27)$$

Thus the Taylor micro-scale scale<sup>5</sup> lies somewhere between the Kolmogorov micro-scale,  $L_K$ , and the integral length scale,  $L$ . Furthermore, these relations illustrate again that turbulent flows contain motions with a broad range of scales and Eq. 1.25 indicates that the higher the Reynolds number, the broader this range of scales. Correlatively, the main difference between

---

<sup>5</sup>The Reynolds number  $Re_\lambda = u\lambda/\nu$  is often used to characterize homogeneous flows and  $Re_\lambda$  satisfies  $Re_\lambda \approx \sqrt{Re_L}$ . In case of isotropic turbulence, Hinze [Hinze, 1959] indicates that the proportionality constant in the above relation is such that  $Re_\lambda = 4\sqrt{Re_L}$ .

two turbulent flows with the same integral scale but with different Reynolds numbers is the size of the smallest eddies.

### 1.2.3 A glimpse at numerical simulations of turbulent flows

Solving the unsteady Navier–Stokes equations implies that all scales of motion have to be resolved from the largest scale down to the Kolmogorov scale  $L_K$ . In other words, the spatial separation of the sampling points  $\Delta$  cannot be larger than  $L_K$ . Thus the number of grid points  $N_{xyz}$  needed to perform a three-dimensional Direct Numerical Simulation (DNS) scales such as:

$$N_{xyz} \approx Re_L^{\frac{9}{4}}. \quad (1.28)$$

The timescale of the smallest eddies also provides a bound for the maximum time step,  $\Delta t$ , allowed. To get an accurate time description, a fluid particle cannot move by more than one grid spacing per time step. The minimum number of time steps necessary to complete a large-eddy turn-over time  $T$  is:

$$N_t \approx \frac{T}{\Delta t} \approx \frac{T}{L_K/u_0} \approx \frac{T}{L/u_0} Re_L^{\frac{3}{4}}. \quad (1.29)$$

Assuming that the CPU time required by a numerical algorithm is proportional to the number of operations, the cost of the simulation scales as:

$$\text{computing time} \propto N_{xyz} \cdot N_t \propto \tilde{C} \cdot Re_L^3 \quad (1.30)$$

where  $\tilde{C}$  is the cost of the algorithm expressed in [*s/grid point/ iteration*] which depends both on the numerical solver and on the speed of the computer. Further, if walls are present, the near-wall structure need to be resolved leading to an even stronger dependence on the Reynolds number. It becomes obvious that for large Reynolds number flows, DNS require computer resources much larger than the available supercomputer capacities<sup>6</sup>.

---

<sup>6</sup>Kaneda *et al.* [Kaneda *et al.*, 2003] performed a DNS (e.g.  $\kappa_{max} L_K \approx 1$ ) of isotropic turbulence in a periodic cube at a Reynolds number based on Taylor’s microscale  $Re_\lambda = 1200$  on a  $4096^3$  points grid e.g.  $N_{xyz} > 68.10^9$  nodes. The calculation was performed on the recently developed Earth Simulator with a peak performance and main memory of 40TFlops and 10TBytes respectively which is far beyond the capacities of “usual” supercomputers! To the authors’ knowledge, this calculation represents the highest value of  $Re_\lambda$  obtained in a DNS.

For practical Reynolds number flows<sup>7</sup>, we cannot solve the dynamics of all scales directly but only those of certain scales. This poses a challenge for accurate simulations of the resolved scales because the non-linearity of the Navier–Stokes equations is responsible for strong interactions between all scales as discussed in the next section.

### 1.3 Inter-scale Coupling in Turbulent Flows

#### 1.3.1 The energy cascade

The most popular feature related to the dynamics of turbulence is the concept of kinetic energy cascade. It tells us that the turbulent kinetic energy (TKE) is created by some external forces or hydrodynamic instabilities at a large scale  $L$  (typically of the order of the integral scale of turbulent fluctuations) and is then transferred by inviscid nonlinear mechanisms toward small scales where the viscous dissipative processes transform it into heat. This mechanism is illustrated in Fig. 1.7 where one can distinguish three typical regions in the energy spectrum  $E(\kappa)$ :

- The first region consists of the largest eddies where turbulence energy is generated by the mean flow. These scales are coupled with the mean field and are dependent on turbulence production mechanisms (external forces, hydrodynamic instabilities). Consequently, they do not possess a universal character. The large-scale region is usually modelled by a spectrum taken to be proportional to  $\kappa^4$ . This subrange is then followed by a peak in which energy is fed at the integral length scale  $L$ . Assuming that the energy-containing eddies break up at a time scale of their turn over, the rate at which energy (per unit mass) enters the cascade is:

$$\varepsilon_I \approx \frac{u_0^2}{L/u_0} = \frac{u_0^3}{L} \quad (1.31)$$

and does not depend on the viscosity  $\nu$ .

- The second region is associated with the intermediate scales  $l$  such as  $L_K \ll l \ll L$  and it is the region in which energy is transferred to smaller

---

<sup>7</sup>In practice, the integral scale of turbulence  $L$  as well as the velocity scale  $u_0$  of the largest eddies are generally about one order of magnitude smaller than the characteristic dimensions of the flow (like the body size  $D$ ) and the free-stream velocity  $U_0$ . Therefore,  $Re_L/Re_D \leq 10^{-2}$  but  $Re_L$  remains quite large because  $Re_D$  usually lies in the range  $10^4 - 10^8$  especially in aeronautical applications.

scales by non-linear interaction with no action by viscosity or condition of formation. The extent of this inertial subrange depends on the Reynolds number. In that region, the only relevant parameters are the length scale under investigation  $\kappa = 1/l$  and the mean dissipation rate of turbulent energy  $\varepsilon_T$ . Since energy is transferred without loss,  $\varepsilon_T$  remains constant and equal to the finite mean energy<sup>8</sup> dissipation rate:

$$\varepsilon_T \approx \varepsilon_I. \quad (1.32)$$

The spectrum in this inertial subrange, frequently called the Kolmogorov spectrum law, reads as:

$$E(\kappa) = K_0 \varepsilon^{2/3} \kappa^{-5/3} \quad (1.33)$$

where  $K_0$  is the Kolmogorov constant that lies in the range 1.4 – 1.7.

- The last region contains the smallest scales for which viscous effects become important and where the kinetic energy is dissipated into heat. The rate of dissipation in the smallest eddies is  $\varepsilon = 2\nu S_{ij} S_{ij}$  where the rate of strain associated with the smallest scales can be evaluated by  $S \approx \frac{v_K}{L_K}$ . Since energy is transferred without loss, we get:

$$\frac{u_0^3}{L} \approx \nu \frac{v_K^2}{L_K^2} \quad (1.34)$$

which combined with the relation  $\frac{v_K L_K}{\nu} = 1$  allows us to recover the Kolmogorov microscales introduced in §1.2.2.

The basic physical mechanism responsible for this energy transfer toward smaller and smaller scales is the vortex stretching: when vortices experience a stretching along their main rotation axis, they are elongated in this direction. In incompressible flows, this will result in a decrease of the diameter of the vortex, the volume occupied by the vortex being constant. This mechanism being inviscid by nature, one can reasonably assume that the angular momentum of the vortex (here modelled as a vortex tube) is an invariant of this transformation, leading to an increase of the axial component of the vorticity. As a final result, the kinetic energy has been transferred toward smaller scales, since the radius of the vortex has been decreased.

---

<sup>8</sup>When conditions are statistically steady.

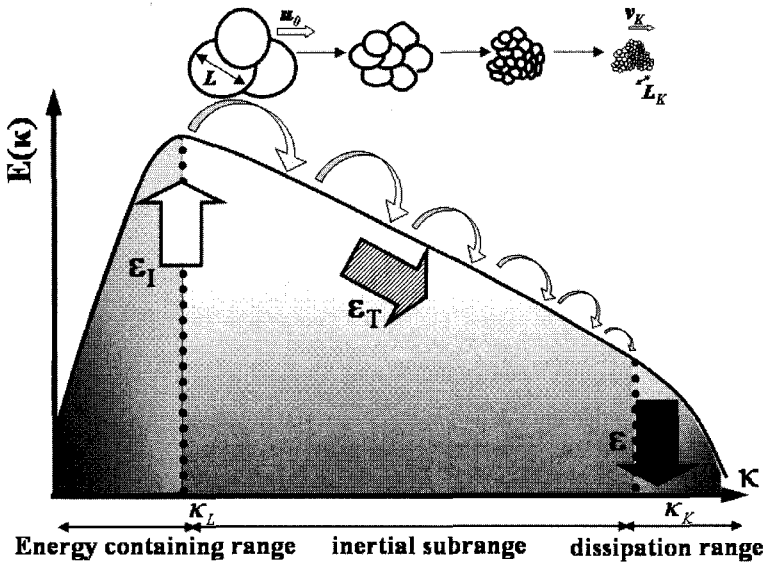


Fig. 1.7 Sketch of the energy cascade. In physical space, the large eddies are broken into smaller and smaller eddies. The energy is injected into the flow by the driving mechanisms at the rate  $\varepsilon_I$ , transferred to smaller scales at the rate  $\varepsilon_T$  and dissipated into heat at the rate  $\varepsilon$ . The local equilibrium assumption is expressed by the equality  $\varepsilon_I = \varepsilon_T = \varepsilon$ . Both scales are logarithmic.

### 1.3.2 Inter-scale interactions

The previously seen local cascade picture of turbulent transfer assumes a primary interaction of each scale of motion with adjacent scales. More precisely, the hypothesis of Kolmogorov states that the cascade is essentially unidirectional: energy is mainly transferred from larger to smaller eddies and the flux of energy in the inertial subrange is independent of the eddy size. However, an important question deals with the localness of the kinetic energy cascade mechanism in terms of wave number: does an eddy of size  $l$  have significant interactions (e.g. transfer of a non-negligible amount of kinetic energy) with much smaller or much larger scales?

To get a deeper insight into the inter-scale couplings in incompressible turbulent flows, it is useful to write the momentum equation in the Fourier space. Noting the wave vector  $\kappa$  and the corresponding velocity mode  $\hat{\mathbf{u}}(\kappa)$  (here the explicit dependence on time is omitted)

$$\widehat{\mathbf{u}}(\boldsymbol{\kappa}) = \frac{1}{(2\pi)^3} \int \mathbf{u}(\mathbf{x}) e^{-i\boldsymbol{\kappa} \cdot \mathbf{x}} d^3 \mathbf{x}, \quad i^2 = -1 \quad , \quad (1.35)$$

and applying the Fourier transform to the momentum equation of the Navier–Stokes equations, one obtains<sup>9</sup>:

$$\left( \frac{\partial}{\partial t} + \nu \boldsymbol{\kappa}^2 \right) \widehat{u}_i(\boldsymbol{\kappa}) = T_i(\boldsymbol{\kappa}) \quad (1.37)$$

in which the linear terms with respect to the velocity amplitude are grouped into the left-hand-side and describe respectively the time dependency and changes due to viscous effects. The non-linear term  $T_i(\boldsymbol{\kappa})$  in the right-hand-side represents the effect of convection and pressure and takes the following the form<sup>10</sup>:

$$T_i(\boldsymbol{\kappa}) = M_{ijm}(\boldsymbol{\kappa}) \int \int \widehat{u}_j(\mathbf{p}) \widehat{u}_m(\mathbf{q}) \delta(\boldsymbol{\kappa} - \mathbf{p} - \mathbf{q}) d^3 \mathbf{p} d^3 \mathbf{q} \quad , \quad (1.39)$$

with:

$$M_{ijm}(\boldsymbol{\kappa}) = -\frac{i}{2} (\kappa_m P_{ij}(\boldsymbol{\kappa}) + \kappa_j P_{im}(\boldsymbol{\kappa})) \quad , \quad (1.40)$$

in which  $\delta$  is the Kronecker symbol ( $\delta(\boldsymbol{\kappa}) = 0$  if  $\boldsymbol{\kappa} \neq 0$ ) and  $P_{ij}(\boldsymbol{\kappa})$  is the projection operator on the plane orthogonal to the vector  $\boldsymbol{\kappa}$ . This operator is written:

$$P_{ij}(\boldsymbol{\kappa}) = \left( \delta_{ij} - \frac{\kappa_i \kappa_j}{\boldsymbol{\kappa}^2} \right). \quad (1.41)$$

Note firstly that the non-linear convective term becomes a convolution in wave number space and it shows that all wave numbers are involved. Secondly, it is observed that the non-linear term makes three wave numbers, *i.e.* three scales appearing, defining a triad. Such interactions are thus referred to as triadic interactions. Note also that this triadic nature of the

<sup>9</sup>Note that continuity requires in spectral space:

$$\nabla \cdot \mathbf{u} = 0 \Leftrightarrow \boldsymbol{\kappa} \cdot \widehat{\mathbf{u}}(\boldsymbol{\kappa}) = 0 \quad (1.36)$$

and shows orthogonality of the wave vector  $\boldsymbol{\kappa}$  and the mode  $\widehat{\mathbf{u}}(\boldsymbol{\kappa})$ .

<sup>10</sup>The relation is obtained by using the following property of the Fourier transformation:

$$f(\mathbf{x})g(\mathbf{x}) \Leftrightarrow \widehat{f} \star \widehat{g} = \int \widehat{f}(\mathbf{p}) \widehat{g}(\boldsymbol{\kappa} - \mathbf{p}) d^3 \mathbf{p} = \int \int \widehat{f}(\mathbf{p}) \widehat{g}(\mathbf{q}) \delta(\boldsymbol{\kappa} - \mathbf{p} - \mathbf{q}) d^3 \mathbf{p} d^3 \mathbf{q} \quad (1.38)$$

where  $\int \delta(\boldsymbol{\kappa}) d\boldsymbol{\kappa} = 1$ .

non-linear interactions is intrinsically related to the mathematical structure of the Navier–Stokes equations.

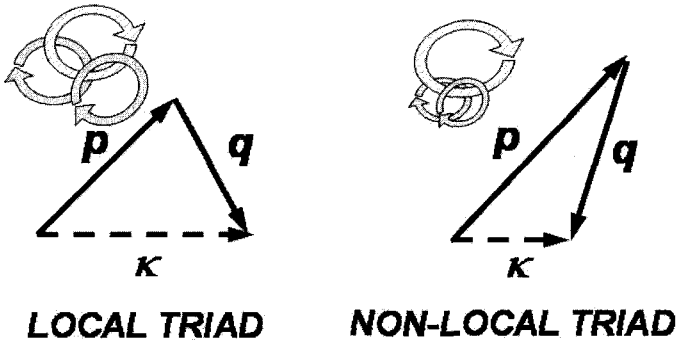


Fig. 1.8 Typology of triadic interactions. The flowfield at wave number  $\kappa$  is seen to interact with the wave vector component  $\mathbf{p}$  and  $\mathbf{q}$  satisfying  $\kappa = \mathbf{p} + \mathbf{q}$ .

Triadic interactions are usually classified according to the topology of the triangle formed by the three wave vectors  $\kappa$ ,  $\mathbf{p}$  and  $\mathbf{q}$  (see Fig. 1.8):

- local interactions are interactions between three scales having approximately the same size, *i.e.*

$$\frac{1}{a} \leq \max \left\{ \frac{p}{\kappa}, \frac{q}{\kappa} \right\} \leq a, \quad a = O(1)$$

- non-local or distant interactions are associated with triads such that  $\kappa \ll p \sim q$  or  $\kappa \sim q \gg p$ , e.g. between one long-wave number and two high-wave-number modes. Correlatively in physical space, these interactions correspond to the interaction between one large scale and two small ones.

It is also possible (see [Lesieur, 1990]) to obtain from Eq. 1.37, an equation describing the evolution of  $E(\kappa)$ , e.g. the energy at a particular wave number  $\kappa$ . This equation includes terms which describe the non-linear transfer of energy from one scale to another via triadic interaction. Theoretical works conducted using asymptotic series expansions, renormalization

methods or two-point closures of turbulence and detailed analyzes of direct numerical simulations show that (see [Sagaut, 2005] for a review):

- The kinetic energy cascade is mainly due to local energy transfers induced by non-local triadic interactions: the two small scales are advected/stretched by the velocity field induced by the large one, while the large one experienced a random forcing due to the two small ones, resulting in a diffusion in the wave number space.
- Most of the kinetic energy exchanges at wave number  $\kappa$  occur within the range  $[\kappa/2, 2\kappa]$ .
- In the asymptotic limit of infinite Reynolds number, distant interactions can represent up to 25% of the total kinetic energy transfers.
- In non-isotropic cases, anisotropy at large scale is observed to contaminate the small scales (anisotropy cascade). Some very non-local anisotropy transfers without kinetic energy transfers are present.

These results show that the dynamics of turbulence is a multiscale phenomenon by nature: the essential non-linear mechanisms are based upon the interactions between scales of very different sizes. Therefore, no scales can be neglected without polluting the dynamics of all scales, including the large ones. A model must be used to mimic the influence of discarded scales.

This page is intentionally left blank

## Chapter 2

# Turbulence Simulation and Scale Separation

### 2.1 Numerical Simulation of Turbulent Flows

As has been mentioned in the first chapter, a turbulent flow is characterized by a very wide range of scales (both in space and time). Due to this specificity, the direct resolution (referred to as DNS – *Direct Numerical Simulation*) of a given three-dimensional problem has been shown to scale as  $O(Re_L^3)$ , where  $Re_L$  denotes the Reynolds number based on the spatial integral scale  $L$ .

Since most of the turbulent flows encountered in practical configurations, and particularly in aerospace applications are characterized by some very high values of the Reynolds number (typically  $10^4 < Re_L < 10^8$ ), the direct numerical simulation of turbulent flows remains out of reach from the capabilities of actual supercomputers. To illustrate this point, Spalart *et al.* [Spalart *et al.*, 1997] indicate that the direct simulation of the flow over the wing of a commercial aeroplane would require the use of  $10^{16}$  discretization points!

For several years it has thus clearly appeared necessary to develop some specific approaches to reduce the cost associated with the simulation of turbulent flows, leading to the emergence of several numerical techniques. The global idea of such approaches is to reduce the number of degrees of freedom of the problem, by resolving only some specific scales of the flow. The principle is then to perform a scale segregation, and to separate the structures of the flow which are identified as being of direct practical interest from other scales which can remain unresolved, and only accounted for through the use of a mathematical model. One common point between the different cost reduction approaches is that they all (at least theoretically) rely on a scale separation operator which performs the distinction between

resolved and unresolved scales. Depending on the intrinsic nature of this scale separation operator, two main classes of methods arise:

- The first one relies on a statistical description of the flow. In this case, the involved scale separation operator thus relies on an averaging procedure. In practice, all the turbulent motion of the flow is then unresolved and has to be described thanks to the use of a mathematical model. Due to this definition, the cost of the simulations is significantly reduced in comparison with DNS, thus leading to some simulations which can be easily performed with usual computers. However, since the resolved field is limited to a statistical description of the flow, the intermittency of the turbulent phenomenon cannot be returned by such simulations, and highly unsteady flow phenomena cannot be accurately described. On the other hand, and because of their affordable computational cost, these approaches (referred to as RANS – *Reynolds-Averaged Navier-Stokes*) are still the most commonly used for industrial applications.
- The second one relies on a scale separation between the largest energy-containing eddies of the flow and the small scales responsible for the energy dissipation. Here, the scale separation operator is then (at least formally) defined as a low-pass filter in the wavenumbers space. Since the cutoff wavenumber can be arbitrarily fixed, this approach then provides a full description of unsteady events, up to the cutoff frequency related to the cutoff wavenumber. This approach (referred to as LES – *Large-Eddy Simulation*) thus appears as an interesting compromise between the prohibitive cost of DNS and the averaged description of the flow provided by RANS. However, the classical assumptions for LES suggest that the cutoff wavenumber should be taken in the inertial range of the energy spectrum<sup>1</sup>, so that the computational costs are rapidly increasing when complex flow physics and realistic values of the Reynolds number are considered.

As already said, one of the main properties of a turbulent flow is its multiscale aspect. Several ranges of characteristic scales co-exist in such flows,

---

<sup>1</sup>A commonly retained assumption in LES is that the small unresolved scales are nearly homogeneous and isotropic.

and are associated to some specific physical mechanisms. For this reason, it can be of great interest to account for this particularity of turbulent flows when deriving some physical and mathematical models and associated numerical techniques for their simulation. Such methods are referred to as the *multilevel* or *multiresolution* approaches, and rely on an explicit splitting of the flow variables into several bands in the wavenumber space. This splitting leads to a hierarchical organization of the flow structures, as a function of their sizes. The global idea of the multilevel approaches will then be to consider some specific numerical treatments for each range of scales from this classification. These methods can then be formally classified in two distinct categories: the first one consists in taking advantage of a multilevel splitting of the flow variables to derive some improved mathematical closures for the turbulent flow simulation approaches. Such improved closures then take into account some more complex flow phenomena than conventional models, thus resulting in a global increased accuracy of the simulations. The second category is, on the other hand, oriented towards a reduction of the cost of the simulations, while globally keeping the same accuracy as conventional approaches. To this end, the global idea is to use some specific numerical treatments for each range of scales of the flow, and more particularly to treat the scales which are associated to the largest computational costs with less accuracy than the other ones.

The aim of this chapter is to present the (classical) scale and multiscale separation concepts. Detailed emphasis will first be put on the two main scale separation approaches used in turbulent flows simulations, namely the averaging and filtering approaches. Then, the extension of the scale separation concept to the case of a multilevel splitting of the flow variables will be carried out. In each case, some specific notations, together with the associated evolution equations for the resolved and unresolved quantities will be derived.

## 2.2 Reducing the Cost of the Simulations

As mentioned above, it is necessary to reduce significantly the cost associated to the numerical simulation of turbulent flows. Such a reduction is practically obtained thanks to some specific methods which rely on the concept of scale separation. This concept will be detailed and discussed in the most general case in this section.

### 2.2.1 Scale separation

At this point, we will place ourselves in the most general case. First of all, we introduce a scale separation operator  $\mathcal{F}$ . Here, no particular form is prescribed for  $\mathcal{F}$ . By applying this separation operator to any variable of the problem  $f(\mathbf{x}, t)$ , where  $\mathbf{x} = (x_1, x_2, x_3)^T$  is the space coordinate vector and  $t$  denotes the time, we obtain the following decomposition of this quantity:

$$f = \bar{f} + f' \quad (2.1)$$

where  $\bar{f} = \mathcal{F}(f)$  will be referred to as the *resolved* part of  $f$ , and  $f' = (Id - \mathcal{F})(f)$  to as its *unresolved* part ( $Id$  denotes the identity operator). In the particular context of turbulence simulation, this decomposition will be applied to the aerodynamic variables such as the velocity field  $\mathbf{u}$ , or the pressure  $P$ .

### 2.2.2 Navier–Stokes-based equations for the resolved quantities

The global idea of all the different cost reduction approaches in turbulence simulation will then be to consider only the resolved variables  $\bar{f}$ , while adding a mathematical closure to take into account the unresolved ones  $f'$ . For this, it is necessary to derive some equations that will allow for the description of the dynamics of the resolved aerodynamic field. As will be seen below, the evolution equations for the resolved field look very similar to the classical Navier–Stokes equations. However, some additional terms appear in the equations, which account for all the missing interactions between the resolved and unresolved fields.

As a starting point, we consider the set of the Navier–Stokes equations written for an incompressible Newtonian fluid:

$$\begin{aligned} \nabla \cdot \mathbf{u} &= 0 \\ \frac{\partial \mathbf{u}}{\partial t} + \nabla \cdot (\mathbf{u} \otimes \mathbf{u}) &= -\nabla p + \nu \nabla^2 \mathbf{u} \end{aligned} \quad (2.2)$$

where  $\mathbf{u} = (u_1, u_2, u_3)^T$  denotes the velocity vector,  $t$  the time,  $p = P/\rho$  with  $P$  the pressure and  $\rho$  the density, and  $\nu$  is the kinematic viscosity of the fluid.

---

<sup>2</sup>Obviously, the general scale separation operator, as it will be detailed later in this chapter is introduced in the aim of reducing the complexity of the problem, *i.e.* decreasing the number of degrees of freedom. As a consequence, such an operator is defined so that it decreases the quantity of information of the considered field.

The Navier–Stokes-based equations for the resolved field are then obtained by applying the scale separation operator  $\mathcal{F}$  on the set of Eqs. (2.2). At this point, it is useful to introduce some notations that will be used in the following. We define the commutator  $[\cdot, \cdot]$  between two operators  $a$  and  $b$  as:

$$[a, b] f = a \circ b(f) - b \circ a(f). \quad (2.3)$$

We also introduce the following cross product operator between two vectors  $\mathbf{u}$  and  $\mathbf{v}$ :

$$\mathcal{B}(\mathbf{u}, \mathbf{v}) = \mathbf{u} \otimes \mathbf{v}. \quad (2.4)$$

After application of the scale separation operator and rewriting the equations as functions of the resolved variables only, the set of the Navier–Stokes-based equations for the resolved field reads:

$$\begin{aligned} \nabla \cdot \bar{\mathbf{u}} &= -A_1 \\ \frac{\partial}{\partial t} \bar{\mathbf{u}} + \nabla \cdot (\bar{\mathbf{u}} \otimes \bar{\mathbf{u}}) &= -\nabla \bar{p} + \nu \nabla^2 \bar{\mathbf{u}} - (A_2 + A_3 + A_4). \end{aligned} \quad (2.5)$$

The four additive terms  $A_1$  to  $A_4$  are some functions of the original (global) field, and cannot be computed directly from the resolved field. Their expressions are given by:

$$\begin{aligned} A_1 &= [\mathcal{F}, \nabla \cdot] \mathbf{u} \\ A_2 &= \nabla \cdot [\mathcal{F}, \mathcal{B}](\mathbf{u}, \mathbf{u}) \\ A_3 &= [\mathcal{F}, \nabla \cdot] \mathcal{B}(\mathbf{u}, \mathbf{u}) + [\mathcal{F}, \nabla] p + \nu [\mathcal{F}, \nabla^2] \mathbf{u} \\ A_4 &= \left[ \mathcal{F}, \frac{\partial}{\partial t} \right] \mathbf{u}. \end{aligned} \quad (2.6)$$

These terms are associated with different sources. Indeed, the term  $A_2$  is directly linked to the non-linearity of the convective term of the Navier–Stokes equations, and thus can not be avoided. On the other hand, the three other terms  $A_1$ ,  $A_3$  and  $A_4$  are relative to some possible commutation errors between the scale separation operator and the spatial and temporal partial derivatives. This indicates that the scale separation operator should be chosen in such a way that it commutes with these differential operators. It should be noticed here that a non-zero commutation error with the space derivatives leads to a non-zero RHS term in the continuity equation, thus meaning that the resolved field is no longer incompressible.

### 2.2.3 Navier–Stokes-based equations for the unresolved quantities

For several reasons that will be specified later in the book, it is also useful to derive some evolution equations for the unresolved field. This particular set of equations is very simply obtained by subtracting the set of the Navier–Stokes-based equations for the resolved field Eqs. (2.5) from the original set of the Navier–Stokes Eqs. (2.2), and using the property  $f' = f - \bar{f}$ . The following set of equations is then obtained for the unresolved field:

$$\begin{aligned} \nabla \cdot \mathbf{u}' &= A_1 \\ \frac{\partial}{\partial t} \mathbf{u}' + \nabla \cdot (\mathbf{u}' \otimes \mathbf{u}' + \mathbf{u}' \otimes \bar{\mathbf{u}} + \bar{\mathbf{u}} \otimes \mathbf{u}') &= -\nabla p' + \nu \nabla^2 \mathbf{u}' + A_2 + A_3 + A_4. \end{aligned} \quad (2.7)$$

The two next sections will now be devoted to the description of two particular approaches of the scale separation procedure: the averaging and filtering approaches.

## 2.3 The Averaging Approach: Reynolds-Averaged Numerical Simulation (RANS)

The idea of averaging consists in forgetting about the whole set of flow details and considers that the flow can be described as a mean flow, smoother than the instantaneous field, and a fluctuating field, defined as the difference between the instantaneous field and the mean field.

### 2.3.1 Statistical average

In order to extract statistics of the flow, any turbulent quantity  $f$  is here split into a *mean* value  $\bar{f}$  and a *fluctuating* value  $f'$  as

$$f = \bar{f} + f'. \quad (2.8)$$

The simplest way to define  $\bar{f}$  is to use the ensemble averaging. One may imagine repeating  $N$  times the experiment with identical boundary conditions, starting from initial conditions as close as possible. Due to the turbulence, any turbulent quantity  $f$  will take different values  $f_i$ ,  $i = 1..N$  for every realization of the flow. The so-called *ensemble average* is obtained by taking the arithmetic mean of the samples  $f_i$  when  $N$  tends to infinity :

$$\bar{f} = \lim_{N \rightarrow \infty} \frac{1}{N} \sum_{i=1}^{i=N} f_i. \quad (2.9)$$

However, for practical reasons, an unsteady computation is only carried out once. When performing time-dependent calculations, decomposition Eq. (2.8) can still be used and the bar operator can be considered as a time-average over  $T$ . The averaging time  $T$  has to be greater than the characteristic time scale of turbulence  $\tau$  and smaller than the characteristic period  $\theta$  for the time evolution of the mean properties :

$$\tau \ll T \ll \theta. \quad (2.10)$$

The causal average operator can thus be defined as :

$$\bar{f}(t) = \frac{1}{T} \int_{t-T}^t f(s) ds \quad \text{with } T \gg \tau \quad (2.11)$$

which is in fact a low-pass filter with  $\frac{1}{T}$  representing the cut-off frequency<sup>3</sup>.

In the case of steady flows, it is common to introduce the temporal average defined as

$$\langle f \rangle_T = \lim_{T \rightarrow \infty} \frac{1}{T} \int_0^T f(s) ds. \quad (2.12)$$

The ergodicity principle, as demonstrated by Monin and Yaglom [Monin and Yaglom, 1971], states that the time-averaged quantity  $\langle f \rangle_T$  converges to the ensemble-averaged quantity  $\bar{f}$  in the sense  $\overline{(\langle f \rangle_T - \bar{f})^2} = 0$  if and only if:

$$\lim_{T \rightarrow \infty} \frac{1}{T} \int_0^T \overline{f' f'} ds = 0. \quad (2.13)$$

For a steady turbulence, this hypothesis thus appears as valid, since the fluid particles are de-correlated for large time separations. That means that in the context of steady flows, the ensemble average (2.9) can be simply replaced by the temporal average (2.12).

---

<sup>3</sup>This URANS approach means that there is a “spectral gap” between the turbulence and the unsteadiness of the mean field.

### 2.3.2 Reynolds-Averaged Navier–Stokes equations

The aim of this section is to derive some evolution equations for the averaged aerodynamic field, *i.e.* to rewrite the set of Eqs. (2.5) in the particular case of a statistical averaging of the flow variables ( $\mathcal{F}$  referring here to a statistical averaging operator). The averaging operator, as defined in the previous section satisfies several mathematical properties ( $a$  denotes a constant parameter, and  $f$  and  $g$  are some functions of space and time):

$$\overline{\overline{a}} = a \quad (2.14)$$

$$\overline{a f} = a \overline{f} \quad (2.15)$$

$$\overline{f + g} = \overline{f} + \overline{g} \quad (2.16)$$

$$\left[ \frac{\partial}{\partial \xi}, \overline{(\cdot)} \right] = 0, \quad \xi = t, x_1, x_2, x_3 \quad (2.17)$$

$$\overline{\overline{f}} = \overline{f} \quad (2.18)$$

$$\overline{f'} = 0 \quad (2.19)$$

$$\overline{f \overline{g}} = \overline{f} \overline{g} \quad (2.20)$$

$$\overline{f g} = \overline{f} \overline{g} + \overline{f' g'}. \quad (2.21)$$

The three first properties are classical and referred to as constant conservation, linearity, and associativity of the averaging operator, respectively. The fourth property (commutation with time and space derivatives) is very important, since it leads to several simplifications in the additional terms (given by Eq. (2.6)) arising in the Navier–Stokes-based equations for the resolved (averaged) quantities.

Indeed, when considering this commutation property, together with the two last properties (idempotence), the following simplification of the additive terms is obtained:

$$\begin{aligned} A_1 = A_3 = A_4 = 0 \\ A_2 = \nabla \cdot \tau_{TRANS} \end{aligned} \quad (2.22)$$

where  $\tau_{TRANS}$  is referred to as the *Reynolds stress tensor* :

$$\tau_{TRANS} = \overline{\mathbf{u}' \otimes \mathbf{u}'}. \quad (2.23)$$

This tensor represents all the interactions between the mean flow and turbulence. It should be noted that its trace is equal to twice the Turbulent Kinetic Energy (TKE)  $k = \frac{1}{2} \overline{u'_i u'_i}$ .

With these simplifications, the set of the so-called *Reynolds-Averaged Navier–Stokes* (RANS) equations is expressed as:

$$\begin{aligned} \nabla \cdot \bar{\mathbf{u}} &= 0 \\ \frac{\partial}{\partial t} \bar{\mathbf{u}} + \nabla \cdot (\bar{\mathbf{u}} \otimes \bar{\mathbf{u}}) &= -\nabla \bar{p} + \nu \nabla^2 \bar{\mathbf{u}} - \nabla \cdot \tau_{RANS}. \end{aligned} \quad (2.24)$$

So far, the Reynolds stress tensor remains an unknown term, since it cannot be expressed as a function of the resolved field only. A specific mathematical closure has then to be introduced to model the effect of the Reynolds stresses. This point has received much attention in the last century, leading to the emergence of a large number of approaches to provide a closure for the Reynolds stress tensor, and a link between the mean field values and the Reynolds stresses. The full and exhaustive survey of such models is beyond the objectives of this book, but the interested reader can refer for instance to the monograph by Piquet [Piquet, 1999]. The next chapters will focus on some specific models which rely on the concept of a multiscale decomposition.

### 2.3.3 Phase-Averaged Navier Stokes equations

In the framework of unsteady flows with a pronounced periodic character, specific averaging procedures have been proposed in the literature. Indeed, to extract the organized wave motion from the background field of finite turbulent fluctuation, Hussain and Reynolds [Hussain and Reynolds, 1970], decompose any fluctuating quantity  $f(\mathbf{x}, t)$  as :

$$f(\mathbf{x}, t) = \bar{f}(t) + \tilde{f}(\mathbf{x}, t) + f'(\mathbf{x}, t) \quad (2.25)$$

where  $\bar{f}$  is the mean value similar to eq. (2.8),  $\tilde{f}$  the statistical contribution of the organized motion and  $f'$  the fluctuating part of turbulence. The authors introduced the phase-average procedure<sup>4</sup> defined as:

$$\langle f(\mathbf{x}, t) \rangle = \lim_{N \rightarrow \infty} \frac{1}{N} \sum_{k=1}^N f(\mathbf{x}, t + t_k) \quad (2.26)$$

where  $t_k$  are the time instants at which the reference phase occurs at location  $\mathbf{x}$ . Eq. (2.26) can be considered as a conditional ensemble average at any point in space of the values of  $f$  that are realized at the time  $t_k = kT$

---

<sup>4</sup>Note that the phase-average is measurable quantity in experiment and not only a mathematical concept.

in the cycle of the  $T$ -periodic motion. The component  $\tilde{f}$  in Eq. (2.25) is then

$$\tilde{f} = \langle f \rangle - \bar{f}. \quad (2.27)$$

Two useful properties that follow from these definitions are given below:

$$\langle f' \rangle = 0 \quad (2.28)$$

$$\overline{\langle f \rangle f'} = \overline{\tilde{f} f'} = 0. \quad (2.29)$$

The first relation indicates that the random fluctuation has zero mean at constant phase. The last relation states that the organized and turbulent motions are uncorrelated. Nevertheless, the use of decomposition given by Eq. (2.8) into the Navier–Stokes equations yields to non-closed system of equations. Indeed, one can show by a suitable manipulation with the Navier–Stokes equations, that the new system contains terms involving the oscillation of  $\langle \mathbf{u}' \otimes \mathbf{u}' \rangle - \mathbf{u}' \otimes \mathbf{u}'$  in the Reynolds stresses of the background turbulence.

To avoid a too complex form of the new system of equations, an alternative has been suggested by Cantwell and Coles [Cantwell and Coles, 1983] which consists in using the decomposition:

$$f = \langle f \rangle + f' \quad (2.30)$$

instead of the decomposition given by Eq. (2.25) where the phase operator can be expressed as:

$$\langle f \rangle = \frac{1}{\Delta\Psi} \int_{t-\Delta\Psi}^t f(t) dt \quad (2.31)$$

with  $\Delta\Psi = T/N$  and  $N$  the number of phases in a period  $T$ . It can be noted that Eq. (2.31) is very close to the URANS operator introduced in the previous section (see Eq. (2.11)). Furthermore, the use of the decomposition (2.30) into the the Navier–Stokes equations shows that the governing dynamical equations are formally equivalent to the classical averaged Navier–Stokes equations. Therefore, the resulting system of equations is sometimes named PANS which states for Phase-Averaged Navier–Stokes equations. The conventional Reynolds stresses  $\langle \mathbf{u}' \otimes \mathbf{u}' \rangle$  are generated by spatial local random fluctuations at constant phase.

## 2.4 The Large Eddy Simulation Approach (LES)

As already mentioned in Section 2.1, the Large-Eddy Simulation technique relies on a decomposition of the aerodynamic field between the large (in a sense to be defined more precisely) and the small scales of the flow, the largest ones being directly resolved, while the effect of the small ones is only represented through the use of a model. The next section discusses in more details the concept of large and small scales separation.

### 2.4.1 Large and small scales separation

In the most common theoretical framework of Large-Eddy Simulation (see Chapter 4 for a survey of possible alternative definitions), this separation is obtained by introducing a low-pass filter (in the wavenumber space)  $G$ , which is characterized by its *cutoff* lengthscale in the physical space:  $\overline{\Delta}$ .

Any quantity  $f$  of the flow, function of  $(\mathbf{x}, t) \in \Omega \times \mathbb{R}^+$  where  $\Omega \subset \mathbb{R}^3$  denotes the physical domain, the filtered variable  $\overline{f}$  is then formally expressed as a convolution product by the filter kernel  $G$ :

$$\begin{aligned} \overline{f}(\mathbf{x}, t) &= G \star f(\mathbf{x}, t) \\ &= \int_0^{+\infty} \int_{\Omega} G(\overline{\Delta}(\mathbf{x}, t), \mathbf{x} - \xi, t - t') f(\xi, t') d\xi dt'. \end{aligned} \quad (2.32)$$

To simplify the following developments, we will restrict ourselves to the simplified usual case, considering only a spatial and isotropic filtering of the variables. In this case,  $\overline{\Delta}(\mathbf{x}, t) = \overline{\Delta}$ . At this point it should however be mentioned that several works exist, which focus on the problem of space-varying cutoff lengths [Ghosal and Moin, 1995; Vasilyev *et al.*, 1998], or explicitly account for time filtering effects [Dakhoul and Bedford, 1986a; Dakhoul and Bedford, 1986b; Pruett, 2000; Pruett *et al.*, 2003; Carati and Wray, 2000].

In the case where  $\overline{\Delta}(\mathbf{x}, t) = \overline{\Delta}$ , relation (2.32) simplifies as:

$$\overline{f}(\mathbf{x}, t) = \int_{\Omega} G(\overline{\Delta}, \mathbf{x} - \xi).f(\xi, t).d\xi. \quad (2.33)$$

The filtered variable  $\overline{f}$  thus defined is then a representation of all the scales with a size larger than  $\overline{\Delta}$ . In spectral space, the length  $\overline{\Delta}$  being associated to the cutoff wavenumber  $\kappa_c = \pi/\overline{\Delta}$ , the filtered variable is then formally

associated to wavenumbers  $\kappa < \kappa_c$ . Obviously, the unresolved part  $f' = f - \bar{f}$  is a representation of the small scales of the flow, referred to as the *subgrid scales*, whose size is smaller than  $\bar{\Delta}$ .

This decomposition of the turbulent field is illustrated in spectral space in Fig. 2.1, in the ideal case of a sharp cutoff filter.

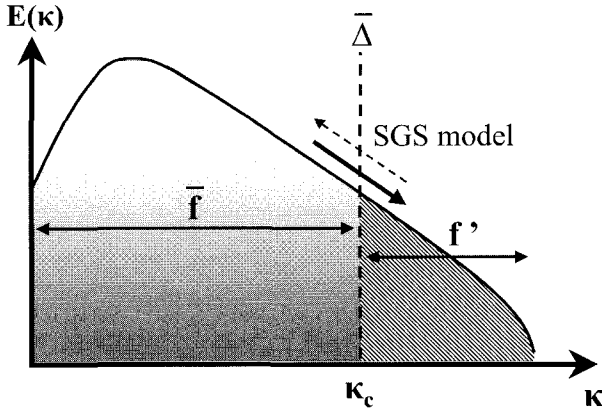


Fig. 2.1 Turbulent field decomposition (sharp cutoff filter).

The most famous filters introduced in the framework of Large Eddy Simulation are the sharp cutoff filter (which has a finite support in spectral space), the box filter (which has a finite support in the physical space), and the Gaussian filter. It is worth mentioning that the filtering operators used in LES are generally not some Reynolds operators<sup>5</sup>. More particularly that means that in general:

$$\overline{\bar{f}} = G \star G \star f \neq \bar{f} \quad (2.34)$$

$$\overline{f'} = G \star (Id - G) \star f \neq 0. \quad (2.35)$$

It has also to be said that the filtering framework introduced in this section is generally only a theoretical view. In practice, Large Eddy Simulations are in most cases performed in the physical space, with the use of some numerical schemes that introduce an additional dissipation. The resulting effect is that the scheme acts as a numerical filter which damps the highest resolved frequencies of the flow. In such a context, the filtering operation

<sup>5</sup>However the sharp cutoff filter satisfies this property.

is thus widely assumed to be implicitly due to a combination of the mesh and the intrinsic dissipation of the numerical scheme. The consequence is quite dramatic, as it means that it is generally impossible to get access to the effective filter of the simulation. For this reason, some numerical approximations of usual filters are introduced when needed (for instance for subgrid scale modelling issues), in which the form of the filter and its cutoff lengthscale are imposed *a priori*. Some authors have analyzed more in detail the effect of the use of low-order numerical schemes on Large Eddy Simulation. Among them, Garnier *et al.* [Garnier *et al.*, 1999] have re-interpreted the numerical scheme as an equivalent Smagorinsky-like model, and showed on the ground of homogeneous isotropic turbulence simulations that low-order dissipative schemes are generally associated to larger values of the *generalized Smagorinsky constant* than the classical range  $C_S = 0.1 - 0.2$ . This concept of generalized coefficient was extended in a later study by Mossi and Sagaut [Mossi and Sagaut, 2003] to the case of a fully developed channel flow. The main conclusion of these works is that such schemes are not well suited for LES, and that there would be no benefit at all in using an explicit subgrid model in combination with such schemes, since the numerical diffusion would mask the effects of the model. This observation is also the basis of the Implicit LES (ILES) approach, which consists in assuming that the numerical dissipation acts on the small scales similarly to an explicit subgrid scale model.

### 2.4.2 Filtered Navier–Stokes equations

In this section, the set of the *filtered Navier–Stokes* equations, which describe the dynamics of the largest scales of the flow, is derived. Again, the starting point will be the general set of the Navier–Stokes-based equations for the resolved field (2.5), where the scale separation operator  $\mathcal{F}$  refers here to the filter  $G$  as introduced in the previous section.

Here, we will restrict ourselves to the common case considering the assumption of commutativity between the filtering operator  $G$  and time and space derivatives. Under these assumptions, the additive terms (2.6) simplify as:

$$\begin{aligned} A_1 &= A_3 = A_4 = 0 \\ A_2 &= \nabla \cdot \tau_{SGS} \end{aligned} \tag{2.36}$$

where  $\tau_{SGS}$  is the *subgrid stress tensor*, defined as:

$$\tau_{SGS} = \overline{\mathbf{u} \otimes \mathbf{u}} - \bar{\mathbf{u}} \otimes \bar{\mathbf{u}}. \quad (2.37)$$

This term represents all the interactions between the resolved and unresolved scales, and requires a mathematical closure since the original velocity field  $\mathbf{u}$  remains unknown in the simulation. As for the Reynolds stress tensor, many works have been devoted to the development of subgrid models for the subgrid stress tensor. In this book, only the models based in the multiscale decomposition will be detailed. For an overview of other existing subgrid closures, the reader can refer for instance to the monograph by Sagaut [Sagaut, 2005].

With these notations, the filtered Navier–Stokes equations finally read:

$$\begin{aligned} \nabla \cdot \bar{\mathbf{u}} &= 0 \\ \frac{\partial}{\partial t} \bar{\mathbf{u}} + \nabla \cdot (\bar{\mathbf{u}} \otimes \bar{\mathbf{u}}) &= -\nabla \bar{p} + \nu \nabla^2 \bar{\mathbf{u}} - \nabla \cdot \tau_{SGS}. \end{aligned} \quad (2.38)$$

Several remarks can be made about this new set of equations, and the subgrid stress-tensor:

- A deeper analysis of the different contributions of the subgrid stress tensor  $\tau_{SGS}$  can be achieved by considering Leonard decomposition [Leonard, 1974]. This splitting of  $\tau_{SGS}$  is obtained by introducing explicitly the identity  $\mathbf{u} = \bar{\mathbf{u}} + \mathbf{u}'$  in its expression (2.37), leading to:

$$\tau_{SGS} = \underbrace{\overline{\bar{\mathbf{u}} \otimes \bar{\mathbf{u}} - \bar{\mathbf{u}} \otimes \bar{\mathbf{u}}}}_{\mathbf{L}} + \underbrace{\overline{\mathbf{u}' \otimes \bar{\mathbf{u}} + \bar{\mathbf{u}} \otimes \mathbf{u}'}}_{\mathbf{C}} + \underbrace{\overline{\mathbf{u}' \otimes \mathbf{u}'}}_{\mathbf{R}}. \quad (2.39)$$

Considering this decomposition, one distinguishes three different types of interactions associated to the three respective tensors  $\mathbf{L}$ ,  $\mathbf{C}$ , and  $\mathbf{R}$ :

- The *Leonard* stress tensor  $\mathbf{L}$  which characterizes the fluctuations of the interactions between the resolved scales themselves. It is to be noted that this tensor is directly computable from the resolved variables, provided an explicit expression (or, at least, an approximation) is available for the filtering operator.
- The *Cross* stress tensor  $\mathbf{C}$  which characterizes the cross interactions between the resolved (large) and subgrid (small) scales of the flow.

- The *Reynolds* subgrid stress tensor  $\mathbf{R}$  which characterizes the direct effect of the small scales of the flow on the resolved field.

It can be easily seen that the RANS approach corresponds to the case  $\mathbf{L} = \mathbf{C} = \mathbf{0}$ .

- If we now consider the real philosophy of Large Eddy Simulation, the simulation should only deal with filtered quantities. This is particularly true when the filter remains explicitly unknown and is just implicitly defined as a combination between the computational grid and the numerical scheme. In that case, the convective term in the filtered equations should then be re-formulated as  $\nabla \cdot (\overline{\mathbf{u}} \otimes \overline{\mathbf{u}})$  since the non-linear term  $\overline{\mathbf{u}} \otimes \overline{\mathbf{u}}$  introduces some unresolved scales associated to wavenumbers  $\kappa > \kappa_c$ . The fully consistent filtered equations should then be rewritten as :

$$\begin{aligned} \nabla \cdot \overline{\mathbf{u}} &= 0 \\ \frac{\partial}{\partial t} \overline{\mathbf{u}} + \nabla \cdot (\overline{\mathbf{u}} \otimes \overline{\mathbf{u}}) &= -\nabla \overline{p} + \nu \nabla^2 \overline{\mathbf{u}} - \nabla \cdot \tau_{SGS}^{cons} \end{aligned} \quad (2.40)$$

where the consistent subgrid stress tensor is expressed as:

$$\tau_{SGS}^{cons} = \overline{\mathbf{u}} \otimes \overline{\mathbf{u}} - \overline{\mathbf{u}} \otimes \overline{\mathbf{u}}. \quad (2.41)$$

- As pointed out by Germano [Germano, 1999], it is to be noted that the filtered Navier–Stokes equations have a form which is strictly similar to the one from the Reynolds–Averaged Navier–Stokes equations (2.24). Indeed, these two sets of equations may only be considered as some particular cases of the general set of equations (2.5) in which no assumption was carried out about the nature of the scale separation operator  $\mathcal{F}$ . This remark motivates the development of a coupling between these two approaches and the definition of some new hybrid strategies combining the advantages of both of them. Such approaches will be detailed in Chapters 7 and 8.

## 2.5 Multilevel/Multiresolution Methods

This section presents the general framework of multilevel methods, in the case of a *hierarchical decomposition*. The hierarchical terms refers to a procedure by which some some coarser and coarser levels of resolution will be obtained by *successive* applications of some scale separation operators

on the original aerodynamic field. In other words, the resolved information will be a decreasing quantity as far as the representation level grows. It has to be mentioned here that some existing multilevel methods – which will be presented later in the book – do not correspond to this formalism, since they consider that the resolved information increases with the resolution level. This will be for instance the case for the statistical multilevel methods presented in Chapter 3.

### 2.5.1 Hierarchical multilevel decomposition

In order to obtain a representation of the function at several resolution levels, we introduce a hierarchy of operators  $\mathcal{F}^{(n)}$ , for  $n = 0$  to  $N$ ,  $N \geq 1$ . We also impose:

$$\mathcal{F}^{(0)} = Id. \quad (2.42)$$

For any  $\{n, m\} \in [1, N] \times [1, n]$ , we then define the operator  $\mathcal{G}_m^n$  as the result of the successive application of the operators  $\mathcal{F}^{(m)}$  to  $\mathcal{F}^{(n)}$ :

$$\mathcal{G}_m^n = \mathcal{F}^{(n)} \circ \mathcal{F}^{(n-1)} \circ \dots \circ \mathcal{F}^{(m+1)} \circ \mathcal{F}^{(m)} \quad (2.43)$$

and:

$$\mathcal{G}_n^n = \mathcal{F}^{(n)}, \quad \mathcal{G}_0^0 = Id. \quad (2.44)$$

In the following,  $\mathcal{F}^{(n)}$  will be referred to as a *primary* scale separation operator, while  $\mathcal{G}_m^n$  will be referred to as a *combined* or *hierarchical* scale separation operator.

Several representation levels of any quantity  $f$  are then obtained by applying the operator  $\mathcal{G}_1^n$  to it, which is equivalent to applying  $\mathcal{G}_0^n$  when considering (2.42). We thus define the representation of  $f$  at the level  $n \in [1, N]$ , noted  $\bar{f}^{(n)}$  by:

$$\begin{aligned} \bar{f}^{(n)} &= \mathcal{G}_1^n(f) \\ &= \mathcal{F}^{(n)} \circ \dots \circ \mathcal{F}^{(1)}(f) \\ &= \mathcal{G}_0^n(f). \end{aligned} \quad (2.45)$$

Obviously, similarly to the scale separation operator  $\mathcal{F}$ , the operators  $\mathcal{F}^{(n)}$  introduced here denote some operators that allow *compressing* of the

information contained in the function  $f$ , leading to some coarser and coarser representation of  $f$  as far as  $n$  grows<sup>6</sup>.

For each level  $n$  considered, the function  $f$  can thus be decomposed into a resolved part  $\bar{f}^{(n)}$  and an unresolved one  $f'_n$ :

$$f = \bar{f}^{(n)} + f'_n \quad (2.46)$$

where the unresolved part of  $f$  at the representation level  $n$  can be simply evaluated by subtraction:

$$\begin{aligned} f'_n &= f - \bar{f}^{(n)} \\ &= (Id - \mathcal{G}_1^n) f. \end{aligned} \quad (2.47)$$

Recursively, and for each level  $n = 1$  to  $N$ , the following decomposition of  $f$  is derived<sup>7</sup>:

$$f = \bar{f}^{(n)} + \sum_{l=0}^{n-1} \delta f^{(l)}. \quad (2.49)$$

In this last expression, the quantity  $\delta f^{(l)}$ , referred to as the *detail* of level  $l$ , corresponds to the complement of information on  $f$  obtained when moving from the representation level  $(l + 1)$  to the level  $l$ , or equivalently to the loss of information when moving from level  $l$  to the coarser level  $(l + 1)$ :

$$\begin{aligned} \delta f^{(l)} &= \bar{f}^{(l)} - \bar{f}^{(l+1)} \\ &= (Id - \mathcal{F}^{(l+1)}) \bar{f}^{(l)} \\ &= f'_{l+1} - f'_l. \end{aligned} \quad (2.50)$$

More generally, the decomposition (2.49) reads, for each representation level  $m < n$ :

$$\bar{f}^{(m)} = \bar{f}^{(n)} + \sum_{l=m}^{n-1} \delta f^{(l)}. \quad (2.51)$$

---

<sup>6</sup>As will be detailed later, it is not necessary that all the different operators belong to the same class of scale separation operators. For instance it appears possible to combine filtering and averaging operators, leading to the class of the so-called RANS/LES strategies which will be discussed in Chapters 7 and 8.

<sup>7</sup>This concept of multilevel representation of the data has been extensively developed by Harten [Harten, 1983; Harten, 1994], who introduced the decomposition (2.49) in the following form:

$$f = \mathcal{M}_{\mathcal{L}} \left( \bar{f}^{(n)}, \delta f^{(n-1)}, \dots, \delta f^{(1)}, \delta f^{(0)} \right). \quad (2.48)$$

This relation is equivalent to the following simple idea:

*The representation of the function  $f$  at a given level  $m$  is obtained directly from its representation at a coarser level  $n$  and from the details corresponding to the loss of information between these two levels.*

### 2.5.2 Practical example: the multiscale/multilevel LES decomposition

A particular case of multiscale separation, as it has been presented in the previous section, is the one used in multilevel Large-Eddy Simulation. The idea is here to obtain a scale hierarchy ranging from large to small scales by means of filtering operators  $G_n$  acting as low pass filters in the wavenumbers space:

$$\mathcal{F}^{(n)} \equiv G_n. \quad (2.52)$$

The filtering operators  $G_n$  are characterized by their respective cutoff lengthscales  $\Delta^{(n)}$ , increasing<sup>8</sup> with  $n$ , *i.e.*  $\Delta^{(n+1)} > \Delta^{(n)}$ .

A filtering operator  $\mathcal{G}_m^n$ , resulting from the successive application of the primary filters  $G_m$  to  $G_n$  is then introduced:

$$\mathcal{G}_m^n = G_n \star G_{n-1} \star \dots \star G_{m+1} \star G_m. \quad (2.53)$$

Thanks to this definition, the resulting hierarchy of filtering operators  $\{\mathcal{G}_1^n\}_{n=1,N}$  allow the definition of several filtering levels of the aerodynamic field. The filtering operators  $\mathcal{G}_1^n$  will then be referred to as *hierarchical* or *combined* filters. In the most general case, they differ from the *primary* filters  $G_n$ . For each aerodynamic variable, such as for instance the velocity field  $\mathbf{u}$ , the filtered field at the level  $n$  will then be:

$$\begin{aligned} \bar{\mathbf{u}}^{(n)} &= \mathcal{G}_1^n \star \mathbf{u} \\ &= G_n \star G_{n-1} \star \dots \star G_1 \star \mathbf{u}. \end{aligned} \quad (2.54)$$

The hierarchical filters  $\mathcal{G}_1^n$  are characterized by their effective cutoff length-scale<sup>9</sup>  $\bar{\Delta}^{(n)}$ . In this framework, the filtered variables at level  $n$  ( $\bar{\mathbf{u}}^{(n)}$ )

<sup>8</sup>Here, it is recalled that this formalism is the one considered in hierarchical multilevel methods. Some other multilevel methods, such as the statistical multilevel approaches are on the other hand based on some increasing values of the cutoff wavenumber  $\kappa^{(n)} = \pi/\Delta^{(n)}$  with  $n$ .

<sup>9</sup>The cutoff lengthscale of the hierarchical filter  $\mathcal{G}_1^n$  generally differs from the one of the primary filter  $G_n$ :  $\bar{\Delta}^{(n)} \neq \Delta^{(n)}$ . The equality is however verified when Reynolds filtering operators are considered as primary filters (sharp cut-off filters for instance).

are then a representation of the flow structures associated to wavenumbers  $\kappa < \kappa_n$ , where  $\kappa_n = \pi/\overline{\Delta}^{(n)}$  is the cutoff wavenumber of the filter  $\mathcal{G}_1^n$ . In a similar way,  $\overline{\mathbf{u}}^{(n)}$  corresponds to a representation of turbulent scales larger than  $\overline{\Delta}^{(n)}$ .

The details between two successive levels  $l$  and  $l + 1$  ( $\delta\mathbf{u}^{(l)} = \overline{\mathbf{u}}^{(l)} - \overline{\mathbf{u}}^{(l+1)}$ ) are then corresponding to the *frequency complement* of the variable  $\mathbf{u}$  between the two filtering levels  $l$  and  $l + 1$ . They represent some flow structures with a size smaller than  $\overline{\Delta}^{(l+1)}$  and larger than  $\overline{\Delta}^{(l)}$ , or equivalently the missing scales between the two description levels  $l + 1$  and  $l$ .

The particular case of multilevel LES which will be detailed in the following chapters of this book consists in resolving only some scales larger than the cutoff lengthscale associated to the finest filtering level ( $n = 1$ ). In this case, the following decomposition of the flow variables will then be considered:

$$\overline{\mathbf{u}}^{(1)} = \overline{\mathbf{u}}^{(n)} + \sum_{l=1}^{n-1} \delta\mathbf{u}^{(l)} \quad (2.55)$$

while the effects of the remaining scales ( $\mathbf{u}'$ ) are only accounted for thanks to the use of a subgrid model. This decomposition is illustrated in the spectral space on Fig. 2.2, in the simple case in which the primary filters  $G_n$  are sharp cut-off filters with respective cut-off wavenumbers  $\kappa_n$ . Obviously, the limit  $\Delta^{(1)} \rightarrow 0$  corresponds to the case of a full resolution of all the scales of the flow (DNS). As will be detailed later in the book, the main idea of the multilevel LES methods will be – without increasing the cost of the simulation – to consider some sufficiently small values of  $\Delta^{(1)}$  to use a simple subgrid closure to represent the effects of the scales associated to  $\mathbf{u}'$ , and minimize the errors due to this parametrization.

### 2.5.3 Associated Navier–Stokes-based equations

As in the general framework involving only one scale separation operator, it is useful to derive some evolution equations for the resolved flow variables at each representation level. For that purpose, the scale separation operator  $\mathcal{G}_1^n$  associated to the representation level  $n$  is applied directly to the set of the Navier–Stokes equations. Again, for a sake of clarity, all the scale separation operators will be assumed to commute with space and time

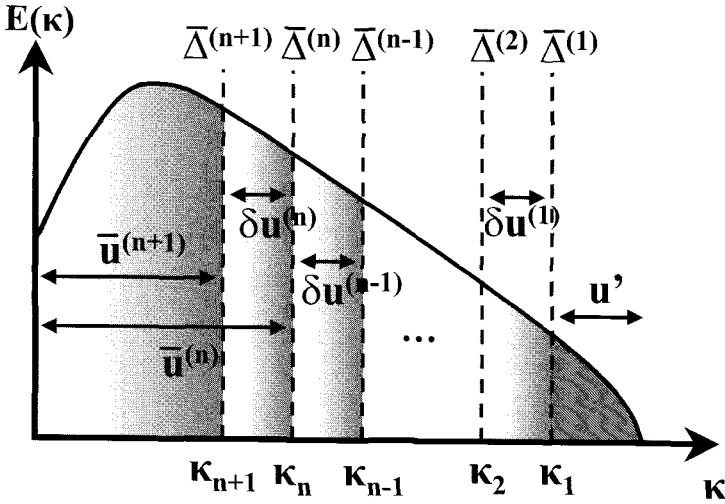


Fig. 2.2 Multilevel decomposition of the turbulent field (sharp cut-off filters).

derivatives. The following set of equations is then obtained for the resolved aerodynamic field at level  $n$ :

$$\begin{aligned} \nabla \cdot \bar{\mathbf{u}}^{(n)} &= 0 \\ \frac{\partial}{\partial t} \bar{\mathbf{u}}^{(n)} + \nabla \cdot \left( \bar{\mathbf{u}}^{(n)} \otimes \bar{\mathbf{u}}^{(n)} \right) &= -\nabla \bar{p}^{(n)} + \nu \nabla^2 \bar{\mathbf{u}}^{(n)} - \nabla \cdot \tau^{(n)} \end{aligned} \quad (2.56)$$

where  $\tau^{(n)}$  remains unknown at the level  $n$ , and arises directly from the non-linearity of the Navier-Stokes equations. This term is written:

$$\tau^{(n)} = \overline{\mathbf{u} \otimes \mathbf{u}}^{(n)} - \bar{\mathbf{u}}^{(n)} \otimes \bar{\mathbf{u}}^{(n)}. \quad (2.57)$$

This tensor cannot be directly computed at the level  $n$ , since the original velocity field  $\mathbf{u}$  appears in its expression. A specific closure is thus needed for this term to close the system of Eqs. (2.56). The closure of this system of equations will be analyzed in detail in the next chapters.

An evolution equation can also be obtained for the details between two consecutive levels  $n$  and  $n+1$ . By simply subtracting the filtered Navier-Stokes equations at a representation level  $n+1$  from the equations (2.56) (representation level  $n$ ), and remembering that  $\bar{\mathbf{u}}^{(n)} = \bar{\mathbf{u}}^{(n+1)} + \delta \mathbf{u}^{(n)}$  and

$\bar{p}^{(n)} = \bar{p}^{(n+1)} + \delta p^{(n)}$ , the following system is derived for the details  $\delta \mathbf{u}^{(n)}$  and  $\delta p^{(n)}$ :

$$\begin{aligned} \nabla \cdot (\delta \mathbf{u}^{(n)}) &= 0 \\ \frac{\partial}{\partial t} \delta \mathbf{u}^{(n)} + \nabla \cdot (\delta \mathbf{u}^{(n)} \otimes \delta \mathbf{u}^{(n)} + \delta \mathbf{u}^{(n)} \otimes \bar{\mathbf{u}}^{(n+1)} + \bar{\mathbf{u}}^{(n+1)} \otimes \delta \mathbf{u}^{(n)}) \\ &= -\nabla \delta p^{(n)} + \nu \nabla^2 \delta \mathbf{u}^{(n)} - \nabla \cdot (\tau^{(n)} - \tau^{(n+1)}). \end{aligned} \quad (2.58)$$

This set of equations will be the main basis of the NLDE (Non-Linear Disturbance Equations) approach [Morris *et al.*, 1997; Labourasse and Sagaut, 2002; Labourasse, 2002], which consists in reconstructing explicitly some turbulent fluctuations around a given mean flow. This approach will be fully detailed in Chapter 8.

## 2.5.4 Classification of existing multilevel methods

Several multilevel methods can be found in literature, which can be classified in different subclasses, depending for instance on the nature of the primary separation operators  $\mathcal{F}_n$ , or on the number of scale separation levels ( $N$ ). This section is a proposal of a possible classification of some existing multilevel methods. Here, it has been chosen to distinguish among the different kind of methods by looking at their range of application. In other words, we will try here to answer the two simple questions: (i) what is the targeted accuracy of the method in terms of wavenumber content of the solution? (ii) what is the aim of the introduction of a multilevel splitting of the flow variables? Following this idea, three main classes of multilevel methods arise, and are detailed in the next subsections.

### 2.5.4.1 Multilevel methods based on resolved-only wavenumbers

These methods aim at increasing the accuracy of the mathematical closure used to represent the missing interactions with the unresolved scales, while keeping the maximum quantity of information in the resolved scales range. In this case, and with the previous formalism, the field of interest will be the resolved field at the finest representation level  $\bar{\mathbf{u}}^{(1)}$ , while coarser representation levels are introduced to perform a deeper analysis of the interactions between the resolved scales of motion. Such a better understanding of the energy exchanges between the resolved scales is then expected to allow the derivation of some improved closures for  $\tau^{(1)}$ .

The main methods belonging to this class, and related to the filtering approach are:

- The dynamic subgrid models based on the Germano's identity [Germano, 1986; Germano, 1992]
- The dynamic subgrid models based on self-similarity, such as the the procedures proposed by Terracol and Sagaut [Terracol and Sagaut, 2003] and Shao *et al.* [Shao *et al.*, 2003].
- The improved models based on an additional separation between large and small resolved scales, such as the Variational Multiscale approach of Hughes [Hughes *et al.*, 1998; Hughes, Mazzei and Jansen, 2000; Hughes *et al.*, 2001; Hughes, Oberai and Mazzei, 2001], and filtered models [Sagaut, Comte and Ducros, 2000].

These different methods will be fully detailed in Chapter 4.

#### 2.5.4.2 Multilevel methods based on higher wavenumbers

In these methods, the “resolved field” is associated to a smaller wavenumber content than what would be really available with the grid. This corresponds to the case in which the field of interest is  $\bar{\mathbf{u}}^{(l)}$ ,  $l > 1$  ( $l = 2$  in most cases). The underlying idea of these methods is to introduce (practically or only theoretically) a high wavenumber content, *i.e.* some fine “unresolved” scales, which will be explicitly used for the derivation of the mathematical closure for  $\tau^{(l)}$ . Such a closure is then expected to be much more accurate than more classical closures based only on the lower wavenumbers.

The main methods in this category are the following:

- The deconvolution-like methods developed in LES, such as the Approximate Deconvolution Model [Adams and Leonard, 1999; Adams, 1999; Adams, 2000b; Stolz and Adams, 1999; Stolz *et al.*, 2001a; Stolz *et al.*, 2001b] or the velocity estimation model [Domaradzki and Saiki, 1997; Domaradzki and Loh, 1999; Loh and Domaradzki, 1999; Domaradzki and Yee, 2000]. For these methods, the general idea is to reconstruct some finer scales to get a deterministic approximation of the subgrid stress tensor. These methods will be detailed in Chapter 5.
- The statistical multiscale modelling approaches developed in the RANS framework. Here, while the simulation is limited to an averaged description of the flow, the idea is to introduce theoretically several bands of in the unresolved part of the spectrum, in order

to introduce some quantities which are more local in the spectral space. The aim is then to derive some closures which better take into account variations in the spectral features of turbulent fluctuations. These approaches will be developed in Chapter 3.

#### 2.5.4.3 Adaptive multilevel methods

These methods aim at adapting the resolved wavenumber content to the complexity of the flow. This adaptation can be static or dynamic, in space and/or time. The global idea is then to increase the range of resolved scales where and/or when required. This can be the case when the flow physics is too complex and would result in a too high degree of error with classical models, or simply when the application itself requires a wide-band description of the flow, such as for instance in aeroacoustics. The main adaptive multilevel methods are:

- The multilevel methods based on the use of a hierarchy of embedded computational grids with different resolutions, for instance by using a *multigrid*<sup>10</sup> algorithm. The Adaptive Mesh Refinement (AMR) technique is also a particular dynamic case of such a method. Indeed, such a grid hierarchy leads to a multilevel decomposition of the flow, since each grid level naturally introduces its own cutoff lengthscale resulting from a combination of both the grid Nyquist cutoff length, and the numerical scheme. These methods will be detailed in Chapters 5 and 6.
- The multilevel methods in which the scale separation relies on the use of some spectral algorithms. In this case, the flow variables are represented thanks to a summation of basis functions in the Fourier space, and it thus appears very simple to perform the scale separation, by simply truncating the Fourier series expansion. (see for instance [Dubois *et al.*, 1999]). Such methods will be described in Chapter 5.
- A last case of multilevel methods belonging to this class is the case of the hybrid RANS/LES approaches. Here, a two-level decomposition of the flow variables is considered, between a filtered (LES) part, and an averaged (RANS) part. In this case, the multilevel

---

<sup>10</sup>The term *multigrid* is introduced to designate a method using different computational grids, and not to the multigrid methods used in steady CFD algorithms to speed up the convergence to a steady state.

method then becomes a *multiresolution* method, since the different resolution levels are obtained with some scale separation operators of different natures. The idea of these methods is then to reduce the cost of the unsteady simulations of turbulence, by using the RANS approach in the major part of the computational domain, while switching to LES in some flow regions of reduced size only, or where the flow can be accurately simulated by LES on relatively coarse grids. Chapters 7 and 8 will be devoted to such approaches.

## 2.6 Summary

This section proposes to summarize the different scale separation approaches which have been described in this chapter. A first possible classification is summarized by Fig. 2.3, which presents in a hierarchical way the different classes of methods, as a function of their scale representation ability.

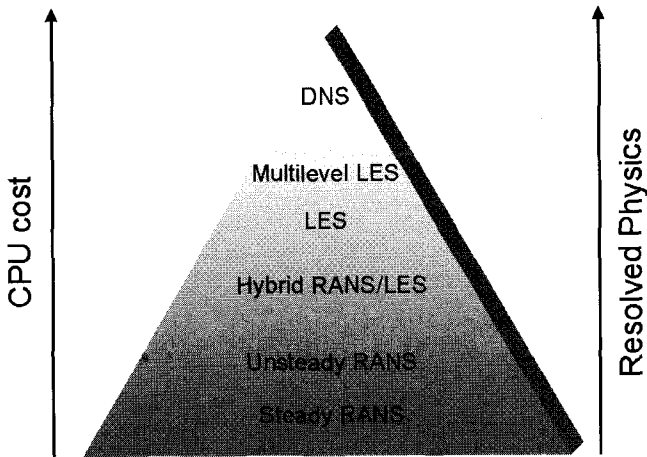


Fig. 2.3 Classification of the most commonly used methods in turbulence simulations.

For each approach, particular attention will be paid to the definition of the resolved and unresolved part, and to their possible multilevel splitting. In each case, some schematic spectral representation of the respective resolved and unresolved parts of the associated energy spectrum are proposed.

The different approaches to simulate turbulence are the following:

- The **Direct Numerical Simulation (DNS)**. This case corresponds to a deterministic representation of all the turbulent scales of the flow, from the largest ones to the smallest dissipation scales (Kolmogorov scale). In that case, all the turbulent scales are associated to the resolved part, while there exist no unresolved part, as illustrated by Fig. 2.4.

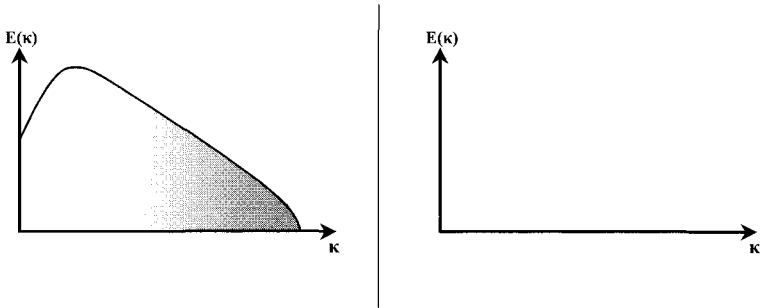


Fig. 2.4 Resolved (left) and unresolved (right) parts of the turbulent spectrum in the case of the DNS approach.

- The **Reynolds-Averaged Navier–Stokes (RANS)**, or **averaging** approach. In this case, the only resolved part corresponds to a statistical representation of the flow, obtained by an averaging procedure. The resolved part then corresponds to an empty turbulent energy spectrum, while all the turbulent scales are modelled, as illustrated by Fig. 2.5.

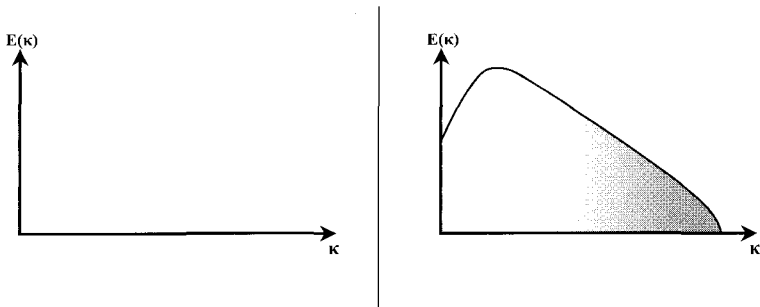


Fig. 2.5 Resolved (left) and unresolved (right) parts of the turbulent spectrum in the case of the RANS (averaging) approach.

- The **Large Eddy Simulation (LES)**, or **filtering** approach. In this approach, only the largest scales of the flow are resolved. As depicted by Fig. 2.6, the resolved part of the flow then corresponds to the scales associated to wavenumbers  $\kappa < \kappa_1$ , where  $\kappa_1$  is referred to as the cutoff wavenumber. The scales associated to greater values of the wavenumber are unresolved, and accounted for through the use of a subgrid model.

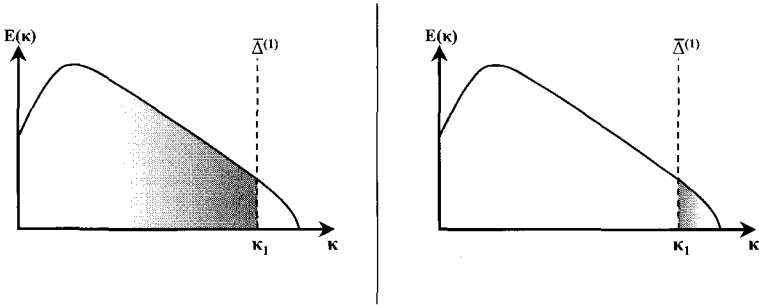


Fig. 2.6 Resolved (left) and unresolved (right) parts of the turbulent spectrum in the case of the LES (filtering) approach.

- The **multiscale statistical** approaches. This case, as the RANS approach, corresponds only to an averaged representation of the flow. The resolved part is then also associated to an empty turbulent energy spectrum, as displayed in Fig. 2.7. However, in this case, the idea will be to use a multiscale splitting of the unresolved turbulent scales, in order to derive an improved closure for the Reynolds stresses. As will be detailed in Chapter 3, the advantage of introducing an additional scale separation in the range of the unresolved wavenumbers is then to be able to take into account a more complex flow physics, such as disequilibrium effects.
- The **multilevel LES** approaches. These approaches, as the standard LES approach, rely on the fact that only the largest turbulent scales are resolved, while the smallest ones are represented by the use of a subgrid model. However, the resolved scales are themselves split into several ranges of scales, associated to several bands in the wavenumbers space, as illustrated by Fig. 2.8. Three main classes of multilevel LES methods then arise, depending on how this splitting is used in practice: to derive some improved subgrid models, based themselves on low or high wavenumbers (see the previous section for a description, and the detailed related approaches in

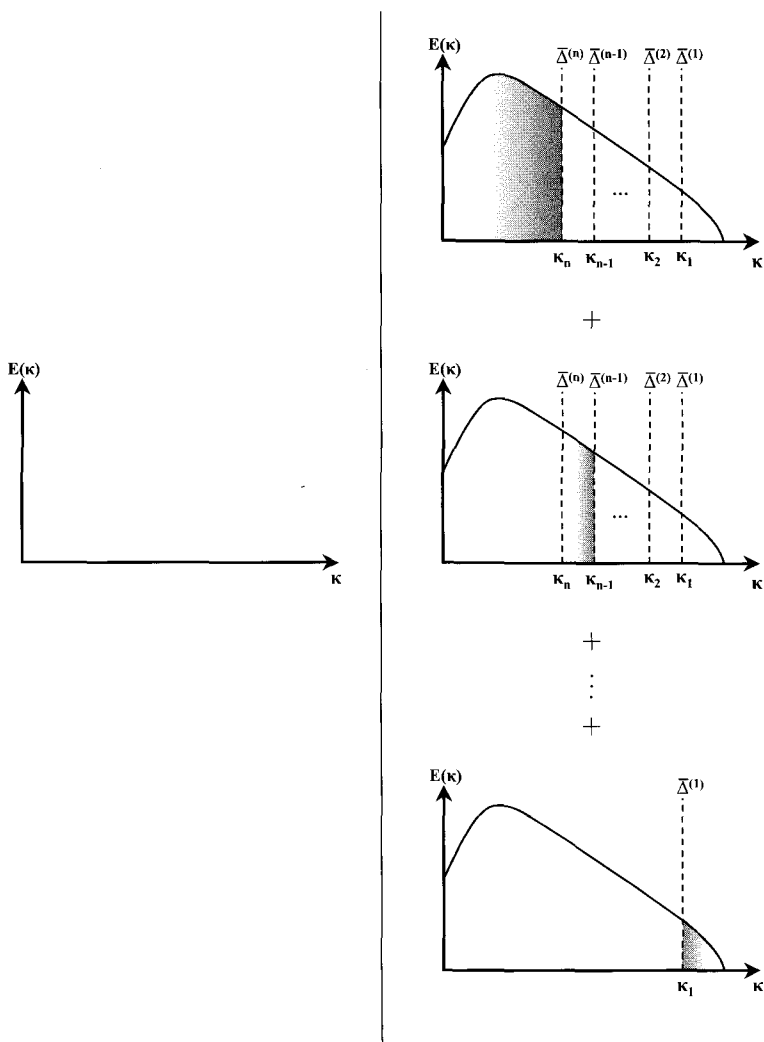


Fig. 2.7 Resolved (left) and unresolved (right) parts of the turbulent spectrum in the case of the multiscale statistical approach.

Chapters 4 and 5), or to adapt the wavenumber content of the solution to flow complexities, thanks to the use of a particular numerical treatment for each wavenumber band defined in the resolved part. The specific methods related to this last point will be detailed in Chapters 5 and 6.

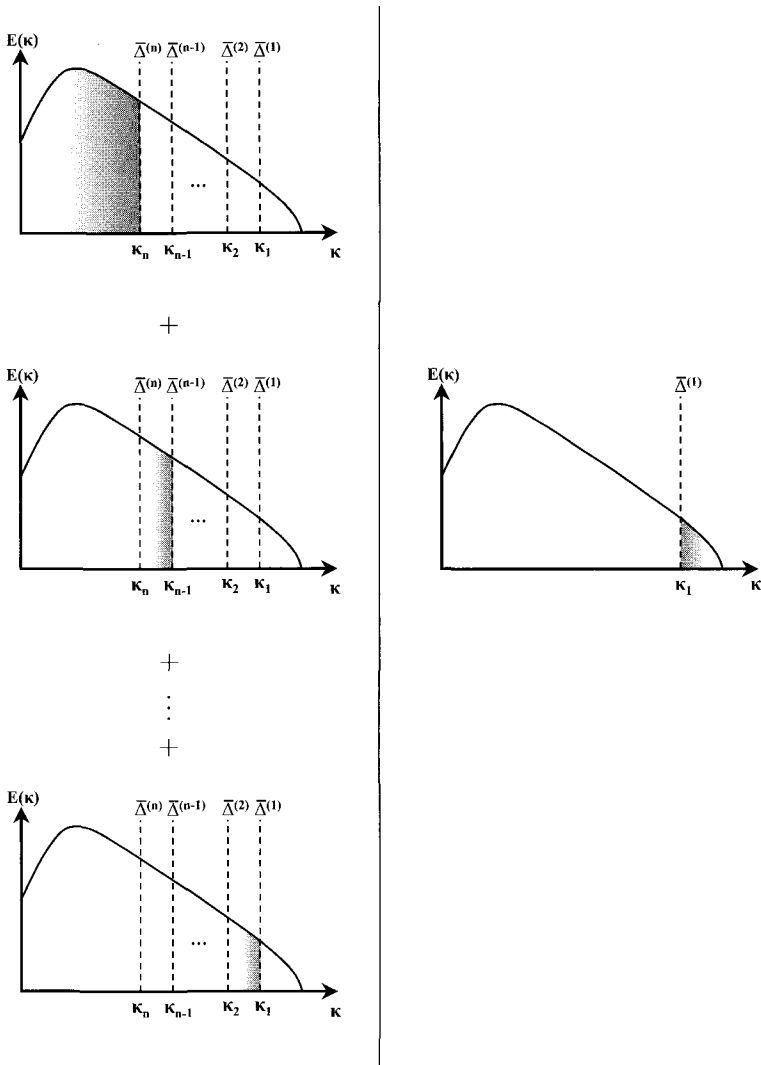


Fig. 2.8 Resolved (left) and unresolved (right) parts of the turbulent spectrum in the case of the multiscale LES approach.

- The **hybrid RANS/LES** approaches. These methods can be seen as a two-level particular case of a multilevel LES approach, in which the coarser resolution level is not defined by a classical LES low-pass filter in wavenumber, but by a statistical average, as in the

RANS approach. Here, as shown in Fig. 2.9, the resolved part is then considered as the sum of an averaged representation of the flow resolved by RANS, and turbulent fluctuations resolved by LES. As will be detailed in Chapters 7 and 8, the transition from (respectively to) an LES wavenumber content to (respectively from) an averaged (RANS) content can be continuous or discontinuous in space, leading to some different classes of methods (namely global and zonal RANS/LES approaches).

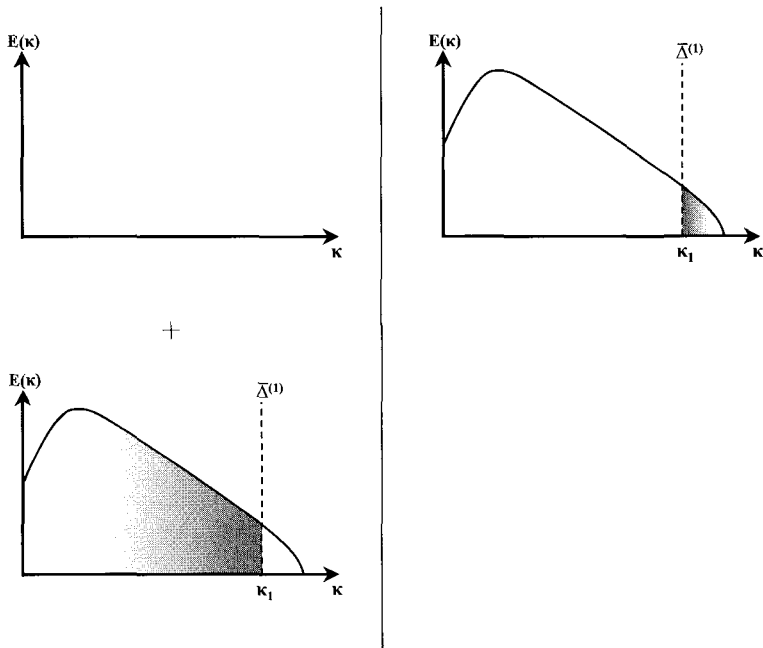


Fig. 2.9 Resolved (left) and unresolved (right) parts of the turbulent spectrum in the case of a hybrid RANS/LES approach.

This page is intentionally left blank

## Chapter 3

# Statistical Multiscale Modelling

### 3.1 General

This chapter is devoted to multiscale statistical modelling for steady simulations of turbulent flows belonging to the RANS family. Before entering a detailed description of concepts and models related to this approach, it is necessary to briefly recall the key elements on which it relies.

Let us first consider classical, single-scale models. They are all defined by a relation between the Reynolds tensor and the mean velocity field. In complex models, this relation can take the form of an integro-differential model involving one or several evolution equations. As an example, let us recall the famous  $k - \varepsilon$  eddy viscosity model, in which the Reynolds stress tensor is modelled as

$$R_{ij} \equiv \overline{u'_i u'_j} = C_\mu \frac{k^2}{\varepsilon} \left( \frac{\partial \bar{u}_i}{\partial x_j} + \frac{\partial \bar{u}_j}{\partial x_i} \right) - \frac{2}{3} k \delta_{ij} \quad (3.1)$$

where the turbulent kinetic energy  $k$  and the turbulent kinetic energy dissipation rate  $\varepsilon$  are evaluated solving *ad hoc* evolution equations, and  $C_\mu$  is a modelling parameter usually taken equal to 0.09. What is of importance in the present case is that both  $k$  and  $\varepsilon$  are integral quantities in the spectral space. As an example,  $k$  is equal to

$$k = \int_0^\infty E(\kappa) d\kappa \quad (3.2)$$

where  $E(\kappa)$  is the energy spectrum and  $\kappa$  denotes the wave number, with  $\kappa = |\boldsymbol{\kappa}|$ . A similar expression can be found for the turbulent dissipation rate  $\varepsilon$ :

$$\varepsilon = 2\nu \int_0^\infty \kappa^2 E(\kappa) d\kappa. \quad (3.3)$$

The use of such a model does not make it possible to account for details in the spectral structure of the turbulent motion, since they rely on spectrally averaged quantities. Therefore, variations in the spectrum shape cannot be captured, yielding a limited capability to represent turbulence in far-from-equilibrium regimes.

The aim of multiscale modelling is to alleviate this weakness by introducing new quantities which are more local in the spectral domain in order to better account for variations in the spectral features of turbulent fluctuations. The common key idea is to introduce a splitting in the spectral space. This is achieved through the definition of a set of wave numbers  $\kappa(p)$  where  $p = 1, \dots, N$ .

Once the cutoff wave numbers have been defined, one can distinguish two classes of models. The first one, pioneered by Schiestel and coworkers [Hanjalić, Launder and Schiestel, 1980; Schiestel, 1983a; Schiestel, 1983b; Schiestel, 1987; Gleize, Schiestel and Couaillier, 1996] and later investigated by Wilcox [Wilcox, 1988a; Wilcox, 1988b] and Kim [Kim and Chen, 1989; Kim, 1991], are based on quantities defined as average over spectral bands. Anticipating discussions developed below, let us illustrate this approach by introducing the partial turbulent kinetic energy (see Fig. 3.1)

$$e^{(p)} = \int_{\kappa^{(p-1)}}^{\kappa^{(p)}} E(\kappa) d\kappa. \quad (3.4)$$

Considering each  $e^{(p)}$  individually, one can now account for complex features of  $E(\kappa)$ , assuming that the number of spectral bands is large enough to allow for an accurate description of spectral details.

The second model type, mainly developed at Ecole Centrale de Lyon in France [Cambon, Jeandel and Mathieu, 1981; Bertoglio and Jeandel, 1986; Laporta, 1995; Parpais, 1997; Touil, 2002] and Los Alamos in the USA [Besnard *et al.*, 1990; Clark and Zemach, 1995], relies on local, non-averaged, quantities in the spectral space. Still considering the description of the turbulent kinetic energy, one now represents it as a set of discrete values (see Fig. 3.1)

$$E(\kappa(1)), E(\kappa(2)), \dots, E(\kappa(N)). \quad (3.5)$$

The full turbulent kinetic energy is recovered in the first case by a simple sum

$$k = \sum_{p=1, N} e^{(p)} \quad (3.6)$$

while, in the second case, it may require the use of a more complex quadrature rule to obtain an accurate evaluation of Eq. (3.2).

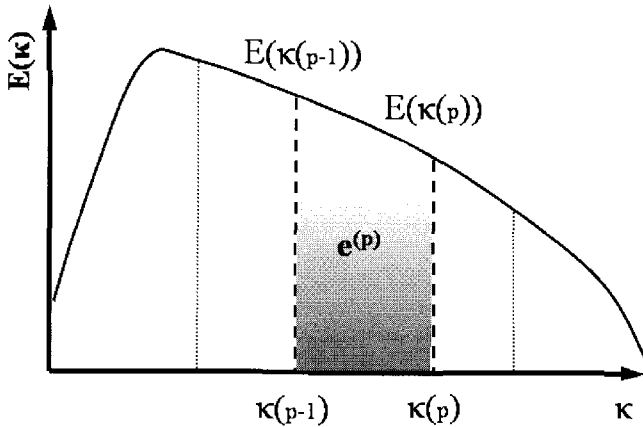


Fig. 3.1 Illustration of the two different approaches: local approaches based on local spectral densities  $E(\kappa(p))$  and band-integrated approaches based on partial kinetic energy  $e^{(p)}$ .

It is worth noting that quantities involved in the first class of models are defined in the physical space, while those of the second class of models are spectral variables.

These two approaches raise the same new closure problem of describing interactions and transfers in both space and wave numbers. Let us illustrate this using the turbulent kinetic energy. Both approaches lead to the definition of energy packets at location  $\mathbf{x}$  in the physical space and of index  $p$  in the spectral decomposition. While the usual, single-scale closures

only address the issue of the destruction/production and the transport (via convection or diffusion) of this energy packet to another place (see Fig. 3.2), the multi-scale approach also introduces the problem of accounting for the transfer of kinetic energy toward other scales and possibly at other locations (see Fig. 3.3). The degree of accuracy of the representation of turbulence dynamics is now much higher, but the price to pay is an increased complexity in the model.

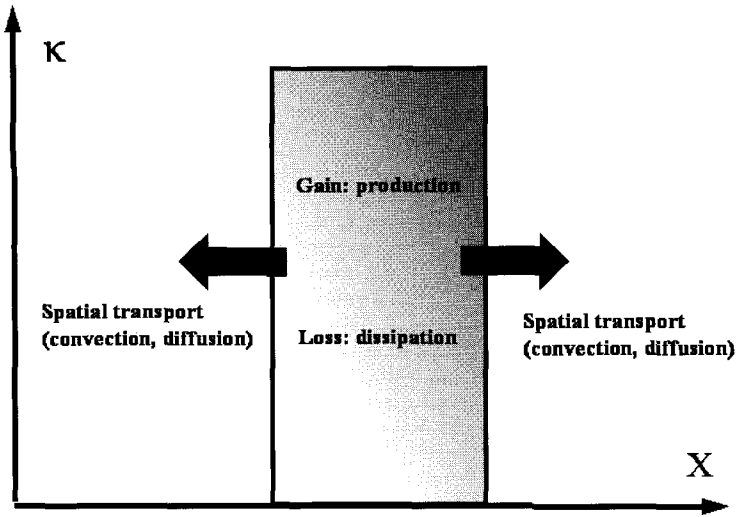


Fig. 3.2 Schematic view of the kinetic energy transfers modelling issue for conventional single-scale models: energy contained in the control cell (defined as a bounded volume) can be transported to other spatial positions by different physical mechanisms (convection, diffusion) governed by nonlinearities or pressure effects. Black arrows symbolize the transfers.

## 3.2 Exact Governing Equations for the Multiscale Problem

### 3.2.1 *Basic equations in physical and spectral space*

The first step in the derivation of governing equations for multiscale Reynolds stress transport equations consists in writing the transport equations for the two-point correlations of turbulent velocity fluctuations. The usual method for deriving statistical moments transport equations leads to [Hinze, 1987]:

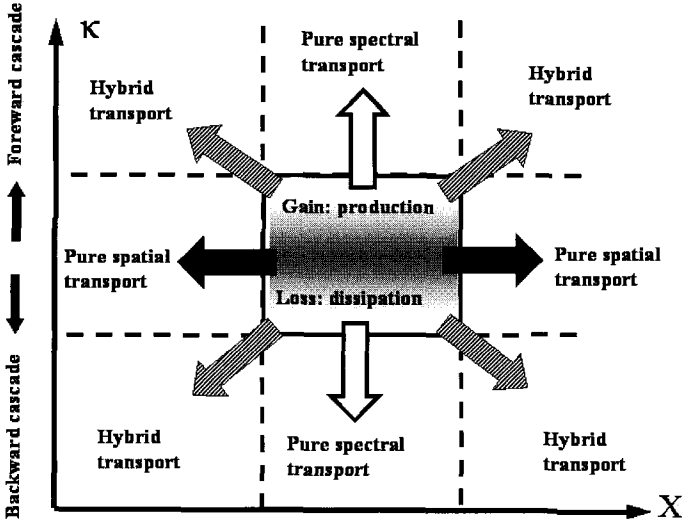


Fig. 3.3 Schematic view of the kinetic energy transfers within the multiscale framework: energy contained in the control cell (defined as a bounded region in the space/wave number plane) can be transferred at the same location but at different wave numbers (localized energy cascade represented by white arrows), or at the same wave number at different spatial positions (spatial transport without cascade, black arrows), or to another location at another scale (non-local cascade, shaded arrows).

$$\begin{aligned}
 & \frac{\partial}{\partial t} \overline{u'_i(\mathbf{X})u'_j(\mathbf{X}')} + \overline{u'_i(\mathbf{X})u'_k(\mathbf{X}')} \frac{\partial \bar{u}_j(\mathbf{X}')}{\partial X_k} + \overline{u'_j(\mathbf{X}')u'_k(\mathbf{X})} \frac{\partial \bar{u}_i(\mathbf{X}')}{\partial X_k} \\
 & + \bar{u}_k(\mathbf{X}) \frac{\partial}{\partial X_k} \overline{u'_i(\mathbf{X})u'_j(\mathbf{X}')} + \bar{u}_k(\mathbf{X}') \frac{\partial}{\partial X'_k} \overline{u'_j(\mathbf{X})u'_i(\mathbf{X}')} \\
 & = - \frac{\partial}{\partial X_k} \overline{u'_i(\mathbf{X})u'_j(\mathbf{X}')u'_k(\mathbf{X})} - \frac{\partial}{\partial X'_k} \overline{u'_i(\mathbf{X})u'_j(\mathbf{X}')u'_k(\mathbf{X}')} \\
 & - \frac{\partial}{\partial X_i} \overline{p'(\mathbf{X})u'_j(\mathbf{X}')} - \frac{\partial}{\partial X'_j} \overline{p'(\mathbf{X}')u'_i(\mathbf{X})} \\
 & + \nu \frac{\partial^2}{\partial X_l \partial X_l} \overline{u'_i(\mathbf{X})u'_j(\mathbf{X}')} + \nu \frac{\partial^2}{\partial X'_l \partial X'_l} \overline{u'_i(\mathbf{X})u'_j(\mathbf{X}')}. \quad (3.7)
 \end{aligned}$$

This equation can be rewritten by introducing the midpoint  $\mathbf{x} = (\mathbf{X} + \mathbf{X}')/2$ , which is such that  $\mathbf{X} = \mathbf{x} - \xi/2$  and  $\mathbf{X}' = \mathbf{x} + \xi/2$ . Defining the two-point correlation tensor  $R(\mathbf{x}, \xi) = \overline{u'_i(\mathbf{x} - \xi/2)u'_j(\mathbf{x} + \xi/2)}$ , expressing the space derivatives with respect to the new coordinates, neglecting terms which scale as  $|\xi|^2$  (which is equivalent to the assumption that the

non-homogenous terms are neglected, leaving the equations for the closest homogeneous anisotropic field), and taking the Fourier transform of Eq. (3.7), one obtains:

$$\begin{aligned}
& \frac{\partial \Phi_{ij}}{\partial t} + \bar{u}_k \frac{\partial \Phi_{ij}}{\partial x_k} + \Phi_{kj} \frac{\partial \bar{u}_i}{\partial x_k} + \Phi_{ik} \frac{\partial \bar{u}_j}{\partial x_k} \\
& + \frac{1}{2} \frac{\partial}{\partial x_k} \left( \widehat{u'_i(\mathbf{X})u'_j(\mathbf{X}')u'_k(\mathbf{X})} + \widehat{u'_i(\mathbf{X})u'_j(\mathbf{X}')u'_k(\mathbf{X}')} \right) \\
& + \nu \kappa_k \left( \widehat{u'_i(\mathbf{X})u'_j(\mathbf{X}')u'_k(\mathbf{X})} - \widehat{u'_i(\mathbf{X})u'_j(\mathbf{X}')u'_k(\mathbf{X}')} \right) \\
& = - \left( \frac{\partial}{\partial x_i} \widehat{p'(\mathbf{X})u'_j(\mathbf{X}')} + \frac{\partial}{\partial x_j} \widehat{p'(\mathbf{X}')u'_i(\mathbf{X})} \right) \\
& + 2 \left( \widehat{p'(\mathbf{X}') \frac{\partial u'_i(\mathbf{X})}{\partial \xi_j}} - \widehat{p'(\mathbf{X}) \frac{\partial u'_i(\mathbf{X}')}{\partial \xi_j}} \right) \\
& + \nu \frac{\partial^2}{\partial x_l \partial x_l} + 8\nu \frac{\partial u'_i(\mathbf{X})}{\partial \xi_l} \frac{\partial u'_j(\mathbf{X}')}{\partial \xi_l} \\
& + \frac{\partial \bar{u}_k}{\partial x_m} \frac{\partial}{\partial \kappa_m} (\kappa_k \Phi_{ij}) \tag{3.8}
\end{aligned}$$

where the hat symbol is related to the Fourier transform,  $\kappa$  is the wave vector,  $\Phi_{ij} = \widehat{u'_i(\mathbf{X})u'_j(\mathbf{X}')}$  and  $\nu^2 = -1$ . A common way of simplifying these equations is to eliminate the directivity in the wave number space, retaining only the modulus of the wave vector. This is achieved by performing an average over shells  $|\kappa| = \text{Cste}$ . Defining the spherical average operator in the Fourier space for an arbitrary function  $f$  as

$$\mathcal{A}(f) \equiv \int_{|\kappa|=\text{Cste}} \widehat{f}(\kappa) dA(\kappa) \tag{3.9}$$

where  $dA(\kappa)$  denotes the elementary surface element (illustrated in Fig. 3.4), one obtains the following evolution equation for  $\phi_{ij}(\kappa) \equiv \mathcal{A}(u_i(\mathbf{x})u_j(\mathbf{x}'))$ :

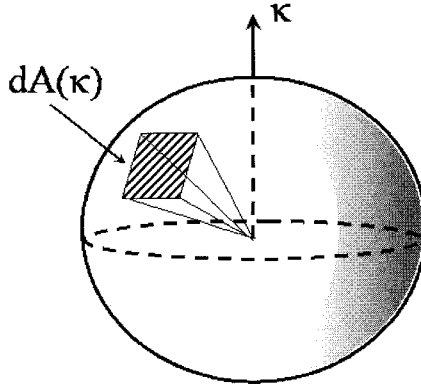


Fig. 3.4 Sphere of constant radius in the wave number space on which spherical average is performed to define the spectral tensor  $\phi_{ij}(\kappa)$ .

$$\begin{aligned}
 & \frac{\partial}{\partial t} \phi_{ij} + \bar{u}_k \frac{\phi_{ij}}{\partial x_k} + \phi_{kj} \frac{\partial \bar{u}_i}{\partial x_k} + \phi_{ik} \frac{\partial \bar{u}_j}{\partial x_k} + \Theta_{ij} + \frac{1}{2} \frac{\partial}{\partial x_k} (T_{ijk} + T_{jik}) \\
 & = -\Pi_{ij} - \left( \frac{\partial}{\partial x_i} P_j + \frac{\partial}{\partial x_j} P_i \right) \\
 & + \nu \frac{\partial^2 \phi_{ij}}{\partial x_l \partial x_l} - V_{ij} + \zeta_{kimj} \frac{\partial \bar{u}_k}{\partial x_m}
 \end{aligned} \tag{3.10}$$

where

$$T_{ijk} = \mathcal{A} \left( \overline{u'_i(\mathbf{X}) u'_j(\mathbf{X}') u'_k(\mathbf{X})} \right) = \mathcal{A} \left( \overline{u'_i(\mathbf{X}') u'_j(\mathbf{X}) u'_k(\mathbf{X}')} \right) \tag{3.11}$$

and

$$\Theta_{ij} = \mathcal{A} \left( \frac{\partial}{\partial \xi_k} \left( \overline{u'_i(\mathbf{X}) u'_j(\mathbf{X}') u'_k(\mathbf{X})} - \overline{u'_i(\mathbf{X}') u'_j(\mathbf{X}) u'_k(\mathbf{X}')} \right) \right) \tag{3.12}$$

are related to triple correlations,

$$\Pi_{ij} = 2\mathcal{A} \left( \overline{p'(\mathbf{X}') \frac{\partial u'_i(\mathbf{X})}{\partial \xi_j}} - \overline{p'(\mathbf{X}) \frac{\partial u'_j(\mathbf{X}')}{\partial \xi_i}} \right) \quad (3.13)$$

and

$$P_i = \mathcal{A} \left( \overline{p'(\mathbf{X}) u'_i(\mathbf{X}')} \right) = \mathcal{A} \left( \overline{p'(\mathbf{X}') u'_i(\mathbf{X})} \right) \quad (3.14)$$

contain the turbulent pressure-velocity interactions,

$$V_{ij} = -8\nu\mathcal{A} \left( \overline{\frac{\partial u'_i(\mathbf{X})}{\partial \xi_l} \frac{\partial u'_j(\mathbf{X}')}{\partial \xi_l}} \right) = \frac{1}{2}\nu \frac{\partial^2 \phi_{ij}}{\partial x_l \partial x_l} + 2\nu\kappa_m^2 \phi_{ij} \quad (3.15)$$

accounts for the viscous effects (both diffusion and dissipation), and

$$\zeta_{kimj} = - \left( \xi_m \frac{\partial}{\partial \xi_k} \overline{u'_i(\mathbf{X}) u'_j(\mathbf{X}')} \right) \quad (3.16)$$

is a pure non-homogeneous contribution. It is worth noting that the following relationships hold:

$$\Pi_{jj} = 0 \quad (3.17)$$

$$\int_0^{+\infty} \phi_{ij}(\kappa) d\kappa = R_{ij} = \overline{u'_i u'_j} \quad (3.18)$$

$$\int_0^{+\infty} T_{ijk}(\kappa) d\kappa = \overline{u'_i u'_j u'_k}. \quad (3.19)$$

The equation for the energy spectrum  $E(\kappa) \equiv \frac{1}{2} \phi_{ii}(\kappa)$  is obtained from Eq. (3.10) in a straightforward manner, yielding (the wave number dependency is omitted for the sake of clarity)

$$\frac{\partial}{\partial t} E + \bar{u}_k \frac{\partial}{\partial x_k} E + \phi_{kj} \frac{\partial \bar{u}_j}{\partial x_k} + \mathcal{F} + \frac{\partial}{\partial x_k} T_k = - \frac{\partial}{\partial x_i} P_i + \nu \frac{\partial^2 E}{\partial x_l \partial x_l} - \mathcal{E} \quad (3.20)$$

with

$$\mathcal{F} = \frac{1}{2} \left( \Theta_{ii} - \frac{\partial \bar{u}_k}{\partial x_m} \zeta_{kimi} \right) \quad (3.21)$$

$$\mathcal{E} = \frac{1}{2} V_{ii} \quad (3.22)$$

$$T_k = \frac{1}{2} T_{iik}. \quad (3.23)$$

### 3.2.2 The multiscale splitting

As explained in Sec. 2.5.1, the multiscale splitting relies on the following decomposition of the turbulent velocity field:

$$\mathbf{u}(\mathbf{x}, t) = \bar{\mathbf{u}}(\mathbf{x}) + \underbrace{\delta \mathbf{u}^{(1)}(\mathbf{x}, t) + \delta \mathbf{u}^{(2)}(\mathbf{x}, t) + \dots + \delta \mathbf{u}^{(n)}(\mathbf{x}, t)}_{\text{fluctuating field}} \quad (3.24)$$

In the present case of multiscale statistical modelling, the  $p$ -th part of the turbulent field is [Hanjalić, Launder and Schiestel, 1980; Schiestel, 1983a; Schiestel, 1983b; Schiestel, 1987] defined as<sup>1</sup>

$$\mathbf{u}^{(p)}(\mathbf{x}, t) = \int_{\kappa_{(p-1)} < |\kappa| \leq \kappa_{(p)}} \hat{\mathbf{u}}(\kappa, t) e^{i\kappa \cdot \mathbf{x}} d\kappa \quad (3.25)$$

where the set of cutoff wave numbers  $\kappa(l)$ ,  $l = 0, \dots, n$  is arbitrarily prescribed. The  $p$ -th order low-pass turbulent field is defined as

$$\tilde{\mathbf{u}}^{(p)} \equiv \sum_{i=1, p} \delta \mathbf{u}^{(i)} = \int_{|\kappa| \leq \kappa_{(p)}} \hat{\mathbf{u}}(\kappa, t) e^{i\kappa \cdot \mathbf{x}} d\kappa. \quad (3.26)$$

Using this definition for  $\tilde{\mathbf{u}}^{(p)}$ , its time-derivative is found to be equal to

$$\frac{d}{dt} \tilde{\mathbf{u}}^{(p)} = \frac{d\tilde{\mathbf{u}}^{(p)}}{dt} + \frac{d\kappa_{(p)}}{dt} \int_{|\kappa| = \kappa_{(p)}} \hat{\mathbf{u}}(\kappa, t) e^{i\kappa \cdot \mathbf{x}} dA(\kappa). \quad (3.27)$$

---

<sup>1</sup>The existence of such a decomposition is assumed, and the mathematical background will not be discussed here.

The first term which appears in the right hand side of Eq. (3.27) is associated with several physical processes: convection, diffusion, pressure effects. The second term is related to the spectral flux induced by a variation of the cutoff wave number  $\kappa(p)$ . Such a variation is found in adaptive multiscale methods, in which the cutoff wave numbers are adapted in order to prevent numerical problems or the appearance of spectral bands with very low energy levels.

### 3.2.3 Governing equations for band-integrated approaches

Usual band-integrated statistical multiscale models [Hanjalić, Launder and Schiestel, 1980; Schiestel, 1983a; Schiestel, 1983b; Schiestel, 1987; Gleize, Schiestel and Couaillier, 1996] are derived by considering the partial turbulent kinetic energy  $e^{(p)}$  and the partial Reynolds stresses  $R_{ij}^{(p)}$ , with

$$e^{(p)} = \int_{\kappa^{(p-1)}}^{\kappa^{(p)}} E(\kappa) d\kappa, \quad R_{ij}^{(p)} = \int_{\kappa^{(p-1)}}^{\kappa^{(p)}} \phi_{ij}(\kappa) d\kappa. \quad (3.28)$$

Noticing that

$$\frac{d}{dt} R_{ij}^{(p)} = \widetilde{\frac{du_i u_j}{dt}}^{(p)} + \frac{d\kappa^{(p)}}{dt} \phi_{ij}(\kappa^{(p)}) \quad (3.29)$$

one deduces from Eq. (3.10) the following evolution equation for the partial Reynolds stresses:

$$\frac{d}{dt} R_{ij}^{(p)} = \underbrace{\mathcal{P}_{ij}^{(p)}}_I + \underbrace{F_{ij}^{(p-1)} - F_{ij}^{(p)}}_{II} + \underbrace{\psi_{ij}^{(p)}}_{III} + \underbrace{\mathcal{D}_{ij}^{(p)}}_{IV} - \underbrace{\Upsilon_{ij}^{(p)}}_V \quad (3.30)$$

where

- Term I is related to the production resulting from the interaction with the mean velocity field:

$$\mathcal{P}_{ij}^{(p)} = - \left( R_{kj}^{(p)} \frac{\partial \bar{u}_i}{\partial x_k} + R_{ik}^{(p)} \frac{\partial \bar{u}_j}{\partial x_k} \right). \quad (3.31)$$

- The total transfer term II takes into account the triadic interactions due to the turbulent kinetic energy cascade (term  $F_{1,ij}^{(p)}$  below), the

rapid term associated to Rapid Distortion effect (*i.e.* the linear coupling with the mean field, term  $F_{2,ij}^{(p)}$  below) and the possible variation of spectral cutoff wave numbers (term  $F_{3,ij}^{(p)}$  below):

$$F_{ij}^{(p)} = \underbrace{\int_0^{\kappa(p)} \Theta_{ij}(\kappa) d\kappa}_{F_{1,ij}^{(p)}} - \underbrace{\frac{\partial U_k}{\partial X_m} \int_0^{\kappa(m)} \zeta_{kimj}(\kappa) d\kappa}_{F_{2,ij}^{(p)}} - \underbrace{\frac{d\kappa(p)}{dt} \phi_{ij}(\kappa(p))}_{F_{3,ij}^{(p)}}. \quad (3.32)$$

- The pressure-induced redistribution term III is equal to

$$\psi_{ij}^{(p)} = \int_{\kappa(p-1)}^{\kappa(p)} \Pi_{ij}(\kappa) d\kappa. \quad (3.33)$$

- The total diffusion term IV takes into account both the molecular diffusion, the pressure-induced diffusion and the turbulent diffusion

$$\mathcal{D}_{ij}^{(p)} = -\frac{\partial}{\partial x_k} T_{ijk}^{(p)} - \left( \frac{\partial G_j^{(p)}}{\partial x_i} + \frac{\partial G_i^{(p)}}{\partial x_j} \right) + \nu \frac{\partial^2 R_{ij}^{(p)}}{\partial x_l \partial x_l} \quad (3.34)$$

where

$$T_{ijk}^{(p)} = \frac{1}{2} \int_{\kappa(p-1)}^{\kappa(p)} (T_{ijk}(\kappa) + T_{jik}(\kappa)) d\kappa \quad (3.35)$$

$$G_i^{(p)} = \int_{\kappa(p-1)}^{\kappa(p)} P_i(\kappa) d\kappa. \quad (3.36)$$

- Term V is related to the viscous dissipation:

$$\Upsilon_{ij}^{(p)} = \int_{\kappa(p-1)}^{\kappa(p)} V_{ij}(\kappa) d\kappa. \quad (3.37)$$

The evolution equation for the partial turbulent kinetic energy is derived from Eq. (3.30) noting that  $e^{(p)} = \frac{1}{2} R_{ii}^{(p)}$ :

$$\frac{d}{dt} e^{(p)} = \mathcal{P}^{(p)} + F^{(p-1)} - F^{(p)} + \mathcal{D}^{(p)} - \Upsilon^{(p)} \quad (3.38)$$

where

$$\mathcal{P}^{(p)} = \frac{1}{2} \mathcal{P}_{ii}^{(p)} \quad (3.39)$$

$$F^{(p)} = \frac{1}{2} F_{ii}^{(p)} = \frac{1}{2} \left( F_{1,ii}^{(p)} + F_{2,ii}^{(p)} + F_{3,ii}^{(p)} \right) \quad (3.40)$$

$$\mathcal{D}^{(p)} = \frac{1}{2} \mathcal{D}_{ii}^{(p)} \quad (3.41)$$

$$\Upsilon^{(p)} = \frac{1}{2} \Upsilon_{ii}^{(p)}. \quad (3.42)$$

### 3.3 Spectral Closures for Band-integrated Approaches

#### 3.3.1 Local versus non-local transfers

We now address the issue of closing the spectrally split equations in Schiestel-type approaches, *i.e.* in approaches based on quantities defined as integral over spectral bands. Before discussing the main elements of the most popular models, it is worth discussing some key assumptions about the localness of the transfers in terms of wave numbers.

The quadratic nonlinearity in the convection term of the Navier–Stokes equations leads to a fully coupled problem, *i.e.* each spectral band is in interaction with all other spectral bands, as shown in Fig. 3.5.

A first simplification consists in neglecting energy exchanges between distant spectral bands. This is supported by Kraichnan’s theoretical analysis in the asymptotic case of isotropic turbulence at infinite Reynolds number, which shows that 75 % of energy transfers at wave number  $\kappa$  occur with wave numbers in the range  $[\kappa/2, 2\kappa]$ . This percentage grows up to 100 % in low-Reynolds number direct numerical simulations. Using this assumption, one deduces a simplified local (in terms of wave number) scheme for the energy balance in a spectral band (see Fig. 3.6).

The spectral scheme can be further simplified using the following assumptions:

- (1) Turbulent kinetic energy production occurs mainly at large scales associated with the peak of the turbulent energy spectrum. Therefore,

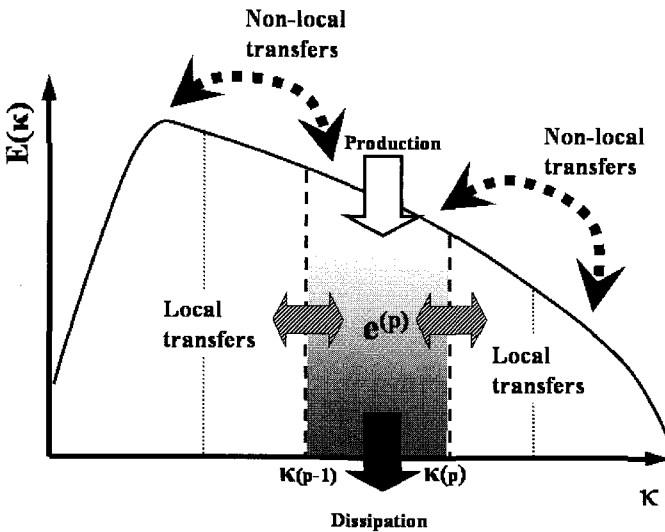


Fig. 3.5 Schematic illustration of the energy budget for the space/wave number control cell number  $p$ : kinetic energy can be created through coupling with the mean flow (instability mechanisms), it is dissipated via viscous effects, and it is transferred to other spectral bands via the energy cascade. Both local transfers toward adjacent spectral bands (shaded arrows) and non local transfers towards distant bands (dashed arrows) are represented. Spatial transport is not represented for the sake of clarity.

this term must be accounted for in the spectral band which includes the spectrum peak and can be neglected in other spectral bands.

- (2) The main energy cascade process is a forward kinetic energy cascade from large scale to small ones. Inverse (backward) cascade is much weaker in average and can therefore be neglected.
- (3) Viscous dissipation is mainly concentrated at small scales (a typical lengthscale for the turbulent dissipation being the Taylor microscale). Subsequently, viscous dissipation must be taken into account in the last spectral band only (*i.e.* at the smallest scales) and neglected in other spectral bands.

The resulting physical scheme in the spectral domain is displayed in Fig. 3.7, which is the cornerstone of all band-integrated multiscale models used in practical simulations.

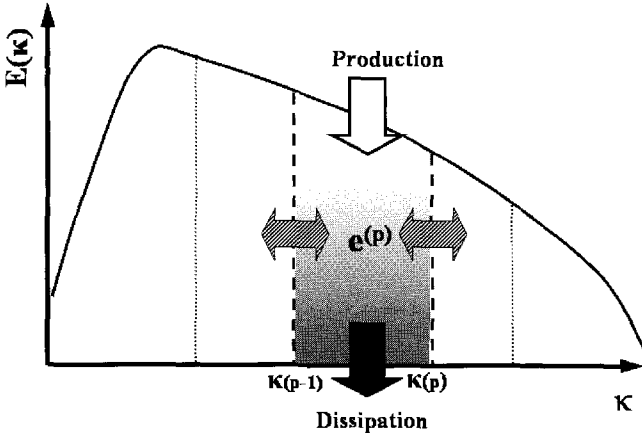


Fig. 3.6 Schematic illustration of the simplified energy budget for the space/wave number control cell number  $p$ , in which interactions with distant spectral bands are neglected. Spatial transport is not represented for the sake of clarity.

### 3.3.2 Expression for the spectral fluxes

As proposed by Schiestel and coworkers [Hanjalić, Launder and Schiestel, 1980; Schiestel, 1983a; Schiestel, 1983b; Schiestel, 1987; Gleize, Schiestel and Couaillier, 1996], an interesting first step is to close the spectral flux term which appears in the partial kinetic energy equation, since it is a scalar term.

The spectral transfer associated with the kinetic energy cascade can be modelled using a large number of models, a very simple one being the one proposed by Kovazsnay:

$$F_{1,ii}^{(p)} = a_1 \sqrt{\kappa(p)^5 E^3(\kappa(p))} \quad (3.43)$$

where  $a_1$  is a heuristic constant to be adjusted. This closure corresponds to a simple spectral viscosity approach based on dimensional analysis. The spectral energy density  $E(\kappa(p))$  needs to be evaluated. It is worth noting that this is not a direct output of the problem, since the quantities  $e(\kappa(p))$  are defined as integral quantities. Therefore, some additional hypotheses are required. A first possibility is to use an a priori analytic spectrum shape, such as those proposed by Pao, von Karman, Kovazsnay [Hinze,

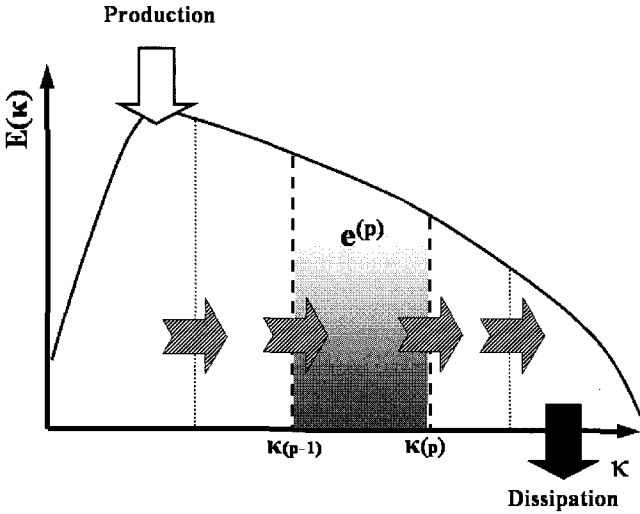


Fig. 3.7 Simplified spectral scheme. Main assumptions are: i) turbulent production occurs at large scales associated with the spectrum peak, ii) the forward kinetic energy cascade overwhelms the backward cascade in the mean and iii) viscous dissipation is concentrated at very small scales.

1987]. Using the Kovazsnay spectrum shape, one obtains:

$$E(\kappa(p)) = K_0 \varepsilon^{2/3} \kappa(p)^{-5/3} \left( 1 - \left( \frac{\kappa(p)}{\kappa_\eta} \right)^{4/3} \right)^2 \quad (3.44)$$

where  $K_0 = 1.4$ ,  $\varepsilon$  and  $\kappa_\eta$  are the Kolmogorov constant, the dissipation rate and the Kolmogorov scale associated wave number, respectively. Another possibility is to compute  $E(\kappa(p))$  directly:

$$E(\kappa(p)) = \beta_p \frac{e^{(p)}}{\kappa(p) - \kappa(p-1)} \quad (3.45)$$

where the coefficients  $\beta_p$  are introduced to manage the possibility of accounting for spectrum shape effects.

The linear transfer term, which accounts for the coupling between the mean velocity gradient and the turbulent fluctuations, needs also to be closed. Following the work of Jeandel, Brison and Mathieu [Jeandel, Brison and Mathieu, 1978], Schiestel and coworkers [Hanjalić, Launder and

Schiestel, 1980; Schiestel, 1983a; Schiestel, 1983b; Schiestel, 1987] propose to write:

$$F_{2,ii}^{(p)} = -\frac{\kappa(p)}{10} \phi_{lq}(\kappa(p)) \frac{\partial \bar{u}_l}{\partial x_q}. \quad (3.46)$$

The spectral tensor  $\phi_{lq}(\kappa(p))$  also requires to be approximated. A simple expression derived from the partial Reynolds stress tensor is

$$\phi_{lq}(\kappa(p)) = b_p^\phi \frac{R_{lq}^{(p)}}{\kappa(p) - \kappa(p-1)} \quad (3.47)$$

where  $b_p^\phi$  is another empirical shape parameter.

The last spectral transfer term, which is associated to changes in the cutoff wave number values, will be discussed in Sec. 3.3.3. In the case where the spectral bands are static, Eqs. (3.43) and (3.46) define a closed form of the spectral flux of kinetic energy.

The problem is now to model the spectral fluxes at the tensorial level, *i.e.* to work on the equations for the partial Reynolds stresses. A simple way to recover a tensorial model is to combine the scalar flux model and a non-dimensional structural anisotropy tensor :

$$F_{1,ij}^{(p)} + F_{2,ij}^{(p)} = \underbrace{\left( F_{1,ii}^{(p)} + F_{2,ii}^{(p)} \right)}_{\text{scalar flux}} \underbrace{\left( b_p \frac{R_{ij}^{(p)}}{E^{(p)}} + \frac{2}{3} (1 - b_p) \delta_{ij} \right)}_{\text{anisotropy tensor}} \quad (3.48)$$

where the weighting parameters  $b_p$  are used to account for the fact that anisotropy is concentrated at large scales<sup>2</sup>: they are close to one for spectral bands associated to large scales, and vanish at very small scales. The resulting form for the full spectral fluxes is

$$F_{ij}^{(p)} = F^{(p)} \left( B_p \frac{R_{ij}^{(p)}}{E^{(p)}} + \frac{2}{3} (1 - B_p) \delta_{ij} \right) \quad (3.49)$$

---

<sup>2</sup>This physical picture is in agreement with Kolmogorov's local isotropy hypothesis.

with

$$B_p = b_p \frac{F_{1,ii}^{(p)} + F_{2,ii}^{(p)}}{F^{(p)}}. \quad (3.50)$$

### 3.3.3 Dynamic spectral splitting

The last spectral flux term to be closed is the one associated with possible changes in the cutoff wave numbers. In order to derive relevant estimates for this flux term, it is necessary to first define the cutoff wave numbers. A natural way to choose the spectral bands is to tie them to some physical properties of the flow.

A possible solution, which makes it possible to account for local (in terms of wave numbers) fluctuations of the spectrum is to choose [Hanjalić, Launder and Schiestel, 1980; Schiestel, 1983a; Schiestel, 1983b; Schiestel, 1987]

$$\kappa(p) = \kappa(p-1) + \alpha_p \frac{F^{(p)}}{(e^{(p)})^{3/2}} \quad (3.51)$$

where  $\alpha_p$  are positive heuristic parameters.

An expression for the time derivative of  $\kappa(p)$  is retrieved from Eqs. (3.32) and (3.40):

$$\frac{d\kappa(p)}{dt} = \frac{F_{1,ii}^{(p)} + F_{2,ii}^{(p)} - F^{(p)}}{E(\kappa(p))}. \quad (3.52)$$

Differentiating Eq. (3.51) with respect to time and using Eq. (3.52) for the time derivative of the cutoff wave numbers, one obtains:

$$\frac{d\kappa(p)}{dt} - \frac{d\kappa(p-1)}{dt} = \alpha_p \frac{d}{dt} \left( \frac{F^{(p)}}{(e^{(p)})^{3/2}} \right) \quad (3.53)$$

$$= \frac{\alpha_p}{(e^{(p)})^{3/2}} \frac{dF^{(p)}}{dt} - \frac{3}{2} \alpha_p F^{(p)} (e^{(p)})^{-5/2} \frac{de^{(p)}}{dt}. \quad (3.54)$$

Combining this last expression with Eqs. (3.38) and (3.45), one recovers the following relation for the evolution of the partial kinetic energy flux:

$$\begin{aligned}
\frac{dF^{(p)}}{dt} &= \frac{1}{\beta_p} \frac{(F^{(p)})^2}{e^{(p)}} \left( \frac{F_{1,ii}^{(p)} + F_{2,ii}^{(p)}}{F^{(p)}} - 1 \right) \\
&\quad - \frac{1}{\beta_p} \frac{F^{(p)} F^{(p-1)}}{e^{(p)}} \frac{E(\kappa(p))}{E(\kappa(p-1))} \left( \frac{F_{1,ii}^{(p-1)} + F_{2,ii}^{(p-1)}}{F^{(p-1)}} - 1 \right) \\
&\quad + \frac{3}{2} \frac{F^{(p)}}{e^{(p)}} \left( \mathcal{P}^{(p)} - \Upsilon^{(p)} + F^{(p-1)} - F^{(p)} \right). \tag{3.55}
\end{aligned}$$

In practice, if a dynamic spectral splitting method is used, this equation for  $F^{(p)}$  is solved for each spectral band in order to get a closed form of the spectral fluxes.

### 3.3.4 Turbulent diffusion terms

Adapting the gradient model proposed by Hanjalić and Launder to the multiscale problem, Schiestel and coworkers [Hanjalić, Launder and Schiestel, 1980; Schiestel, 1983a; Schiestel, 1983b; Schiestel, 1987] propose the following model for the triple-correlation term:

$$T_{ijl}^{(p)} = -0.22 \frac{k R_{ql}}{F^{(1)}} \frac{\partial R_{ij}^{(p)}}{\partial x_q} \tag{3.56}$$

where  $k \equiv \sum_p e^{(p)}$  and  $R_{ql} \equiv \sum_p R_{ql}^{(p)}$  are the total turbulent kinetic energy and the total Reynolds stresses, respectively.

The pressure-velocity correlation induced diffusion can be closed using Hirt's hypothesis, leading to

$$G_i^{(p)} = \frac{k^2}{F^{(p)}} \frac{\partial R_{iq}^{(p)}}{\partial x_q}. \tag{3.57}$$

However, as quoted by Gleize [Gleize, 1994], this term is very often neglected since the underlying physics is still largely unknown the proposed model is believed to be a rough one.

### 3.3.5 Viscous dissipation term

In most approaches it is assumed that the dissipation is mostly isotropic since it is mainly associated with very small scales for which Kolmogorov's

local isotropy assumption is assumed to hold. As a result, one can write

$$\Upsilon_{ij}^{(p)} = \frac{2}{3}\Upsilon^{(p)}\delta_{ij}. \quad (3.58)$$

To simplify the model, the scalar dissipation term  $\Upsilon^{(p)}$  is usually assumed to be equal to zero for all spectral bands (*i.e.* at very large scales) except the last one, where the viscous dissipation is evaluated thanks to the local equilibrium hypothesis, meaning that the viscous dissipation rate is equal to the kinetic energy transfer rate:

$$\Upsilon^{(p)} = F^{(p-1)}. \quad (3.59)$$

### 3.3.6 Pressure term

Let us now consider the pressure term. Since the pressure-induced dynamics is very complex, a common way to close the spectrally-split equations is to use the usual single-scale models for each spectral band. Performing this way, the pressure term is split into a linear rapid term and a non-linear slow term. Using the Launder-Reece-Rodi model as a corner stone (see [Piquet, 1999] for a detailed introduction to usual single-scale closures), one obtains [Hanjalić, Launder and Schiestel, 1980; Schiestel, 1983a; Schiestel, 1983b; Schiestel, 1987]:

$$\begin{aligned} \psi_{ij}^{(p)} &= -c_{1,p}F^{(p)}\left(\frac{R_{ij}^{(p)}}{e^{(p)}} - \frac{2}{3}\delta_{ij}\right) - c_{2,p}\left(\mathcal{P}_{ij}^{(p)} - \frac{2}{3}\mathcal{P}^{(p)}\delta_{ij}\right) \\ &= \psi_{1,ij}^{(p)} + \psi_{2,ij}^{(p)}. \end{aligned} \quad (3.60)$$

This model can be supplemented by an additional echo-term to account for the presence of solid walls.

## 3.4 A Few Multiscale Models for Band-integrated Approaches

### 3.4.1 Multiscale Reynolds stress models

The general N-level multiscale Reynolds stress model is defined by the following equations, which must be solved for each spectral band  $p = 1, N$

[Schiestel, 1983a; Schiestel, 1983b; Schiestel, 1987; Gleize, Schiestel and Couaillier, 1996]:

$$\frac{d}{dt}R_{ij}^{(p)} = \mathcal{P}_{ij}^{(p)} + F_{ij}^{(p-1)} - F_{ij}^{(p)} + \psi_{ij}^{(p)} + \mathcal{D}_{ij}^{(p)} - \Upsilon_{ij}^{(p)} \quad (3.61)$$

$$\frac{d}{dt}e^{(p)} = \mathcal{P}^{(p)} + F^{(p-1)} - F^{(p)} + \mathcal{D}^{(p)} - \Upsilon^{(p)} \quad (3.62)$$

$$\begin{aligned} \frac{dF^{(p)}}{dt} = & \frac{1}{\beta_p} \frac{(F^{(p)})^2}{e^{(p)}} \left( \frac{F_{1,ii}^{(p)} + F_{2,ii}^{(p)}}{F^{(p)}} - 1 \right) \\ & - \frac{1}{\beta_p} \frac{F^{(p)}F^{(p-1)}}{e^{(p)}} \frac{E(\kappa(p))}{E(\kappa(p-1))} \left( \frac{F_{1,ii}^{(p-1)} + F_{2,ii}^{(p-1)}}{F^{(p-1)}} - 1 \right) \\ & + \frac{3}{2} \frac{F^{(p)}}{e^{(p)}} \left( \mathcal{P}^{(p)} - \Upsilon^{(p)} + F^{(p-1)} - F^{(p)} \right). \end{aligned} \quad (3.63)$$

### 3.4.2 Multiscale eddy-viscosity models

The multiscale Reynolds stress models involve a large number of additional unknowns, and therefore induce a large extra computational cost. To simplify the model while still accounting for several turbulent scales, it is possible to turn to multiscale models based on an eddy-viscosity approach, which will not require to solve evolution equations for each partial Reynolds stress.

The eddy-viscosity assumption is usually written as follows:

$$R_{ij}^{(p)} = \frac{2}{3}e^{(p)}\delta_{ij} - \nu_t^{(p)} \left( \frac{\partial \bar{u}_i}{\partial x_j} + \frac{\partial \bar{u}_j}{\partial x_i} \right). \quad (3.64)$$

The partial eddy viscosity is defined as

$$\nu_t^{(p)} = C_\mu^{(p)} \frac{k^2}{F^{(p)}} \quad (3.65)$$

where the  $C_\mu^{(p)}$  must be adjusted empirically.

### 3.5 Spectral Closures for Local Approaches

We now address the methods based on quantities which are local in the wave number space, *i.e.* which are not defined as integral over spectral bands as in Schiestel-type models. It is recalled that an important difference between band-integrated models and local models is that the former involve quantities defined in the physical space, while the latter are based upon spectral variables. As a consequence, usual single-scale closures expressed in the physical space are not as useful as in the previous case, and spectral closures developed within the framework of two-point models of turbulence are preferred as a starting point. Such methods have been proposed by Jeandel, Mathieu, Bertoglio and coworkers at Ecole Centrale de Lyon who derived the SCIT models<sup>3</sup> [Jeandel, Brison and Mathieu, 1978; Cambon, Jeandel and Mathieu, 1981; Bertoglio and Jeandel, 1986; Laporta, 1995; Parpais, 1997; Parpais *et al.*, 1999; Touil, 2002] and Besnard, Harlow, Zemach and Welsh at Los Alamos, who proposed the BHRZ model [Besnard *et al.*, 1990; Clark and Zemach, 1995].

#### 3.5.1 Local multiscale Reynolds stress models

The first class of local models deals with the closure of Eq. (3.10) for the spectral tensor  $\phi_{ij}(\kappa)$ .

Since the spectral tensor is known, both the advective term, the production term and the viscous term  $V_{ij}$  can be directly computed. All other terms must be closed.

The remaining terms can be grouped into five parts:

- (1) The linear transfer term
- (2) The linear pressure term
- (3) The non-linear homogeneous transfer term, which is responsible for the kinetic energy cascade in the homogeneous case
- (4) The non-linear non-homogeneous transfer term, which vanishes in the homogeneous case
- (5) The pressure-deformation term

A large number of closures for each of these terms can be found in the literature. Since an exhaustive presentation is out of the scope of the

---

<sup>3</sup>SCIT stands for Spectral Closure for Inhomogeneous Turbulence.

present book, it is chosen to emphasize the most recent closures still in use in research groups involved in the development of such multiscale models.

### 3.5.1.1 Closures for the linear transfer term

The linear transfer term is defined as

$$T_{ij}^{\text{lin}}(\mathbf{x}, \kappa, t) \equiv \frac{\partial \bar{u}_i}{\partial x_m} \int_{|\kappa|=\text{Cste}} \frac{\partial}{\partial \kappa_m} (\kappa_l \Phi_{ij}) dA(\kappa). \quad (3.66)$$

It accounts for the vortex stretching imposed by the mean velocity gradient. A general requirement is that this term has no contribution on the total turbulent kinetic energy<sup>4</sup>, *i.e.*

$$\int_0^{+\infty} T_{ij}^{\text{lin}}(\mathbf{x}, \kappa, t) d\kappa = 0. \quad (3.67)$$

A simple phenomenological model shows that this term is associated with a direct energy cascade when small turbulent structures are elongated along their main axis. Therefore, a simple model is proposed by Touil and Bertoglio [Touil, 2002] who represent this term as a spectral flux (a similar expression for the trace of this tensor was also advocated by Clark and Zemach [Clark and Zemach, 1995]):

$$T_{ij}^{\text{lin}}(\mathbf{x}, \kappa, t) = C_{\text{lin}} |\bar{\mathbf{S}}| \frac{\partial}{\partial \kappa} (\kappa \phi_{ij}(\mathbf{x}, \kappa, t)) \quad (3.68)$$

with

$$|\bar{\mathbf{S}}| = \sqrt{2\bar{S}_{ij}\bar{S}_{ij}}, \quad \bar{S}_{ij} = \frac{1}{2} \left( \frac{\partial \bar{u}_i}{\partial x_j} + \frac{\partial \bar{u}_j}{\partial x_i} \right). \quad (3.69)$$

When the constant  $C_{\text{lin}}$  is taken strictly negative, this model accounts for the direct energy cascade only, *i.e.* no backscatter is allowed. Bertoglio and Touil obtained the optimal value  $C_{\text{lin}} = -0.03$  in the case of two-dimensional uniform shear flows.

A much more complex model was also proposed by Cambon and coworkers [Cambon, Jeandel and Mathieu, 1981] and Besnard *et al.* [Besnard *et al.*,

---

<sup>4</sup>This constraint comes from the kinetic energy conservation property of the incompressible Euler equations.

1990], which is expected to lead to a better description of the mean velocity gradient:

$$\begin{aligned}
T_{ij}^{\text{lin}}(\mathbf{x}, \kappa, t) = & \left(1 - \frac{3}{2}c_b\right) \left(\overline{S}_{in} \frac{\partial}{\partial \kappa} (\kappa \phi_{nj}) + \overline{S}_{jn} \frac{\partial}{\partial \kappa} (\kappa \phi_{in})\right) \\
& - \frac{4}{3} \delta_{ij} \frac{\partial \overline{u}_n}{\partial x_m} \frac{\partial}{\partial \kappa} (\kappa \phi_{nm}) \Big) + \left(c_b - \frac{7}{10}\right) \overline{S}_{ij} \frac{\partial}{\partial \kappa} (\kappa \phi_{mm}) \\
& + \left(\frac{7}{2}c_b - \frac{8}{3}\right) \frac{\partial \overline{u}_n}{\partial x_m} \frac{\partial}{\partial \kappa} (\kappa \phi_{nm}) \tag{3.70}
\end{aligned}$$

where  $c_b$  is an arbitrary parameter. This parameter is related to the amplitude of the mean flow/turbulence coupling. Clark and Zemach [Clark and Zemach, 1995] found  $c_b = 0.761$  to yield the best results in the homogeneous shear case, which is very close to the value  $c_b = 0.77$  retained by Touil and Bertoglio [Touil, 2002].

### 3.5.1.2 Closures for the linear pressure term

The linear pressure term, also referred to as the rapid pressure term, is equal to

$$P_{ij}^{\mathcal{L}} = 2 \frac{\partial \overline{u}_l}{\partial x_m} \int_{|\kappa|=\text{Cste}} \frac{\kappa_l}{\kappa^2} (\kappa_i \Phi_{mj} + \kappa_j \Phi_{im}) dA(\kappa). \tag{3.71}$$

Cambon [Cambon, Jeandel and Mathieu, 1981] and Besnard [Besnard *et al.*, 1990] propose the following closure:

$$\begin{aligned}
P_{ij}^{\mathcal{L}} = & c_b \left( \frac{\partial \overline{u}_i}{\partial x_n} \phi_{nj} + \frac{\partial \overline{u}_j}{\partial x_n} \phi_{in} \right) - \frac{2}{3} c_b \delta_{ij} \frac{\partial \overline{u}_m}{\partial x_n} \phi_{mn} \\
& + (8c_b - 6) \left( \frac{\partial \overline{u}_n}{\partial x_i} \phi_{nj} + \frac{\partial \overline{u}_n}{\partial x_j} \phi_{in} \right) - \frac{2}{3} (8c_b - 6) \delta_{ij} \frac{\partial \overline{u}_m}{\partial x_n} \phi_{nm} \\
& + \left( \frac{11}{5} - 3c_b \right) \left( \frac{\partial \overline{u}_i}{\partial x_j} + \frac{\partial \overline{u}_j}{\partial x_i} \right) \phi_{nn}. \tag{3.72}
\end{aligned}$$

This model is linear with respect to the spectral tensor  $\phi_{ij}$ . It is obtained using a linear model for  $\Phi_{ij}$  with respect to  $\phi_{ij}$  which takes into account the incompressibility constraint and the symmetries of  $\Phi_{ij}$ . The parameter  $c_b$  is the same as for the linear transfer term.

### 3.5.1.3 Closures for the non-linear homogeneous transfer term

This term, denoted  $T_{ij}^{\text{NLH}}$  below, is closed according to Touil and Bertoglio [Touil, 2002] as the sum of an isotropic and an deviatoric part:

$$T_{ij}^{\text{NLH}} = \frac{2}{3} (T^{+\mathcal{N}\mathcal{L}} + T^{-\mathcal{N}\mathcal{L}} + \alpha T^{+\mathcal{L}}) \delta_{ij} + ((1 - \alpha)T^{+\mathcal{L}} + T^{-\mathcal{L}}) \frac{\phi_{ij}}{E} \quad (3.73)$$

where  $\alpha$  is an arbitrary constant which is a measure of the effect of the non-linear homogeneous transfer on the isotropy. The case  $\alpha \neq 0$  corresponds to the assumption that the kinetic energy cascade results in an increase of the anisotropy, while  $\alpha = 0$  is associated to pure return to isotropy. Touil and Bertoglio found  $\alpha = 0.2$  to yield the best results in the mean uniform shear case. Terms appearing in Eq. (3.73) are discussed below:

- $T^{+\mathcal{N}\mathcal{L}}(\mathbf{x}, \kappa, t)$  is related to the gain of kinetic energy at wave number  $\kappa$  resulting from non-local energy transfers. It is parametrized using the Eddy Damped Quasi Normal Markovian (EDQNM) theory proposed by Orszag [Orszag, 1970].

The usual EDQNM model for this term is

$$T^{+\mathcal{N}\mathcal{L}}(\mathbf{x}, \kappa, t) = \int \theta_{\kappa pq}(\mathbf{x}, t) (c_x c_y + c_z^3) \frac{\kappa^2}{q} E(\mathbf{x}, q, t) E(\mathbf{x}, p, t) \delta(\kappa - \mathbf{p} - \mathbf{q}) H(\kappa, p, q) d\mathbf{p} d\mathbf{q} \quad (3.74)$$

where  $c_x, c_y$  and  $c_z$  are geometrical parameters of the triad  $(\kappa, \mathbf{p}, \mathbf{q})$  (see Fig. 3.8),  $\theta_{\kappa pq}$  is a characteristic time scale for triple correlations associated to the triad and  $H(\kappa, p, q)$  is a function which is zero for local triads and 1 for non-local ones<sup>5</sup>.

The common EDQNM form for  $\theta_{\kappa pq}(\mathbf{x}, t)$  is

$$\theta_{\kappa pq}(\mathbf{x}, t) = \frac{1 - e^{-(\eta(\kappa) + \eta(p) + \eta(q))}}{\eta(\kappa) + \eta(p) + \eta(q)} \quad (3.75)$$

---

<sup>5</sup>Local triads are triads such that

$$\frac{1}{R} \leq \frac{\kappa}{p}, \frac{\kappa}{q}, \frac{p}{q} \leq R$$

where  $R$  is an arbitrary parameters. Touil and Bertoglio use  $R = 3$  in their simulations.

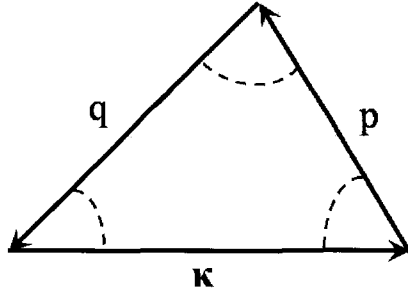


Fig. 3.8 Definition of topological parameter in the EDQNM model:  $c_x = \cos(q, p)$ ,  $c_y = \cos(\kappa, q)$  and  $c_z = \cos(p, \kappa)$ .

where the eddy damping rate  $\eta(\kappa)$  is given by an ad hoc model. Touil and Bertoglio use the simplest one, which was proposed by Pouquet and coworkers [Pouquet *et al.*, 1975]

$$\eta(\kappa) = \nu\kappa^2 + 0.355\sqrt{\int_0^\kappa r^2 E(r) dr}. \quad (3.76)$$

More complex forms of the damping rate, which are designed to account for rotation, shear or stratification effects can be found in the literature.

- $T^{-\mathcal{NL}}(\mathbf{x}, \kappa, t)$  is related to the loss of kinetic energy at wave number  $\kappa$  resulting from non-local energy transfers. The corresponding EDQNM model is

$$T^{-\mathcal{NL}}(\mathbf{x}, \kappa, t) = - \int \theta_{\kappa pq}(\mathbf{x})(c_x c_y + c_z^3) \frac{p^2}{q} E(\mathbf{x}, q, t) E(\mathbf{x}, \kappa, t) \delta(\kappa - \mathbf{p} - \mathbf{q}) H(\kappa, p, q) d\mathbf{p} d\mathbf{q}. \quad (3.77)$$

- $T^{+\mathcal{L}}(\mathbf{x}, \kappa, t)$  is related to the gain of kinetic energy at wave number  $\kappa$  resulting from local energy transfers. The EDQNM model is

$$T^{+\mathcal{L}}(\mathbf{x}, \kappa, t) = \int \theta_{\kappa pq}(\mathbf{x})(c_x c_y + c_z^3) \frac{\kappa^2}{q} E(\mathbf{x}, q, t) E(\mathbf{x}, p, t) \delta(\kappa - \mathbf{p} - \mathbf{q}) (1 - H(\kappa, p, q)) d\mathbf{p} d\mathbf{q}. \quad (3.78)$$

- $T^{-\mathcal{L}}(\mathbf{x}, \kappa, t)$  is related to the loss of kinetic energy at wave number  $\kappa$  resulting from local energy transfers. The EDQNM model is

$$T^{-\mathcal{L}}(\mathbf{x}, \kappa, t) = - \int \theta_{\kappa pq}(\mathbf{x})(c_x c_y + c_z^3) \frac{p^2}{q} E(\mathbf{x}, q, t) E(\mathbf{x}, \kappa, t) \delta(\kappa - \mathbf{p} - \mathbf{q}) (1 - H(\kappa, p, q)) d\mathbf{p} d\mathbf{q}. \quad (3.79)$$

The main underlying assumptions are : (i) the EDQNM closure derived for isotropic turbulence holds in the present case (ii) only local transfers are responsible for the return to isotropy mechanisms. An important feature of these EDQNM-based closures is that they are fully non-local in terms of wave numbers: all possible interactions between distant wave numbers are taken into account. This is seen observing that the models are defined as integrals over the whole spectral domain.

#### 3.5.1.4 Closures for the non-linear non-homogeneous transfer term

Non-homogeneous transfer terms  $T_{ij}^{\text{NLNH}}$  are associated with spatial derivatives. Therefore, a simple idea consists in approximating them as the divergence of a spatial flux. An eddy-viscosity assumption yields

$$T_{ij}^{\text{NLNH}} = \frac{\partial}{\partial x_k} \left( \nu_T^b \frac{\partial \phi_{ij}}{\partial x_l} \right) \quad (3.80)$$

where the amplitude of the turbulent diffusion is tuned using the turbulent diffusion parameter  $\nu_T^b$ . Three different expressions for the eddy viscosity have been proposed. In an early version of the SCIT model, Parpais and Bertoglio [Parpais, 1997] proposed

$$\nu_T^b(\mathbf{x}, \kappa, t) = \int_0^\infty \frac{E(\mathbf{x}, \kappa, t)}{A_2 \sqrt{\kappa^3 E(\mathbf{x}, \kappa, t)} + A_s \mathcal{T}^*(\mathbf{x}, t)} d\kappa \quad (3.81)$$

where  $A_2 = 1/0.6$  and  $A_s = 3/\sqrt{2}$  are optimal values for two-dimensional shear flows. The time scale  $\mathcal{T}^*$  is defined as follows:

$$T^* = \sqrt{2\overline{S}_{ij}\overline{S}_{ij} + 2\overline{\Omega}_{ij}\overline{\Omega}_{ij}}, \quad \overline{\Omega}_{ij} = \frac{1}{2} \left( \frac{\partial \overline{u}_i}{\partial x_j} - \frac{\partial \overline{u}_j}{\partial x_i} \right). \quad (3.82)$$

This is a modified version accounting for the mean shear of the eddy viscosity proposed by Besnard et al. [Besnard *et al.*, 1990]

$$\nu_T^b(\mathbf{x}, \kappa, t) = c_\nu \int_0^\infty \sqrt{\frac{E(\mathbf{x}, \kappa, t)}{\kappa^3}} d\kappa \quad (3.83)$$

where the optimal value for  $c_\nu$  in two-dimensional shear flows was found to be 0.1 by Besnard et al. and 0.6 by Laporta and Bertoglio [Laporta, 1995] for two-dimensional mixing layers. The model developed by Parpais and Bertoglio [Parpais, 1997] is observed to be more robust, *i.e.* the proposed values of the constants are found to be more general. A simpler version in the framework of the SCIT model is proposed by Touil and Bertoglio [Touil, 2002], whose form is similar to usual  $k - \varepsilon$  formulations of the eddy viscosity:

$$\nu_T^b(\mathbf{x}, \kappa, t) = c'_\nu \frac{\int_0^\infty E(\mathbf{x}, \kappa, t) d\kappa}{\int_0^\infty \kappa^2 E(\mathbf{x}, \kappa, t) d\kappa}. \quad (3.84)$$

Bertoglio and Touil found  $c'_\nu = 0.5$  to yield the best results in a two-dimensional plane channel flow.

### 3.5.2 Local multiscale eddy-viscosity models

A local multiscale eddy viscosity model was proposed by Parpais and Bertoglio [Parpais, 1997; Parpais *et al.*, 1999] on the grounds of previous researches dealing with the development of the SCIT model. This model can be interpreted as a simplified scalar form of the tensorial local model described above. It consists in closing Eq. (3.20).

The production term associated with the interaction of the turbulent fluctuations with the mean velocity gradients is modelled as follows:

$$-E(\mathbf{x}, \kappa, t) \left( \frac{2}{3} \delta_{ij} - \frac{A_0 S_{ij}(\mathbf{x}, t)}{A_1 \sqrt{\kappa^3 E(\mathbf{x}, \kappa, t)} + A_s T^*(\mathbf{x}, t)} \right) \frac{\partial \overline{u}_i}{\partial x_j} \quad (3.85)$$

where the coefficients are set equal to  $A_0 = 0.71$ ,  $A_1 = 0.28$  and  $A_s = 3/\sqrt{2}$  to recover good results in the homogeneous shear case.

The full non-linear homogeneous transfer term, including the pressure contribution, is closed using the EDQNM theory, yielding

$$\int \theta_{\kappa pq}(x, t) \frac{c_x c_y + c_z^3}{q} E(\mathbf{x}, q, t) (\kappa^2 E(\mathbf{x}, p, t) - p^2 E(\mathbf{x}, \kappa, t)) \times \delta(\kappa - \mathbf{p} - \mathbf{q}) d\mathbf{p} d\mathbf{q}. \quad (3.86)$$

The non-homogeneous transport term is parametrized using an eddy-viscosity closure

$$\frac{\partial}{\partial x_i} \left( \nu_T^b(\mathbf{x}, \kappa, t) \frac{\partial E(\mathbf{x}, \kappa, t)}{\partial x_i} \right) \quad (3.87)$$

where the eddy viscosity is given by Eq. (3.81).

The full viscous term is

$$-2\nu\kappa^2 E(\mathbf{x}, \kappa, t) + \frac{\nu}{2} \frac{\partial^2}{\partial x_l \partial x_l} E(\mathbf{x}, \kappa, t). \quad (3.88)$$

The coupling with the momentum equation for the mean velocity field is achieved using an eddy-viscosity closure, the turbulent eddy viscosity being defined as

$$\nu_T(\mathbf{x}, t) = \int_0^\infty \frac{A_0 E(\mathbf{x}, \kappa, t)}{A_1 \sqrt{\kappa^3 E(\mathbf{x}, \kappa, t)} + A_s \mathcal{T}^*(\mathbf{x}, t)} d\kappa. \quad (3.89)$$

### 3.6 Achievements and Open Issues

Simulations of turbulent flows carried out using multiscale RANS models are rare when compared to those based on single-scale models. The main reasons are that multiscale models:

- (1) involve a large number of empirical constants which must be adjusted, rendering their optimization more difficult than for single-scale models
- (2) induce a significant implementation effort, and the numerical treatment of the additional evolution equations requires some care
- (3) lead to an increase of the numerical cost.

Nevertheless, some significant achievements can be found in the literature.

Band-integrated models have been applied to homogeneous turbulence [Schiestel, 1983b; Wilcox, 1988b; Rubinstein, 2000], to boundary layer flows [Wilcox, 1988b], to the supersonic flow over a swept bump in a duct [Gleize, Schiestel and Couaillier, 1996], to divergent channel flows [Kim, 1991], to plane jets [Schiestel, 1983b; Schiestel, 1987], to plane wake [Schiestel, 1987], to round jets [Schiestel, 1987]. Kim and Chen [Kim and Chen, 1989] applied a two-scale  $k-\varepsilon$  model to a large number of test cases: fully developed channel flow and pipe flow, jet exhausting in a moving stream, wake-boundary layer interaction, wall jet, backward facing step flows, confined coaxial jet with or without swirl. It is worth noting that all these examples are based on two-bands, two-equations closures. The two bands are associated to turbulence production and turbulence dissipation, respectively. Such models require to solve 4 additional evolution equations (2 for partial kinetic energies, 2 for the spectral fluxes) if the full closure is considered, and only two if spectral bands are static. The fact that only very few spectral bands are used is coherent with the assumption that interactions between distant bands can be neglected, since there are no distant bands in this spectral decomposition. But, in the case where a large number of spectral bands are used, the issue of accounting for these interactions arise. The multiscale modification of traditional turbulence models is observed to potentially lead to very impressive improvements in the quality of the results in flows which are out of equilibrium, as shown by Gleize in the case of the flow around a wing at high angle of attack. The multiscale models are observed to better capture the flow dynamics, leading to a very satisfactory prediction of the evolution with respect to the angle of attack of the aerodynamic forces exerted on the wing (see Fig. 3.9). All models yield satisfactory results at low angle of attack (fully attached flow), while only multiscale models give good results at high angle of attack (separated flows). The differences between the prediction of a traditional, single-scale model and its multiscale, 2-bands counterpart is illustrated in Fig. 3.10 which compares iso-values of the predicted eddy viscosities.

Local models have been used to compute homogeneous turbulent flows [Besnard *et al.*, 1990; Clark and Zemach, 1995; Touil, 2002], turbulent mixing layer flow [Besnard *et al.*, 1990], fully developed channel flow [Parpais, 1997; Touil, 2002], backward facing step flow [Parpais, 1997; Touil, 2002], wall jet [Parpais, 1997], flow in a plane diffuser [Touil, 2002], and flow around a 2D wing [Touil, 2002]. The number of additional trans-

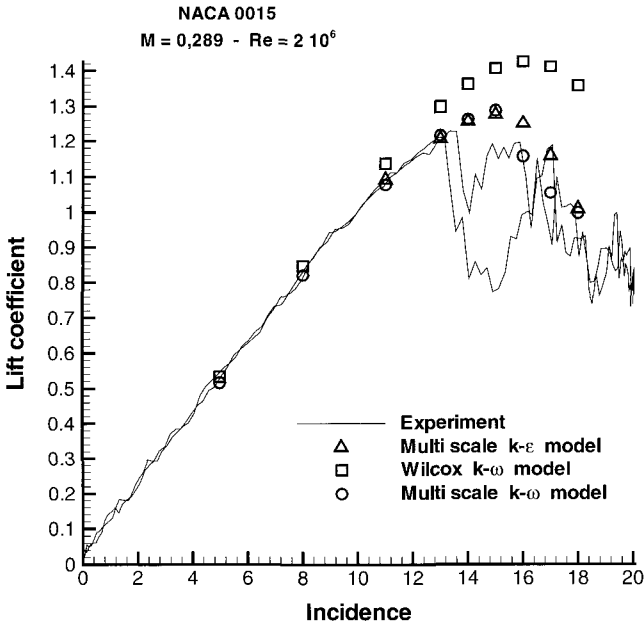


Fig. 3.9 Evolution of the mean lift coefficient versus the angle of attack. Courtesy of V. Gleize, ONERA, France.

port equations used in practice is much higher than for band-integrated models: Touil and Bertoglio recommend to use 40 wave numbers to recover an accurate description of the turbulent energy spectrum. We now illustrate the local methods considering the computation of the subsonic turbulent flow around the Aérospatiale F2A wing performed by Touil and Bertoglio [Touil, 2002]. The chord-based Reynolds number is equal to  $2.1 \cdot 10^6$ , the Mach number is 0.15 and the angle of attack is set equal to 13 degrees, which is near the maximum lift configuration. The authors solve the governing equations (compressible Navier–Stokes equations + 40-bands multiscale eddy-viscosity model) on a unstructured grid using a finite-element method. The mean flow features are illustrated in Fig. 3.11 which displays the mean streamlines in the vicinity of the wing. In the spectral domain, the smallest and the largest wave numbers are equal to  $3/2C$  and  $181597/C$ , respectively, where  $C$  is the chord of the profile. The total turbulent kinetic energy distribution is plotted in Fig. 3.12. It is observed that the multi-scale model is able to account for the recirculation bubble and the wake relaxation, while usual two-equation models fail. Another striking feature

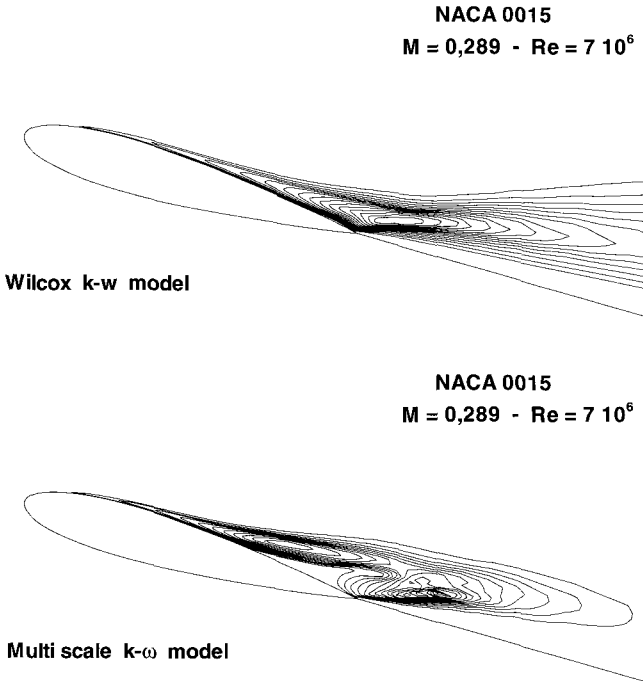


Fig. 3.10 Iso-values of the predicted eddy-viscosities. Courtesy of V. Gleize, ONERA, France.

of the multiscale model is that the transition to turbulence is naturally captured, without any artificial triggering technique as in usual computations. Details of the kinetic energy spectrum in the flow are displayed in Fig. 3.13. It is seen here that the method is able to predict the damping of large-scale structures in the near-wall region, while an inertial range is recovered at smaller scales. The analysis of the compensated spectra reveals the existence of a bump at the beginning of the dissipation range of the spectrum, which indicates that the turbulence is out of equilibrium in the wake. This point is illustrated looking at Fig. 3.14 which displays an indicator of non-equilibrium: it is observed that turbulence is locally out of equilibrium everywhere, including in the far wake. This is coherent with the idea that the global equilibrium achieved in turbulent regions results from a combination of spatial transport (mainly due to advection here) and interscale transfers, but not to interscale transfers only.



Fig. 3.11 Mean flow around the F2A wing: streamlines. The recirculation bubble on the suction side near the leading edge is correctly captured. Courtesy of H. Touil and J.P. Bertoglio, LMFA, France.

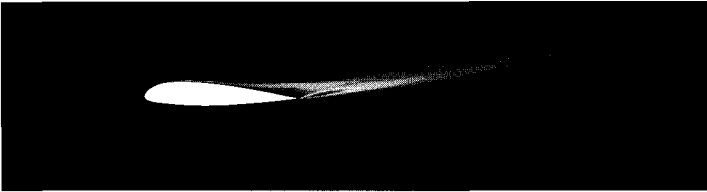


Fig. 3.12 Mean flow around the F2A wing: turbulent kinetic energy. Courtesy of H. Touil and J.P. Bertoglio, LMFA, France.

As a matter of fact, multiscale approaches are not new (significant results have been obtained in the early 1980s), but some open issues remain. One of the main problems is the development of multiscale models well suited for local refinement. A classical problem, already faced when dealing with single-scale models, is the use of local grid refinement or non-conformal grids: in these cases, the conservation of basic quantities at the interfaces must be carefully enforced. But an important fact is that this problem address the development of ad hoc numerical methods and does not impact the physical modelling. A new problem arises if the spectral splitting is allowed to vary (both the number of spectral bands and the value of cutoff wave numbers) in adjacent grid cells. The mapping of the spectral space in each cell being now non-conformal, the couplings are now much more complex to handle and multiscale models described above need to be revisited. Differences in local couplings (both in space and wave numbers) between a fully conformal, band-integrated multiscale method and a spectrally non-conformal one are illustrated by comparison of Fig. 3.15 and Fig. 3.16. It is worth noting that in Schiestel's approach, which includes the dynamic spectral splitting procedure, spatial variations of the cutoff wave numbers  $\kappa(p)$  are not explicitly taken into account. The equivalent

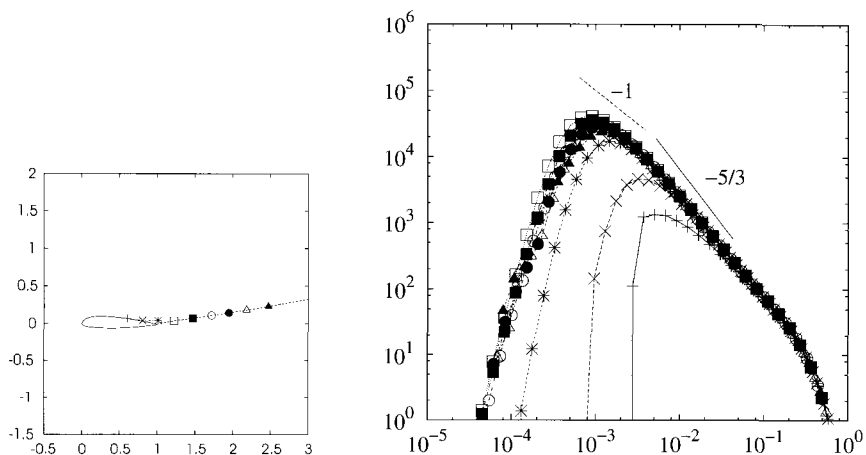


Fig. 3.13 Turbulent energy spectrum predicted at different locations using the SCIT local multiscale model. Left: positions where the spectrum is shown. Right: spectra. Symbols are related to the position of the virtual numerical probes. Transition of the spectrum slope and the rise of the inertial range is recovered. Courtesy of H. Touil and J.P. Bertoglio, LMFA, France.

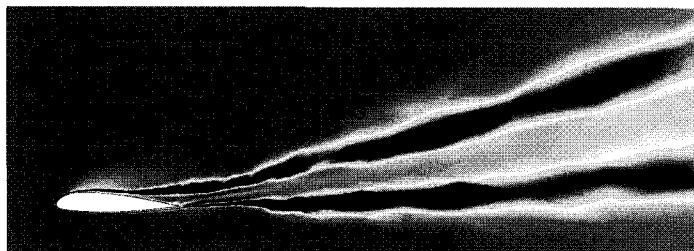


Fig. 3.14 Mean flow around the F2A wing: turbulence non-equilibrium indicator. Courtesy of H. Touil and J.P. Bertoglio, LMFA, France.

problem arising in local multiscale models such as BHRZ and SCIT is a spectrum interpolation problem, which must preserve both the kinetic energy and main spectrum features (location and value of peaks, slope in the inertial range if any). It is worth noting that the use of a spatially-varying spectral splitting seems to be required to maximize the gain coming from the multiscale approach in flows in which the turbulence spectrum exhibits large spectral variations. The use of dynamic spectral splittings as not yet been considered within the framework of local multiscale models.

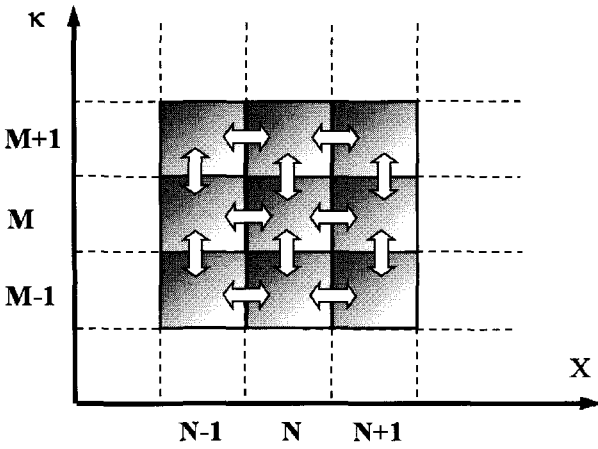


Fig. 3.15 Schematic view of local couplings in a fully conformal multiscale method. Arrows represent energy transfers which must be modelled. Non local couplings and hybrid spatial/spectral transport are not plotted for the sake of clarity.

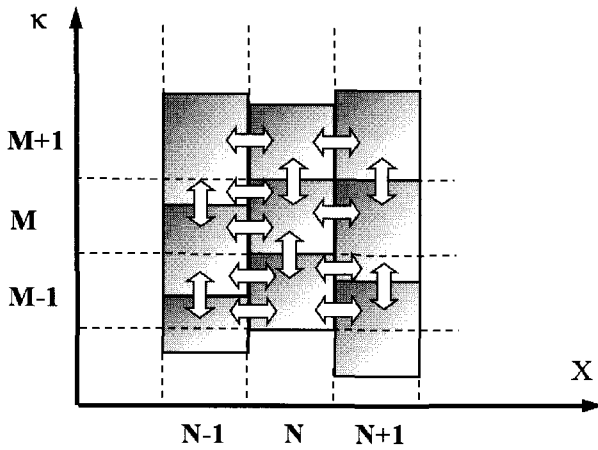


Fig. 3.16 Schematic view of local couplings in a spectrally non conformal but spatially conformal multiscale method. Arrows represent energy transfers which must be modelled. Non local couplings and hybrid spatial/spectral transport are not plotted for the sake of clarity.

This page is intentionally left blank

## Chapter 4

# Multiscale Subgrid Models: Self-adaptivity

### 4.1 Fundamentals of Subgrid Modelling

#### 4.1.1 *Functional and structural subgrid models*

As proposed by Sagaut [Sagaut, 2005], subgrid models can be grouped in two families:

- Functional subgrid models, which aim at enforcing the correct kinetic energy balance of the resolved scales. The subgrid model is therefore not necessarily designed to provide a reliable description of the subgrid stress tensor, but to mimic the kinetic energy transfers. The synthetic subgrid force  $\mathcal{F}_{\text{LES}}$  introduced in the momentum equation is such that

$$\int_{T_0}^T \int_V \bar{\mathbf{u}} \cdot \mathcal{F}_{\text{LES}} dV dt \simeq \int_{T_0}^T \int_V \tau_{\text{LES}} : \bar{\mathbf{S}} dV dt \quad (4.1)$$

where  $[T_0, T]$  and  $V$  are arbitrary time interval and spatial control volume, respectively (which can be simplified a pointwise values in some finite-difference-based approaches). Based on the understanding of the isotropic incompressible turbulence, functional subgrid models are designed to provide a net kinetic energy drain of resolved scales. It is recalled that  $\tau_{\text{LES}}$  refers to the exact subgrid stress tensor. This is a direct consequence of the dominance of the forward kinetic energy cascade, which leads to a net mean energy transfer toward subgrid scales across the cutoff. The most popular functional models are the explicit subgrid viscosity models, in which the intensity of the kinetic energy drain is tuned via a nonlinear viscosity  $\nu_{\text{sgs}}$ , leading to

$$\mathcal{F}_{\text{LES}} = \nabla \cdot (\nu_{\text{sgs}} (\nabla \bar{\mathbf{u}} + \nabla^T \bar{\mathbf{u}})) \quad (4.2)$$

where the functional dependence of  $\nu_{\text{sgs}}$  with respect to available information remains to be explicated.

- Structural models, whose purpose is to provide a high fidelity representation of the subgrid tensor  $\tau_{\text{LES}}$ .

#### 4.1.2 The Gabor-Heisenberg curse

Since Large-Eddy Simulation technique consists in solving directly the large-scales of the flow and the associated dynamics, it requires to perform three-dimensional simulations. The very reason for that is that the dynamics of the turbulent large scales is intrinsically three-dimensional. As a consequence, LES practitioners are seeking for subgrid models whose associated computational cost will be small with respect to the one required to solve the Navier-Stokes equations for the large scales.

Consequently, almost all existing subgrid models expressed in the physical space are basically local in that sense that their value at location  $\mathbf{x}$  and time  $t$  will depend only on quantities taken at the same location and the same time. This spatial localness is wanted for the sake of computing efficiency and data storage minimization. But the quest for localness has a direct consequence, which originates in the Gabor-Heisenberg uncertainty principle: the more local in space the subgrid model will be, the less accurate in the wave number space it will be. The uncertainty principle is illustrated in Fig. 4.1.

Let us note that the localness issue in the physical space is also faced when the question of the accuracy of the discrete approximation of space derivatives involved in the computation of subgrid models is addressed. For local numerical methods (finite difference, finite volume, finite element), the order of accuracy of discrete operators is directly tied to the number of degrees of freedom used. The larger is this number, the higher is the accuracy, but the wider is the stencil of the discrete operator, and therefore the less local is the discrete operator (see Fig. 4.2). It is also worth noting that the numerical error is concentrated at small scales (*i.e.* high wave numbers).

This lack of accuracy in the spectral space has a direct impact onto the efficiency of the model. It must be remembered here that the ideal subgrid model has to answer the two following questions:

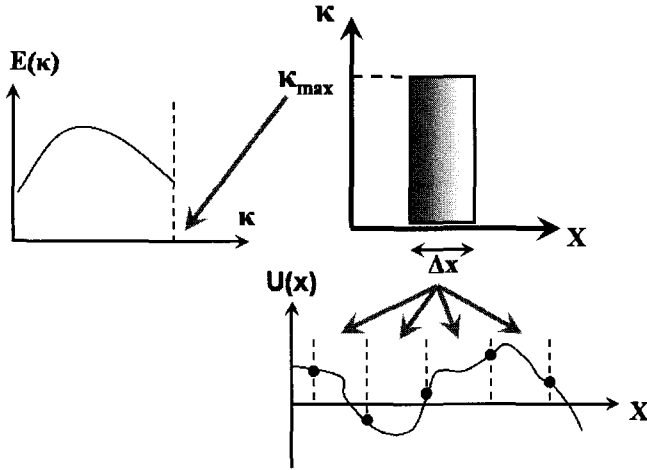


Fig. 4.1 Illustration of the Gabor-Heisenberg uncertainty principle. Choice of the mesh size  $\Delta x$  in the physical space automatically leads to the definition of the maximum wavenumber  $\kappa_{\max}$ . The uncertainty principle states that the product  $\Delta x \cdot \kappa_{\max}$ , which is equal to the area of the control cell in the upper right corner of the figure, is an invariant.

- (1) Is the flow at position  $\mathbf{x}$  and time  $t$  under-resolved, *i.e.* are there some subgrid scales which must be modelled?
- (2) If subgrid scales exist, what is the amplitude of the kinetic energy transfer across the cutoff (functional model approach) or what is the structure of the instantaneous subgrid tensor (structural model approach)?

The first question is as important as the second one, and it cannot be answered without using additional information. As a matter of fact, some foreknowledge about the characteristic features of an under-resolved turbulent field is required to perform the diagnosis and to conclude on the necessity of switching a subgrid model on. But using some theoretical or empirical prior knowledge during the simulation is not the whole task: the computed solution must be analyzed to yield a definitive answer. Subgrid models which have the capability of answering this question are referred to as *self-adaptive* models, because they are able to distinguish between fully resolved regions in which the simulation is a Direct Numerical Simulation and under-resolved regions, in which a subgrid model is required.

The two main strategies to solve this very difficult problem are the following:

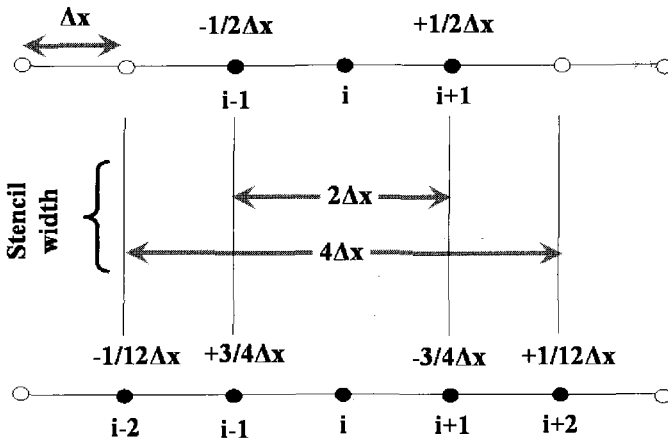


Fig. 4.2 Stencils and coefficients of the second-order accurate (top) and fourth-order accurate (bottom) centered finite-difference scheme for the first order derivative  $\partial/\partial x$  at grid point number  $i$ . The increase of the stencil width is a natural consequence of the accuracy gain, leading to a less local operator, which rises new problems near boundaries of the computational domain.

- the use of additional evolution equations for new variables which are tied to the subgrid scales, like the subgrid kinetic energy. Such a transport equation automatically makes the subgrid model non-local in both space and time, because of the memory effect due to advection along the trajectories.
- the use of a multilevel approach, which is based on the decomposition of the resolved velocity field into several wave number bands. These bands are then used to carry out some comparisons with the external knowledge dealing with turbulent under-resolved fields.

The first approach (introduction of new physical variables) leads to the definition of new subgrid characteristic scales (velocity scale, time scale, length scale), but is not automatically associated to a multiresolution-type technique based on an advanced spectral splitting of the solution. These subgrid models will not be discussed in the present book, the emphasis being put on the second strategy.

It is important to note that the physical localness/spectral accuracy problem is the main one here. The energy transfers associated with the

kinetic energy cascade being mostly local, the resolved scales which are responsible for the largest part of the energetic interactions with subgrid scales are the smallest ones. An accurate subgrid model is therefore expected to mainly depend upon these scales and to act on them, meaning that it is local in the wave number space. This need for spectrally localized subgrid models naturally open the way for models based on a spectral splitting of the resolved velocity field, in which large resolved scales will be separated from the small resolved ones. This splitting of the resolved field is a common feature shared by all subgrid models and closure strategies discussed in the present chapter. What is specific of each multilevel model or strategy is the way this spectral splitting is used to improve the usual single scale subgrid models, in which the resolved velocity field is treated as a monolithic block.

The self-adaptive character of the subgrid closures discussed below comes from the fact that being localized in the spectral space, they are more sensitive to the local state (fully resolved/under resolved) of the flow. A fully resolved flow being characterized by a very low energy level at the smallest resolved scales, an ideal spectrally localized subgrid model should be able to give an exact answer to the question of the existence of the subgrid scales. The increased sensitivity with respect to the small scales which are responsible for most of the energy transfers toward the unresolved scales is also expected to result in a better capability to account for non-equilibrium effects (e.g. rotation effects) which modify the energy transfer rate toward the subgrid scales.

Let us consider a generic single scale subgrid model expressed as

$$\tau_{ij} = C f_{ij}(\overline{\Delta}, \overline{\mathbf{u}}) \quad (4.3)$$

where  $C$  is an arbitrary constant,  $\overline{\Delta}$  is the cutoff length scale associated with the LES resolution and  $\overline{\mathbf{u}}$  is the full resolved field. The model  $f$  is the most general one, and can have an integro-differential expression. One can also write  $\overline{\Delta} = \overline{\Delta}^{(1)}$  and  $\overline{\mathbf{u}}^{(1)}$  according to the multilevel formalism introduced in Sec. 2.5.1. Such a model will be classified as a single scale one, since only one cutoff level and one cutoff length are involved.

Two different but compatible strategies can be followed to improve this model using a multilevel decomposition. First, one can try to use the spectral splitting to optimize the value of the constant  $C$ , which is now a function of both space and time. Such a relationship can be formally

written as

$$\tau_{ij} = C(\overline{\Delta}^{(1)}, \overline{\mathbf{u}}^{(1)}, \overline{\Delta}^{(2)}, \overline{\mathbf{u}}^{(2)}, \dots) f_{ij}(\overline{\Delta}, \overline{\mathbf{u}}). \quad (4.4)$$

Such models are referred to as dynamic models, using the term coined by Germano and coworkers. They represent the lowest degree of modification of single-scale closures, and can be interpreted as an optimal projection of the true subgrid tensor  $\tau_{ij}$  onto the space spanned by  $f_{ij}(\overline{\Delta}, \overline{\mathbf{u}})$ . The optimality is here tied to the definition of an error measure and the minimization of the corresponding residual. Two families of dynamic procedures are presented below: procedures based on the Germano identity (Sec. 4.2) and procedures based on self-similarity assumptions (Sec. 4.3). In both cases, the error estimate to be minimized is obtained inserting the subgrid model into an exact relation fulfilled by the exact subgrid term. Since the model is not perfect, the original relation is not satisfied, and a residual can be computed, which is a measure of the committed modelling error. The constant  $C$  is then chosen so as to minimize a given norm of this residual (see Fig. 4.3).

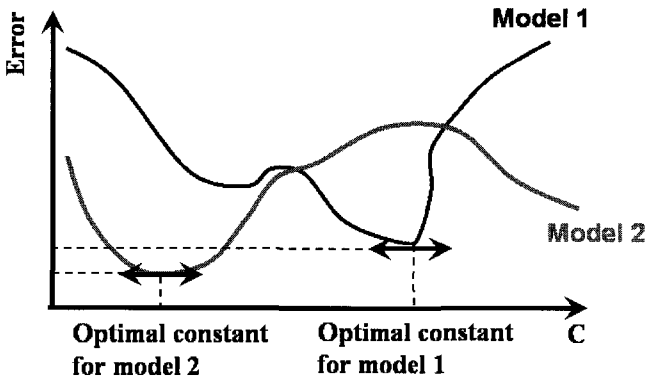


Fig. 4.3 Illustration of the dynamic procedure principle. The two lines (black and grey) are related to different subgrid models, whose constant are adjusted dynamically. It is important noting that both the minimal error and the value of the constant are model-dependent.

The second strategy consists in modifying the model itself, rendering it sensitive to the spectral splitting of the resolved field, yielding

$$\tau_{ij} = C' f_{ij}(\overline{\Delta}^{(1)}, \overline{\mathbf{u}}^{(1)}, \overline{\Delta}^{(2)}, \overline{\mathbf{u}}^{(2)}, \dots). \quad (4.5)$$

The arbitrary constant  $C'$  is a priori not equal to the one of the original single-scale model,  $C$ . The most complete frameworks are the Variational Multiscale method proposed by Hughes (Sec. 4.4) and the Multilevel Large-Eddy Simulation method of Terracol and Sagaut (Sec. 5.4.2).

The two strategies can of course be coupled, leading to the definition of a dynamic multiscale model:

$$\tau_{ij} = C'(\overline{\Delta}^{(1)}, \overline{\mathbf{u}}^{(1)}, \overline{\Delta}^{(2)}, \overline{\mathbf{u}}^{(2)}, \dots) f_{ij}(\overline{\Delta}^{(1)}, \overline{\mathbf{u}}^{(1)}, \overline{\Delta}^{(2)}, \overline{\mathbf{u}}^{(2)}, \dots). \quad (4.6)$$

## 4.2 Germano-type Dynamic Subgrid Models

This section is devoted to the most popular dynamic procedure for arbitrary constant adjustment, *i.e.* those relying on the Germano identity. This technique was proposed by Germano and coworkers in the early 1990s [Germano *et al.*, 1991; Germano, 1992; Germano, 1996; Germano, 2001], and has been extensively used and improved by many research groups, the most active one on this topic being certainly the Center for Turbulence Research at Stanford University.

### 4.2.1 Germano identity

The Germano identity is an exact relation which ties the subgrid tensor at different levels of filtering [Germano *et al.*, 1991; Germano, 1992; Germano, 1996; Germano, 2001]. Several alternative formulations exist, which are discussed below.

#### 4.2.1.1 Two-level multiplicative Germano Identity

We first consider the multiplicative Germano identity. For the sake of simplicity, but without any loss of generality, the presentation is restricted to the case of the two-level Germano identity. The generalized formulation for an arbitrary number of filtering levels will be discussed later on. The filtering paradigm is used in this section to model the large-eddy simulation

scale separation at each resolution level. But it is important noting that the Germano relation is more general and is not restricted to the convolution filtering case and formally equivalent expression can be straightforwardly obtained using alternative definitions for the scale separation operator, such as projection onto a truncated basis.

A sequential application of two filters,  $G_1$  and  $G_2$  to the exact solution  $u$  yields

$$\bar{u}^{(2)} = G_2 \star \bar{u}^{(1)} = G_2 \star G_1 \star u. \quad (4.7)$$

Here,  $\bar{u}^{(2)}$  corresponds to the resolved field for the double filtering  $(G_2 \star) \circ (G_1 \star)$ . The two filtering levels are illustrated in Fig. 4.4.

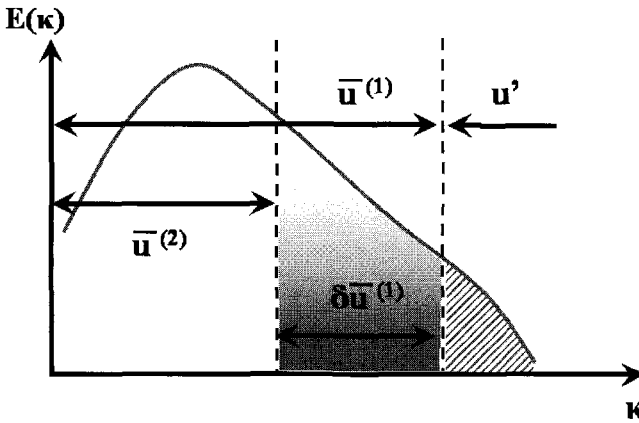


Fig. 4.4 Spectral splitting for the basic Germano dynamic procedure. The scale separation operator is chosen here to be a sharp cutoff filter.

As proposed by Germano [Germano, 1986], the subgrid tensor associated with the second filtering level is defined as the following generalized central moment:

$$\tau_{ij}^{(2)} = \overline{u_i u_j}^{(2)} - \overline{u_i}^{(2)} \overline{u_j}^{(2)}. \quad (4.8)$$

The part of the subgrid tensor associated to the second filtering level which can be computed from the resolved field at the first filtering level is

$$\mathcal{L}_{ij}^{(2)} = G_2 \star \left( \overline{u_i^{(1)}} \overline{u_j^{(1)}} \right) - \overline{u_i^{(2)}} \overline{u_j^{(2)}}. \quad (4.9)$$

Combining these two relations, one obtains the Germano identity, which is an exact relation between the subgrid tensors computed at two different filtering levels:

$$\tau_{ij}^{(2)} = G_2 \star \tau_{ij}^{(1)} + \mathcal{L}_{ij}^{(2)}. \quad (4.10)$$

This relation can be interpreted as follows. The subgrid tensor at the second filtering level is equal to the sum of the subgrid tensor at the  $G_1$  level filtered at the  $G_2$  level and the subgrid tensor at the  $G_2$  level calculated from the field resolved at the  $G_1$  level. This relation is local in space and time and is independent of the filter used. This identity can be referred to as the *multiplicative Germano identity* [Germano, 2001], because it is based on a sequential application of the two filters.

#### 4.2.1.2 Multilevel Germano Identity

We now present the general,  $N$ -level Germano identity (see [Sagaut, 2005]). Let us consider  $N$  filtering levels,  $G_i, i = 1, N$ , with associated characteristic lengths  $\overline{\Delta}_1 \leq \overline{\Delta}_2 \leq \dots \leq \overline{\Delta}_N$  [Germano, 1998; Terracol, Sagaut and Basdevant, 2000; Sagaut *et al.*, 2000].

We define the  $n$ th level filtered variable  $\overline{\phi}^{(n)}$  (where  $\phi$  is a dummy variable) as

$$\overline{\phi}^{(n)} = G_n \star G_{n-1} \star \dots \star G_1 \star \phi = \mathcal{G}_1^n \star \phi \quad (4.11)$$

with

$$\mathcal{G}_m^n \equiv G_n \star G_{n-1} \star \dots \star G_m, \mathcal{G}_n^n = Id, \quad \forall m \in [1, n]. \quad (4.12)$$

Let  $\tau_{ij}^{(n)} = \overline{u_i u_j}^{(n)} - \overline{u_i}^{(n)} \overline{u_j}^{(n)}$  be the subgrid tensor associated to the  $n$ th filtering level. The classical two-level Germano identity (4.10) reads

$$\tau_{ij}^{(n+1)} = G_{n+1} \star \tau_{ij}^{(n)} + \mathcal{L}_{ij}^{(n+1)} \quad (4.13)$$

where

$$\mathcal{L}_{ij}^{(n+1)} = G_{n+1} \star \left( \overline{u_i^{(n)}} \overline{u_j^{(n)}} \right) - \overline{u_i^{(n+1)}} \overline{u_j^{(n+1)}}. \quad (4.14)$$

Simple algebraic developments lead to the following relation between two filtering levels  $n$  and  $m$ , with  $m < n$ :

$$\tau_{ij}^{(n)} = \mathcal{L}_{ij}^{(n)} + \sum_{k=m+1, n-1} \mathcal{G}_{k+1}^n \mathcal{L}_{ij}^{(k)} + \mathcal{G}_{m+1}^n \tau_{ij}^{(m)} \quad (4.15)$$

resulting in a fully general multilevel identity.

#### 4.2.1.3 Generalized Germano Identity

The basic formulation of the Germano identity can be further extended by considering an additional operator, which can be a non-linear integro-differential one (see [Sagaut, 2005; Morinishi and Vasilyev, 2002]). A more general multiplicative identity is obtained by applying the arbitrary operator  $\mathcal{L}$  to the basic identity, yielding

$$\begin{aligned} \mathcal{L}\{[G_2 \star G_1 \star, \mathcal{B}](u_i, u_j)\} &= \mathcal{L}\{[G_2 \star, \mathcal{B}] \circ (G_1 \star)(u_i, u_j) \\ &\quad + (G_2 \star) \circ [G_1 \star, \mathcal{B}](u_i, u_j)\}. \end{aligned} \quad (4.16)$$

where  $[\cdot, \cdot]$  is the commutator defined by relation (2.3), and  $\mathcal{B}$  is the bilinear operator:  $\mathcal{B}(\alpha, \beta) = \alpha\beta$ . For linear operators, we get the simplified formulation

$$\begin{aligned} \mathcal{L}\{[G_2 \star G_1 \star, \mathcal{B}](u_i, u_j)\} &= \mathcal{L}\{[G_2 \star, \mathcal{B}] \circ (G_1 \star)(u_i, u_j)\} \\ &\quad + \mathcal{L}\{(G_2 \star) \circ [G_1 \star, \mathcal{B}](u_i, u_j)\}. \end{aligned} \quad (4.17)$$

This new way of extending the Germano relation can be easily combined with the general N-level Germano identity, leading to a fully general exact relation.

## 4.2.2 Derivation of dynamic subgrid models

We now show how, using one of the Germano identities, the optimal value of the constant  $C$  in Eq. (4.3) [Germano *et al.*, 1991]. The first step consists in defining two scale separation levels, associated with the two operators  $G_1$  and  $G_2$ . The first level usually represents the scale separation intrinsically introduced by the simulation<sup>1</sup> while the second one, very often referred to as the *test level*, is reached in practical simulation by applying an explicit scale-separation operator to the computed solution. The second step consists in assuming that the *same subgrid model* with the *same constant* can be

---

<sup>1</sup>This is the so-called *effective filter* or *grid filter*, which originates in the combination of the numerical grid and the numerical method.

applied to parametrize the subgrid motions at the two levels of resolution, yielding

$$\tau_{ij}^{(1)} = C f_{ij}(\bar{\Delta}^{(1)}, \bar{\mathbf{u}}^{(1)}) \quad (4.18)$$

$$\tau_{ij}^{(2)} = C f_{ij}(\bar{\Delta}^{(2)}, \bar{\mathbf{u}}^{(2)}) \quad (4.19)$$

where  $f_{ij}$  denotes a generic subgrid model. The error estimate is obtained inserting Eqs. (4.18) and (4.19) into the Germano identity (the two-level multiplicative Germano identity (4.10) is used here to illustrate the process), leading to the definition of the residual  $E_{ij}$

$$E_{ij} = C f_{ij}(\bar{\Delta}^{(2)}, \bar{\mathbf{u}}^{(2)}) - G_2 \star \left( C f_{ij}(\bar{\Delta}^{(1)}, \bar{\mathbf{u}}^{(1)}) \right) - \left( G_2 \star \left( \bar{u}_i^{(1)} \bar{u}_j^{(1)} \right) - \bar{u}_i^{(2)} \bar{u}_j^{(2)} \right). \quad (4.20)$$

The key idea is to find the local (in both space and time) value of  $C$  which minimizes the residual  $E_{ij}$ , which is zero in the ideal case where the subgrid model  $f_{ij}$  is perfect. Two difficulties arise immediately.

The first one is that the constant appears inside the scale separation operator in the second term in the right hand side of Eq. (4.20). Solving this problem leads to the definition of the non-local Fredholm problem of the second kind. A method based on the resolution of this new problem was proposed by Ghosal *et al.* [Ghosal *et al.*, 1995]. But, since this procedure requires a non-trivial code development and induces a significant extra-computational cost, almost all authors assume the parameter  $C$  is varying slowly enough in space, leading to

$$E_{ij} = C \underbrace{\left( f_{ij}(\bar{\Delta}^{(2)}, \bar{\mathbf{u}}^{(2)}) - G_2 \star f_{ij}(\bar{\Delta}^{(1)}, \bar{\mathbf{u}}^{(1)}) \right)}_{M_{ij}^{(2)}} - \underbrace{\left( G_2 \star \left( \bar{u}_i^{(1)} \bar{u}_j^{(1)} \right) - \bar{u}_i^{(2)} \bar{u}_j^{(2)} \right)}_{\mathcal{L}_{ij}^{(2)}}. \quad (4.21)$$

The second problem is that Eq. (4.21) results in six relations, while there is only one adjustable parameter. A first solution is to consider a tensorial constant  $C_{ij}$ , each component being directly computed from the preceding relation. Numerical experiments show that this solution is not very satisfactory from a numerical point of view. To alleviate this problem

in a more satisfactory way, Germano proposes to introduce an auxiliary tensor  $A_{ij}$ , and to search for the value of  $C$  that will minimize the scalar quantity  $E_{ij}A_{ij}$ . Germano and coworkers [Germano *et al.*, 1991] originally used  $A_{ij} = \overline{S_{ij}^{(1)}}$ , while Lilly [Lilly, 1992] later chose  $A_{ij} = E_{ij}$ , leading to the definition of the following least-square minimization problem:

*Find  $C(x, t)$  such that  $E_{ij}E_{ij}$  is minimum.*

Since  $E_{ij}E_{ij}$  is a quadratic convex function of  $C$ , the existence and the uniqueness of the optimal solution, noted  $C_d$ , is guaranteed. It is computed in practice writing

$$\frac{\partial E_{ij}E_{ij}}{\partial C_d} = 0 \quad . \quad (4.22)$$

The solution is

$$C_d = \frac{\mathcal{L}_{ij}^{(2)} M_{ij}^{(2)}}{M_{ij}^{(2)} M_{ij}^{(2)}} \quad . \quad (4.23)$$

This optimal definition in the least-square sense is observed to be efficient in practice. Dynamic models are found to have powerful self-adaptivity capabilities:

- They vanish in regions where the flow is fully resolved.
- They recover the theoretical asymptotic behaviors in some critical regions, e.g. they decay correctly in the very near wall region in equilibrium boundary layers.
- They can, at least partially, take into account the numerical error, e.g. the kinetic energy rate damping of the resolved scales will be reduced if a non-negligible numerical dissipation is present.

But all dynamic models suffer the same stability weakness: the dynamic constant  $C_d$  defined by Eq. (4.23) is observed to take some quasi-infinite values at some points, and it also can take negative values at the same location for long times. To remedy these problems, a large number of regularization procedure have been investigated (see [Sagaut, 2005; Germano, 2001] for reviews): clipping between arbitrary bounds, spatial averaging over neighboring nodes or homogeneous direction or along streamlines. All these smoothing procedures make the dynamic constant

more regular and alleviate most of the numerical problems, but the regularized constant is not the optimal one anymore.

### 4.2.3 *Dynamic models and self-similarity*

The use of the same value of the constant for the subgrid model at the two filtering levels appearing in Eqs. (4.20) and (4.21) implicitly relies on the two following self-similarity assumptions:

- The two cutoff lengths are such that both cutoffs are located in the inertial range of the kinetic energy spectrum;
- The filter kernels associated to the two filtering levels are themselves self-similar.

These two constraints are not automatically satisfied, and the validity of the dynamic procedure for computing the constant requires a careful analysis.

#### 4.2.3.1 *Turbulence self-similarity*

Meneveau and Lund [Meneveau and Lund, 1997] propose an extension of the dynamic procedure for a cutoff located in the viscous range of the spectrum. Writing the constant of the subgrid-scale model  $C$  as an explicit function of the filter characteristic length, the Germano–Lilly procedure leads to

$$C(\overline{\Delta}^{(1)}) = C(\overline{\Delta}^{(2)}) = C_d. \quad (4.24)$$

Let  $\eta$  be the Kolmogorov length scale. It was said in the introduction that the flow is fully resolved if  $\overline{\Delta}^{(1)} = \eta$ . Therefore, the dynamic procedure is consistent if, and only if

$$\lim_{\overline{\Delta}^{(1)} \rightarrow \eta} C_d = C(\eta) = 0. \quad (4.25)$$

Numerical experiments carried out by the two authors show that the Germano–Lilly procedure is not consistent, because it returns the value of the constant associated to the test filter level

$$C_d = C(\overline{\Delta}^{(2)}) \quad (4.26)$$

yielding

$$\lim_{\overline{\Delta}^{(1)} \rightarrow \eta} C_d = C(r\eta) \neq 0, \quad r = \overline{\Delta}^{(2)} / \overline{\Delta}^{(1)}. \quad (4.27)$$

Numerical tests also showed that taking the limit  $r \rightarrow 1$  or computing the two values  $C(\overline{\Delta})$  and  $C(r\overline{\Delta})$  using least-square-error minimization without assuming them to be equal yield inconsistent or ill-behaved solutions. A solution is to use prior knowledge to compute the dynamic constant. A robust algorithm is obtained by redefining the Germano identity based residual as follows:

$$E_{ij} = \mathcal{L}_{ij} - C(\overline{\Delta}^{(1)}) \left( g(\overline{\Delta}^{(1)}, r) f_{ij}(\overline{\Delta}^{(2)}, \overline{\mathbf{u}}^{(2)}) - G_2 \star f_{ij}(\overline{\Delta}^{(1)}, \overline{\mathbf{u}}^{(1)}) \right) \quad (4.28)$$

where  $g(\overline{\Delta}^{(1)}, r) = C(r\overline{\Delta}^{(1)})/C(\overline{\Delta}^{(1)})$  is approximated by the following simple analytical fitting in the case  $r = 2$ :

$$g(\overline{\Delta}^{(1)}, 2) \approx \max(100, 10^{-x}), \quad x = 3.23(Re_{\frac{2}{\overline{\Delta}^{(1)}}}^{-0.92} - Re_{\overline{\Delta}^{(1)}}^{-0.92}) \quad (4.29)$$

where the mesh-Reynolds numbers are evaluated as:

$$Re_{\overline{\Delta}^{(1)}} = \frac{(\overline{\Delta}^{(1)})^2 |\overline{\mathbf{S}}^{(1)}|}{\nu}, \quad Re_{\frac{2}{\overline{\Delta}^{(1)}}} = \frac{4 (\overline{\Delta}^{(1)})^2 |\overline{\mathbf{S}}^{(2)}|}{\nu}.$$

Other cases can be considered where the similarity hypothesis between the subgrid stresses at different resolution levels may be violated, leading to different values of the constant [Porté-Agel, Meneveau and Parlange, 2000]. Among them:

- The case of a very coarse resolution, with a cutoff located at the very beginning of the inertial range or in the production range.
- The case of a turbulence undergoing rapid strains, where a transition length  $\Delta_T \propto S^{-3/2} \varepsilon^{1/2}$  appears. Here,  $S$  and  $\varepsilon$  are the strain magnitude and the dissipation rate, respectively. Dimensional arguments show that, roughly speaking, scales larger than  $\Delta_T$  are rapidly distorted but have no time to adjust dynamically, while scales smaller than  $\Delta_T$  can relax faster via nonlinear interactions.

For each of these cases, scale dependence of the model near the critical length scale is expected, which leads to a possible loss of efficiency of the classical Germano–Lilly dynamic procedure.

A more general dynamic procedure, which does not rely on the assumption of scale similarity or location of the cutoff in the dissipation range, was proposed by Porté-Agel *et al.* [Porté-Agel, Meneveau and Parlange, 2000]. This new scale-dependent dynamic procedure is obtained by considering a third filtering level (*i.e.* a second test-filtering level) with a characteristic cutoff length scale  $\overline{\Delta}^{(3)} > \overline{\Delta}^{(2)}$ . Writing the Germano identity between level  $\overline{\Delta}^{(1)}$  and level  $\overline{\Delta}^{(3)}$  leads to

$$\begin{aligned} \mathcal{L}_{ij}^{(3)} &\equiv G_3 \star \left( \overline{u}_i^{(1)} \overline{u}_j^{(1)} \right) - \overline{u}_i^{(3)} \overline{u}_j^{(3)} \\ &= C(\overline{\Delta}^{(3)}) f_{ij}(\overline{\Delta}^{(3)}, \overline{\mathbf{u}}^{(3)}) - C(\overline{\Delta}^{(1)}) G_3 \star f_{ij}(\overline{\Delta}^{(1)}, \overline{\mathbf{u}}^{(1)}). \end{aligned} \quad (4.30)$$

By taking

$$M_{ij}^{(3)} = \left( \Lambda(\overline{\Delta}^{(3)}, \overline{\Delta}^{(1)}) f_{ij}(\overline{\Delta}^{(3)}, \overline{\mathbf{u}}^{(3)}) - \overline{f_{ij}(\overline{\Delta}^{(1)}, \overline{\mathbf{u}}^{(1)})}^{(3)} \right) \quad (4.31)$$

with

$$\Lambda(\overline{\Delta}^{(3)}, \overline{\Delta}^{(1)}) = \frac{C(\overline{\Delta}^{(3)})}{C(\overline{\Delta}^{(1)})} \quad (4.32)$$

we obtain the following value for the constant at level  $\overline{\Delta}^{(1)}$ :

$$C(\overline{\Delta}^{(1)}) = \frac{\mathcal{L}_{ij}^{(3)} M_{ij}^{(3)}}{M_{ij}^{(3)} M_{ij}^{(3)}}. \quad (4.33)$$

By now considering relation (4.23), which expresses the Germano identity between the first two filtering levels, where  $M_{ij}^{(2)}$  is now written as

$$M_{ij}^{(2)} = \left( \Lambda(\overline{\Delta}^{(2)}, \overline{\Delta}^{(1)}) f_{ij}(\overline{\Delta}^{(2)}, \overline{\mathbf{u}}^{(2)}) - G_2 \star f_{ij}(\overline{\Delta}^{(1)}, \overline{\mathbf{u}}^{(1)}) \right) \quad (4.34)$$

and by equating the values of  $C(\overline{\Delta}^{(1)})$  obtained using the two test-filtering levels, we obtain the following relation:

$$\left( \mathcal{L}_{ij}^{(2)} M_{ij}^{(2)} \right) \left( M_{ij}^{(3)} M_{ij}^{(3)} \right) - \left( \mathcal{L}_{ij}^{(3)} M_{ij}^{(3)} \right) \left( M_{ij}^{(2)} M_{ij}^{(2)} \right) = 0 \quad (4.35)$$

which has two unknowns,  $\Lambda(\overline{\Delta}^{(2)}, \overline{\Delta}^{(1)})$  and  $\Lambda(\overline{\Delta}^{(3)}, \overline{\Delta}^{(1)})$ . In order to obtain a closed system, some additional assumptions are needed. It is proposed in [Porté-Agel, Meneveau and Parlange, 2000] to assume a power-law scaling of the dynamic constant,  $C(x) \propto x^r$ , leading to

$$C(a\overline{\Delta}^{(1)}) = C(\overline{\Delta}^{(1)})a^r. \quad (4.36)$$

For this power-law behavior, the function  $\Lambda(., .)$  does not depend on the scales but only on the ratio of the scales, *i.e.*  $\Lambda(x, y) = (x/y)^r$ . Using this simplification, (4.35) appears as a fifth-order polynomial in  $C(\overline{\Delta}^{(1)})$ . The dynamic constant is taken equal to the largest root.

This scale-dependent dynamic model needs to be stabilized, as other dynamic models. Averaging over homogeneous direction was implemented by Porté-Agel and coworkers, resulting in a stable subgrid closure which was applied to a neutral atmospheric boundary layer flow [Porté-Agel, Meneveau and Parlange, 2000]. The time-averaged profiles of the dynamic constant computed at three different levels using the scale-dependent procedure are plotted versus the distance to the wall in Fig. 4.5. It is interesting to note the value computed using the traditional Germano procedure is very close to the one obtained at the *test filter level*, *i.e.*  $C(\overline{\Delta}^{(2)})$ , and not at the *grid filter level*,  $C(\overline{\Delta}^{(1)})$ , showing the weakness of the original procedure.

Non-dimensional gradient of the mean streamwise velocity profile computed using the scale-dependent procedure is compared with the one computed using the traditional approach in Fig. 4.6. The scale-dependent procedure is observed to yield a better prediction in the vicinity of the wall (the gradient is nearly constant and close to one) than the traditional procedure, which yields erroneous results because the test filter is located outside the inertial range in this region.

The scale-dependent dynamic procedure is also observed to greatly improve the prediction of second-order statistical moments, leading to a very accurate prediction of the velocity spectrum (see Fig. 4.7).

The scale-dependent procedure is observed to be efficient but the need for homogeneous directions precludes its use in complex three-dimensional configurations. To alleviate this problem, Bou-Zeid and coworkers [Bou-Zeid, Meneveau and Parlange, 2005] recently coupled the scale-dependent dynamic model with the Lagrangian averaging technique introduced by Meneveau [Meneveau, Lund and Cabot, 1996]. Using this advanced regularization technique, Eq. (4.35) is replaced by

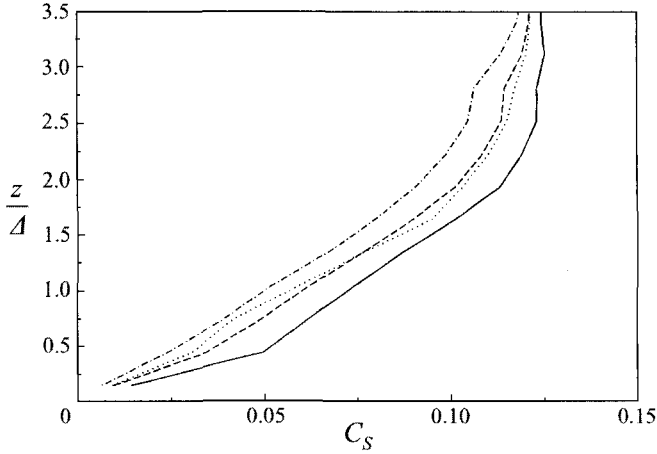


Fig. 4.5 Vertical distribution of the time-averaged value of the dynamic constant obtained using the scale-dependent multilevel dynamic procedure in a neutral atmospheric boundary layer flow. Solid line:  $C(\overline{\Delta}^{(1)})$ ; Dashed line:  $C(\overline{\Delta}^{(2)} = 2\overline{\Delta}^{(1)})$ ; Dash-dotted line:  $C(\overline{\Delta}^{(3)} = 4\overline{\Delta}^{(1)})$ . The dotted line corresponds to the value obtained using the traditional Germano-Lilly procedure. Reproduced from [Porté-Agel, Meneveau and Parlange, 2000] with permission of Cambridge University Press.

$$\left\langle \mathcal{L}_{ij}^{(2)} M_{ij}^{(2)} \right\rangle_{\text{Lag}} \left\langle M_{ij}^{(3)} M_{ij}^{(3)} \right\rangle_{\text{Lag}} - \left\langle \mathcal{L}_{ij}^{(3)} M_{ij}^{(3)} \right\rangle_{\text{Lag}} \left\langle M_{ij}^{(2)} M_{ij}^{(2)} \right\rangle_{\text{Lag}} = 0 \quad (4.37)$$

where  $\langle \phi \rangle_{\text{Lag}}$  denotes the Lagrangian average of the variable  $\phi$  along streamlines, and is defined as

$$\langle \phi \rangle_{\text{Lag}} = \int_{-\infty}^t \phi(x(t'), t') W(t - t') dt'. \quad (4.38)$$

The function  $W(t - t')$  is introduced to account for vanishing memory effects. In practice, an exponential decay is assumed to adequately represents auto-decorrelation due to the chaotic nature of turbulent motion.

The Lagrangian averaged quantities are therefore solutions of the following advection-relaxation equation:

$$\frac{\partial \langle \phi \rangle_{\text{Lag}}}{\partial t} + \bar{\mathbf{u}}^{(1)} \cdot \nabla \langle \phi \rangle_{\text{Lag}} = \frac{1}{T^{(1)}} \left( \phi - \langle \phi \rangle_{\text{Lag}} \right) \quad (4.39)$$

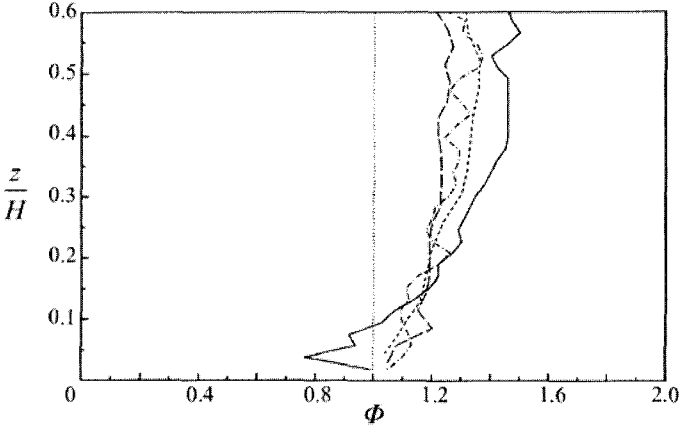


Fig. 4.6 Non-dimensional gradient of the mean streamwise velocity from simulations that use the scale-dependent dynamic procedure at three resolutions: fine grid (dot-dashed line), medium grid (long-dashed line) and coarse grid (short-dashed line). Results obtained on the fine grid using the traditional dynamic procedure corresponds to the solid line. The vertical dotted line corresponds to the classical log-law, which is expected to hold in the lower 10 % of the computational domain. Reproduced from [Porté-Agel, Meneveau and Parlange, 2000] with permission of Cambridge University Press.

where  $T^{(p)}$  is an *ad hoc* relaxation characteristic time scale associated with the level of filtering at which the variable  $\phi$  under consideration is defined. This time scale is defined for quantities of interest here defined at the  $p$ th level of filtering as

$$T^{(p)} = \overline{\Delta}^{(1)} \frac{3}{2} \left( \left\langle \mathcal{L}_{ij}^{(p)} M_{ij}^{(p)} \right\rangle_{\text{Lag}} \left\langle M_{ij}^{(p)} M_{ij}^{(p)} \right\rangle_{\text{Lag}} \right)^{-1/8}. \quad (4.40)$$

This procedure is implemented in an efficient way in practice using the following discrete scheme

$$\langle \phi \rangle_{\text{Lag}}(\mathbf{x}, t^{n+1}) = \epsilon^{(1)} \phi(\mathbf{x}, t^{n+1}) + (1 - \epsilon^{(1)}) \langle \phi \rangle_{\text{Lag}}(\mathbf{x} - \overline{\mathbf{u}}^{(1)}(\mathbf{x}, t^n) \Delta t, t^n) \quad (4.41)$$

where  $\Delta t$  is the time step of the numerical integration, the time  $t^n$  is equal to  $n\Delta t$ , and the filtering-level-dependent weighting parameter is defined as

$$\epsilon^{(p)} = \frac{\Delta t / T^{(p)}}{1 + \Delta t / T^{(p)}}. \quad (4.42)$$

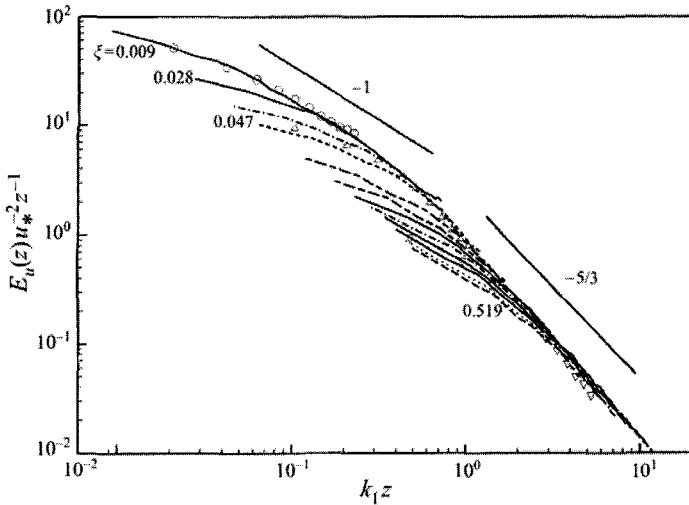


Fig. 4.7 Normalized streamwise velocity spectra versus normalized wave number at different heights  $\xi$  computed using the scale-dependent dynamic procedure. Fine grid: solid line; coarse grid: symbols. The transition between the  $-1$  and the  $-5/3$  slope is well recovered, while the traditional dynamic model fails. Reproduced from [Porté-Agel, Meneveau and Parlange, 2000] with permission of Cambridge University Press.

Therefore, only one interpolation step is needed in practice to compute  $\langle \phi \rangle_{\text{Lag}}(\mathbf{x} - \bar{\mathbf{u}}^{(1)}(\mathbf{x}, t^n) \Delta t, t^n)$ , leading to a very small computational overhead.

This Lagrangian scale-dependent dynamic model was successfully applied in atmospheric boundary layer flows with smooth and rough surfaces by Bou-Zeid and coworkers [Bou-Zeid, Meneveau and Parlange, 2005]. A schematic view of the application to a boundary layer with a sudden change in the wall surface roughness is displayed in Fig. 4.8.

The computed mean value of the dynamic constant and the predicted subgrid dissipation using the Lagrangian-averaged scale-dependent procedure are referred to their counterparts obtained using the original scale-dependent procedure in Fig. 4.9. The Lagrangian-average procedure is observed to yield a better adaptation of the dynamic procedure with respect to the local feature of the flow. As indicated at the end of Sec. 4.2.2, the regularization procedures used to stabilize the dynamic constant calculation result in a loss of optimality, because the spatial averaging process destroy the link with local features of the flow. The Lagrangian averaging

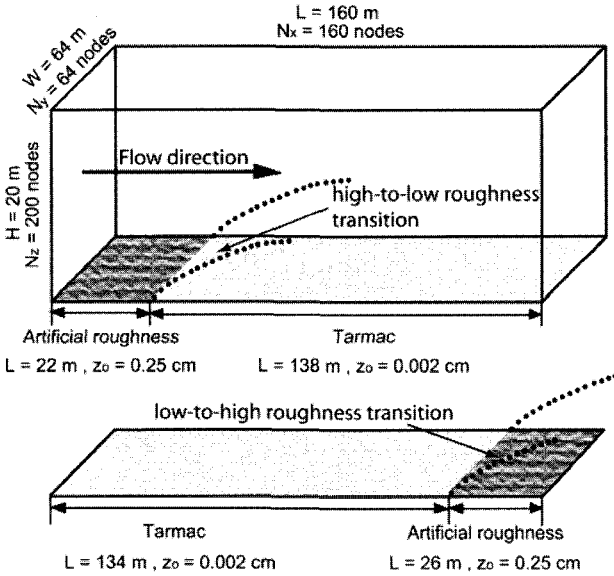


Fig. 4.8 Schematic view of the computational domain in the case of a boundary layer flow with varying surface roughness. Reproduced from [Bou-Zeid, Meneveau and Parlange, 2005] with permission of American Institute of Physics.

alleviates this problem, since the averaging is performed along streamlines, which carry physical information. Therefore, the optimality is preserved in a much better way.

#### 4.2.3.2 Scale-separation operator self-similarity

We now consider the problem of the filter self-similarity. Let  $\mathcal{G}_1^1 = G_1$  and  $\mathcal{G}_1^2$  be the filter kernels associated with the first and second filtering level. We assume that the filter kernels are rewritten in a form such that:

$$\bar{\mathbf{u}}^{(1)}(\mathbf{x}) = \mathcal{G}_1^1 \star \mathbf{u}(\mathbf{x}) = \int \mathcal{G}_1^1 \left( \frac{|\mathbf{x} - \xi|}{\Delta^{(1)}} \right) \mathbf{u}(\xi) d\xi \quad (4.43)$$

$$\bar{\mathbf{u}}^{(2)}(\mathbf{x}) = \mathcal{G}_1^2 \star \mathbf{u}(\mathbf{x}) = \int \mathcal{G}_1^2 \left( \frac{|\mathbf{x} - \xi|}{\Delta^{(2)}} \right) \mathbf{u}(\xi) d\xi. \quad (4.44)$$

We also introduce the test filter  $G_2$ , which is defined such that

$$\bar{\mathbf{u}}^{(2)} = \mathcal{G}_1^2 \star \mathbf{u} = G_2 \star \bar{\mathbf{u}}^{(1)} = G_2 \star G_1 \star \mathbf{u}. \quad (4.45)$$

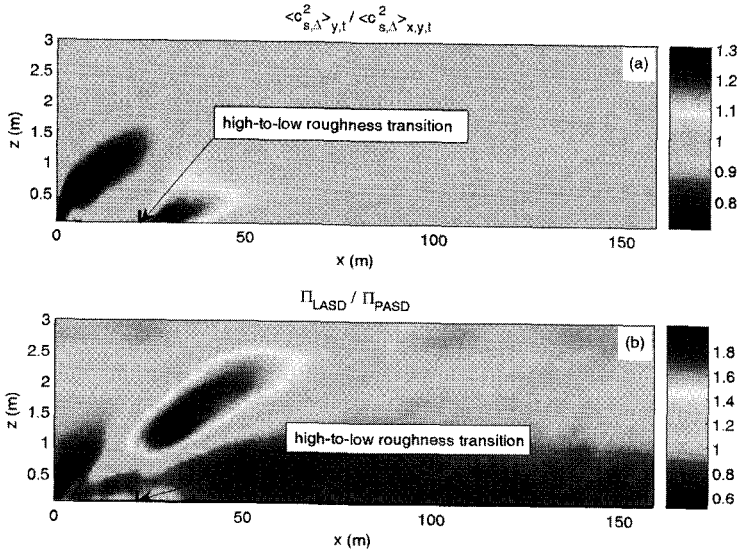


Fig. 4.9 Sensitivity of subgrid model to surface roughness for a high-to-low roughness transition. (a): plot of the dynamic coefficient for the Lagrangian-Averaged Scale-Dependent (LASD) dynamic model referred to the one computed using the Planar-Averaged Scale-Dependent (PASD) procedure. Here, planar-average refers to average in the homogeneous direction of the flow. (b): ratio of the associated subgrid dissipation. Reproduced from [Bou-Zeid, Meneveau and Parlange, 2005] with permission of American Institute of Physics.

The filters  $\mathcal{G}_1^1$  and  $\mathcal{G}_1^2$  are self-similar if and only if

$$\mathcal{G}_1^1(y) = \frac{1}{r^d} \mathcal{G}_1^2\left(\frac{y}{r}\right), \quad r = \overline{\Delta}^{(2)} / \overline{\Delta}^{(1)}. \quad (4.46)$$

Hence, the two filters must have identical shapes and may only differ by their associated characteristic length. The problem is that in practice only  $G_2$  is known, and the self-similarity property might not be *a priori* verified. Carati and Vanden Eijnden [Carati and Vanden Eijnden, 1997] show that the interpretation of the resolved field is fully determined by the choice of the test filter  $G_2$ , and that the use of the same model for the two levels of filtering is fully justified. This is demonstrated by re-interpreting previous filters in the following way. Let us consider an infinite set of self-similar filters  $\{F_n \equiv F(l_n)\}$  defined as

$$F_n(x) = \frac{1}{r^n} \mathcal{F}\left(\frac{x}{l_n}\right), \quad l_n = r^n l_0 \quad (4.47)$$

where  $\mathcal{F}$ ,  $r > 1$  and  $l_0$  are the filter kernel, an arbitrary parameter and a reference length, respectively. Let us introduce a second set  $\{F_n^* \equiv F^*(l_n^*)\}$  defined by

$$F_n^* \equiv F_n \star F_{n-1} \star \dots \star F_{-\infty}. \quad (4.48)$$

For positive kernel  $\mathcal{F}$ , we get the following properties:

- The length  $l_n^*$  obeys the same geometrical law as  $l_n$ :

$$l_n^* = r l_{n-1}^*, \quad \text{and} \quad l_n^* = \frac{r}{\sqrt{r^2 - 1}} l_n. \quad (4.49)$$

- $\{F_n^*\}$  constitute a set of self-similar filters.

Using these two set of filters, the classical filters involved in the dynamic procedure can be defined as self-similar filters:

$$G_2(\Delta) = F_n(l_n) \quad (4.50)$$

$$\mathcal{G}_1^1(\overline{\Delta}^{(1)}) = F_{n-1}^*(l_{n-1}^*) \quad (4.51)$$

$$\mathcal{G}_1^2(\overline{\Delta}^{(2)}) = F_n^*(l_n^*). \quad (4.52)$$

For any test-filter  $G_t \equiv G_2$  and any value of  $r$ , the first filter operator  $\mathcal{G}_1^1 = G_1$  can be constructed explicitly:

$$G_1 = G_t(\Delta/r) \star G_t(\Delta/r^2) \star \dots \star G_t(\Delta/r^\infty). \quad (4.53)$$

This relation shows that for any test filter of the form (4.50), the two filtering operators can be rewritten as self-similar ones, justifying the use of the same model at all the filtering levels.

### 4.3 Self-Similarity Based Dynamic Subgrid Models

We now present other dynamic procedures for constant adjustment which do not use the Germano identity. They are based on other exact relationships. A common feature of the procedures discussed below is that they are all based on properties of the statistical self-similar state of isotropic

turbulence. They are therefore expected to be useful for fully developed turbulent flows at scales small enough to satisfy the Kolmogorov local isotropy hypothesis.

#### 4.3.1 Terracol–Sagaut procedure

This method proposed by Terracol and Sagaut [Terracol and Sagaut, 2003] relies on the hypothesis that the computed resolved kinetic energy spectrum obeys a power-law like

$$E(\kappa) = E_0 \kappa^\alpha \quad (4.54)$$

where  $\alpha$  is the scaling parameter. It is worth noting that Barenblatt [Barenblatt, 1996] suggests that both  $E_0$  and  $\alpha$  might be Reynolds-number dependent. A more accurate explicit form for the kinetic energy spectrum is

$$E(\kappa) = K_0 \varepsilon^{2/3} \kappa^{-5/3} (\kappa \Lambda)^\zeta \quad (4.55)$$

where  $K_0 = 1.4$  is the Kolmogorov constant,  $\Lambda$  a length scale and  $\zeta$  an intermittency factor. Under this assumption, the mean subgrid dissipation rate across a cutoff wave number  $\kappa_c$ ,  $\varepsilon(\kappa_c)$ , scales like

$$\varepsilon(\kappa_c) = \varepsilon_0 \kappa_c^\gamma, \quad \gamma = \frac{3\alpha + 5}{2} = \frac{3}{2}\zeta. \quad (4.56)$$

where  $\varepsilon_0$  is a  $\kappa_c$ -independent parameter. It is observed that in the Kolmogorov case ( $\alpha = -5/3$ ), one obtains  $\gamma = 0$ , leading to a constant dissipation rate.

Let us now introduce a set of cutoff wave numbers  $\kappa_n$ , with  $\kappa_1 > \kappa_2 > \dots$  and  $\kappa_p \propto 1/\overline{\Delta}^{(p)}$ . The following recursive law is straightforwardly derived from (4.56)

$$\frac{\varepsilon(\kappa_n)}{\varepsilon(\kappa_{n+1})} = R_{n,n+1}^\gamma, \quad R_{n,n+1} = \frac{\kappa_n}{\kappa_{n+1}} \quad (4.57)$$

leading to the following two-level evaluation of the parameter  $\gamma$ :

$$\gamma = \frac{\log(\varepsilon(\kappa_n)/\varepsilon(\kappa_{n+1}))}{\log(R_{n,n+1})}. \quad (4.58)$$

Now introducing a generic subgrid model for the  $n$ th cutoff level

$$\tau_{ij}^{(n)} = C f_{ij}(\bar{u}^{(n)}, \bar{\Delta}^{(n)}) \quad (4.59)$$

where  $C$  is the constant of the model to be dynamically computed, the dissipation rate can also be expressed as

$$\varepsilon(\kappa_n) = -\tau_{ij}^{(n)} \bar{S}_{ij}^{(n)} = -C f_{ij}(\bar{u}^{(n)}, \bar{\Delta}^{(n)}) \bar{S}_{ij}^{(n)}. \quad (4.60)$$

Eq. (4.57) shows that the ratio  $\varepsilon(\kappa_n)/\varepsilon(\kappa_{n+1})$  is independent of the model constant  $C$ . Using this property, Terracol and Sagaut propose to introduce two test filter levels  $\kappa_2$  and  $\kappa_3$  ( $\kappa_1$  being the grid filter level where the equations must be closed, *i.e.*  $\bar{\Delta}^{(1)} = \bar{\Delta}$ ).

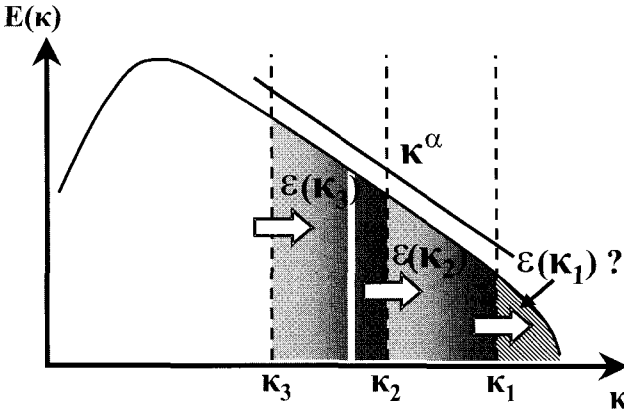


Fig. 4.10 Three-level spectral splitting considered for the dynamic procedure of Terracol and Sagaut (the scale separation operator is chosen here to be a sharp cutoff filter). Reliable estimations of the slope  $\alpha$  and of the subgrid dissipation at the two cutoff wavenumbers  $\kappa_2$  and  $\kappa_3$  is expected to provide the correct value of the subgrid dissipation  $\varepsilon(\kappa_1)$  at the cutoff wavenumber  $\kappa_1$ .

The intermittency factor  $\gamma$  is then computed using relation (4.58), and one obtains the following evaluation for the subgrid dissipation rate at the grid filter level:

$$\varepsilon(\kappa_1) = R_{1,2}^\gamma \varepsilon'(\kappa_2) \quad (4.61)$$

where  $\varepsilon'(\kappa_2)$  is evaluated using a reliable approximation of the subgrid tensor to close the sequence (in practice, a scale-similarity model is used in [Terracol and Sagaut, 2003]). This procedure is described by Fig. 4.10. The corresponding value of  $C$  for the model at the grid level is then deduced from (4.60):

$$C = R_{1,2}^\gamma \frac{\varepsilon'(\kappa_2)}{-f_{ij}(\bar{\mathbf{u}}^{(1)}, \bar{\Delta}^{(1)}) \bar{S}_{ij}^{(1)}}. \quad (4.62)$$

The authors applied successfully their approach to homogeneous isotropic turbulence simulations (in the inviscid limit), using the standard form of the Smagorinsky closure for  $f_{ij}$  at the finest level. Their results exhibited a flow behavior which was at least as good as the one obtained using the dynamic Smagorinsky model [Germano *et al.*, 1991], or the Smagorinsky model using the optimal theoretical value of  $C$ . This is illustrated by Fig. 4.11, which displays a comparison of the kinetic energy spectrum obtained in the self-similar regime using these three different approaches, on a  $64^3$  computational grid. The approach was also applied by the authors to some plane channel flow simulations, considering moderate to significant values of the Reynolds number (skin friction Reynolds numbers from  $Re_\tau = 180$  up to  $Re_\tau = 2000$  were considered). At the finest level, a scale-similarity model was retained by the authors. For the two respective cases corresponding to  $Re_\tau = 180$  and  $Re_\tau = 590$ , the results were compared to those obtained without any subgrid model, and with a dynamic Smagorinsky model [Germano *et al.*, 1991], showing an improvement of both mean and turbulent profiles (see Fig. 4.12). For the higher Reynolds number cases, an asymptotic behavior of the near-wall velocity fluctuations was observed, as shown in Fig. 4.13.

#### 4.3.2 Shao procedure

Another procedure was developed by Shao [Shao *et al.*, 2003; Cui *et al.*, 2004] starting from the Kolmogorov-Meneveau equation for filtered third-

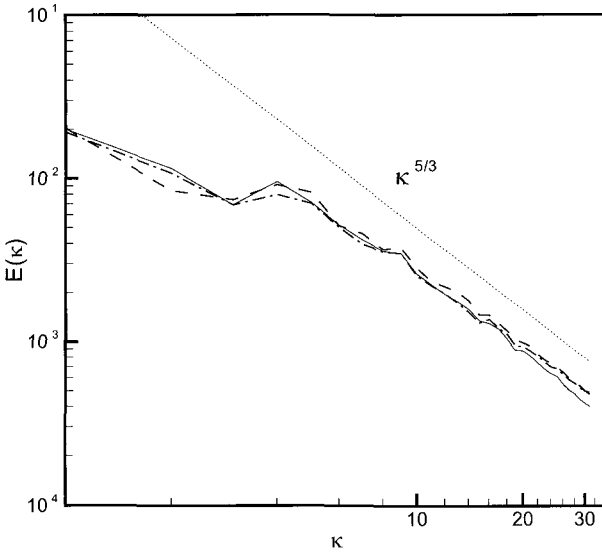


Fig. 4.11 Kinetic energy spectrum obtained in homogeneous isotropic turbulence simulations, in the self-similar regime. Solid line: dynamic procedure of Terracol and Sagaut; dashed line: Smagorinsky model with  $C = 0.18$ , dash-dotted line: dynamic Smagorinsky model [Germano *et al.*, 1991]. From [Terracol and Sagaut, 2003] with permission of American Institute of Physics.

order velocity structure function:

$$-\frac{4}{5}r\varepsilon = \overline{D}_{LLL} - 6G_{LLL} \quad (4.63)$$

where  $\overline{D}_{LLL}$  is the third-order longitudinal velocity correlation of the filtered field

$$\overline{D}_{LLL}(r) = \langle [\overline{\mathbf{u}}(x+r) - \overline{\mathbf{u}}(x)]^3 \rangle \quad (4.64)$$

where  $\langle \cdot \rangle$  denotes the statistical average operator,  $G_{LLL}(r)$  is the longitudinal velocity-stress correlation tensor

$$G_{LLL}(r) = \langle \overline{u}_1(x)\tau_{11}(x+r) \rangle \quad (4.65)$$

and  $\varepsilon = -\tau_{ij}\overline{S}_{ij}$  is the average subgrid dissipation.

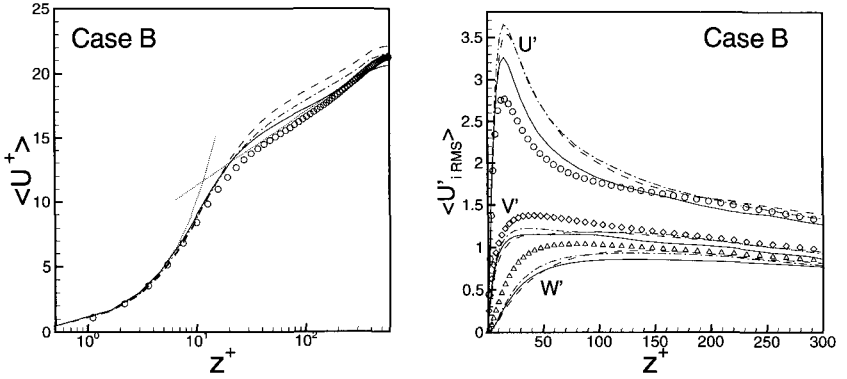


Fig. 4.12 Plane channel flow results (wall units are used) at  $Re_\tau = 590$  obtained using the dynamic procedure of Terracol and Sagaut (solid line), the dynamic Smagorinsky model (dashed line), and without subgrid modelling (dash-dotted line). Symbols correspond to the DNS results of [Moser *et al.*, 1999]. Left: mean streamwise velocity profiles; right: RMS velocity fluctuations profiles. From [Terracol and Sagaut, 2003] with permission of American Institute of Physics.

Now assuming that the following self-similarity law is valid

$$G_{LLL}(r) \propto r^p \quad (4.66)$$

where  $p = -1/3$  corresponds to the Kolmogorov local isotropy hypotheses, one obtains the following relationship for two space increments  $r_1$  and  $r_2$ :

$$\frac{0.8r_1\varepsilon + \overline{D}_{LLL}(r_1)}{0.8r_2\varepsilon + \overline{D}_{LLL}(r_2)} = \left(\frac{r_1}{r_2}\right)^{-1/3}. \quad (4.67)$$

Now introducing the same generic subgrid closure as for the Germano identity based subgrid models

$$\tau_{ij} = C f_{ij}(\overline{\mathbf{u}}^{(1)}, \overline{\Delta}^{(1)}) \quad , \quad (4.68)$$

and inserting it into (4.67) to compute  $\varepsilon = -\tau_{ij}^{(1)} \overline{S}_{ij}^{(1)}$ , taking  $r_1 = \overline{\Delta}^{(1)}$  and  $r_2 > r_1$ , the new dynamic value of the constant  $C$  is

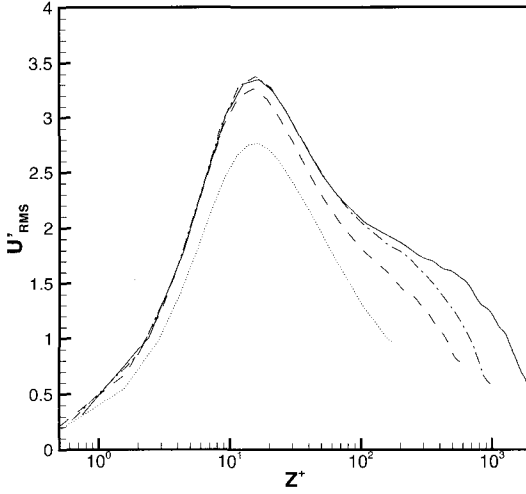


Fig. 4.13 Asymptotic behavior of the near-wall velocity fluctuations in plane channel flow simulations, observed using the dynamic procedure of Terracol and Sagaut (wall units are used). Dotted line:  $Re_\tau = 180$ ; dash-dotted line:  $Re_\tau = 590$ ; dashed line:  $Re_\tau = 1050$ ; solid line:  $Re_\tau = 2000$ . From [Terracol and Sagaut, 2003] with permission of American Institute of Physics.

$$C = \frac{\left(\frac{\bar{\Delta}^{(1)}}{r_2}\right)^{-1/3} \bar{D}_{LLL}(r_2) - \bar{D}_{LLL}(\bar{\Delta}^{(1)})}{0.8 f_{ij}(\bar{\mathbf{u}}^{(1)}, \bar{\Delta}^{(1)}) \bar{S}_{ij}^{(1)} \left( \bar{\Delta}^{(1)} - \left(\frac{\bar{\Delta}^{(1)}}{r_2}\right)^{-1/3} r_2 \right)}. \quad (4.69)$$

The only fixed parameter in the Shao procedure is the scaling parameter  $p$  in (4.66). This parameter can be computed dynamically introducing a third space increment  $r_3$ , leading to the definition of a dynamic procedure with the same properties as the one proposed by Terracol and Sagaut. The proposal of Shao can also be extended to subgrid models with several adjustable constant by introducing an additional space increment for each new constant and solving a linear algebra problem.

#### 4.4 Variational Multiscale Methods and Related Subgrid Viscosity Models

We now present subgrid models based on the Variational Multiscale method pioneered by Hughes [Hughes, 1995; Hughes and Stewart, 1996; Hughes

*et al.*, 1998; Hughes, Mazzei and Jansen, 2000] (see [Hughes, Scovazzi and Franca, 2004] for a survey). This method makes the functional  $f_{ij}$  in Eq. (4.3) sensitive to the smallest resolved scales, leading to the definition of models formally similar to Eq. (4.5).

#### 4.4.1 Hughes VMS approach and extended formulations

The original formulation by Hughes deals with a general framework in computational mechanics (not restricted to fluid mechanics) based on a Galerkin-type representation of the physical unknowns [Hughes, 1995; Hughes and Stewart, 1996; Hughes *et al.*, 1998; Hughes, Mazzei and Jansen, 2000]. The first applications to the problem of turbulence were published in 2001 [Hughes *et al.*, 2001; Hughes, Oberai and Mazzei, 2001; Winckelmans and Jeanmart, 2001]. The concepts developed within this finite-element framework are more general than the original presentation, and will therefore be presented here using the same multilevel framework as in the other chapters. A major difference with the original formulation is that equations will be written here using the strong formulation of the Navier–Stokes equations, while the original developments were carried out using the weak formulation of the problem. The important point is that all equations given below are general ones, which do not explicitly depend upon the exact features of the scale separation operator used to split the resolved field.

The key idea is to split the resolved field  $\bar{\mathbf{u}}^{(1)}$  into two parts, namely the large resolved scales  $\bar{\mathbf{u}}^{(2)}$  and the small resolved scales  $\delta\bar{\mathbf{u}}^{(1)}$ , leading the following decomposition of the total field

$$\mathbf{u} = \underbrace{\bar{\mathbf{u}}^{(2)} + \delta\bar{\mathbf{u}}^{(1)}}_{\bar{\mathbf{u}}^{(1)}} + \mathbf{u}' \quad (4.70)$$

where, following the nomenclature introduced in Chap. 2,  $\mathbf{u}'$  is the subgrid, unresolved part. The associated evolution equation are

$$\nabla \cdot \bar{\mathbf{u}}^{(2)} = 0 \quad (4.71)$$

$$\frac{\partial}{\partial t} \bar{\mathbf{u}}^{(2)} + \nabla \cdot \left( \bar{\mathbf{u}}^{(2)} \otimes \bar{\mathbf{u}}^{(2)} \right) = -\nabla \bar{p}^{(2)} + \nu \nabla^2 \bar{\mathbf{u}}^{(2)} - \nabla \cdot \boldsymbol{\tau}^{(2)} \quad (4.72)$$

$$\nabla \cdot \delta \mathbf{u}^{(1)} = 0 \quad (4.73)$$

$$\begin{aligned} \frac{\partial}{\partial t} \delta \mathbf{u}^{(1)} + \nabla \cdot \left( \delta \mathbf{u}^{(1)} \otimes \delta \mathbf{u}^{(1)} + \delta \mathbf{u}^{(1)} \otimes \bar{\mathbf{u}}^{(2)} + \bar{\mathbf{u}}^{(2)} \otimes \delta \mathbf{u}^{(1)} \right) \\ = -\nabla \delta p^{(1)} + \nu \nabla^2 \delta \mathbf{u}^{(1)} - \nabla \cdot \left( \tau^{(1)} - \tau^{(2)} \right). \end{aligned} \quad (4.74)$$

Before detailing the Variational Multiscale method, it is worth decomposing the subgrid term which appears in the right hand side of Eq. (4.72) into its computable and non-computable parts:

$$\begin{aligned} \tau^{(2)} &\equiv \overline{\mathbf{u} \otimes \mathbf{u}}^{(2)} - \bar{\mathbf{u}}^{(2)} \otimes \bar{\mathbf{u}}^{(2)} \\ &= \overline{\left( \bar{\mathbf{u}}^{(2)} + \delta \mathbf{u}^{(1)} + \mathbf{u}' \right) \otimes \left( \bar{\mathbf{u}}^{(2)} + \delta \mathbf{u}^{(1)} + \mathbf{u}' \right)}^{(2)} - \bar{\mathbf{u}}^{(2)} \otimes \bar{\mathbf{u}}^{(2)} \\ &= \underbrace{\overline{\left( \bar{\mathbf{u}}^{(2)} + \delta \mathbf{u}^{(1)} \right) \otimes \left( \bar{\mathbf{u}}^{(2)} + \delta \mathbf{u}^{(1)} \right)}^{(2)}}_{T_1} - \bar{\mathbf{u}}^{(2)} \otimes \bar{\mathbf{u}}^{(2)} \\ &\quad + \underbrace{\overline{\left( \bar{\mathbf{u}}^{(2)} + \delta \mathbf{u}^{(1)} \right) \otimes \mathbf{u}'}^{(2)} + \overline{\mathbf{u}' \otimes \left( \bar{\mathbf{u}}^{(2)} + \delta \mathbf{u}^{(1)} \right)}^{(2)}}_{T_2} \\ &\quad + \underbrace{\overline{\mathbf{u}' \otimes \mathbf{u}'}^{(2)}}_{T_3}. \end{aligned} \quad (4.75)$$

Here,  $T_1$  represents the computable part of the subgrid tensor since it involves only  $\bar{\mathbf{u}}^{(2)}$  and  $\delta \mathbf{u}^{(1)}$ , which are known since the computed solution is  $\bar{\mathbf{u}}^{(1)}$ . This term accounts for the interaction between the large resolved scales and the small resolved scales. The two other terms,  $T_2$  and  $T_3$ , cannot be computed because they involve the subgrid field  $u'$  and must therefore be modelled.

Several methods inspired by Hughes works have been published [Winckelmanns and Jeanmart, 2001; Jeanmart and Winckelmanns, 2002; Vreman, 2003], in which the localness in the wave number space is increased by using at least one of the two following ideas:

- (1) To use  $\delta \mathbf{u}^{(1)}$  instead of  $\bar{\mathbf{u}}^{(1)}$  in a classical subgrid model (or at least in some part of it).
- (2) To restrict the influence of the subgrid scales to the smallest resolved scales (*i.e.* on  $\delta \mathbf{u}^{(1)}$ ) and to neglect it on the large scales (*i.e.* to

neglect  $\tau^{(2)}$  or  $T_2 + T_3$  in Eq. (4.72)). This point was emphasized by Scott Collis [Scott Collis, 2001], who derived in the weak form the full equations, which are equivalent to the strong form of multilevel equations of Terracol *et al.* [Terracol *et al.*, 2001; Terracol *et al.*, 2003].

Let us illustrate these possibilities using the Smagorinsky model, which is the most popular subgrid viscosity model. The usual single scale expression for this model is

$$\tau^* = -2 \underbrace{(C\bar{\Delta})|\mathbf{S}(\bar{\mathbf{u}})|\mathbf{S}(\bar{\mathbf{u}})}_{\nu_{\text{sgs}}(\bar{\Delta}, \bar{\mathbf{u}})}, \quad \mathbf{S}(\bar{\mathbf{u}}) = (\nabla\bar{\mathbf{u}} + \nabla^T\bar{\mathbf{u}}) \quad (4.76)$$

where  $\tau^* = \tau - \frac{\tau_{kk}}{3}Id$  and  $\nu_{\text{sgs}}(\bar{\Delta}, \bar{\mathbf{u}})$  are the deviatoric part of the subgrid tensor<sup>2</sup> and the subgrid viscosity, respectively. The surrogate for the subgrid tensor appears as being composed of two parts: the subgrid viscosity and the tensorial component. Each part can be localized in the wave number space, leading to four possible combinations:

- (1) Both parts are computed using  $\delta\mathbf{u}^{(1)}$ , yielding the so-called Small-Small model:

$$\tau^* = -2(C\bar{\Delta}^{(1)})^2|\mathbf{S}(\delta\mathbf{u}^{(1)})|\mathbf{S}(\delta\mathbf{u}^{(1)}) \quad (4.77)$$

- (2) The Large-Small model

$$\tau^* = -2(C\bar{\Delta}^{(1)})^2|\mathbf{S}(\bar{\mathbf{u}}^{(1)})|\mathbf{S}(\delta\mathbf{u}^{(1)}) \quad (4.78)$$

- (3) The Small-Large model

$$\tau^* = -2(C\bar{\Delta}^{(1)})^2|\mathbf{S}(\delta\mathbf{u}^{(1)})|\mathbf{S}(\bar{\mathbf{u}}^{(1)}) \quad (4.79)$$

- (4) The Large-Large model, which is the usual single-scale Smagorinsky model

$$\tau^* = -2(C\bar{\Delta}^{(1)})^2|\mathbf{S}(\bar{\mathbf{u}}^{(1)})|\mathbf{S}(\bar{\mathbf{u}}^{(1)}) \quad (4.80)$$

---

<sup>2</sup>The deviatoric part is used here in place of the full tensor for consistency reason, since  $\mathbf{S}(\bar{\mathbf{u}})$  is traceless in incompressible flows.

The Small-Large model was not considered in the original work of Hughes, and its links with filtered subgrid models will be discussed later on.

To get a deeper understanding in the way the Variational Multiscale method type models act on the resolved field, let us recall that in practice a sole equation for  $\bar{\mathbf{u}}^{(1)}$  is solved: Eqs. (4.72) and (4.74) are not implemented and are presented for pedagogical purpose only. Let us rewrite the true governing equation as

$$\begin{aligned} \frac{\partial}{\partial t} \bar{\mathbf{u}}^{(1)} + \nabla \cdot \left( \bar{\mathbf{u}}^{(1)} \otimes \bar{\mathbf{u}}^{(1)} \right) &= -\nabla \bar{p}^{(1)} + \nu \nabla^2 \bar{\mathbf{u}}^{(1)} \\ &\quad - \underbrace{\nabla \cdot \tau^{(2)}}_{\mathcal{A}} - \underbrace{\nabla \cdot \left( \tau^{(1)} - \tau^{(2)} \right)}_{\mathcal{B}} \end{aligned} \quad (4.81)$$

where the parts of the subgrid term acting on the largest resolved scales and the smallest resolved scales have been written separately.

The variants of the Smagorinsky model presented above are more sensitive to small scales than the original Smagorinsky model, but they *a priori* act on the whole resolved field  $\bar{\mathbf{u}}^{(1)}$ . This is obvious for the Small-Large model, which is proportional to  $\mathbf{S}(\bar{\mathbf{u}}^{(1)})$ . The case of the Small-Small model and the Large-Small model is more complex: these models will not act on the large scale field if  $\mathbf{S}(\bar{\mathbf{u}}^{(1)})$  and  $\bar{\mathbf{u}}^{(2)}$  are orthogonal.

To enforce localness of the effect of the subgrid model, *i.e.* to make sure that it will act on the  $\delta \mathbf{u}^{(1)}$  field only, a possible technique is to apply the test scale separation operator on it and to neglect the term  $\mathcal{A}$  in the right hand side of Eq. (4.81). Recalling that

$$\bar{\mathbf{u}}^{(2)} = \mathcal{F} \left( \bar{\mathbf{u}}^{(1)} \right), \quad \delta \mathbf{u}^{(1)} = (Id - \mathcal{F}) \left( \bar{\mathbf{u}}^{(1)} \right) \quad (4.82)$$

it is possible to identify both subgrid contribution as follows

$$\tau^{(1)} = f \left( \bar{\Delta}^{(1)}, \bar{\mathbf{u}}^{(1)}, \delta \mathbf{u}^{(1)} \right) \quad (4.83)$$

$$\tau^{(2)} = \mathcal{F} \left( \tau^{(1)} \right) + \mathcal{F} \left( \bar{\mathbf{u}}^{(1)} \otimes \bar{\mathbf{u}}^{(1)} \right) - \mathcal{F} \left( \bar{\mathbf{u}}^{(1)} \right) \otimes \mathcal{F} \left( \bar{\mathbf{u}}^{(1)} \right) \quad (4.84)$$

where  $f$  is any model in the list given above. A localized subgrid model contribution is recovered taking

$$\begin{aligned} \mathcal{A} = 0, \quad \mathcal{B} = \nabla \cdot & \left( (Id - \mathcal{F}) \left( f \left( \overline{\Delta}^{(1)}, \overline{\mathbf{u}}^{(1)}, \delta \mathbf{u}^{(1)} \right) \right) \right. \\ & \left. - \left( \mathcal{F} \left( \overline{\mathbf{u}}^{(1)} \otimes \overline{\mathbf{u}}^{(1)} \right) - \mathcal{F} \left( \overline{\mathbf{u}}^{(1)} \right) \otimes \mathcal{F} \left( \overline{\mathbf{u}}^{(1)} \right) \right) \right). \end{aligned} \quad (4.85)$$

It is worth noting that another possible way to obtain a localized contribution for  $\mathcal{B}$  is directly suggested by Eq. (4.81). It consists in applying the same model at the two filtering levels, the total subgrid contribution being approximated as

$$\mathcal{A} = 0, \quad \mathcal{B} = \nabla \cdot \left( f \left( \overline{\Delta}^{(1)}, \overline{\mathbf{u}}^{(1)} \right) - f \left( \overline{\Delta}^{(2)}, \overline{\mathbf{u}}^{(2)} \right) \right). \quad (4.86)$$

#### 4.4.2 Implementation of the scale separation operator

Equations given above are fully general, but the properties of the VMS methods are observed in practice to be very sensitive to details of the implementation.

A first solution consists in projecting all the unknowns on adequate functional subspaces spanned by a finite dimension basis, and to identify an orthogonal decomposition operator which will be defined as a projection operator. Defining the space of the fully resolved solution as  $\mathcal{V}_1$ , one can write

$$\overline{\mathbf{u}}^{(1)} \in \mathcal{V}_1 \quad (4.87)$$

and introducing the orthogonal decomposition

$$\mathcal{V}_1 = \mathcal{V}_2 \oplus \mathcal{W}_1 \quad (4.88)$$

with

$$\overline{\mathbf{u}}^{(2)} \in \mathcal{V}_2, \quad \delta \mathbf{u}^{(1)} \in \mathcal{W}_1 \quad (4.89)$$

one obtains a scale separation operator by operating the projection of all variables defined in  $\mathcal{V}_1$  onto the two subspaces  $\mathcal{V}_2$  and  $\mathcal{W}_1$ . This projection has to be applied to the solution field  $\overline{\mathbf{u}}^{(1)}$ , but also to the subgrid term if a localized subgrid contribution is sought. Such an approach is very appealing if the numerical method is based on a set of orthogonal basis functions,

like Fourier spectral methods or Galerkin method based on hierarchical bases. The projection step then simplifies as a simple truncation on the original basis which spans  $\mathcal{V}_1$ . Let us illustrate this considering the following orthogonal modal decomposition of the resolved LES field:

$$\bar{\mathbf{u}}^{(1)}(x, t) \Rightarrow \sum_{k=1, N} a_k(x, t) \phi_k(x, t) \quad (4.90)$$

where the functions  $\phi_k(x, t)$  are the basis functions and  $a_k(x, t)$  are the coefficients of the modal decomposition. The orthogonality property is expressed as

$$\langle \phi_i, \phi_j \rangle_{\mathcal{V}_1} = 0 \quad \text{if } i \neq j \quad (4.91)$$

where  $\langle \phi_i, \phi_j \rangle_{\mathcal{V}_1}$  is related to an arbitrarily chosen inner product in  $\mathcal{V}_1$ . The model coefficients are defined as

$$a_k = \frac{\langle \bar{\mathbf{u}}^{(1)}, \phi_k \rangle_{\mathcal{V}_1}}{\langle \phi_k, \phi_k \rangle_{\mathcal{V}_1}}. \quad (4.92)$$

Assuming that each function  $\phi_k$  can be associated to a characteristic length  $\lambda_k$  and that the basis is ordered so that  $\lambda_1 \geq \lambda_2 \geq \dots \geq \lambda_N$ , the scale separation is easily expressed as

$$\bar{\mathbf{u}}^{(2)}(x, t) = \sum_{k=1, M} a_k(x, t) \phi_k(x, t) \quad , \quad M < N \quad (4.93)$$

$$\delta \mathbf{u}^{(1)}(x, t) = \sum_{k=M+1, N} a_k(x, t) \phi_k(x, t). \quad (4.94)$$

Several authors use this approach: the Fourier basis and orthogonal polynomial pseudo-spectral basis were used in [Hughes *et al.*, 2001; Hughes, Oberai and Mazzei, 2001; Holmen *et al.*, 2004], and the Variational Multiscale Method was also implemented within the Discontinuous Galerkin method on unstructured grids using the hierarchical Dubiner basis in [Scott Collis, 2002; Munts, Hulshoff and de Borst, 2004].

Another solution is to define a discrete filter, which will be used to operate the auxiliary scale separation. This approach is very similar to the

usual implementation of dynamic models and can be interpreted as the implementation of a convolution filter. In this case, orthogonality of the separation is not *a priori* guaranteed, and is filter-dependent. This approach is very general, and can be easily implemented within all numerical frameworks. It is worth noting that the filtering approach can easily be recast using the modal decomposition introduced above as:

$$\bar{\mathbf{u}}^{(2)}(x, t) = \sum_{k=1, N} C_k^>(x, t) a_k(x, t) \phi_k(x, t) \quad (4.95)$$

$$\delta \mathbf{u}^{(1)}(x, t) = \sum_{k=1, N} C_k^<(x, t) a_k(x, t) \phi_k(x, t) \quad (4.96)$$

where  $C_k^>$  and  $C_k^< \equiv (1 - C_k^>)$  are the filter coefficients. The projection approach discussed above is recovered as a generalized sharp cutoff filter. A discrete filter approach was implemented in [Sagaut and Levasseur, 2005a] within a Fourier spectral method and in [Levasseur *et al.*, 2005b] in a finite-element method.

A third solution, proposed by Koobus and Fahrat [Koobus and Farhat, 2004] on unstructured grids in a Finite Element Volume method, is to use a multigrid-type restriction operator, which relies on a cell agglomeration step (see Fig. 4.14). Here, the large resolved scales  $\bar{\mathbf{u}}^{(2)}$  are defined as the restriction of the fine solution  $\bar{\mathbf{u}}^{(1)}$  on a coarser mesh. The cell agglomeration can be interpreted as a special type of discrete filter. Its implementation is very easy in all codes already offering multigrid-type capabilities, since the restriction and prolongation operators of the original multigrid algorithms can be directly used.

Whatever method is used to operate the scale separation between  $\bar{\mathbf{u}}^{(2)}$  and  $\delta \mathbf{u}^{(1)}$ , the spectral features of the multiscale methods have been observed to have a strong impact on the solution. It has been observed by several authors [Holmen *et al.*, 2004; Hughes, Wells and Wray, 2004; Sagaut and Levasseur, 2005a] that both the value of the cutoff wave number associated to the scale separation operator and the transfer function (in the Fourier space) of this operator are important parameter. In the case where the scale separation operator induces a sharp decomposition in the Fourier space and the effect of the subgrid model is strictly restricted to  $\delta \mathbf{u}^{(1)}$ , long range triadic interactions are totally neglected and spurious kinetic energy pile-up may occur in the  $\bar{\mathbf{u}}^{(2)}$ . The spectral transfers:

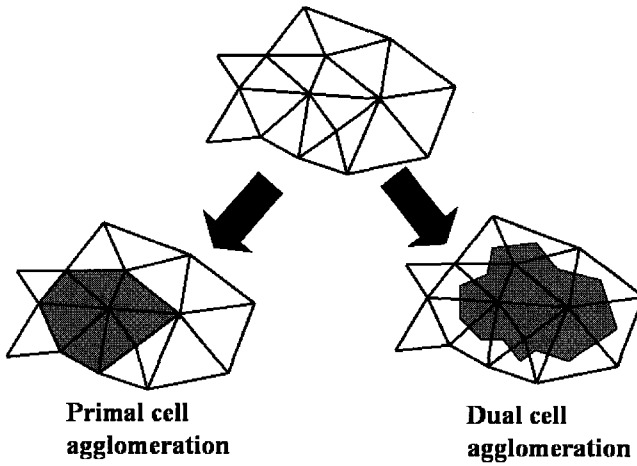


Fig. 4.14 Cell agglomeration in a two-dimensional unstructured grid. Two strategies exist: agglomeration of the primal cells or of the dual cells. Primal cells are the white triangles, while the shaded areas represent the agglomerated cells.

associated with each component of the subgrid tensor are illustrated in Fig. 4.15.

This can be explained by the fact that distant energy transfers represent up to 25% of the full kinetic energy transfers, according to the theoretical analysis of Kraichnan. These transfers are responsible for the existence of a plateau in the spectral eddy viscosity for low wave numbers predicted by theoretical analysis and observed in direct numerical simulations. Recent analyses prove that long range energy transfer are mainly due to subgrid Reynolds stresses ( $T_3$  in Eq. (4.75) ) while short range transfers are mainly driven by cross terms ( $T_2$  in Eq. (4.75) ). This spurious energy pile-up can be prevented by using a scale separation with a smooth transfer function in the Fourier space, which will allow for the existence of a spectral overlap between  $\bar{\mathbf{u}}^{(2)}$  and  $\delta\mathbf{u}^{(1)}$ . This spectral overlap makes the subgrid model acting also on the low wave numbers, even if the model is strictly restricted to  $\delta\mathbf{u}^{(1)}$ . Examples based on the use of the Gaussian filter in a Fourier decomposition of the turbulent field are given in [Sagaut and Lévassieur, 2005a]. It is important to note that similar conclusions dealing with the necessity of accounting for long range transfers in the equation for  $\bar{\mathbf{u}}^{(2)}$  were drawn by Terracol, Sagaut and Basdevant [Terracol *et al.*, 2001] within the framework of Multilevel Large-eddy simulation methods (see Sec. 5.4.2).

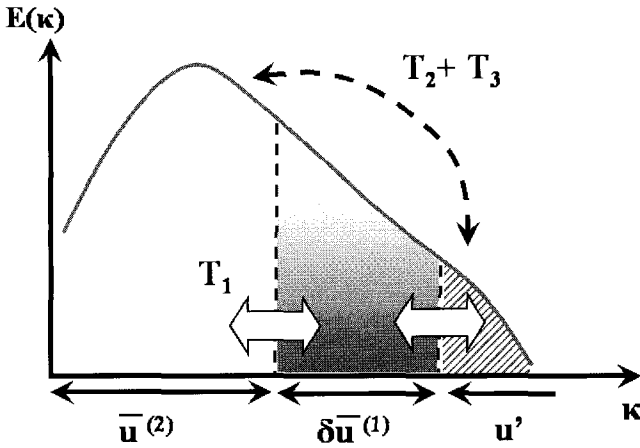


Fig. 4.15 Spectral transfers associated with the basic Variational Multiscale method. Scale separations operators are assumed here to be sharp cutoff.

#### 4.4.3 Bridging with hyperviscosity and filtered models

Variational Multiscale method based variants of the Smagorinsky model can also be reinterpreted within other existing frameworks. In the case where the scale separation operator can be interpreted as a differential operator, some multiscale models are observed to be very similar with hyperviscosity subgrid closures [Winckelmans and Jeanmart, 2001; Jeanmart and Winckelmans, 2002; Sagaut and Levasseur, 2005a].

This is in particular true in the case where the scale separation operator can be assimilated to a convolution filter with a symmetric kernel  $G$ . Writing

$$\bar{\mathbf{u}}^{(2)}(x) = \int G(x - \xi)\bar{\mathbf{u}}^{(1)}(\xi)d\xi \tag{4.97}$$

and assuming that the resolved field is smooth enough to make the following Taylor series expansion relevant

$$\bar{\mathbf{u}}^{(1)}(\xi) = \sum_{p=0,\infty} (-1)^p \frac{(x - \xi)^p}{p!} \frac{d^p}{dx^p} \bar{\mathbf{u}}^{(1)}(x) \tag{4.98}$$

the small scale field is approximated as

$$\delta \mathbf{u}^{(1)}(x) = - \sum_{p=1, \infty} M_{2p}(G) \frac{(x - \xi)^{2p}}{2p!} \frac{d^{2p}}{dx^{2p}} \bar{\mathbf{u}}^{(1)}(x) \quad (4.99)$$

where  $M_p(G)$  denotes the  $p$ th-order moment of the filter kernel  $G$ . For the Gaussian and the top-hat filter, one has  $M_p(G) \propto (\bar{\Delta}^{(1)})^p$ . Retaining only the leading order term, one obtains

$$\delta \mathbf{u}^{(1)}(x) = \alpha_G \left( \bar{\Delta}^{(1)} \right)^p \nabla^2 \bar{\mathbf{u}}^{(1)}(x) \quad (4.100)$$

where  $\alpha_G$  is a filter-dependent parameter. Inserting this simplified expression into previous definitions of the multiscale variants of the Smagorinsky models discussed above, one obtains the following higher-order differential surrogates:

- For the Small-Small model

$$\tau^* = 2|\alpha_G| \alpha_G C^2 \left( \bar{\Delta}^{(1)} \right)^6 |\mathbf{S}(\nabla^2 \bar{\mathbf{u}}^{(1)})| |\mathbf{S}(\nabla \bar{\mathbf{u}}^{(1)})| \quad (4.101)$$

- For the Large-Small model

$$\tau^* = 2\alpha_G C^2 \left( \bar{\Delta}^{(1)} \right)^4 |\mathbf{S}(\bar{\mathbf{u}}^{(1)})| |\mathbf{S}(\nabla^2 \bar{\mathbf{u}}^{(1)})| \quad (4.102)$$

- For the Small-Large model

$$\tau^* \simeq -2|\alpha_G| C^2 \left( \bar{\Delta}^{(1)} \right)^4 |\mathbf{S}(\nabla^2 \bar{\mathbf{u}}^{(1)})| |\mathbf{S}(\bar{\mathbf{u}}^{(1)})| \quad (4.103)$$

The increased localness in terms of wave number of the Small-Small model and the Large-Small model is associated to the fact that the dissipative operator is now associated to an iterated Laplacian operator as in hyperviscosity models. The Small-Large model is associated to an usual Laplacian operator, but the subgrid viscosity is now computed using  $\nabla^2 \bar{\mathbf{u}}^{(1)}$  as an input, exactly as in filtered subgrid models proposed by Ducros *et al.* [Ducros, Comte and Lesieur, 1996] and extended by Sagaut and coworkers [Sagaut, Comte and Ducros, 2000].

## Chapter 5

# Structural Multiscale Subgrid Models: Small Scales Estimations

This chapter presents the multilevel approaches which rely on an estimation of some small scales of the flow in order to obtain improved subgrid closures and/or representation of the flow. From the pure modelling point of view the knowledge of some scales smaller than the resolved ones at any filtering level allows for the derivation of some structural subgrid models, which may be much more representative of the real interactions of the resolved and unresolved scales than models based only on resolved scales. As will be detailed, there exist different possible ways which make it possible to generate some small scales.

The first one relies on an *approximate deconvolution* of the filtered field, which aims at inverting the filtering operation. Such approaches, referred to as the *deconvolution* methods are based on the explicit introduction of two different filtering levels, by mean of some explicit discrete filters. These approaches will be described in Sec. 5.1.

A second possible approach is based on a multifractal reconstruction of the subgrid vorticity field. This approach will be presented in Sec. 5.2.

The third approach relies on an explicit resolution of the small scales, coupled with the use of a sequence of computational grids with different spatial resolution. Such a resolution of the small scales is then made possible by minimizing the effort devoted to their computation either in time by using a multigrid cycling approach, or in space by the use of a zonal multigrid or multidomain approach. These approaches, based on a multigrid hierarchy will be fully described in Secs. 5.3, 5.4, and 5.5.

## 5.1 Small-scale Reconstruction Methods: Deconvolution

The general idea of these methods is to perform a structural modelling of the subgrid terms by getting an approximation of the unresolved missing scales. In practice, it is then necessary to reconstruct a velocity field with a higher wavenumber content than the resolved field. For this reason, these methods are generally referred to as *deconvolution* approaches since they aim at inverting the filtering operation formally obtained by a convolution product.

By denoting  $\bar{\mathbf{u}} = G \star \mathbf{u}$  the resolved field, the first common step in deconvolution approaches is to reconstruct an approximate de-filtered velocity field, which will be used to compute explicitly the subgrid terms:

$$\mathbf{u}^* \simeq G^{-1} \star \bar{\mathbf{u}}. \quad (5.1)$$

The following simple model can then be retained for the subgrid-stress tensor  $\tau$ :

$$\tau = \overline{\mathbf{u} \otimes \mathbf{u}} - \bar{\mathbf{u}} \otimes \bar{\mathbf{u}} \simeq \overline{\mathbf{u}^* \otimes \mathbf{u}^*} - \bar{\mathbf{u}^*} \otimes \bar{\mathbf{u}^*}. \quad (5.2)$$

The problem is then how to define the approximate de-filtered velocity field, or equivalently how to approximate the inverse of the filtering operator<sup>1</sup>. Indeed, it has to be recalled here that in most cases the exact filtering operator remains unknown, and also that an additional difficulty relies on the fact that the grid used for the simulations correspond to a finite support in both physical and spectral spaces, so that a limited range of wavenumbers can be represented. For these two reasons, it remains impossible to compute exactly the de-filtered velocity field.

Several approaches can be found in the literature to reconstruct an approximate de-filtered field. A common point between these approaches is that they all introduce two levels of filtering of the solution.

According to the notations introduced in Chap. 2, the resolved field will be the one at the coarser level:  $\bar{\mathbf{u}} = \bar{\mathbf{u}}^{(2)}$ , while the finest level will only be used to compute the approximate de-filtered field:  $\mathbf{u}^* = \bar{\mathbf{u}}^{(1)}$ , which in

---

<sup>1</sup>It can be remarked that one of the first and most famous structural model, as proposed by Bardina *et al.* [Bardina *et al.*, 1980] can be interpreted as a simplification of relations (5.1) and (5.2), where the two filtering levels are the same, *i.e.*  $G^{-1} = Id$ , therefore leading to the following well-known possible closure for  $\tau$ :

$$\tau \simeq \overline{\bar{\mathbf{u}} \otimes \bar{\mathbf{u}}} - \bar{\mathbf{u}} \otimes \bar{\mathbf{u}}.$$

return will provide an expression<sup>2</sup> for  $\tau^{(2)}$  as:

$$\tau^{(2)} \simeq G_2 \star \left( \bar{\mathbf{u}}^{(1)} \otimes \bar{\mathbf{u}}^{(1)} \right) - \bar{\mathbf{u}}^{(2)} \otimes \bar{\mathbf{u}}^{(2)} \quad (5.3)$$

where it is recalled that  $\bar{\mathbf{u}}^{(2)} = \mathcal{G}_1^2(\mathbf{u}) = G_2 \star G_1 \star \mathbf{u}$  and  $\bar{\mathbf{u}}^{(1)} = G_1 \star \mathbf{u}$ . This two-level decomposition of the velocity field is illustrated by Fig. 5.1 in the spectral space.

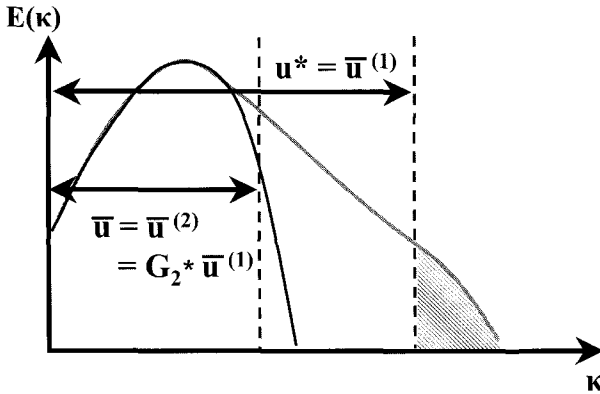


Fig. 5.1 Two-level spectral splitting used for the deconvolution approaches.

The idea of deconvolution is not so new. Indeed, the early works of Leonard [Leonard, 1974] and Clark *et al.* [Clark *et al.*, 1979] already introduced this concept. More recently, Shah and Ferziger [Shah and Ferziger, 1995], proposed a structural model based on an approximate inversion of the filtering operator. However, in all these approaches, the filtered and the de-filtered field are both represented on the same computational grid, so that they are in practice associated to the same spectral content. In that context, the deconvolution step alone therefore does not make it possible to really introduce finer scales in the deconvolved field. Despite a high practical correlation between the modelled and real subgrid terms, this gen-

<sup>2</sup>It is to be remarked here that considering expression (5.3) for  $\tau^{(2)}$  is equivalent to neglect all the interactions associated to wavenumbers larger than  $\kappa_1$ . This means that the energy transfers have to be local in the wavenumbers space. This is also equivalent to neglect the term  $G_2 \star \tau^{(1)}$  in the relation of Germano written for  $\tau^{(2)}$ .

erally results in a global under-dissipative behavior of the resulting subgrid model since some interactions between large and small scales are still not accounted for.

In some more recent works, this point has received much attention, and two main methods have been particularly developed, which propose to explicitly introduce smaller scales in the deconvolved field. This can be done practically in two ways. The first one, as proposed by Domaradzki and his coworkers when developing the velocity estimation model [Domaradzki and Saiki, 1997; Domaradzki and Loh, 1999; Loh and Domaradzki, 1999; Domaradzki and Yee, 2000] is to introduce an additional finer grid in the simulation to represent the deconvolved field. This method will be detailed in Sec. 5.1.1. The second possible technique, as introduced by Adams and coworkers [Adams and Leonard, 1999; Adams, 1999; Adams, 2000b; Stolz and Adams, 1999; Stolz *et al.*, 2001a; Stolz *et al.*, 2001b] relies on the explicit introduction of the filtering operator in the simulation to define the filtered field<sup>3</sup>. In that case, the grid is therefore able to represent some smaller scales than those represented by the filtered field. The explicit knowledge of the filter also makes it possible to compute the approximate deconvolved field by its repeated application. The so-called Approximate Deconvolution Model (ADM) will be exhaustively detailed in Sec. 5.1.2.

### 5.1.1 *The velocity estimation model*

Domaradzki and his co-workers [Domaradzki and Loh, 1999; Loh and Domaradzki, 1999] propose an evaluation of the approximate de-filtered field  $\bar{\mathbf{u}}^{(1)}$  in two successive steps: in the first step, referred to as the *deconvolution step*, the filtering operator  $G_2$  is inverted, on the grid used for the simulation, and corresponding to the representation  $\bar{\mathbf{u}}^{(2)}$  of the velocity field, which will be considered as the “coarse” grid. Then, this field is interpolated on a twice finer grid where some smaller scales are generated during the second step referred to as the *non-linear step*. These two steps are also respectively referred to as the *kinematic* and *dynamic* steps by the authors. The different versions of the resulting *Velocity Estimation Model* are corresponding to several modifications and improvements of the original version developed in the spectral space by Domaradzki and Saiki [Domaradzki and Saiki, 1997] for incompressible flows. The two successive

---

<sup>3</sup>At this point, it may be recalled that the filtering operator is generally omitted in LES, and only considered as resulting implicitly from the discretization grid and the numerical scheme.

steps can be summarized as follows:

(1) **Deconvolution step**

This step consists in computing an intermediate velocity field  $\tilde{\mathbf{u}}^d$  such that  $G_2 \star \tilde{\mathbf{u}}^d = \bar{\mathbf{u}}^{(2)}$ . For this, the filter  $G_2$  is assumed to be a box or Gaussian filter with a cutoff lengthscale  $\Delta^{(2)} = 2\Delta x$  where  $\Delta x$  denotes the space step. The Simpson's rule gives a second-order finite-difference approximation of such a filter (in one space dimension) as:

$$\bar{\mathbf{u}}^{(2)} = G_2 \star \tilde{\mathbf{u}}^d(x) = \frac{1}{6} (\tilde{\mathbf{u}}^d(x - \Delta x) + 4\tilde{\mathbf{u}}^d(x) + \tilde{\mathbf{u}}^d(x + \Delta x)). \quad (5.4)$$

This expression results in a tri-diagonal system of equations for the values  $\tilde{\mathbf{u}}^d(x)$ . These values may then be considered as an approximate de-filtered field for which the filtering operation has been inverted.

However, at this point, this deconvolved field is still represented on the LES mesh, and thus does not introduce any scales smaller than those already resolved. Indeed, the exact deconvolution should only be possible if the two fields  $\bar{\mathbf{u}}^{(2)}$  and  $\bar{\mathbf{u}}^{(1)}$  had the same spectral support, even if the exact filter was known. This is obviously not the case with discretization procedures, since grid sampling removes some high wavenumber modes to the continuous field, which are irremediably lost and cannot be recovered. For this reason, the "deconvolved" field  $\tilde{\mathbf{u}}^d$  is unable to provide the exact subgrid stresses, and leads generally to an under-dissipative subgrid model. To get around this problem, Domaradzki *et al.* have introduced a second step in their method, which is to generate some smaller scales on a finer grid, by non-linear interactions. This step is referred to as the non-linear or dynamic step.

(2) **Non-linear step**

This second step of the estimation procedure, as mentioned above, aims at generating explicitly some scales twice smaller than the smallest grid-resolved scales by means of non-linear interactions. For this purpose, the deconvolved field obtained in the first step is first interpolated<sup>4</sup> on a twice finer computational grid, such that some finer missing scales can be represented. Such scales are however still not present and require an additional procedure to be generated. The original procedure proposed by the authors relies on the direct use of the non-linear term from

---

<sup>4</sup>The authors used cubic splines for this interpolation.

the filtered Navier–Stokes equations for  $\tilde{\mathbf{u}}^d$ :  $-\tilde{u}_j^d \frac{\partial}{\partial x_j} \tilde{u}_i^d$ . This term is a production term for all the resolved scales on the fine auxiliary grid, and is therefore not exclusively linked to the production of small scales. For this reason, the large-scale effects have to be discarded. The first one is the advection by the large scales, which can be removed by subtracting the large scale component in the advective velocity, leading to the following intermediate expression for the non-linear term:

$$N_i^* = -(\tilde{u}_j^d - G_2 \star \tilde{u}_j^d) \frac{\partial}{\partial x_j} \tilde{u}_i^d. \quad (5.5)$$

In order to restrict the effects of this term to the smallest scales only, its filtered contribution is also removed, leading to the following final expression for the small-scales production term:

$$N_i' = N_i^* - G_2 \star N_i^* = -(Id - G_2) \star \left( (\tilde{u}_j^d - G_2 \star \tilde{u}_j^d) \cdot \frac{\partial}{\partial x_j} \tilde{u}_i^d \right). \quad (5.6)$$

In order to use this non-linear term to generate explicitly the small scales, an estimation of the production time  $\theta$  during which it has to be applied has to be derived. The authors highlight the fact that this time can be interpreted physically as the large eddy turnover time. For this purpose, the authors use the assumption that the kinetic energy of the small scales generated by  $N_i'$  during the time  $\theta$  should be equal to a fraction  $R^2$  of the one from the smallest resolved scales:

$$(\theta N_i')^2 = R^2 (\tilde{u}_i^d - \overline{\tilde{u}_i^d})^2. \quad (5.7)$$

This expression finally gives:

$$\theta = R \sqrt{\frac{(\tilde{u}_i^d - \overline{\tilde{u}_i^d})^2}{(N_i')^2}}. \quad (5.8)$$

The ratio parameter  $R$  is dependent on the filter, and can be evaluated for some particular filter shapes (under the assumption of an inertial range), leading to an average value of  $R = 0.5$ . The resulting expression for the final deconvolved velocity field on the fine grid is the following:

$$\begin{aligned} \bar{\mathbf{u}}^{(1)} &= \tilde{\mathbf{u}}^d + \theta \mathbf{N}' \\ &= \tilde{\mathbf{u}}^d + \tilde{\mathbf{u}}' \end{aligned} \quad (5.9)$$

where  $\tilde{\mathbf{u}}'$  is the velocity field associated to the small scales produced by the non-linear step. This expression of  $\bar{\mathbf{u}}^{(1)}$  is finally used to compute the subgrid stress tensor on the coarse grid level.

This approach has been applied by the authors in some plane channel flow computations. For these simulations, some values of the skin-friction Reynolds number of  $Re_\tau = 180$  and  $Re_\tau = 1050$  were considered. The complete (two-step) estimation procedure was shown to yield to some results which compare well with DNS and experimental ones, and also to provide reliable estimations of the energy budget. The authors also investigated a simplified version of the procedure, by neglecting the second (non-linear) step. In this case, the simulations exhibited an under-dissipative behavior, therefore showing that pure deconvolution on the same grid as the computational grid does not allow the recovering of a reliable estimation of the unfiltered velocity field.

As an example, their results for the highest considered value of the Reynolds number are reported here. The results obtained using the full estimation procedure (deconvolution + non-linear step) are compared to those from some simulations using only the deconvolution step, or no subgrid model at all. For these simulations, some rather coarse meshes were considered ( $48 \times 64 \times 65$  points in the respective streamwise, spanwise, and wall-normal directions). The results were also compared with the reference LES performed by Piomelli [Piomelli, 1993] in a similar configuration, as well as to the experimental results of Wei and Willmarth [Wei and Willmarth, 1989]. Figure 5.2 displays the mean streamwise velocity profiles obtained in this case. It can be observed that the LES using only the deconvolution step without the non-linear step leads to some results which are very similar to the ones obtained without any subgrid model, therefore revealing an under-dissipative behavior. However, the use of the full estimation procedure leads to some results in good agreement with the reference ones. Figure 5.3 displays the velocity fluctuations profiles obtained with the full estimation procedure. Here, it is observed that the location of the peak of the streamwise velocity fluctuation is well located, but overestimated by about 20%.

In a later study, Domaradzki and Yee [Domaradzki and Yee, 2000] proposed a modified version of the dynamic step, in order to get a better correlation between the large and the (new) small scales of the flow. In this case, the estimated velocity field  $\bar{\mathbf{u}}^{(1)}$  is no longer used to compute the subgrid-stress tensor on the coarse grid, but to perform time advancement

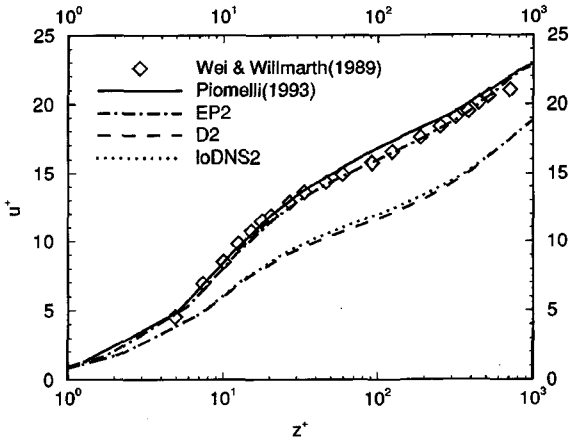


Fig. 5.2 Mean streamwise velocity profiles in the high-Reynolds channel flow configuration ( $Re_\tau = 1050$ ). Symbols: experiment from Wei and Willmarth, 1989; solid line: LES from Piomelli, 1993; dash-dotted line: LES with the subgrid-scale estimation model; dashed line: pure deconvolution; dotted line: no-model LES. From [Domaradzki and Loh (1999)], with permission of American Institute of Physics.

on the fine grid level. The effects of the small scales on the large ones is then represented through the real Navier–Stokes dynamics on the fine grid instead of the approximated subgrid stress model on the coarse one. The modified non-linear step is organized as follows:

- The first step relies on the calculation of the approximate deconvolved field  $\bar{\mathbf{u}}^{(1)}$  on the fine grid, as given by formula (5.9), at the time  $t$ .
- The corresponding fine-grid flow variables are then advanced in time according to the Navier–Stokes dynamics on the fine grid level during an integration time of  $T$ :

$$\bar{\mathbf{u}}^{(1)}(t+T) = NS_T(\bar{\mathbf{u}}^{(1)}(t)) \quad (5.10)$$

where  $NS_T$  denotes symbolically the resolution of the Navier–Stokes equations during an integration time  $T$ . According to the authors, the time  $T$  must be chosen short enough to ensure that no unphysical equipartition of energy at large scales can occur during this time. Indeed, the (direct) Navier–Stokes equations are solved on the fine grid without any subgrid model, and thus may lead to erroneous scales interactions at high Reynolds numbers since the grid is not fine enough.

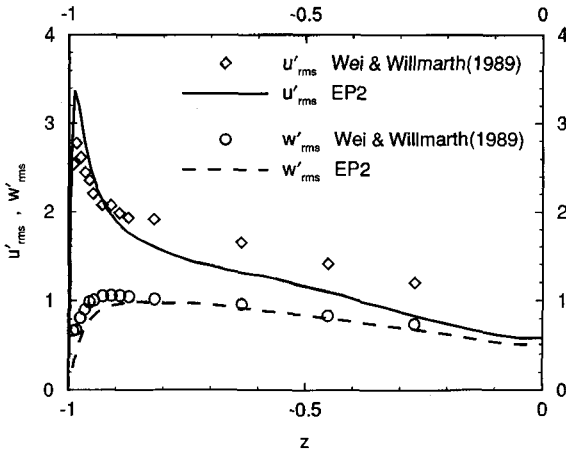


Fig. 5.3 RMS fluctuations of velocity in the high-Reynolds channel flow configuration ( $Re_\tau = 1050$ ). Symbols: experiment from Wei and Willmarth, 1989; solid line: LES with the subgrid-scale estimation model. From [Domaradzki and Loh (1999)], with permission of American Institute of Physics.

The authors found values of  $T$  between 1% and 3% of the large eddy turnover time to be adapted to their isotropic turbulence computations.

- The fine-grid velocity field obtained at the time  $t + T$  is then finally transferred back to the coarse grid level during the *reduction* step, as:

$$\bar{\mathbf{u}}^{(2)}(t + T) = G_2 \star \left( \mathcal{I}_{1 \rightarrow 2} \left( \bar{\mathbf{u}}^{(1)}(t + T) - \tilde{\mathbf{u}}'(t) \right) \right) \quad (5.11)$$

where  $\mathcal{I}_{1 \rightarrow 2}$  denotes an interpolation operator from the fine to the coarse grid. It is to be noted that the original perturbation velocity  $\tilde{\mathbf{u}}'(t)$  is first subtracted from the Navier–Stokes solution on the fine grid before filtering and sampling on the coarse grid. This is done to ensure that the modifications of the (coarse grid) filtered field  $\bar{\mathbf{u}}^{(2)}$  are only due to the Navier–Stokes dynamics, and to eliminate spurious effects due to the combination of the estimation and reduction steps.

This modified approach was applied by the authors to the simulation of high-Reynolds homogeneous isotropic turbulence, in which both the  $\kappa^{-5/3}$  spectrum and Kolmogorov constant value were well recovered.

While time integration on a twice finer mesh involves much more CPU requirements than integration on the coarse grid only (eight times more points in three dimensions, and two times smaller time steps to ensure the

validity of the CFL condition), this approach presents some advantages. Indeed, the effects of the small scales on the large-resolved ones is directly represented by the Navier–Stokes dynamics. As a consequence, since no particular form of the subgrid terms is considered, the backscatter effects are taken into account, and the closure appears (at least theoretically) able to account for some specific physical flow phenomena (compressible flows<sup>5</sup>, reactive flows), as well as numerical and commutation errors.

### 5.1.2 The Approximate Deconvolution Model (ADM)

Stolz, Adams and Kleiser [Stolz *et al.*, 2001a], following the ideas introduced by Geurts [Geurts, 1997], propose a small scales reconstruction method, in which the introduction of an additional fine computational grid is avoided by introducing explicitly the filtering operator in the simulation. In their approach, the cutoff lengthscale  $\bar{\Delta}$  of the filtering operator is therefore explicitly imposed, and chosen to be larger than the mesh size  $\Delta x$ . As a consequence, the corresponding cutoff wavenumber  $\kappa_c$  is smaller than the grid (Nyquist) cutoff wavenumber  $\kappa_N = \pi/\Delta x$ . This therefore allows the representation of some smaller scales than the resolved ones on the same the computational grid, without introducing an additional grid as in the velocity estimation approach.

The authors propose to define the simulation filter  $G_2$  by using some Padé approximants [Lele, 1994], and recommend a cutoff wavenumber value of  $\kappa_c = 2/3\kappa_N$ . The inverse  $G_2^{-1}$  of this filter is approximated by a truncation at  $N$  of its series expansion as:

$$G_2^{-1} \simeq Q_N = \sum_{l=0}^N (Id - G_2)^l. \quad (5.12)$$

The authors indicate that a sufficient accuracy is reached for  $N = 5$ . The approximate deconvolved velocity field  $\bar{\mathbf{u}}^{(1)}$  can therefore be obtained by repeated filtering of  $\bar{\mathbf{u}}^{(2)}$  as:

$$\bar{\mathbf{u}}^{(1)} \simeq \sum_{l=0}^N (Id - G_2)^l \star \bar{\mathbf{u}}^{(2)}. \quad (5.13)$$

The subgrid-stress tensor is then directly computed from this approximate deconvolved field.

---

<sup>5</sup>The extension of the velocity estimation model to the case of compressible turbulence has been carried out by Dubois *et al.* [Dubois *et al.*, 2002].

However, this procedure does not allow a description of the interactions between the resolved scales and the scales associated to wavenumber values larger than the Nyquist cutoff wavenumber ( $\kappa > \kappa_N$ ), *i.e.* the scales smaller than the mesh size. For that reason, the authors have found necessary to introduce a regularization step<sup>6</sup> in their method, which is based on the introduction of an additional term in the filtered continuity equation. This *relaxation* term  $\mathcal{R}$  aims at removing explicitly some energy from the wavenumber band  $\kappa_c < \kappa < \kappa_N$ . Its expression is given by:

$$\mathcal{R} = -\chi(Id - Q_N G_2) \star \bar{\mathbf{u}}^{(2)} \quad (5.14)$$

The filtered continuity equation for the resolved field  $\bar{\mathbf{u}}^{(2)}$  finally reads as follows:

$$\frac{\partial}{\partial t} \bar{\mathbf{u}}^{(2)} + \nabla \cdot \left( G_2 \star \left( \bar{\mathbf{u}}^{(1)} \otimes \bar{\mathbf{u}}^{(1)} \right) \right) = -\nabla \bar{p}^{(2)} + \nu \nabla^2 \bar{\mathbf{u}}^{(2)} - \chi (Id - Q_N G_2) \star \bar{\mathbf{u}}^{(2)} \quad (5.15)$$

where the deconvolved field  $\bar{\mathbf{u}}^{(1)}$  is approximated by relation (5.13).

The operator  $(Id - Q_N G_2)$  is positive semidefinite, therefore leading to a purely dissipative effect of the relaxation term  $\mathcal{R}$ . It is to be noted that the relaxation parameter  $\chi$  can be interpreted as the inverse of a relaxation time. The use of this relaxation term can therefore be seen as the application of a secondary filter on the solution every  $1/(\chi \Delta t)$  time step (where  $\Delta t$  denotes the time step), which acts only on the unresolved but represented wavenumbers in the range  $\kappa_c < \kappa < \kappa_N$ .

According to the authors, the simulations do not in practice exhibit a strong dependency to the value of  $\chi$ . In their works dealing with the extension of the method to the case of compressible flows [Stolz *et al.*, 2001b], the authors derived a dynamic procedure to evaluate this parameter. The value of  $\chi$  is then adjusted dynamically in both space and time such that the small scale kinetic energy (associated to the highest resolved wavenumbers  $\kappa_c < \kappa < \kappa_N$ ) remains constant during time advancement. For that purpose, the authors make use of the structure function<sup>7</sup>  $F_s$ :

---

<sup>6</sup>It should be noted that in some recent works dealing with the application of the ADM to the simulation of transitional boundary layers [Schlatter *et al.*, 2004], the authors finally only consider this regularization term to represent the interactions with subgrid scales. The resulting approach is referred to as ADM-RT (ADM-Relaxation Term).

<sup>7</sup>The authors use in practice the discrete local second-order form of the structure function, involving in three dimensions and on a structured mesh the sixth neighboring points of the considered point.

$$F_s(\mathbf{x}, t) = \|\Phi(\mathbf{x} + \mathbf{r}, t) - \Phi(\mathbf{x}, t)\|_{\|\mathbf{r}\|=\Delta x}^2 \quad (5.16)$$

where  $\Phi = (Id - Q_N G_2) \star \bar{\mathbf{u}}^{(2)}$  in the incompressible framework. Two estimations<sup>8</sup> are then necessary to get a local estimation of the relaxation parameter  $\chi$ :

- First, an estimate of the energy generated during one time step  $\Delta t$  in the range  $\kappa_c < \kappa < \kappa_N$  without any regularization is computed, by solving eq. 5.15 with  $\chi = 0$ . This quantity is given by:

$$\Delta k_{\chi=0} = F_s(\mathbf{x}, t + \Delta t)|_{\chi=0} - F_s(\mathbf{x}, t) \quad (5.17)$$

- Secondly, the energy that would be dissipated by using an arbitrary<sup>9</sup> value  $\chi_0$  of the regularization parameter  $\chi$  is given by:

$$\Delta k_{\chi=\chi_0} = F_s(\mathbf{x}, t + \Delta t)|_{\chi=\chi_0} - F_s(\mathbf{x}, t)|_{\chi=\chi_0}. \quad (5.18)$$

Given these two estimates, a simple rule is then used to get the proper local<sup>10</sup> value of the relaxation parameter:

$$\chi = \chi_0 \frac{\Delta k_{\chi=0}}{\Delta k_{\chi=\chi_0}}. \quad (5.19)$$

According to the authors, the time variations of this parameter are quite small, such that its evaluation can be carried out only every 5-10 iterations.

The authors performed some extensive validations of this approach, in both the incompressible and compressible (the compressible formulation of the method is detailed in [Stolz *et al.*, 2001b]) regimes. It was assessed in academic cases such as isotropic decaying turbulence and plane channel flows, where some accurate results were obtained even with the use of quite coarse grids.

In [Stolz *et al.*, 2001b], the authors present an application of their technique to the simulation of a supersonic compression ramp flow where shock-turbulence interaction occurs. The flow configuration can be seen in Fig. 5.4: the boundary layer along a compression ramp with a deflection

<sup>8</sup>For that purpose, the authors use a simple backward Euler scheme.

<sup>9</sup>The more obvious value for  $\chi_0$  is the estimated value of  $\chi$  at the previous time step.

<sup>10</sup>For stability reasons, the authors introduce an additional spatial smoothing of  $\chi$ , together with a maximum threshold value.

angle of  $18^\circ$  is considered, at a flow Mach number of  $M = 3$ . The associated Reynolds number (based on the free-stream quantities and the inflow boundary layer mean momentum thickness) is  $Re_\theta = 1685$ . A LES using the approximate deconvolution model has been performed on a  $334 \times 31 \times 91$  grid (which has to be compared to the one used to perform a DNS on the same configuration with  $1001 \times 81 \times 181$  grid points [Adams, 2000a]). The authors report a reduction of the computational effort for the LES by a factor of 30 in comparison with the DNS.

The numerical Schlieren views reported in Fig. 5.4 show that the instantaneous large-scale behavior provided by the LES is very similar to the one provided by the DNS.

Figure 5.5 compares the mean profiles of the primitive flow variables<sup>11</sup> obtained by LES to those obtained by DNS, at ten different downstream stations. The first station is located in the oncoming boundary layer, the last one downstream of the corner, in the reattached boundary layer, while the eight other stations are located in the vicinity of the corner. An overall good agreement is observed between the LES and filtered DNS results, for all variables. It can be checked that the position of the shock is well reproduced by the LES. A similar agreement is obtained on the turbulent fluctuations (see Fig. 5.6).

---

<sup>11</sup>The velocity components are replaced by the velocity components expressed in a local cartesian system aligned with the walls (contravariant velocity).

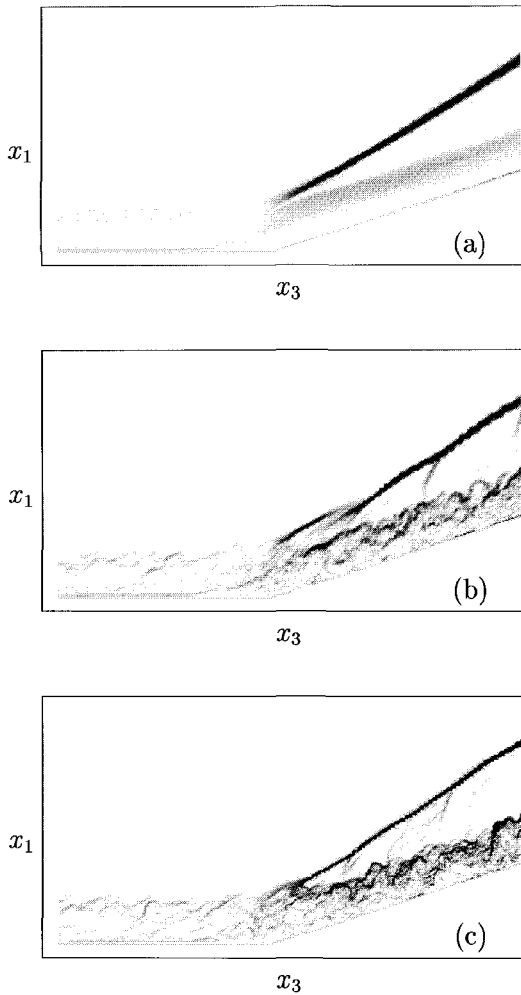


Fig. 5.4 Numerical Schlieren view of the flow ( $\|\nabla\rho\|$  contours) in the compression ramp configuration; (a) spanwise and time average from LES; (b) instantaneous spanwise average from LES; (c) instantaneous spanwise average from DNS. The approximate deconvolution model is used for the LES. From [Stolz *et al.* (2001)], with permission of American Institute of Physics.

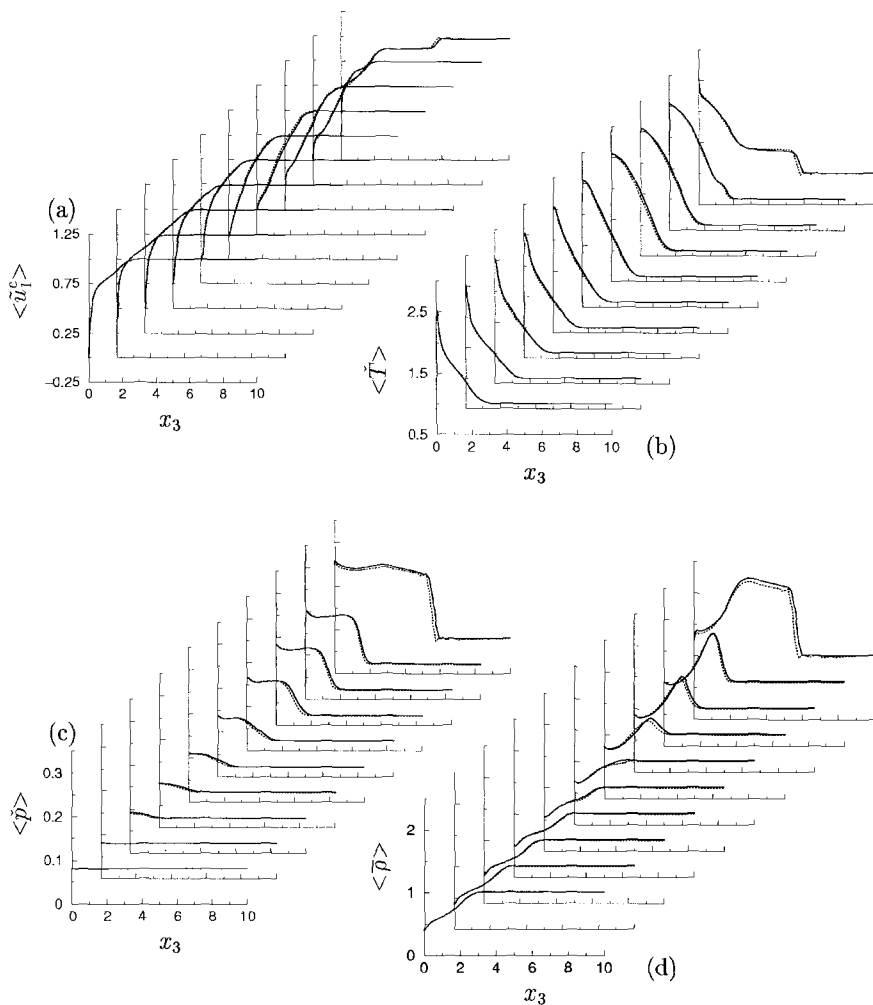


Fig. 5.5 Mean profiles of (a) streamwise contravariant velocity, (b) temperature, (c) pressure, and (d) density, at different downstream stations, in the compression ramp configuration. Solid line: filtered DNS; dotted line: LES with the approximate deconvolution model. From [Stolz *et al.* (2001)], with permission of American Institute of Physics.

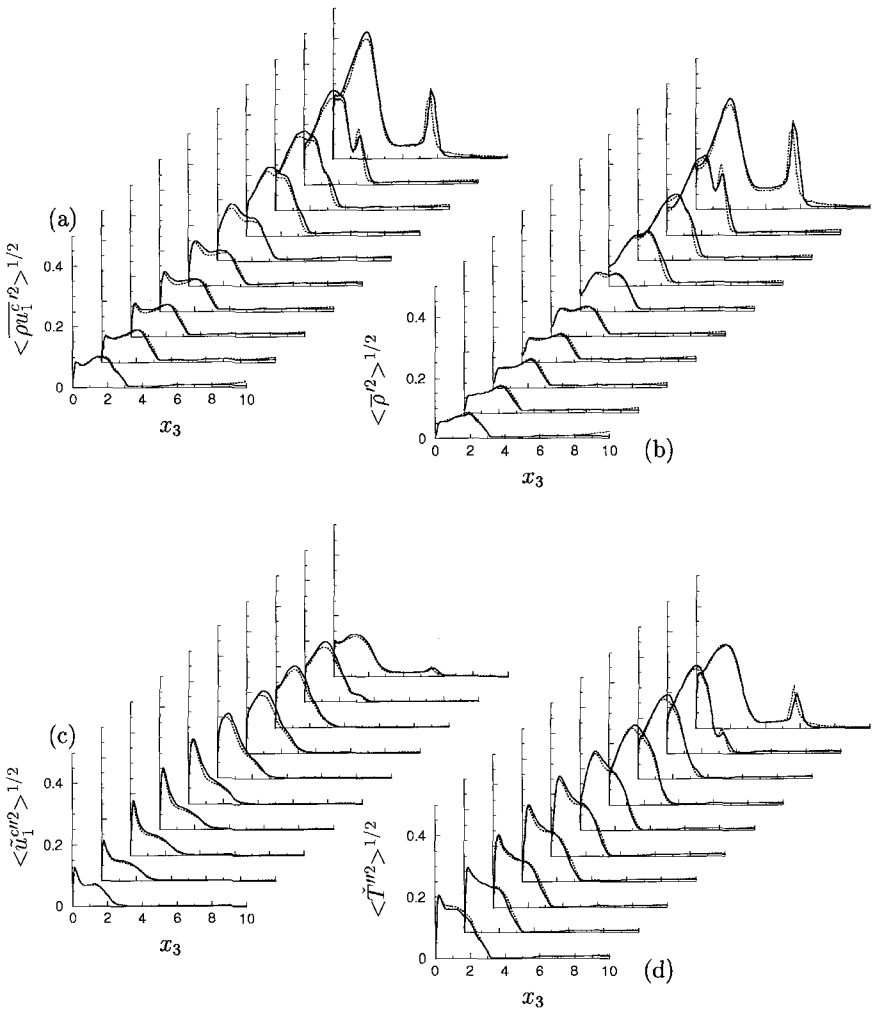


Fig. 5.6 RMS fluctuation profiles of (a) streamwise contravariant momentum, (b) density, (c) streamwise velocity, and (d) temperature, at different downstream stations, in the compression ramp configuration. Solid line: filtered DNS; dotted line: LES with the approximate deconvolution model. From [Stolz *et al.* (2001)], with permission of American Institute of Physics.

## 5.2 Small Scales Reconstruction: Multifractal Subgrid-scale Modelling

### 5.2.1 General idea of the method

Following the same idea of deriving a structural subgrid model, Burton and Dahm [Burton and Dahm, 2005a; Burton and Dahm, 2005b] propose to perform an explicit evaluation of the subgrid velocity by using a multifractal representation of the subgrid vorticity field<sup>12</sup>.

First, the following decomposition of the velocity field is considered

$$\mathbf{u} = \overline{\mathbf{u}}^{(1)} + \mathbf{u}' \quad (5.20)$$

where the resolution level 1 corresponds to the grid filtering level, with a cutoff lengthscale of  $\overline{\Delta}^{(1)}$ . The subgrid stress tensor is then decomposed thanks to Leonard's decomposition as:

$$\begin{aligned} \tau^{(1)} &= \overline{\mathbf{u} \otimes \mathbf{u}}^{(1)} - \overline{\mathbf{u}}^{(1)} \otimes \overline{\mathbf{u}}^{(1)} \\ &= \tau^R + \tau^* \end{aligned} \quad (5.21)$$

where  $\tau^R$  is a fully resolved quantity:

$$\tau^R = \overline{\overline{\mathbf{u}}^{(1)} \otimes \overline{\mathbf{u}}^{(1)}}^{(1)} - \overline{\mathbf{u}}^{(1)} \otimes \overline{\mathbf{u}}^{(1)} \quad (5.22)$$

and the unresolved part  $\tau^*$  is the sum of the cross- and Reynolds terms:

$$\tau^* = \overline{\overline{\mathbf{u}}^{(1)} \otimes \mathbf{u}'}^{(1)} + \overline{\mathbf{u}' \otimes \overline{\mathbf{u}}^{(1)}}^{(1)} + \overline{\mathbf{u}' \otimes \mathbf{u}'}^{(1)}. \quad (5.23)$$

This tensor appears as the only term that requires modelling. In this aim, the authors propose to perform a reconstruction of the subgrid velocity fluctuations  $\mathbf{u}'$ , by first performing a reconstruction of the associated subgrid vorticity field  $\omega' = \nabla \times \mathbf{u}'$ .

From the knowledge of the subgrid vorticity field  $\omega'$ , the subgrid velocity can then be recovered thanks to Biot-Savart integral:

$$\mathbf{u}'(\mathbf{x}, t) = \frac{1}{4\pi} \int_{\xi} \omega'(\xi, t) \times \frac{\mathbf{x} - \xi}{|\mathbf{x} - \xi|^3} d\xi^3. \quad (5.24)$$

---

<sup>12</sup>Notice that a fractal reconstruction procedure was proposed by Scotti and Meneveau [Scotti and Meneveau, 1999], who performed a direct reconstruction of the subgrid velocity fluctuations. Using the fractality of the velocity field, these authors developed a fractal interpolation technique to compute the velocity fluctuations by interpolation of a resolved coarse-grid velocity field on a finer grid.

Since this expression of the subgrid velocity is an integral value, it is then expected to be less sensitive to modelling errors on  $\omega'$  than if it was based on a direct reconstruction of  $\mathbf{u}'$ .

### 5.2.2 Multifractal reconstruction of subgrid vorticity

Multifractal fields result from the repeated application of a scale-invariant multiplicative process to an initial field. In turbulent flows, gradient-magnitude fields such as enstrophy, kinetic energy dissipation rate, or scalar energy dissipation exhibit such a multifractal scale-similarity.

On this basis, a multifractal reconstruction of the vorticity field is proposed in [Burton and Dahm, 2005a], starting from the grid scale  $\Delta^{(1)}$ , down to the viscous length  $\eta$ . The procedure consists in two separate cascades which distribute the subgrid vorticity magnitude  $|\omega'|$  and orientation vectors  $\mathbf{e}_{\omega'}$  to each of the subscales between  $\eta$  and  $\Delta^{(1)}$ . These two cascades are described below.

#### 5.2.2.1 Vorticity magnitude cascade

The first step of the reconstruction is to get an estimation of the subgrid vorticity magnitude  $|\omega'|$ . To do so, a secondary filtering level is first introduced explicitly thanks to the use of a secondary filtering operator  $G_2$ , characterized<sup>13</sup> by its cutoff length  $\Delta^{(2)} = r\Delta^{(1)}$ , with  $r > 1$ .

The idea is then to estimate the subgrid enstrophy  $\Omega'$  as a function of the enstrophy at the smallest resolved scales  $\Omega^\delta$ , as detailed below.

The global vorticity can be expressed using the following triple decomposition:

$$\omega = \nabla \times \mathbf{u} = \omega^{(2)} + \omega^\delta + \omega' \quad (5.25)$$

where:

$$\omega^{(2)} = \nabla \times \mathbf{u}^{(2)} \quad (5.26)$$

$$\omega^\delta = \nabla \times \delta \mathbf{u}^{(1)} \quad (5.27)$$

$$\omega' = \nabla \times \mathbf{u}'. \quad (5.28)$$

---

<sup>13</sup>For the following developments, it will be assumed that the filter  $G_2$  is a sharp cutoff filter, and thus that its cutoff length and the one of the combined filter  $G_2 \star G_1$  are the same i.e:  $\bar{\Delta}^{(2)} = \Delta^{(2)}$ .

We recall (see Chapter 2) that  $\bar{\mathbf{u}}^{(2)} = G_2 \star \bar{\mathbf{u}}^{(1)}$  and  $\delta \mathbf{u}^{(1)} = \bar{\mathbf{u}}^{(1)} - \bar{\mathbf{u}}^{(2)}$ . For each of the three range of scales introduced in decomposition (5.25), the associated enstrophies are introduced:

$$\Omega^{(2)} = \omega^{(2)} \cdot \omega^{(2)} \quad (5.29)$$

$$\Omega^\delta = \omega^\delta \cdot \omega^\delta \quad (5.30)$$

$$\Omega' = \omega' \cdot \omega'. \quad (5.31)$$

The following expression is then derived for the average enstrophy  $\Omega = \omega \cdot \omega$ :

$$\Omega = \Omega^{(2)} + \Omega^\delta + \Omega' + 2 \left( \omega' \cdot \omega^{(2)} + \omega' \cdot \omega^\delta + \omega^{(2)} \cdot \omega^\delta \right). \quad (5.32)$$

Neglecting averages over the cross terms<sup>14</sup>, we get:

$$\Omega \simeq \Omega^{(2)} + \Omega^\delta + \Omega'. \quad (5.33)$$

The spectrum  $\Omega(\kappa)$  associated to the total enstrophy field is therefore the sum of the three respective spectra  $\Omega^{(2)}(\kappa)$ ,  $\Omega^\delta(\kappa)$ , and  $\Omega'(\kappa)$ , and the enstrophies associated to the intermediate and subgrid fields,  $\Omega^\delta$ , and  $\Omega'$  can be approximated as:

$$\Omega^\delta = \int_{\kappa_2}^{\kappa_1} \Omega(\kappa) d\kappa \quad (5.34)$$

$$\Omega' = \int_{\kappa_1}^{\kappa_\eta} \Omega(\kappa) d\kappa \quad (5.35)$$

where  $\kappa_1$ ,  $\kappa_2$  and  $\kappa_\eta$  are the wavenumbers associated to  $\Delta^{(1)}$ ,  $\Delta^{(2)}$  and  $\eta$  (dissipation scale) respectively. Figure 5.7 displays schematically these two last quantities.

On dimensional grounds the enstrophy is shown to scale as  $\Omega(\kappa) \propto \kappa^{1/3}$  in the inertial range, leading finally to the following estimation of  $\Omega'$  as a function of  $\Omega^\delta$ :

$$\Omega' = A \Omega^\delta \left[ \left( \frac{\kappa_\eta}{\kappa_1} \right)^{4/3} - 1 \right] \quad (5.36)$$

where  $A = \left( 1 - r^{-4/3} \right)^{-1}$ .

---

<sup>14</sup>According to the authors, widely disparate scale ranges in the vorticity field display a low correlation factor.

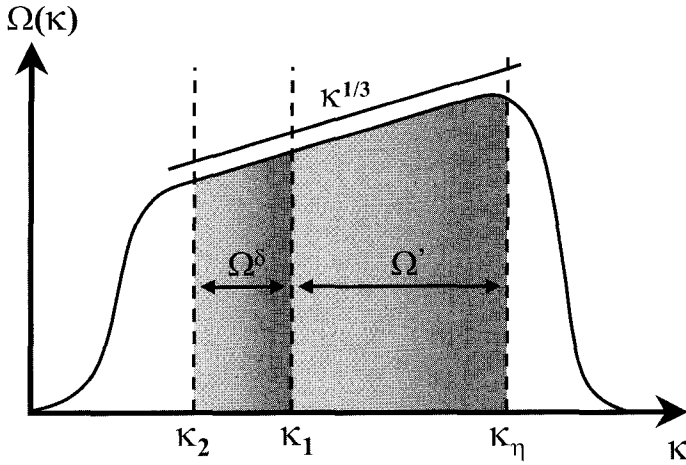


Fig. 5.7 Approximate multiscale decomposition of the enstrophy spectrum considered for the multifractal reconstruction of subgrid vorticity.

The subgrid enstrophy is then distributed over each grid scale cell by a three-dimensional stochastic multiplicative cascade, leading to the following expression for the subgrid vorticity magnitude into each inner-scale cell:

$$|\omega'|(\mathbf{x}, t) = \left( \Omega' (2N)^3 \prod_{n=1}^N \mathcal{M}_n(\mathbf{x}, t) \right)^{1/2} \quad (5.37)$$

where  $N \equiv \log_2(\Delta^{(1)}/\eta)$  represents the number of cascade steps, and the multipliers  $\mathcal{M}_n$  determine randomly the division between the scales ( $0 < \mathcal{M}_n < 1$ ), satisfying a scale-invariant distribution  $\mathcal{P}(\mathcal{M})$  for the enstrophy field.

#### 5.2.2.2 Vorticity orientation cascade

The orientations in the subgrid vorticity field  $\omega'$  at each level of the multifractal cascade are computed so that they decorrelate at successively smaller scales from the local orientations  $\mathbf{e}^\delta(\mathbf{x}, t)$  (the orientation is defined by a unit vector) of the vorticity at the smallest resolved scales,  $\omega^\delta$ .

At each scale  $n$  of the cascade (5.37), the unit orientation vector is computed as:

$$\mathbf{e}^{n+1} = \mathbf{e}^n + \mathbf{f}^n \quad (5.38)$$

where the decorrelation increment  $\mathbf{f}^n$  at step  $n$  is defined by two stochastic spherical decorrelation angles  $\phi$  and  $\theta$  (see Fig. 5.8):

$$\begin{aligned} f_\alpha &= \sin \phi \cos \theta \\ f_\beta &= \sin \phi \sin \theta \\ f_\gamma &= \cos \phi - 1 \end{aligned} \quad (5.39)$$

In the present multifractal model, the correlation between two successive orientation vectors is directly governed by the value of the multiplier  $\mathcal{M}_n$ . Direct numerical simulation data show that this correlation is weak for low values of the multifractal multiplier, while it is very close to one for  $\mathcal{M}_n \simeq 0.95$ . The later case is consistent with the experimental observation that vorticity exhibits a preferred alignment with the intermediate eigen direction of the local strain rate tensor over a large range of scales.

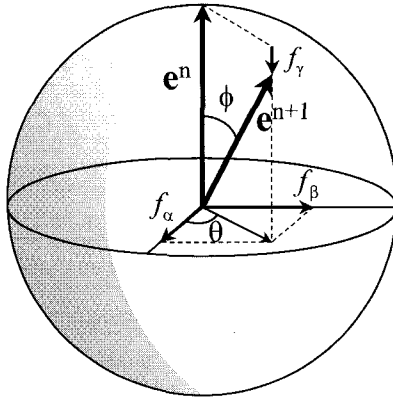


Fig. 5.8 Description of the decorrelation vector  $\mathbf{f}^n$  of the vorticity orientation  $\mathbf{e}^{n+1}$  from the orientation at previous step  $\mathbf{e}^n$ .

At the end of the cascade ( $N$  steps), the following stochastic model for the subgrid vorticity is derived:

$$\omega'(\mathbf{x}, t) = |\omega'| \left( \mathcal{I} \mathbf{e}^\delta(\mathbf{x}, t) + (1 - \mathcal{I}) \sum_{n=1}^N \mathbf{f}^n \right) \quad (5.40)$$

where the intermittency factor  $\mathcal{I}$  is defined from a correlation between  $\omega^\delta$  and  $\omega'$  as:

$$\mathcal{I} = \frac{\int_{\mathbf{x}} \omega' \cdot \omega^\delta d\mathbf{x}^3}{\int_{\mathbf{x}} |\omega'| |\omega^\delta| d\mathbf{x}^3}. \quad (5.41)$$

Assuming that the correlations between the multifractal multipliers  $\mathcal{M}_n$  and the decorrelation increments  $\mathbf{f}^n$  is small and that the decorrelation cascade is isotropic, one obtains the following estimate for the mean value of the subgrid vorticity vector:

$$\langle \omega'(\mathbf{x}, t) \rangle = \mathcal{I}(2^N)^{3/2} \left\langle \sqrt{\mathcal{M}_1 \mathcal{M}_2 \dots \mathcal{M}_N} \right\rangle \sqrt{\Omega'} \mathbf{e}^\delta(\mathbf{x}, t). \quad (5.42)$$

### 5.2.2.3 Reconstruction of the subgrid velocity field

The next step in the derivation of the multifractal model consists in: (i) assuming that at each grid point the subgrid vorticity is equal to its mean value given by Eq. (5.42), *i.e.*  $\omega'(\mathbf{x}, t) \approx \langle \omega'(\mathbf{x}, t) \rangle$  and (ii) that the subgrid velocity is equal to its mean value, which is obtained inserting the mean subgrid vorticity vector into the Biot-Savart law (5.24). After some algebra, one obtains

$$\begin{aligned} \mathbf{u}'(\mathbf{x}, t) &\approx \langle \mathbf{u}'(\mathbf{x}, t) \rangle \\ &= \mathcal{I} 2^{3N/2} \left\langle \sqrt{\mathcal{M}_1 \mathcal{M}_2 \dots \mathcal{M}_N} \right\rangle \sqrt{2^{4N/3} - 1} \sqrt{A} \mathbf{u}^\delta(\mathbf{x}, t). \end{aligned} \quad (5.43)$$

For practical simulations, it is assumed that the multifractal multipliers are statistically weakly correlated, yielding  $\mathcal{I} = 0.372^{-(2/3+3/2)N} \left\langle \sqrt{\mathcal{M}} \right\rangle^{-N}$ , leading to the definition of a closed model.

## 5.3 Multigrid-based Decomposition

As has been extensively described since the beginning of this book, the multilevel methods rely on the introduction of several representation levels of the solution. In the particular LES context, each representation level is considered as a filtering level. Equivalently, each level is defined by its cutoff length, therefore only accounting for a limited range of spatial scales, with a typical size smaller than this cutoff length. With this formalism, the

different filtering levels are obtained by applying recursively some low-pass filters (in the wavenumber space) on the original solution of the Navier–Stokes equations, which can be explicitly known filters, or – in most cases – some approximations of expected filters.

Such a formalism is fully consistent when the numerical method used for the simulation is based on a spectral representation of the solution, since in this case some simple truncations of the series representation of the solution allow defining exactly the different filtering levels. Moreover, such a truncation leads to an effective reduction of the number of degrees of freedom when considering coarser and coarser representation levels of the solution. Such methods have been extensively studied by Dubois and his coworkers, who developed the *Dynamic MultiLevel* (DML) methods [Dubois *et al.*, 1999], which will be detailed in Sec. 6.2.2.

The situation is however quite different when the resolution is performed directly in the physical space, by mean of some finite-volume or finite-difference solvers. Indeed, in such a case: i. any filtering operator must have a compact support in the physical space, and ii. the mesh itself and the numerical scheme introduce their own implicit filtering of the solution. The direct consequence is that the real effective filter remains unknown during the simulation. For that reason, some methods, such as the scale-residual model and the approximate deconvolution approaches described in the previous sections, make use of some approximations of the filtering operation, and suppose an *a priori* form of the filtering operator. It is to be noted that such approximate filters act as some smoothing operators on the solution, but do not allow a practical reduction of the complexity of the problem, since the number of degrees of freedom remains the same after applying the filtering operator.

A possible efficient way to perform the filtering operation in the physical space, leading simultaneously to an effective reduction of the number of degrees of freedom of the solution from the finest to the coarsest representation level, is based on a multigrid architecture. Such a representation of the solution relies on the use of several computational grids, with different mesh resolutions. Indeed, each grid level  $n$ , denoted by  $\Omega_n$ , with a characteristic mesh size  $\Delta^{(n)}$ , can only represent some structures with a size larger than the Nyquist cutoff length<sup>15</sup>,  $2\Delta^{(n)}$ , and therefore defines

---

<sup>15</sup>In practice, the smallest flow structures that can be represented by the mesh are larger than  $2\Delta^{(n)}$ , since the numerical scheme acts as an additional filter which damps the highest grid-resolved wavenumbers.

naturally a filtering level. Figure 5.9 illustrates the link existing between different grid levels and the spectral representation of the solution, in the case of a fully embedded multigrid hierarchy.

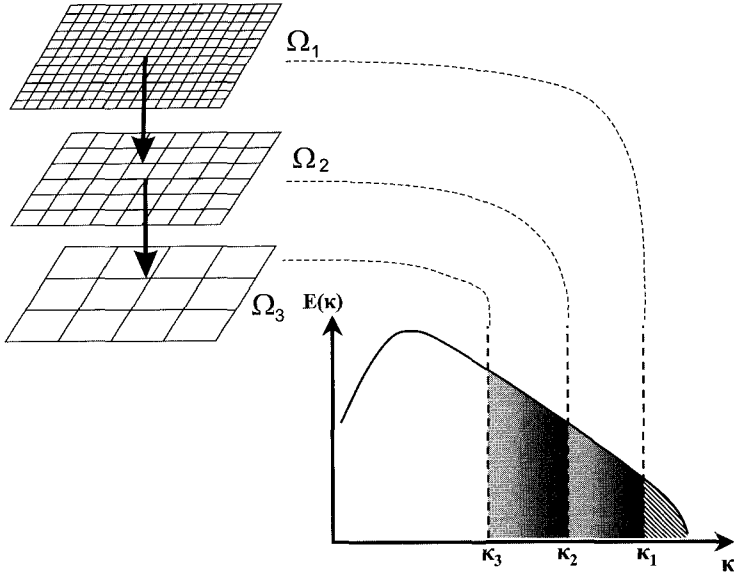


Fig. 5.9 Filtering levels definition by the way of a multigrid hierarchy.

The aim of multigrid-based methods is to adapt the grid resolution in time and/or in space to the physical phenomena occurring in the flow, and therefore to reduce as much as possible the computational resources associated to its resolution. It is to be noted that such techniques often appear as unavoidable when some numerical methods based on the use of structured grids are considered, therefore making it difficult to adapt the mesh resolution in particular flow regions while keeping an overall reasonable number of mesh points. In this context, two main classes of multigrid-based strategies exist, and will be detailed in the next sections:

- The global multigrid methods, which are based on fully embedded grids. In this case, each grid level is a discretization of the entire computational domain, and is generally defined, starting from the finest

level, by keeping only one point out of  $m$  from the previous finer level ( $m$  is a user-specified parameter). As will be detailed in the next section, the numerical methods based on such a grid hierarchy make use of a cycling algorithm in time between the different grid levels, in order to reduce the computational cost.

- The local multigrid methods, and the multidomain methods, where the grid levels are only partially nested, or are corresponding to different domains of the computational area. In that case, which will be detailed in Sec. 5.5, a saving in computational resources is obtained by limiting the use of fine meshes to some regions with a reduced spatial extent.

In each case, the intergrid coupling represents the key point of the algorithm. This coupling differs from one method to another, but introduces in all cases some intergrid transfer operators, allowing interpolation of the data from one grid level to another. These intergrid operators<sup>16</sup> can be divided into two classes:

- The fine-to-coarse interpolation operators, generally referred to as the *restriction* operators. These operators, denoted by  $R_{n \rightarrow n+1}$  allow the transfer of the information from a given grid level  $n$  to the coarser one  $n + 1$ . Considering the multilevel splitting of the variables defined in chapter 2, the filtered flow variables at any “coarse” representation level ( $n > 1$ ) are therefore defined recursively from the flow variables at the finest grid level<sup>17</sup>, by applying successively the restriction operators. At any level  $n > 1$ , the filtered flow variables are thus defined as:

$$\begin{aligned} \bar{\mathbf{u}}^{(n)} &= R_{n-1 \rightarrow n} \bar{\mathbf{u}}^{(n-1)} \\ &= (R_{n-1 \rightarrow n} \circ R_{n-2 \rightarrow n-1} \circ \cdots \circ R_{1 \rightarrow 2}) \bar{\mathbf{u}}^{(1)}. \end{aligned} \quad (5.44)$$

It thus appears that the restriction operator  $R_{n \rightarrow n+1}$  allows performing explicitly the filtering step from level  $n$  to level  $n + 1$ , and acts as the discrete equivalent of the primary filter  $G_{n+1}$ . For that reason, this operator can be chosen such that it also damps the highest resolved wavenumbers from a continuous point of view, while sampling simul-

---

<sup>16</sup>The two terms *restriction* and *prolongation* correspond to the ones usually used in the multigrid methods developed for convergence acceleration in steady computations, see [Wesseling, 1991] for instance.

<sup>17</sup>The discretization step on the finest grid is considered as the application of the primary filter  $G_1$  on the continuous solution of the Navier–Stokes equations.

taneously the flow variables on a coarser grid. That means that the effective filtering step between two consecutive levels is not only due to the implicit cutoff of the coarse grid, but can also be controlled by some modifications of the discrete restriction operator.

- The coarse-to-fine interpolation operators, referred to as the *prolongation* operators. These operators, denoted by  $P_{n \rightarrow n-1}$ , allow the interpolation of the flow variables from any grid level  $n > 1$  to the finer level  $n - 1$ . Ideally, these operators should act as the inverse of the filtering (restriction) operator  $R_{n-1 \rightarrow n}$ . However, because of the mesh truncation, some information has been irremediably lost<sup>18</sup> during the transfer of information from level  $n - 1$  to level  $n$ . For that reason, the prolongation step itself does not allow the recovering of the missing information between the successive levels  $n - 1$  and  $n$ . This information is contained in the details  $\delta \mathbf{u}^{(n-1)}$  of level  $n - 1$ , which are computed as:

$$\begin{aligned} \delta \mathbf{u}^{(n-1)} &= \bar{\mathbf{u}}^{(n-1)} - P_{n \rightarrow n-1} \bar{\mathbf{u}}^{(n)} \\ &= (Id - P_{n \rightarrow n-1} \circ R_{n-1 \rightarrow n}) \bar{\mathbf{u}}^{(n-1)}. \end{aligned} \quad (5.45)$$

From a practical point of view, the prolongation operators should be taken as close as possible from the continuous identity operator, in order to avoid any additional filtering to the filtered variables at the coarse level.

The introduction of several grid levels raises two main issues that need to be met to perform a reliable coupling between them:

- The first one deals with the problem of the subgrid closure that has to be introduced at each filtering level. This point has been investigated in detail by Terracol and coworkers [Terracol *et al.*, 2001; Terracol *et al.*, 2003], who derived some specific multilevel closures (see Sec. 5.4.2.2 for details).
- The second point deals with the reconstruction of the missing information when transferring the flow variables from a given grid level to a finer one. It is to be noted that this problem arises both in global and zonal multigrid algorithms, either in the full computational domain, or at a coupling interface between two consecutive grid levels when zonal methods are considered. Possible techniques are: i. the use of a tempo-

---

<sup>18</sup>This point is also highlighted by Domaradzki and Loh [Domaradzki and Loh, 1999] and justifies the non-linear step of the velocity estimation model.

ral freezing of the high-wavenumber content of the solution (quasi-static approximation, see Sec. 5.4.2); or ii. an explicit reconstruction of its content (see Sec. 5.5).

The next two sections are devoted to the description of multigrid-based multilevel approaches.

## 5.4 Global Multigrid Approaches: Cycling Methods

This section investigates the multilevel methods which are based on the use of several grid levels, which are properly nested, and cover the entire computational domain. Due to this particularity, no reduction of the memory requirements can be expected for the simulation<sup>19</sup>. In order to reduce the cost of the simulations, several authors have proposed to use a cycling between the different grid levels during time integration, in order to reduce as much as possible the time devoted to the resolution of the finest resolved scales of the flow at the first grid level.

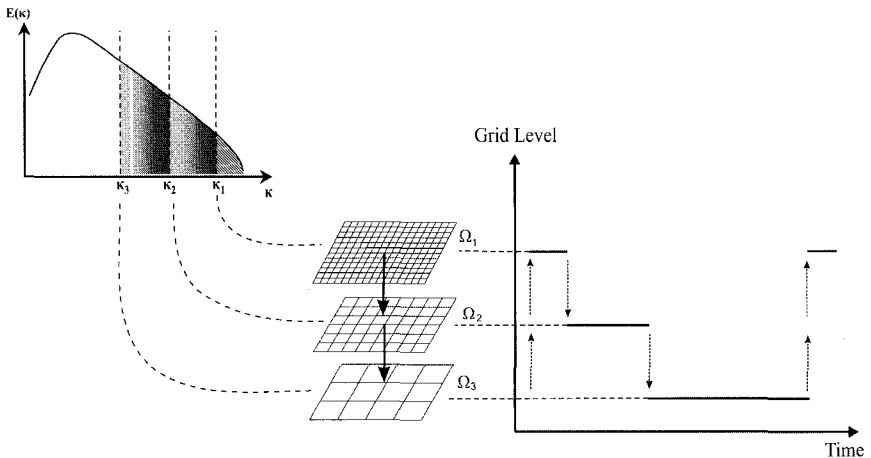


Fig. 5.10 Schematic representation of a multilevel cycling procedure.

<sup>19</sup>The memory requirements for such approaches are in fact larger than those from a classical monolevel approach, due to the introduction of the coarse grid levels ( $n > 1$ ), by a factor of  $\sum_{l=1}^N \left(\frac{1}{8}\right)^{(l-1)}$  in three dimensions.

### 5.4.1 The multimesh method of Voke

This approach, referred to as *multiple mesh simulation*, or *multimesh* [Voke, 1989; Voke, 1990] appears as one of the first attempts to use a multigrid-based approach to perform LES. It is based on the use of  $N$  nested grid levels, where, starting from the finest one (level 1), each coarser grid level  $n > 1$  is obtained by keeping only every other grid point from the finer level  $n - 1$  in each space direction. While the multimesh method should theoretically be applied to any number of grid levels, Voke indicates that there are strong arguments in favor of a simple two-level algorithm.

The idea of the method is then to perform some V-cycles between the different grid levels during time advancement, with the aim to minimize the computations at the fine grid levels. The underlying idea is then to solve the smallest resolved scales of the flow at the fine grid level only, and with less accuracy than the largest ones, being resolved at both the coarse and fine grid levels. One *multimesh cycle* can be described as follows:

- (1) The cycle is started at the finest grid level, where the flow variables are known. Starting from this fine-grid field, some coarser representations of the flow are successively generated on the coarser grid levels, by interpolation:

$$\bar{\mathbf{u}}^{(n+1)} = R_{n \rightarrow n+1} \left( \bar{\mathbf{u}}^{(n)} \right) \quad (5.46)$$

where we recall that  $R_{n \rightarrow n+1}$  denotes an interpolation (restriction) operator from the grid level  $n$  to the coarser grid level  $n + 1$ . This step is referred to as the *injection* step by the author, and is chosen such that it preserves continuity ( $\nabla \cdot \bar{\mathbf{u}}^{(n+1)} = 0$ ).

At this step, the velocity details  $\delta \mathbf{u}^{(n)}$  between the two levels  $n$  and  $n + 1$  are also stored on the fine mesh. These quantities are referred to as the *residual velocity field* by the author and are computed as:

$$\delta \mathbf{u}^{(n)} = \bar{\mathbf{u}}^{(n)} - R_{n \rightarrow n+1} \left( \bar{\mathbf{u}}^{(n)} \right). \quad (5.47)$$

- (2) The solution is then advanced during an integration time  $T$  at the coarsest grid level ( $n = N$ ), by solving the filtered Navier–Stokes equations at this level:

$$\bar{\mathbf{u}}^{(N)}(t + T) = \overline{NS}_T \left( \bar{\mathbf{u}}^{(N)}(t) \right) \quad (5.48)$$

where  $\overline{NS}_T$  denotes the resolution of the filtered Navier–Stokes equations (including the modelled subgrid terms) during the time  $T$ .

- (3) The solution obtained during the previous step is then interpolated to the coarser grid level  $N - 1$ , where the residual velocity field computed in the first step is added. The updated value of the velocity field at this level is thus computed as:

$$\bar{\mathbf{u}}^{(N-1)}(t + T) = P_{N \rightarrow N-1} \left( \bar{\mathbf{u}}^{(N)}(t + T) \right) + \delta \mathbf{u}^{(N)}(t). \quad (5.49)$$

These last two steps allow the achievement of a new realization of the large-scale eddy motion at a moderate cost, while keeping some small scales structures, which are however not completely correlated with the large ones.

- (4) The two last steps are then repeated recursively from level  $N - 1$  to the finest level. In order to get a significant reduction of the computational cost of the simulation, Voke proposes the use of an *equal cost* strategy, that is to say that the computational time required to perform time advancement has to be the same at each grid level. To achieve this, and due to the fact that moving from a level to a coarser one involves eight times less computational grid points, and twice larger time steps, the integration time at each grid level is chosen to be equal to  $T/16$  at level  $N - 1$ ,  $T/256$  at level  $N - 2$  (if any), and so on to the finest level.

These four steps define one cycle of the multimesh algorithm, each cycle being ended at the finest grid level. Fig. 5.11 illustrates schematically one cycle of the multimesh algorithm, in the case of a three-level algorithm. Before the application of any cycle, the author proposes to perform a coarse grid simulation to reach a reliable initial flowfield.

This algorithm has been applied in some plane channel flow computations by the author, using an eddy-viscosity closure at each level, and for a moderate value of the skin-friction Reynolds number ( $Re_\tau \simeq 200$ ). In these simulations, only two grid levels were considered.

#### 5.4.2 The multilevel LES method of Terracol et al.

This approach is based on the ideas developed by Voke [Voke, 1990] of using a multigrid cycling algorithm to perform unsteady turbulence simulations. There however exist two main differences between this method and the one proposed by Voke. First of all, a different cycling procedure in time is used between the different grid levels. The second point, which appears to be a



For that reason, the integration times at the coarse grid levels have been significantly reduced by the authors in comparison to the approach by Voke. In its first version [Terracol *et al.*, 2001], one multigrid cycle was composed of only one time step at each level. The number of grid levels was also imposed as a parameter of the method (up to four grid levels were considered by the authors during their computations). A second version was then proposed by the authors [Terracol *et al.*, 2003] to adjust dynamically in time both the number of grid levels to be used and the integration times at each level. Such a dynamic cycling method was derived in order to ensure as far as possible the validity of the quasi-static approximation, or equivalently to impose that the time variations of the details from each filtering level remain negligible (in a way to be defined) during one multigrid cycle. This improved strategy will be fully described in Sec. 6.2.3.

Another point dealing with the cycling strategy is that one cycle is started by integration of the filtered Navier–Stokes equations at the finest grid level, such that the details (computed during the fine-to-coarse restriction step) are stored as late as possible during the multigrid cycle, such that they remain frozen during a period as short as possible.

One cycle can be described as follows:

- (1) The cycle starts at the time  $t$  on the finest grid:  $n = 1$
- (2) The filtered variables at level  $n$  are time-advanced by solving the filtered Navier–Stokes equations during a given integration time<sup>20</sup>  $\Delta T_n$ :

$$\bar{\mathbf{u}}^{(n)}(t^{(n-1)} + \Delta T_n) = \overline{NS}_{\Delta T_n} \left( \bar{\mathbf{u}}^{(n)}(t^{(n-1)}) \right) \quad (5.51)$$

where  $t^{(n-1)} = t + \sum_{l=1}^{n-1} \Delta T_l$  is the time at the end of the integration at level  $n - 1$ .

- (3) If the current grid level is not the coarsest one ( $n < N$ ), the fine-to-coarse restriction step is applied. The filtered field at level  $n + 1$  is

---

<sup>20</sup>This integration time may be different from the time step  $\Delta t_n$  used to ensure the CFL stability condition at the grid level  $n$ . In the equal-cost cycling strategy of Voke,  $\Delta T_N = T$ , and  $\Delta T_n = \Delta T_{n+1}/16$  for  $n < N$ . In the first version of their cycling algorithm, Terracol *et al.* retained one time step as a fixed value for the integration time at each level:  $\Delta T_n = \Delta t_n$ , while the second version detailed in Sec. 6.2.3 leads to some dynamic estimations of  $\Delta T_n$ .

obtained as:

$$\bar{\mathbf{u}}^{(n+1)} = R_{n \rightarrow n+1} \left( \bar{\mathbf{u}}^{(n)} \right). \quad (5.52)$$

At this step, the details from level  $n$  are also computed and stored at grid level  $n$  as:

$$\delta \mathbf{u}^{(n)} = \bar{\mathbf{u}}^{(n)} - P_{n+1 \rightarrow n} \left( R_{n \rightarrow n+1} \left( \bar{\mathbf{u}}^{(n)} \right) \right). \quad (5.53)$$

- (4) If the current grid level is still not the coarsest one, the two last steps (2) and (3) are repeated at level  $n + 1$ , and recursively until  $n = N$ .
- (5) At the end of one cycle (time  $t^{(N)}$ ), the filtered variables at each finer level  $n < N$  are then re-generated during the prolongation step, by combining an interpolation of the coarser grid values, and the frozen details stored during the cycle:

$$\bar{\mathbf{u}}^{(n)} \left( t^{(N)} \right) = P_{n+1 \rightarrow n} \left( \bar{\mathbf{u}}^{(n+1)} \left( t^{(N)} \right) \right) + \delta \mathbf{u}^{(n)} \left( t^n \right). \quad (5.54)$$

This operation is applied recursively up to the finest grid level. At each level, the details have thus been kept frozen during a time of  $t^{(N)} - t^{(n)} = \sum_{l=n+1}^N \Delta T_l$ .

Fig. 5.12 illustrates one cycle of the cycling algorithm, in the three-level case.

#### 5.4.2.2 Multilevel subgrid closures

In their works, Terracol *et al.* [Terracol *et al.*, 2001; Terracol *et al.*, 2003] highlighted the great influence of the subgrid closure used at the coarse grid levels. Indeed, the finest computational grid is usually chosen such that it matches the classical LES requirements in terms of grid resolution. For that reason, the coarser grid levels are generally much too coarse to solve the filtered Navier–Stokes equations with a standard subgrid model, since the resolved scales may not satisfy the classical LES hypothesis, resulting in a bad behavior of the model.

Two specific possible multilevel closures were therefore proposed in their studies. The major idea relies on the fact that, at a given “coarse” level  $n > 1$ , some smaller scales than the grid-resolved ones are already resolved at finer grid levels, and therefore appear to be of great interest to compute the subgrid terms, since they are associated to a significant part of the subgrid information. The proposed improved closures therefore directly

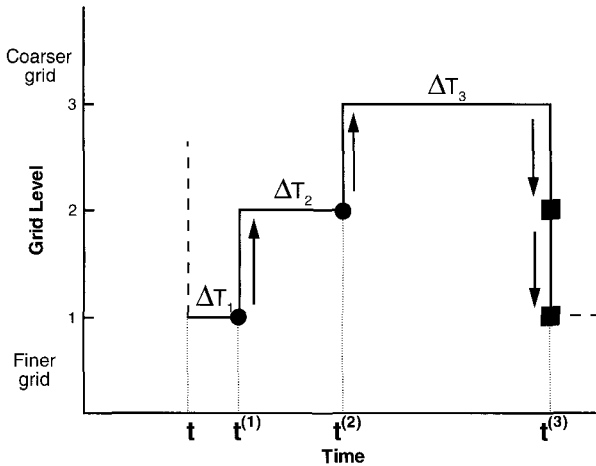


Fig. 5.12 One cycle of Terracol's multilevel LES method, for three grid levels. Filled circles indicate the storage of the velocity details during the injection step. Filled squares indicate the updating step of the velocity field (interpolation from coarser grid level + frozen velocity detail).

take into account the information resolved at finer levels<sup>21</sup>. Such closures used at the coarse grid levels are thus expected to be much more accurate than conventional ones, since no particular hypothesis is required for the unresolved scales of motion.

### (a) Dynamic mixed multilevel closure

The first proposed closure is based on the derivation of a dynamic mixed closure, as proposed by Zang *et al.* [Zang *et al.*, 1993] in the classical LES context. The  $N$ -level extension of this approach performed by Terracol *et al.* can be described in the incompressible formalism<sup>22</sup> as follows.

First, the following decomposition of the velocity field is considered at level  $n$ :

$$\mathbf{u} = \bar{\mathbf{u}}^{(n)} + \sum_{l=1}^{n-1} \delta \mathbf{u}^{(l)} + \mathbf{u}'. \quad (5.55)$$

It is worth noting that three main contributions arise in this decomposition of the velocity field:

<sup>21</sup>One can note that the possible use of improved multilevel closures on the coarse levels was already mentioned by Voke at the end of his works.

<sup>22</sup>The original developments were carried out in the context of compressible flows.

- $\bar{\mathbf{u}}^{(n)}$  is the resolved velocity field at level  $n$ , and is formally associated to some scales with a typical size larger than the grid cutoff length  $\bar{\Delta}^{(n)}$ .
- $\delta\mathbf{u}^{(l)}$  ( $l < n$ ) is the velocity fluctuation between the two successive resolution levels  $l$  and  $l + 1$ . An important point is that this quantity is associated to some smaller scales than the scales resolved at level  $n$ , but which are however resolved during the global simulation. As a consequence, they can be directly used to compute the subgrid terms at level  $n$ .
- $\mathbf{u}'$  represents the subgrid velocity fluctuations at the finest resolution level, and is thus associated to some scales that remain unresolved during the simulation.

The main idea of the multilevel closures is to use directly a maximum amount of resolved information, or in other words to use in a deterministic way both the resolved field  $\bar{\mathbf{u}}^{(n)}$  at level  $n$ , but also the information carried by the details from finer levels  $\delta\mathbf{u}^{(l)}$  ( $l < n$ ).

By introducing decomposition (5.55) in the expression of the subgrid term  $\tau^{(n)}$  at grid level  $n$ , the following decomposition of this term is obtained<sup>23</sup>:

$$\tau^{(n)} = \mathbf{L}^{(n)} + \mathbf{C}^{(n)} + \mathbf{R}^{(n)} \quad (5.56)$$

where the three terms  $\mathbf{L}^{(n)}$ ,  $\mathbf{C}^{(n)}$ , and  $\mathbf{R}^{(n)}$  refer respectively to the resolved, cross, and Reynolds stress tensors of the subgrid-stress tensor:

- $\mathbf{L}^{(n)}$  is based on all the resolved scales of the simulation, so that it represents the resolved part of the subgrid stress tensor  $\tau^{(n)}$  at level  $n$ . Its expression is given by:

$$\begin{aligned} \mathbf{L}^{(n)} = & \mathcal{G}_1^n \left( \left( \bar{\mathbf{u}}^{(n)} + \sum_{l=1}^{n-1} \delta\mathbf{u}^{(n)} \right) \otimes \left( \bar{\mathbf{u}}^{(n)} + \sum_{l=1}^{n-1} \delta\mathbf{u}^{(n)} \right) \right) \\ & - \mathcal{G}_1^n \left( \bar{\mathbf{u}}^{(n)} + \sum_{l=1}^{n-1} \delta\mathbf{u}^{(n)} \right) \otimes \mathcal{G}_1^n \left( \bar{\mathbf{u}}^{(n)} + \sum_{l=1}^{n-1} \delta\mathbf{u}^{(n)} \right). \end{aligned} \quad (5.57)$$

---

<sup>23</sup>This decomposition can be seen as a  $N$ -level generalization of Germano's consistent decomposition

This tensor is not only based on the grid-resolved scales at the level  $n$ , but also takes advantage of the smaller scales resolved at finer levels. It can be interpreted as an extension of Bardina's scale similarity model to the multilevel case. This term accounts for a rather large amount of scales interactions: the large scales interactions, as the classical Bardina term, but also the interactions between large scales and the small scales resolved on the finer levels, and between these small scales themselves. This part of the subgrid stress-tensor is thus associated to all the deterministic information that is directly resolved.

- $\mathbf{C}^{(n)}$  is the cross-term tensor. It accounts for interactions between the large scales and the subgrid scales from the finest level (which remains unresolved), and between small scales resolved at finer levels and the unresolved subgrid scales.

This term reads:

$$\begin{aligned}
 \mathbf{C}^{(n)} &= \mathcal{G}_1^n \left( \left( \bar{\mathbf{u}}^{(n)} + \sum_{l=1}^{n-1} \delta \mathbf{u}^{(n)} \right) \otimes \mathbf{u}' \right) \\
 &\quad - \mathcal{G}_1^n \left( \bar{\mathbf{u}}^{(n)} + \sum_{l=1}^{n-1} \delta \mathbf{u}^{(n)} \right) \otimes \mathcal{G}_1^n (\mathbf{u}') \\
 &\quad + \mathcal{G}_1^n \left( \mathbf{u}' \otimes \left( \bar{\mathbf{u}}^{(n)} + \sum_{l=1}^{n-1} \delta \mathbf{u}^{(n)} \right) \right) \\
 &\quad - \mathcal{G}_1^n (\mathbf{u}') \otimes \mathcal{G}_1^n \left( \bar{\mathbf{u}}^{(n)} + \sum_{l=1}^{n-1} \delta \mathbf{u}^{(n)} \right).
 \end{aligned} \tag{5.58}$$

- $\mathbf{R}^{(n)}$  is the Reynolds stress-tensor, and accounts for all the interactions between the unresolved subgrid scales. Its expression is:

$$\mathbf{R}^{(n)} = \mathcal{G}_1^n (\mathbf{u}' \otimes \mathbf{u}') - \mathcal{G}_1^n (\mathbf{u}') \otimes \mathcal{G}_1^n (\mathbf{u}'). \tag{5.59}$$

It thus appears that the subgrid stress tensor at each level is composed of three different contributions, associated to different kinds of scale interactions. Using this property, it is to be noted that the first tensor involved into this decomposition ( $\mathbf{L}^{(n)}$ ) is directly resolvable, since it accounts only for some interactions between some scales which are resolved during the simulation. Since this tensor accounts directly for a large amount of subgrid interactions, the authors therefore propose to keep its expression when deriving a subgrid closure for  $\tau^{(n)}$ . The only terms which are subject to

a statistical representation are then the cross and Reynolds subgrid terms,  $\mathbf{C}^{(n)}$  and  $\mathbf{R}^{(n)}$  respectively.

Following the developments of Zang *et al.* in the classical monolevel case, Terracol *et al.* propose to model these two terms using a Smagorinsky model for which an appropriate value of the Smagorinsky coefficient is computed by mean of the dynamic procedure.

First, the subgrid stress tensors at two consecutive filtering levels  $n$  and  $n + 1$  are modelled using similar expressions, involving the same constant  $C_d^{(n)}$ , as:

$$\tau^{(n)} = \mathbf{L}^{(n)} - 2C_d^{(n)} \left( \Delta^{(n)} \right)^2 \left| \overline{\mathbf{S}}^{(n)} \right| \overline{\mathbf{S}}^{(n)} \quad (5.60)$$

$$\tau^{(n+1)} = \mathbf{L}^{T(n)} - 2C_d^{(n)} \left( \Delta^{(n+1)} \right)^2 \left| \overline{\mathbf{S}}^{(n+1)} \right| \overline{\mathbf{S}}^{(n+1)} \quad (5.61)$$

where  $\left| \overline{\mathbf{S}}^{(n)} \right| = \sqrt{2\overline{\mathbf{S}}^{(n)} : \overline{\mathbf{S}}^{(n)}}$ .

The tensor  $\mathbf{L}^{T(n)}$  is obtained<sup>24</sup> similarly to  $\mathbf{L}^{(n)}$  by introducing the velocity field decomposition (5.55) at level  $n$  into the expression of  $\tau^{(n+1)}$ :

$$\begin{aligned} \mathbf{L}^{T(n)} &= \mathcal{G}_1^{n+1} \left( \left( \overline{\mathbf{u}}^{(n)} + \sum_{l=1}^{n-1} \delta \mathbf{u}^{(n)} \right) \otimes \left( \overline{\mathbf{u}}^{(n)} + \sum_{l=1}^{n-1} \delta \mathbf{u}^{(n)} \right) \right) \\ &\quad - \mathcal{G}_1^{n+1} \left( \overline{\mathbf{u}}^{(n)} + \sum_{l=1}^{n-1} \delta \mathbf{u}^{(n)} \right) \otimes \mathcal{G}_1^{n+1} \left( \overline{\mathbf{u}}^{(n)} + \sum_{l=1}^{n-1} \delta \mathbf{u}^{(n)} \right). \end{aligned} \quad (5.62)$$

By applying the two-level Germano identity (4.10) to the two parametrizations of the subgrid-stress tensors (5.60) and (5.61), the following relation is derived:

$$\mathcal{L}^{(n+1)} = \left( \mathbf{L}^{T(n)} - G_{n+1} \star \mathbf{L}^{(n)} \right) - 2C_d^{(n)} \mathbf{M}^{(n+1)} \quad (5.63)$$

where the tensor  $\mathbf{M}^{(n)}$  is given by:

$$\mathbf{M}^{(n+1)} = \left( \Delta^{(n+1)} \right)^2 \left| \overline{\mathbf{S}}^{(n+1)} \right| \overline{\mathbf{S}}^{(n+1)} - \left( \Delta^{(n)} \right)^2 G_{n+1} \star \left( \left| \overline{\mathbf{S}}^{(n)} \right| \overline{\mathbf{S}}^{(n)} \right) \quad (5.64)$$

---

<sup>24</sup>The reader should take note of the fact that  $\mathbf{L}^{T(n)} \neq \mathbf{L}^{(n+1)}$ , which should be obtained from the the velocity field decomposition at level  $n + 1$  instead of the one at level  $n$ .

and

$$\mathcal{L}^{(n+1)} = G_{n+1} \star \left( \bar{\mathbf{u}}^{(n)} \otimes \bar{\mathbf{u}}^{(n)} \right) - \bar{\mathbf{u}}^{(n+1)} \otimes \bar{\mathbf{u}}^{(n+1)}. \quad (5.65)$$

As in the original dynamic procedure of Germano *et al.* [Germano *et al.*, 1991], an optimized value for the coefficient  $C_d^{(n)}$  is then obtained by a least-square minimization of the residual of relation (5.63):

$$C_d^{(n)} = - \frac{\left( \mathcal{L}^{(n+1)} - \left( \mathbf{L}^{T(n)} - G_{n+1} \star \mathbf{L}^{(n)} \right) \right) : \mathbf{M}^{(n+1)}}{2\mathbf{M}^{(n+1)} : \mathbf{M}^{(n+1)}}. \quad (5.66)$$

Because of the presence of the scale-similarity term  $\mathbf{L}^{(n)}$  in the parametrization of  $\tau^{(n)}$ , which exhibits in practice a high degree of correlation with the real subgrid stress tensor at level  $n$ , the authors report some values of  $C_d^{(n)}$  which are roughly one order of magnitude lower than the values obtained with the classical dynamic Smagorinsky model.

The authors however also indicate that this model is subject to the same limitations as the dynamic Smagorinsky model, since some numerical instabilities can occur when too important variations or intense negative values of the parameter  $C_d^{(n)}$  are obtained. To alleviate this phenomenon, they recommend the use of some stabilization techniques such as space averaging or clipping.

### (b) Generalized multilevel closure

The second possible multilevel closure that was proposed and used by the authors relies directly on the use of the generalized Germano identity, as already developed in Chapter 4. Indeed, this relation expresses the subgrid terms at any coarse level  $n > 1$  as a function of the resolved field at finer levels, while the only unresolved contribution is due to the subgrid term from the finest representation level ( $n = 1$ ). The expression of the subgrid-stress tensor at any level  $n > 1$  then reads:

$$\begin{aligned} \tau^{(n)} \simeq & \mathcal{G}_2^n \left( f_{sgs} \left( \bar{\Delta}^{(1)}, \bar{\mathbf{u}}^{(1)} \right) \right) \\ & + \sum_{m=1}^{n-1} \mathcal{G}_{m+2}^n \left( G_{m+1} \star \left( \bar{\mathbf{u}}^{(m)} \otimes \bar{\mathbf{u}}^{(m)} \right) - \bar{\mathbf{u}}^{(m+1)} \otimes \bar{\mathbf{u}}^{(m+1)} \right) \end{aligned} \quad (5.67)$$

where the only parametrization ( $f_{sgs}$  denotes a usual subgrid model) occurs for the subgrid-stress tensor from the finest level  $\tau^{(1)}$ .

Such a closure appears very general, since no particular hypothesis is performed on the nature of the interactions with the subgrid scales (except

at the finest level), thus accounting for some complex physical phenomena such as for instance backscatter.

#### 5.4.2.3 Examples of application

The two proposed models were assessed by the authors in some plane channel flow simulations [Terracol *et al.*, 2001; Terracol *et al.*, 2003]. For the results presented in this part, the V-cycling strategy between the different grid levels is simply based on integration times equivalent to one time step at each level<sup>25</sup>, the time step being chosen to ensure a CFL number of roughly one at each grid level. The value of the skin-friction Reynolds number  $Re_\tau$  which has been considered is 590 (some computations at the lower value  $Re_\tau = 180$  were also carried out by the authors). Three different multilevel simulations (using three grid levels<sup>26</sup>) have been carried out: the first one uses a classical dynamic Smagorinsky closure at each level; the second one uses the dynamic mixed multilevel closure; and the last one uses the generalized multilevel closure (the dynamic Smagorinsky model is retained at the finest grid level). In each case, the finest grid level matches the classical LES resolution requirements, and each coarser one is defined from the previous one by keeping every other grid point in each space direction.

The results are compared to the DNS results of Moser *et al.* [Moser *et al.*, 1999] on the same configuration, and to some fine-grid monolevel LES results where the dynamic Smagorinsky model is used.

As shown by Figs. 5.13 and 5.14, the multilevel simulations using an adapted multilevel subgrid closure lead to some results in good agreement with those from the fine monolevel LES, for both mean and fluctuating quantities. This is however not the case with a usual dynamic Smagorinsky model at each level, since the coarsest grid appears too coarse to use a fully statistical modelling of the subgrid scales. The authors report the fact that the near wall streaks, while not resolvable on the coarse grid levels, are well reproduced during the multilevel simulations, thus showing the ability of the method to account for some physical phenomena resolved only at the finest level.

---

<sup>25</sup>See Sec. 6.2.3 for some results obtained with a dynamic version of the cycling procedure

<sup>26</sup>With three grid levels and the simple cycling procedure, the authors report a reduction of a factor of roughly five in CPU time in comparison with a fine monolevel simulation.

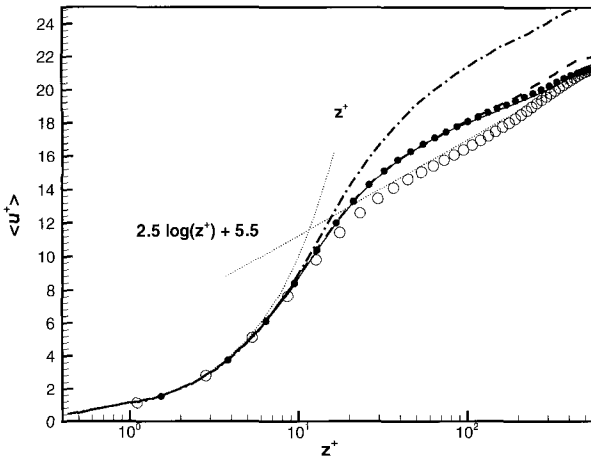


Fig. 5.13 Mean streamwise velocity profiles for the plane channel flow simulations at  $Re_\tau = 590$ . Open circles: DNS (Moser *et al.*, 1999); Filled circles: fine monolevel LES (dynamic Smagorinsky model); Dash-dotted line: three-level simulation with the dynamic Smagorinsky model at each level; Solid line: three-level simulation with the dynamic mixed multilevel closure; Dashed line: three-level simulation with the generalized multilevel closure. From (Terracol, 2001).

## 5.5 Zonal Multigrid/Multidomain Methods

This section investigates the use of zonal multidomain methods, which aim at increasing locally only the resolution of the mesh. Such mesh refinements indeed appear necessary in some flow regions corresponding to the presence of small turbulent structures which require a deterministic resolution. This may be for instance the case in the lower part of the boundary layer in the case of wall-bounded flows, where the turbulence near the walls is subject to strong anisotropic events. In such configurations, the use of partially embedded grids, or different domains with different grid resolution makes it possible to introduce some regions of high resolution, without increasing the overall cost of the simulation. Fig. 5.15 illustrates the two possible classes of method which allow such a local grid refinement<sup>27</sup>:

<sup>27</sup>As can be observed on Fig. 5.15, the zonal multigrid methods are more difficult to implement in a numerical solver than the multidomain approaches. Indeed, the solver has to be adapted to handle several grid levels and perform a coupling between them. However, the practical applicability of the method is easier than the multidomain approach, since it requires less domain partitioning when introducing a new refinement level (see Fig. 5.15).

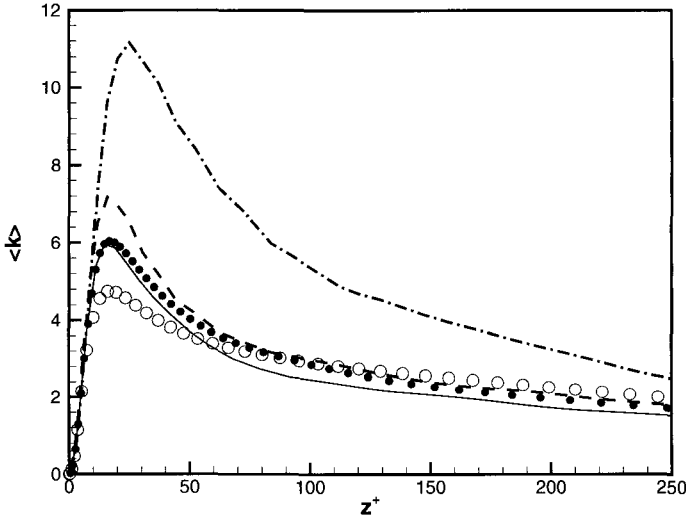


Fig. 5.14 Resolved turbulent kinetic energy profiles for the plane channel flow simulations at  $Re_\tau = 590$ . Open circles: DNS (Moser *et al.*, 1999); Filled circles: fine monolevel LES (dynamic Smagorinsky model); Dash-dotted line: three-level simulation with the dynamic Smagorinsky model at each level; Solid line: three-level simulation with the dynamic mixed multilevel closure; Dashed line: three-level simulation with the generalized multilevel closure. From (Terracol, 2001).

- (1) Zonal multigrid methods (left part in Fig. 5.15) are based on the use of several grid levels, the finer ones being embedded partially in the coarser ones. The coarsest grid level is therefore a discretization of the entire computational domain, while finer and finer grids correspond to some flow regions with smaller and smaller spatial extent. In this case, the intergrid coupling problem in the parts of a grid level overlapped by finer grid levels is exactly the same as in the global multigrid approaches, and therefore involves the same kind of numerical techniques<sup>28</sup> (intergrid transfer operators, adapted subgrid closure in these parts). These methods have been widely investigated in the past for steady CFD computations, and usually coupled with the use of an adaptive refinement strategy<sup>29</sup>. The main techniques which make use of such a zonal multi-

<sup>28</sup>As the global multigrid approaches, the local approaches may also introduce a cycling algorithm in time. However, in most cases, CPU saving is only expected by reducing the spatial extent of the fine grid regions, and a classical time-consistent integration algorithm is used in time, the timestep being imposed by the finer grid.

<sup>29</sup>The use of adaptive refinement techniques for LES will be developed in Chapter 6.

grid hierarchy are the Adaptive Mesh Refinement (AMR) technique developed by Berger *et al.* [Berger, 1982; Berger and Olinger, 1984; Berger and Colella, 1989] and Quirk [Quirk, 1994], and the MultiLevel Adaptive Technique developed by Caltagirone, Angot and Khadra [Caltagirone *et al.*, 1995; Angot *et al.*, 1992] and by Mc Cormick [Mc Cormick, 1994].

- (2) Multidomain methods (right part in Fig. 5.15) are based on the use of several computational domains, which do not overlap each other, and correspond to different mesh resolution.

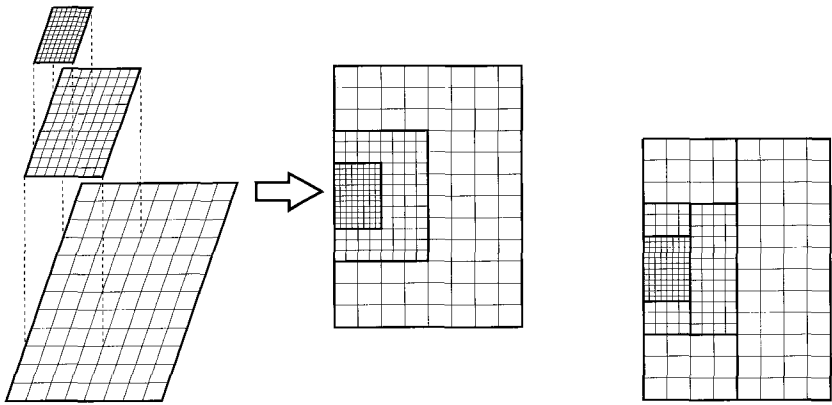


Fig. 5.15 Partitioning of the computational domain in the case of a zonal multigrid method (left), and a multidomain approach (right). Thick lines correspond to the boundaries of the different domains.

As highlighted in the various works based on the use of a zonal multigrid (or multidomain) approach, it is imposed to the grid hierarchy to obey to some specific topological constraints. These constraints may be summarized as the fact that any grid level  $n$  can only exchange some information with its immediate next finer or coarser level  $n-1$  and  $n+1$  respectively. This point is illustrated in the three-level case by Fig. 5.16 displaying a coherent (left part) and an incoherent (right part) organization of the levels.

The main difficulty that arises in both zonal multigrid and multidomain approaches is the coupling at the interface between two levels with different grid resolution. The typical problem encountered in such a configuration is described by Fig. 5.17. Indeed, when interfacing two domains, referred

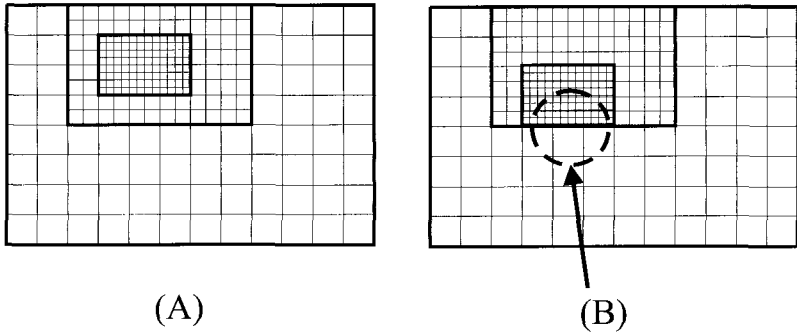


Fig. 5.16 (A) Coherent multilevel organization; (B) Incoherent organization: the finest level ( $n = 1$ ) cannot exchange directly some information with the coarsest level ( $n = 3$ ).

to as the fine and the coarse domain<sup>30</sup>, there exists theoretically a jump in the wavenumber content of the solution through the interface, since the fine grid allows the resolution of some finer turbulent structures than the coarse one.

In most cases, this frequency jump is not accounted for, and some numerical approaches based on a continuous treatment of the flow variables (or of the numerical fluxes) are considered in the various works dealing with this topic. However, such a treatment leads to the generation of a buffer layer in the fine grid domain, in which some turbulent structures smaller than those resolved on the coarse grid are *progressively* regenerated. This feature is illustrated by Fig. 5.18. In this layer, the solution is an intermediate representation between the two filtering levels  $n$  and  $n + 1$ , as in the “gray area” typical of any global RANS/LES approach (see Chapter 7). This implies that the coupling boundaries between two successive grid levels should be located in some regions where the flow structures are well represented on both the two levels, which may become a very strong and penalizing assumption when considering fully turbulent flows.

Several authors have been developing some numerical solvers which are based on the use of locally refined grids to save computational resources when performing LES or DNS of turbulent flows.

For instance, Sullivan *et al.* [Sullivan *et al.*, 1996] developed a grid nesting method to perform LES of planetary boundary layer flows with

<sup>30</sup>For the sake of clarity, only two domains – associated to the consecutive filtering levels  $n$  and  $n + 1$  – will be considered in the following developments, which however apply to an arbitrary number of levels.

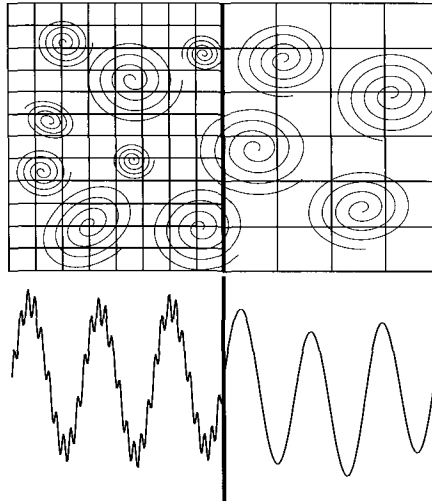


Fig. 5.17 Sketch of the coupling problem at the interface between two domains/grids with different spatial resolutions.

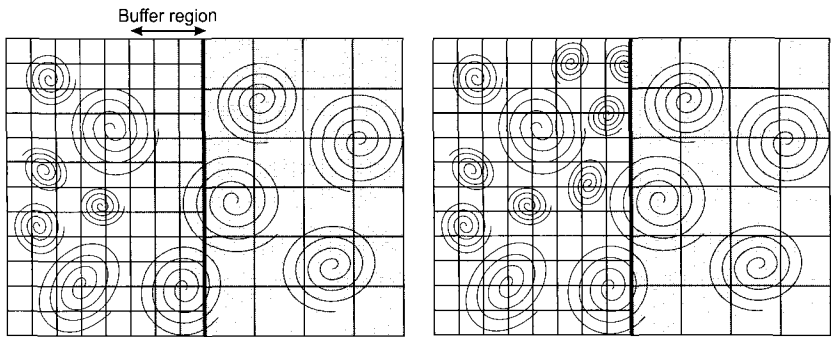


Fig. 5.18 Zonal multilevel LES approach with continuous (left), and discontinuous (right) coupling at the interface. A continuous treatment creates a buffer layer (“gray zone”) in which smaller structures are progressively regenerated.

streamwise periodicity. In their approach, some Dirichlet conditions derived by interpolating the coarser mesh variables were used to define the boundary conditions for the fine grid (except at physical boundaries of the domain). A correction of the coarse grid numerical fluxes was also performed to ensure fluxes continuity in the overlapping regions and at the interfaces between two grid levels.

A similar approach was also applied by Boersma *et al.* [Boersma *et al.*, 1997] to the simulation of a two-dimensional time-developing mixing layer. In this work, the authors showed the ability of such an approach to increase locally the accuracy by increasing the resolution. However, they mention the fact that the fine-to-coarse grid communication should become a key element of the method for fully three-dimensional turbulent flow simulation.

Manhart [Manhart, 1999] and Manhart and Friedrich [Manhart and Friedrich, 1999] applied a similar methodology to perform some DNS of turbulent boundary layers at moderate Reynolds numbers. The approach was applied to both the case of a zero pressure gradient and to the case of a turbulent boundary layer subject to a streamwise adverse pressure gradient, for some values of the Reynolds number based on the inlet momentum thickness ranging from  $Re_\theta = 300$  to  $Re_\theta = 800$ .

Kravchenko *et al.* [Kravchenko *et al.*, 1996; Kravchenko *et al.*, 1999] developed a B-spline/spectral method for the DNS of turbulent flows, which was also used to perform a LES of the flow past a cylinder at a significant Reynolds number [Kravchenko and Moin, 2000]. In this approach, a highly accurate interpolation of the flow variables, based on the use of a B-spline technique, was used at the coupling interfaces between two domains with different grid resolution, therefore leading to a highly accurate continuous treatment between them.

While most of the works dealing with multidomain (or zonal multi-grid) approaches rely on a continuous treatment between two adjacent domains, a radically different approach has been developed by Quéméré *et al.* [Quéméré *et al.*, 2001]. Indeed, in these works dealing with the development of a multidomain approach for LES, the authors propose to explicitly take into account the different characteristic lengths associated to two adjacent domains with different grid resolution. Their approach therefore introduces a discontinuity of the flow variables at the coupling interface between two consecutive grid levels  $n$  and  $n + 1$ . It is recalled at this point that level  $n$  corresponds to a finer mesh resolution than level  $n + 1$ .

In their works, the authors consider the case of two adjacent, partially coincident domains  $\Omega_n$  and  $\Omega_{n+1}$ , of respective associated characteristic cell sizes  $\Delta^{(n)}$  and  $\Delta^{(n+1)} = r\Delta^{(n)}$ , where the aspect ratio  $r$  is an integer larger than unity<sup>31</sup>.

---

<sup>31</sup>In practice, the authors investigated some values of the aspect ratio  $r$  between two and four.

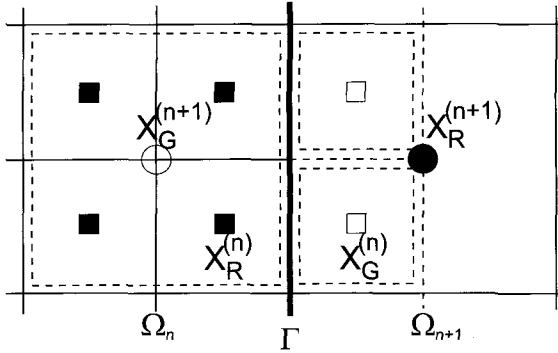


Fig. 5.19 Schematic representation of the coupling problem at the interface between two domains/grids with different spatial resolutions. Filled symbols represent real cell centers (referred to as  $\mathbf{x}_R$ ), and empty symbols the ghost cell centers (dashed lines indicate the location of the ghost cells, referred to as  $\mathbf{x}_G$ ). Squares are points of the fine grid, and circles points of the coarse grid.

This configuration is described in Fig. 5.19, for  $r = 2$ , in the case of a cell-centered representation of the flow variables. The problem is then to define in a proper way some values for the aerodynamic quantities in the ghost cells belonging to each domain, accounting for the jump in the wavenumber content of the solution illustrated by Fig. 5.17. At the interface  $\Gamma$  between the two domains, the problem is formulated as<sup>32</sup>:

$$\bar{\mathbf{u}}^{(n)}|_{\Gamma} \neq \bar{\mathbf{u}}^{(n+1)}|_{\Gamma}. \quad (5.68)$$

This relation is fully consistent with the following multiscale decomposition:

$$\bar{\mathbf{u}}^{(n)} = \bar{\mathbf{u}}^{(n+1)} + \delta\mathbf{u}^{(n)} \quad (5.69)$$

where the velocity detail  $\delta\mathbf{u}^{(n)}$  may be non-negligible in the case of developed turbulence. Therefore, a continuous treatment of the flow variables at the interface would thus only be possible in flow regions corresponding to very low values of  $\delta\mathbf{u}^{(n)}$ , e.g. low-turbulence regions. However, in such cases, the method should become inefficient in terms of computational resources saving.

Following this observation, the authors have proposed a method to transfer properly the information between the two domains without loosing

<sup>32</sup>As pointed out by the authors, the discontinuity of the flow variables at the interface also implies a discontinuity in the numerical fluxes on the respective fine and coarse sizes of the interface, leading to a non-conservative boundary treatment.

accuracy in the high wavenumber content of the fine domain in the vicinity of the coupling interface  $\Gamma$ . This coupling is two-way:

- (1) The fine-to-coarse coupling is the easiest one to perform, and appears as quite straightforward. Indeed, it is necessary to remove the information associated to the highest resolved wavenumbers from the field resolved at level  $n$  to define properly some values of the filtered aerodynamic field at level  $n + 1$ . This coupling is based on the use of the restriction operator  $R_{n \rightarrow n+1}$ , which makes it possible to evaluate the value of  $\bar{\mathbf{u}}^{(n+1)}$  in the ghost cell of the domain  $\Omega_{n+1}$  (at point  $\mathbf{x}_G^{(n+1)}$ ) from the values of  $\bar{\mathbf{u}}^{(n)}$  in the real cells of the domain  $\Omega_n$  (denoted by  $\mathbf{x}_R^{(n)}$ ). The values of  $\bar{\mathbf{u}}^{(n+1)}$  at point  $\mathbf{x}_G^{(n+1)}$  are therefore evaluated as:

$$\begin{aligned} \bar{\mathbf{u}}^{(n+1)}(\mathbf{x}_G^{(n+1)}) &= R_{n \rightarrow n+1} \left( \bar{\mathbf{u}}^{(n)}(\mathbf{x}_R^{(n)}) \right) \\ &= \frac{1}{\mathcal{V}_G^{(n+1)}} \int_{\mathcal{V}_G^{(n+1)}} \bar{\mathbf{u}}^{(n)}(\xi) d\xi \\ &= \frac{1}{\mathcal{V}_G^{(n+1)}} \sum_{\mathbf{x}_R^{(n)} \in \mathcal{V}_G^{(n+1)}} \bar{\mathbf{u}}^{(n)}(\mathbf{x}_R^{(n)}) \cdot \mathcal{V}_R^{(n)} \end{aligned} \quad (5.70)$$

where  $\mathcal{V}_R^{(n)}$  denotes the volume of the fine grid real cell with center  $\mathbf{x}_R^{(n)}$ , and  $\mathcal{V}_G^{(n+1)}$  the volume of the coarse grid ghost cell with center  $\mathbf{x}_G^{(n+1)}$ . It is to be noted that this restriction operator acts as a discrete box filter with a cutoff lengthscale equal to  $\left(\mathcal{V}_G^{(n+1)}\right)^{1/3}$ .

- (2) The coarse-to-fine coupling is somewhat more difficult to perform. Indeed, in this case, it is necessary to add some high-wavenumber information to the field values known at the coarse level.

Following relation (5.69), the values of the field in the ghost cells of the fine level are expressed as:

$$\bar{\mathbf{u}}^{(n)}(\mathbf{x}_G^{(n)}) = \bar{\mathbf{u}}^{(n+1)}(\mathbf{x}_G^{(n)}) + \delta \mathbf{u}^{(n)}(\mathbf{x}_G^{(n)}). \quad (5.71)$$

The values of the field at the fine grid ghost point  $\mathbf{x}_G^{(n)}$  at the coarse filtering level,  $\bar{\mathbf{u}}^{(n+1)}(\mathbf{x}_G^{(n)})$  is expressed by prolongation of the values of  $\bar{\mathbf{u}}^{(n+1)}$  at the coarse grid points:

$$\bar{\mathbf{u}}^{(n+1)}(\mathbf{x}_G^{(n)}) = P_{n+1 \rightarrow n} \left( \bar{\mathbf{u}}^{(n+1)}(\mathbf{x}_{R,G}^{(n+1)}) \right) \quad (5.72)$$

where the subscript  $R, G$  is introduced since both real and ghost points may be used for the prolongation interpolator<sup>33</sup>.

To provide an estimation of the details  $\delta \mathbf{u}^{(n)}$  at the fine grid ghost points, the authors propose to perform a zero-th-order extrapolation of their value in the last row of real fine grid cells close to the interface:

$$\delta \mathbf{u}^{(n)}(\mathbf{x}_G^{(n)}) = C_\delta \cdot \delta \mathbf{u}^{(n)}(\mathbf{x}_R^{(n)}) \quad (5.73)$$

where the coefficient  $C_\delta$  is introduced to ensure the stability of the approach<sup>34</sup>. The value of  $\delta \mathbf{u}^{(n)}$  in the last row of real cells of the fine grid is computed as:

$$\begin{aligned} \delta \mathbf{u}^{(n)}(\mathbf{x}_R^{(n)}) &= \bar{\mathbf{u}}^{(n)}(\mathbf{x}_R^{(n)}) - \bar{\mathbf{u}}^{(n+1)}(\mathbf{x}_R^{(n)}) \\ &= \bar{\mathbf{u}}^{(n)}(\mathbf{x}_R^{(n)}) - P_{n+1 \rightarrow n} \left( \bar{\mathbf{u}}^{(n+1)}(\mathbf{x}_{R,G}^{(n+1)}) \right). \end{aligned} \quad (5.74)$$

The authors applied their method to the simulation of plane channel flow computations, for skin-friction Reynolds number values up  $Re_\tau = 590$ , where some fine grids were considered in the vicinity of the walls, while the core region of the channel was treated using a coarse grid. Several aspect ratios of the mesh resolution between the two grids have been investigated (between two and four), and up to three-level computations were performed. In all cases, the obtained results were comparable to those from fine monolevel simulations. The approach has also been extended by the authors in a later study [Quéméré and Sagaut, 2002] to the case of zonal RANS/LES coupling, as will be detailed in Chapter 8.

In some more recent works, carried out by Mary and Nolin, this approach has been applied to the simulation of some more complex flow such as the flow over a three-dimensional delta wing [Mary, 2003], or the flow past an A-airfoil wing profile [Mary and Nolin, 2004].

---

<sup>33</sup>In their works, Quéméré *et al.* used a third-order accurate interpolation operator involving a ten-point stencil (in three dimensions).

<sup>34</sup>The authors found the value  $C_\delta = 1$  to lead to a quite strong overestimation of the reconstructed turbulent fluctuation. The value  $C_\delta = 0.95$  was found as a good compromise.

This page is intentionally left blank

## Chapter 6

# Unsteady Turbulence Simulation on Self-adaptive Grids

### 6.1 Turbulence and Self-adaptivity: Expectations and Issues

We now discuss multiscale/multilevel methods for turbulence simulation that rely on the use of self-adaptive grids. The term grid is here to be understood in a general sense, which includes all methods in which the number of degrees of freedom and/or their locations in the space/wave number domain is evolving during the computation. Therefore, usual computational grids for finite volume and finite difference methods but also generalized  $h/p$  methods are included in the present discussion.

The purpose of such a method is to significantly lower the cost of the simulation by optimizing the number of degrees of freedom used to capture the dynamics of the resolved scales. While a purely static grid will be associated to the maximum computational cost, a gain is sought here by taking into account the features of the resolved scales and adapting the computational grid to them.

The methods addressed in this chapter provide such a reduction, and lead to a *multilevel description of the resolved scales*. Using these methods therefore brings in the additional issue of the coupling of the usual turbulence models with the dynamic grid representation of the resolved scales, new turbulence closures best suited being sometimes required.

Grid refinement/adaptation basically requires us to define a refinement criterion which will trigger the modification of the grid. Such a criterion is generally based on two different elements: a quantity whose amplitude will be checked, and an arbitrary threshold level beyond which the grid will be refined. This quantity is usually defined or interpreted as a measure of

the error committed in the representation of the large scales<sup>1</sup>. Numerical methods based on adaptive grids are not new and are discussed in many textbooks [Rüde, 1993; Mc Cormick, 1989; Mc Cormick, 1992; Dubois *et al.*, 1999], but it will be shown here that the turbulent nature of the solution brings in new deep theoretical and practical problems.

To illustrate the specific problems associated with the simulation of turbulence, let us consider the following continuous generic conservation law system, whose exact solution solution is  $u$ :

$$\frac{\partial u}{\partial t} + \nabla \cdot F(u, u) = 0 \quad (6.1)$$

where  $F(u, u)$  is a nonlinear flux which accounts for all acceleration terms including possible external forcing terms. We further assume that  $u$  is a turbulent solution in the sense that it is chaotic and exhibits a broadband spectrum, and that its smallest active scales have a characteristic size  $\eta$  (the Kolmogorov scale in the common turbulence theory).

Let now consider the computed discrete approximation of  $u$ ,  $u_h$ . For the sake of simplicity, it is assumed that the computational grid has a characteristic mesh size  $h$ , and that the numerical method used to compute  $u_h$  has a characteristic resolution length  $h_r$ . The maximal cutoff frequency of the simulation, conceptually associated to the Nyquist frequency, is based on  $h_r$ . We can make the distinction between two general classes of simulation approaches:

- (1) Approaches in which the ideal targeted solution is grid-independent, *i.e.* the ideal solution is sensitive to neither  $h$  nor  $h_r$ . Both Reynolds Averaged Numerical Simulation (RANS) methods and Direct Numerical Simulation (DNS) belong to this category.
  - (a) Direct Numerical Simulation is characterized by  $h_r \approx \eta$ . The targeted solution is the instantaneous exact solution of the original problem.
  - (b) In the case of RANS,  $h_r \gg \eta$  since all turbulent fluctuations are modelled, and one can define a characteristic length scale for the mean field,  $\bar{h}$ , which is such that

---

<sup>1</sup>Many methods are based on the tracking of regions with large gradients of the solution, with the implicit assumptions that the committed error in the numerical approximation is maximum in these regions, while it will be much smaller in areas where the computed field varies smoothly.

$$\bar{h} \gg h_r \gg \eta. \quad (6.2)$$

The targeted solution is not the exact solution, but its statistical average.

- (2) Approaches whose ideal solution definition can intrinsically be tied to the resolution of the simulation. A typical example is Large Eddy Simulation in which  $h_r \gg \eta$ . It is worth noting that the ideal solution is not the exact solution, but its restriction onto an arbitrary basis associated to a given set of degrees of freedom. Therefore, if this basis is directly tied to  $h_r$ , changing  $h$  and/or  $h_r$  automatically leads to a change in the definition of the ideal LES solution.

Let us now consider the discrete problem, which is written as follows:

$$\frac{\delta u_h}{\delta t} + \nabla_h \cdot F_h(u_h, u_h) = 0 \quad (6.3)$$

where  $\delta/\delta t$ ,  $\nabla_h$  and  $F_h$  are the discrete approximations of  $\partial/\partial t$ ,  $\nabla$  and  $F$ , respectively. The approximated flux  $F_h$  is assumed to fulfill the consistency condition  $\lim_{h \rightarrow 0} F_h(u, u) = F(u, u)$ .

Let us introduce the bases for the definition of an error estimate, which will be used to decide where and when to refine the computational grid (*i.e.* to change  $h_r$  and/or  $h$ ). The key problem in ensuring the reliability of the results is to control the error  $\text{Err}(h_r, \lambda) = \|u - u_h\|_{\mathcal{M}}$ , where  $\|\cdot\|_{\mathcal{M}}$  is an arbitrary norm. The characteristic scale  $\lambda$  of the ideal targeted solution is equal to  $\eta$  and  $\bar{h}$  for DNS and RANS, respectively. In most LES simulations, one has  $\lambda \propto h_r$ . Since the solution is assumed to be chaotic, all discrepancies in the boundary and initial conditions between the exact and the discrete problem will be continuously amplified. Therefore, only control of the statistical moments (or in an equivalent way of the probability density function) of the solution can be expected over long times. A relevant definition of the error must rely on statistical moments of  $u$  and  $u_h$  and must be consistent with the definition of Direct Numerical Simulation, *i.e.*

$$\lim_{h_r \rightarrow 0} \text{Err}(h_r, \lambda) = 0. \quad (6.4)$$

A deeper insight into the nature of the committed error is recovered by identifying the different sources of error:

$$\text{Err}(h_r, \lambda) = \text{Err}_{\Pi}(h_r, \lambda) + \text{Err}_h(h_r, \lambda) + \text{Err}_r(h_r, \lambda) \quad (6.5)$$

where

- $\text{Err}_{\Pi}(h_r, \lambda)$  is the projection error, associated to the fact that the exact continuous solution is approximated using a finite number of degrees of freedom (even if some numerical approximations, like the finite element method, provide the users with continuous approximations of the exact solution). This is an intrinsic error that can not be eliminated in the general case. A consistency constraint is

$$\lim_{h_r \rightarrow 0} \text{Err}_{\Pi}(h_r, \lambda) = 0. \quad (6.6)$$

- $\text{Err}_h(h_r, \lambda)$  represents the discretization error, which is related to the fact that space and time derivatives are not evaluated in an exact way:

$$\nabla_h(u) - \nabla(u) \neq 0. \quad (6.7)$$

The numerical method being consistent, we have

$$\lim_{h_r \rightarrow 0} \text{Err}_h(h_r, \lambda) = 0. \quad (6.8)$$

- $\text{Err}_r(h_r, \lambda)$  is the resolution error, which is not equivalent to the discretization error. It accounts for the fact that, even if the derivatives are exactly evaluated, the flux function is not exact since all scales of the exact solution are not resolved:

$$F_h(u_h, u_h) \neq F_h(u, u) = F(u, u). \quad (6.9)$$

Accordingly to the definition of DNS,  $\text{Err}_r(h_r, \eta)$  vanishes when  $h_r \approx \eta$ . In both RANS and LES approaches the non-linear flux function  $F(u, u)$  includes the selected turbulence model for unresolved scales of motion. The resolution error consequently takes into account the modelling error, which originates in the turbulence model flaws.

The problem is therefore to minimize both the numerical and resolution error, the best (or ideal) solution being defined as

$$\text{Err}(h_r, \lambda) = \text{Err}_{\Pi}(h_r, \lambda) \quad (\text{ideal solution}) \quad (6.10)$$

which is equivalent to say that

$$\text{Err}_h(h_r, \lambda) + \text{Err}_r(h_r, \lambda) = 0. \quad (6.11)$$

Let us now consider the three cases identified above:

- In DNS, both the projection error and the resolution error are assumed to be small, the main error source being the discretization error. Dynamic grid techniques will therefore aim at decreasing its intensity. The error sensor should be designed so that to track the discretization error. Convergence of the refinement technique is ensured since the ideal solution is not an explicit function of the mesh size.
- In RANS, the projection error is small<sup>2</sup> with respect to the discretization error and the resolution error. Since the resolution error mainly comes from the modelling error and that RANS-type models do not explicitly depend upon  $h$  and  $h_r$ , the purpose of the grid-refinement techniques will be the same as in DNS, i.e. to reduce the discretization error. Since they do not raise specific closure problems, AMR-RANS methods will not be detailed here. Their efficiency is illustrated in Fig. 6.1, which displays the mesh and the viscous turbulent flow obtained around a 2D transonic airfoil using a multigrid-AMR technique along with the Wilcox  $k - \omega$  turbulence models (see [Jouhaud, Montagnac and Tourette, 2005] for details).
- The LES case is much more complex if the scale separation length between resolved and unresolved scales is an explicit function of  $h$  and/or  $h_r$ . Here, the three error terms are a priori important, but since the exact solution is not known, only the discretization and the resolution error can be tracked down in the simulation. The purpose of grid refinement is then to reduce these two errors, but the error estimate must be constructed carefully. As a matter of fact, a change in the mesh size (and then in  $h$  and  $h_r$ ) will lead to an error decrease, but also in a change in the ideal targeted solution. The convergency of the error estimation-minimization loop toward the original ideal LES is not

---

<sup>2</sup>It must be remembered here the ideal RANS solution is not the instantaneous turbulent field, but its statistical average, which is usually a very smooth function that can easily be captured on a relatively coarse grid.

guaranteed in the general case, too crude an error estimate leading to a DNS-type simulation.

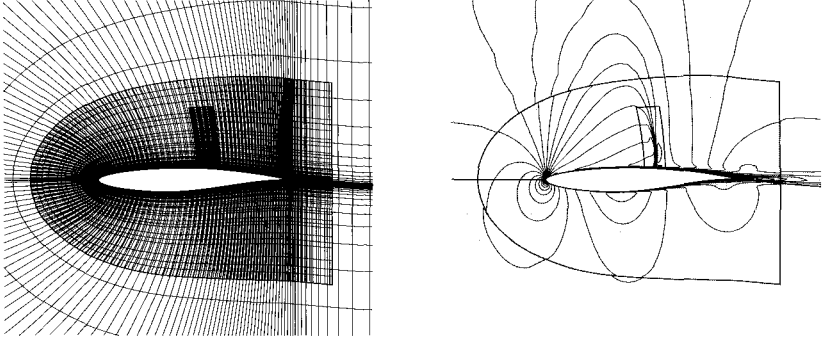


Fig. 6.1 AMR-RANS simulation of the compressible flow around a 2D airfoil. Left: adapted grid, with 3 refinement levels; Right: Mach number isolines. Courtesy of J.C. Jouhaud, CERFACS, France.

## 6.2 Adaptive Multilevel DNS and LES

This section describes the DNS and LES methods which are based on an adaptation of the grid<sup>3</sup> dynamically in time, in order to minimize the error  $\text{Err}(h_r, \lambda)$ .

The case of dynamic local multilevel LES, which relies on a dynamic adaptation of the mesh resolution locally both in space and time, will be detailed in Sec. 6.2.1.

Some other techniques, based on a global adaptation of the grid resolution in the overall computational domain will be also investigated. These techniques include the Dynamic MultiLevel (DML) method, which is detailed in Sec. 6.2.2, and the dynamic multilevel LES technique developed by Terracol, Sagaut and Basdevant, presented in Sec. 6.2.3.

---

<sup>3</sup>We recall that the term *grid* stands for all the methods with varying numbers of freedom, and not only for those based on the use of a discretization mesh in the physical space.

### 6.2.1 Dynamic Local Multilevel LES

These techniques rely on the basis of Adaptive Mesh Refinement (AMR) methods, and aim at increasing locally in space the grid resolution, in a dynamical way. This is done in practice by superimposing finer grids on an initial coarse grid in the flow regions where an increased grid resolution is needed. This leads naturally to a local multigrid hierarchy as the one described in Sec. 5.5.

In such a case, the coupling between the different filtering/grid levels obeys the same formalism as local multigrid techniques, and will therefore not be detailed again. The reader is referred to the developments presented in Sec. 5.5.

One of the crucial points in dynamic mesh techniques is the localization of the regions that require an improvement in the grid resolution. At this point, one usually introduces a *refinement sensor* to identify the flow regions in which the discretization and resolution errors are expected to be significant<sup>4</sup>. This sensor has therefore to be designed so that it detects the flow regions where the error is large. Since the error includes different contributions, different kinds of refinement sensors can be used:

- (1) The numerical sensors which aim at estimating the discretization error. These ones are certainly the most commonly used in AMR-based calculations performed in the RANS and DNS frameworks.

The simplest idea consists of looking at the gradients of the solution, which are large in regions relative to strong and rapid variations of the solution and the occurrence of significant discretization errors.

Another popular sensor is the one based on Richardson extrapolation [Berger and Olinger, 1984], which consists in comparing predictions of the solution at several grid levels with different resolution. This comparison provides an estimate of the local truncation error.

While these classical sensors are known to yield reliable estimates of the discretization error, they result in too important grid refinements within the framework of LES. As a matter of fact, a fully turbulent field is characterized by a chaotic behavior of the flow and strong local variations of the solution. The Richardson extrapolation being based on an asymptotic error estimate, it is only valid in the DNS limit.

---

<sup>4</sup>We recall that in the particular LES context, the projection error cannot be controlled, since the resolved field depends explicitly on the characteristic resolution length  $h_r$ .

- (2) The sensors which aim to detect the existence of unresolved scales. The previous sensors do generally not account for any subgrid information. Indeed, if the solution varies sufficiently smoothly, some high-frequency phenomena – still not resolved by the current mesh – may remain unresolved, and escape the previous sensors. Let us consider the grid-resolved velocity field  $\bar{\mathbf{u}}$ . A possible way to estimate the subgrid fluctuations  $\mathbf{u}'$  of the flow relies on the following self-similarity assumption:

$$\mathbf{u}' = \mathbf{u} - \bar{\mathbf{u}} \quad (6.12)$$

$$\simeq \bar{\mathbf{u}} - \widehat{\bar{\mathbf{u}}} \quad (6.13)$$

where the hat notation denotes the application of a secondary test filter. A possible sensor consists in refining the grid in flow regions associated with values of  $\mathbf{u}'$  larger than a user-defined threshold.

It can be remarked that the use of a second-order finite difference approximation of the Gaussian filter with a cutoff length taken equal to  $2h$  leads to the following estimate of  $\mathbf{u}'$  (the developments are carried out in one dimension of space only for a sake of clarity):

$$\mathbf{u}'(x) = \bar{\mathbf{u}}(x) - \widehat{\bar{\mathbf{u}}}(x) \quad (6.14)$$

$$= \bar{\mathbf{u}}(x) - \frac{1}{6} (\bar{\mathbf{u}}(x-h) + 4\bar{\mathbf{u}}(x) + \bar{\mathbf{u}}(x+h)) \quad (6.15)$$

$$= \frac{h^2}{6} \frac{\partial^2 \bar{\mathbf{u}}}{\partial x^2}(x) + \mathcal{O}(h^3) \quad (6.16)$$

yielding  $\mathbf{u}' \propto \frac{\partial^2 \bar{\mathbf{u}}}{\partial x^2}$ . Note that this quantity corresponds also to a popular sensor in AMR simulations.

Such a detection of the unresolved small scales of the flow may lead to an effective reduction of the projection error. However, in the LES context, the use of such a sensor may also lead to a too important degree of refinement, *i.e.* the mesh resolution tends toward the DNS limit, which is the direct consequence of the search for the minimization of the projection error.

- (3) The sensors which detect the flow regions where the modelling (resolution) error is important. As stated above, the refinement sensors based on some estimations of the numerical truncation error, or on the detection of unresolved subgrid scales lead to too crude criteria in the specific LES context, since they all lead to the use of prohibitive DNS-like grids. Therefore, it appears necessary to develop some specific refine-

ment sensors for LES, which will be based on the analysis of the local physical features of the flow. Indeed, in LES, grid refinement should overcome only in some flow regions where the physical assumptions used to develop the subgrid models are not fulfilled. On the other hand, the subgrid models are generally very efficient in accounting for the unresolved scales in the flow regions where the turbulence at small scales is essentially isotropic. An appropriate sensor for LES should then be designed so that it will be able to detect unresolved scale anisotropy.

Following this idea, Mitran [Mitran, 2001] combines the use of the Richardson extrapolation error estimate along with a combination of two physical sensors: the enstrophy  $|\nabla \times \bar{\mathbf{u}}|$ , and the helicity  $|(\nabla \times \bar{\mathbf{u}}) \cdot \bar{\mathbf{u}}|$ . This physical sensor makes it possible to detect elongated tubular structures, allowing the segregation between interesting subgrid dynamics and nearly isotropic subgrid turbulence. However, Mitran mentions that imposing some appropriate threshold values for the indicators remains an open flow-dependent problem.

Another possible physical refinement indicator relies on the approach proposed by Léonard *et al.* [Léonard *et al.*, 2005a; Léonard *et al.*, 2005b]. This indicator is based on the computation of the slope of the energy spectrum in the highest resolved wavenumbers, therefore making it possible to detect the flow regions where the turbulence is not isotropic. The authors base their approach on a wavelet representation of the solution.

First, the following wavelets coefficients are considered:

$$w_{m,j} = \langle f, \psi_{m,j} \rangle = \int_{-\infty}^{+\infty} f(x) \psi_{m,j}(x) dx \quad (6.17)$$

where the two indices  $m$  and  $j$  refer respectively to the *scale* ( $m = 0$  corresponds to the finest scale) and the *position* in space. The function  $f$  may be chosen as a characteristic variable of the flow.

The basis functions  $\psi_{m,j}$  are obtained by dilatation and translation of a *mother wavelet*  $\psi$ . The authors chose to use a redundant wavelet in their study:

$$\psi_{m,j}(x) = 2^{-m} \psi \left( \frac{x-j}{2^m} \right). \quad (6.18)$$

These wavelets correspond to larger and larger scales as  $m$  increases, *i.e.* their support increases with  $m$ .

The analysis of the wavelets coefficient  $w_{m,j}$  is therefore an efficient way to evaluate the local energy of each scale at each grid point. In practice, the finite-difference approximation developed by Sjögreen and Yee [Sjögreen and Yee, 2004] was retained by the authors to compute the wavelet coefficients<sup>5</sup>:

$$w_{m,j} = f_j^{m-1} - (f_{j-1}^{m-1} + f_{j+1}^{m-1}) / 2 \quad (6.19)$$

where the representation of the function  $f$  at the level  $m$  is given by:

$$f_j^m = (f_{j-1}^{m-1} + f_{j+1}^{m-1}) / 2. \quad (6.20)$$

As first proposed by Sjögreen and Yee [Sjögreen and Yee, 2004], the authors then introduce the local Hölder exponent<sup>6</sup>  $\alpha_j$  to analyze the regularity of the function  $f$ , defined thanks to the following relation:

$$\log_2 r_{m,j} = \alpha_j m + C \quad (6.21)$$

where  $C$  is a constant, and:

$$r_{m,j} = \max_{k=-2^m p, 2^m q} |w_{m,j+k}|. \quad (6.22)$$

The two parameters  $p$  and  $q$  define the stencil of the wavelet decomposition.

By considering an appropriate function  $f$  to perform the wavelet analysis, the Hölder exponent can be interpreted as a local evaluation of the slope of the Fourier energy spectrum<sup>7</sup>. Indeed, the authors considered the vorticity field  $\nabla \times \bar{\mathbf{u}}$ , and, assuming a power law of the form  $E(\kappa) \propto \kappa^{-\beta}$  for the energy spectrum, derived the following relation:

$$\alpha_j = \frac{\beta - 3}{2}. \quad (6.23)$$

The local Hölder exponent therefore appears as a possible refinement sensor, the grid being refined in flow regions such that  $\beta < 5/3$ . Equiv-

---

<sup>5</sup>Here, only one-dimensional developments are detailed for a sake of clarity. The approach can be simply extended in the three space directions to derive the fully three-dimensional method.

<sup>6</sup>Relying on this quantity, Sjögreen and Yee [Sjögreen and Yee, 2004] use different families of wavelets to detect shocks, turbulent fluctuations, and spurious fluctuations.

<sup>7</sup>The link between wavelet coefficients and the Kolmogorov decaying law was studied by Farge *et al.* [Farge *et al.*, 1996] and Perrier *et al.* [Perrier *et al.*, 1995].

alently, the refinement threshold is imposed naturally thanks to relation (6.23), and the grid may be refined in regions where small scales anisotropy is detected *i.e.*:

$$\text{refine if: } \alpha_j < -\frac{2}{3}. \quad (6.24)$$

As an illustration, Fig. 6.2 presents the fine-grid organization obtained dynamically by applying this refinement technique during a LES of a three-dimensional turbulent mixing layer, in the inviscid limit, and for a Mach number value of  $M = 0.2$ .

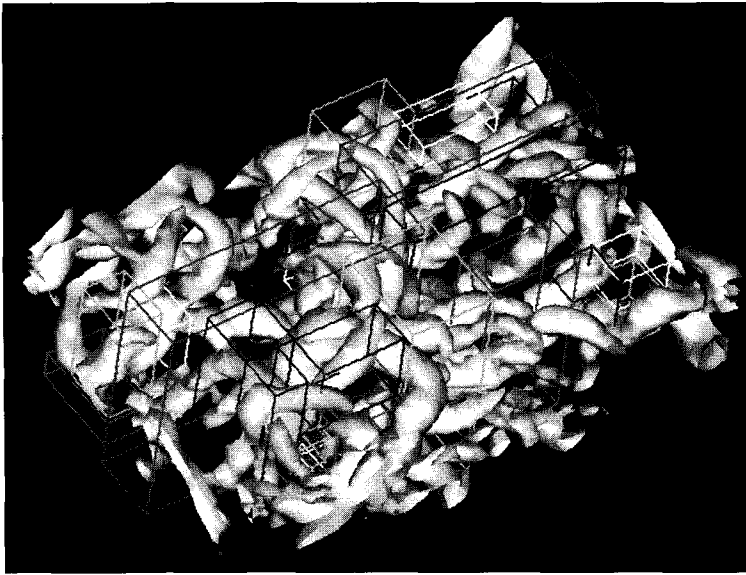


Fig. 6.2 Dynamic grid organization obtained in the case of a subsonic turbulent mixing layer. Courtesy of S. Léonard, ONERA, France.

### 6.2.2 *The Dynamic MultiLevel (DML) method of Dubois, Jauberteau and Temam*

This section describes the main characteristics of the DML method developed by Dubois, Jauberteau and Temam. For a more detailed presentation, the reader can refer to [Dubois *et al.*, 1999].

### 6.2.2.1 Spectral multilevel decomposition

The following developments are restricted to the fully periodic case<sup>8</sup>, which makes it possible to consider a fully three-dimensional spectral approach. Let us consider the computational domain as a cube with a size of  $L_1$  in each space direction. The velocity field  $\mathbf{u}$  can therefore be expressed thanks to the following Fourier expansion:

$$\mathbf{u}(\mathbf{x}, t) = \sum_{\kappa \in \mathbb{Z}^3} \hat{\mathbf{u}}(\kappa, t) e^{i\kappa L_1 \cdot \mathbf{x}} \quad (6.25)$$

where  $\kappa_{L_1} = 2\pi\kappa/L_1$ . This expansion is then truncated at order  $N$  as:

$$\bar{\mathbf{u}}^{(N)}(\mathbf{x}, t) = \sum_{\kappa \in S_N} \hat{\mathbf{u}}(\kappa, t) e^{i\kappa_{L_1} \cdot \mathbf{x}} = P_N \mathbf{u}(\mathbf{x}, t) \quad (6.26)$$

where  $P_N$  denotes the projector on the modes  $\kappa$  such that  $|\kappa| \leq \frac{N}{2}$  *i.e.* on  $S_N$ :

$$S_N = \left\{ \kappa \in \mathbb{Z}^3 / |\kappa_j| \leq \frac{N}{2}, j = 1, 2, 3 \right\}. \quad (6.27)$$

In order to get a reliable representation of the flow variables, the parameter  $N$  is chosen such that  $N > \frac{L}{\eta}$ , *i.e.* scales down to the Kolmogorov dissipation scale  $\eta$  can be captured. In practice  $|\kappa_N| = \frac{N}{2} \geq 1.5|\kappa_\eta|$  is found to be sufficient to consider expansion (6.26) as a DNS representation of the flow ( $\kappa_\eta$  is the wavenumber associated to Kolmogorov scale).

Similarly to Eq. (6.26) a multiscale representation of  $\mathbf{u}$  can be considered, by introducing a hierarchy of truncation order  $N_M < N_{M-1} < \dots < N_1 < N_0 = N$ , which makes it possible to obtain coarser representations of  $\mathbf{u}$  as  $N_i$  decreases (respectively as the level  $i$  increases):

$$\begin{aligned} \bar{\mathbf{u}}^{(N_i)}(\mathbf{x}, t) &= P_{N_i} \bar{\mathbf{u}}^{(N)}(\mathbf{x}, t) \\ &= \sum_{\kappa \in S_{N_i}} \hat{\mathbf{u}}(\kappa, t) e^{i\kappa_{L_1} \cdot \mathbf{x}} \end{aligned} \quad (6.28)$$

where  $P_{N_i}$  is the projector on the modes  $\kappa$  such that  $|\kappa| \leq \frac{N_i}{2}$ .

---

<sup>8</sup>The DML method was originally developed for isotropic homogeneous turbulence simulation, and then extended to the case of bi-periodic channel flow, which will not be discussed here.

Notice that  $P_{N_i}$  is a projective filter *i.e.*:

$$P_{N_{i_2}} \left( P_{N_{i_1}} \bar{\mathbf{u}}^{(N)} \right) = P_{N_{i_2}} \bar{\mathbf{u}}^{(N)}, \text{ for } N_{i_2} < N_{i_1}. \quad (6.29)$$

By introducing the operator  $Q_{N_{i_2}}^{N_{i_1}} : \mathbf{u} \rightarrow P_{N_{i_1}} \mathbf{u} - P_{N_{i_2}} \mathbf{u}$ , one obtains an expression for the intermediate scales (details) between two levels  $i_2$  and  $i_1$  ( $i_1 < i_2, N_{i_2} < N_{i_1}$ )<sup>9</sup>:

$$\begin{aligned} \delta \mathbf{u}_{N_{i_2}}^{N_{i_1}} &= \bar{\mathbf{u}}^{(N_{i_1})} - \bar{\mathbf{u}}^{(N_{i_2})} = Q_{N_{i_2}}^{N_{i_1}} \bar{\mathbf{u}}^{(N)} \\ &= \sum_{\kappa \in S_{N_{i_1}} \setminus S_{N_{i_2}}} \hat{\mathbf{u}}(\kappa, t) e^{i\kappa L_1 \cdot \mathbf{x}}. \end{aligned} \quad (6.31)$$

The following decomposition of the DNS field  $\bar{\mathbf{u}}^{(N)}$  is finally obtained (we recall that  $N = N_0$ ):

$$\bar{\mathbf{u}}^{(N)} = \bar{\mathbf{u}}^{(N_i)} + \delta \mathbf{u}_{N_i}^N. \quad (6.32)$$

The multilevel decomposition of the flow variables that will be considered below is illustrated by Fig. 6.3.

### 6.2.2.2 Associated Navier–Stokes-based equations

In their study, Dubois, Jauberteau and Temam consider a particular form of the Navier–Stokes equations, which is based on the use of the Leray–Helmholtz decomposition. First, the Leray–Helmholtz projection operator  $\mathcal{P}_{LH}$  of the vector  $\mathbf{v}$  is introduced :

$$\mathbf{v} = \nabla q + \mathbf{w} \quad (6.33)$$

where  $\mathbf{w}$  is such that  $\nabla \cdot \mathbf{w} = 0$  (so that it is a curl vector). This decomposition is shown to be unique.

---

<sup>9</sup>It should be remarked that, with the notations introduced in Chapter 2, we get:

$$\delta \mathbf{u}_{N_{i_2}}^{N_{i_1}} = \sum_{l=i_1}^{i_2-1} \delta \mathbf{u}^{(l)}. \quad (6.30)$$

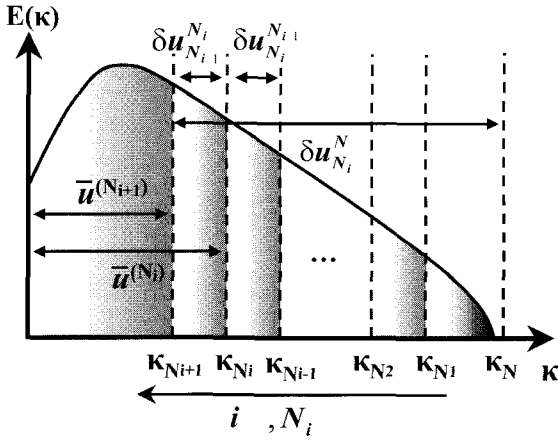


Fig. 6.3 Multilevel decomposition of the turbulent field in the DML approach.

By applying the projector  $\mathcal{P}_{LH} : \mathbf{v} \rightarrow \mathbf{w}(\mathbf{v})$  to the Navier–Stokes equations<sup>10</sup> (2.2), the following equation is derived for  $\bar{\mathbf{u}}^{(N)}$ :

$$\frac{\partial \bar{\mathbf{u}}^{(N)}}{\partial t} + B(\bar{\mathbf{u}}^{(N)}, \bar{\mathbf{u}}^{(N)}) = -\nu A \bar{\mathbf{u}}^{(N)} \tag{6.34}$$

where  $A$  is the Stokes operator:

$$A \mathbf{u} = -\mathcal{P}_{LH} \nabla^2 \mathbf{u} \tag{6.35}$$

and:

$$B(\mathbf{u}, \mathbf{v}) = \mathcal{P}_{LH} \nabla \cdot (\mathbf{u} \otimes \mathbf{v}). \tag{6.36}$$

It is worth noting that the projection onto a divergence-free space makes the pressure term to disappear.

By applying the scale separation operator  $P_{N_i}$  to Eq. (6.34), and considering the decomposition (6.32), the following evolution equation for the large-scale field  $\bar{\mathbf{u}}^{(N_i)}$  is obtained:

$$\frac{\partial \bar{\mathbf{u}}^{(N_i)}}{\partial t} + P_{N_i} B(\bar{\mathbf{u}}^{(N_i)}, \bar{\mathbf{u}}^{(N_i)}) = -\nu A \bar{\mathbf{u}}^{(N_i)} - P_{N_i} B_{int}(\bar{\mathbf{u}}^{(N_i)}, \delta \mathbf{u}_{N_i}^N) \tag{6.37}$$

---

<sup>10</sup>Here, since  $\bar{\mathbf{u}}^{(N)}$  is associated to a DNS-like discretization, no subgrid term appears in the Navier–Stokes-based equations written for  $\bar{\mathbf{u}}^{(N)}$ .

where  $B_{int}$  is the non-linear interaction term between large and small scales, which is classically split into a cross term and a Reynolds term:

$$\begin{aligned}
 B_{int} \left( \bar{\mathbf{u}}^{(N_i)}, \delta \mathbf{u}_{N_i}^N \right) &= B \underbrace{\left( \bar{\mathbf{u}}^{(N_i)}, \delta \mathbf{u}_{N_i}^N \right)}_{\text{Cross term}} + B \left( \delta \mathbf{u}_{N_i}^N, \bar{\mathbf{u}}^{(N_i)} \right) \\
 &+ \underbrace{B \left( \delta \mathbf{u}_{N_i}^N, \delta \mathbf{u}_{N_i}^N \right)}_{\text{Reynolds term}}.
 \end{aligned} \tag{6.38}$$

### 6.2.2.3 Quasi-static approximation

In 2D, the theoretical works of Foias *et al.* [Foias *et al.*, 1988] lead to the following inequalities, for sufficiently large values of  $N_i (< N)$ :

$$\left| \delta \mathbf{u}_{N_i}^N \right|_2 \leq \left| \bar{\mathbf{u}}^{(N_i)} \right|_2 \tag{6.39}$$

$$\left\| \delta \mathbf{u}_{N_i}^N \right\| \leq \left\| \bar{\mathbf{u}}^{(N_i)} \right\| \tag{6.40}$$

$$\left| \frac{\partial}{\partial t} \delta \mathbf{u}_{N_i}^N \right|_2 \leq \left| \frac{\partial}{\partial t} \bar{\mathbf{u}}^{(N_i)} \right|_2 \tag{6.41}$$

where  $|\cdot|_2$  and  $\|\cdot\|$  denote respectively the norms associated to kinetic energy and enstrophy.

In 3D, numerical results [Dubois *et al.*, 1998; Dubois and Jauberteau, 1998] indicate that relation (6.39) is valid for  $\kappa_{N_i} > \kappa_L$  and that relations (6.40) and (6.41) are valid for  $\kappa_{N_i} > \kappa_{\mathcal{E}}$ , where  $\kappa_{\mathcal{E}}$  is the wavenumber associated to the maximum of the enstrophy spectrum.

Some estimations of the time variation of the small scales,  $\frac{\partial}{\partial t} \delta \mathbf{u}_{N_i}^N$ , and of the time variation of the non-linear interaction term between the large and the small scales,  $\frac{\partial}{\partial t} B_{int} \left( \bar{\mathbf{u}}^{(N_i)}, \delta \mathbf{u}_{N_i}^N \right)$ , were also obtained, showing that their norms decrease as  $\kappa_{N_i}$  increases.

The global idea of the dynamic multiresolution methods was then derived from these estimations. It consists in neglecting the variations associated to these terms during a certain interval of time. This approximation is referred to as the *quasi-static approximation*.

On the basis of the above estimations, the possible duration of this approximation is therefore expected to increase with  $N_i$ .

#### 6.2.2.4 General description of the spectral multilevel method

Dubois *et al.* developed several multilevel methods relying on the quasi-static approximation, which are based on the use of a V-cycling strategy between the different computational levels. A hierarchy of  $M + 1$  different representation levels of the solution is introduced, with, as previously,  $N_M < N_{M-1} < \dots < N_1 < N_0 = N$ . It is recalled that the finest level is associated to a DNS-like resolution. The approach may then be considered as a dynamic multilevel DNS method.

For each cycle (one cycle may consists in several V-cycles), three parameters are introduced: two levels  $i_1$  and  $i_2$  (with  $0 \leq i_1 < i_2 \leq M$ ) associated to the coarsest and finest resolution levels during the current cycle ( $N_{i_2} < N_{i_1}$ ), respectively, and  $n_V$  which represents the number of V-cycles to be performed between the resolution levels  $i_1$  and  $i_2$  within the current cycle. These parameters are derived from error estimates, as detailed in the next section.

During each cycle, the resolution level  $i$  varies between  $i_1$  and  $i_2$ , and the Navier–Stokes-based equations (6.37) at this level are re-written using the following triple decomposition of  $\bar{\mathbf{u}}^{(N)} = \bar{\mathbf{u}}^{(N_0)}$ :

$$\begin{aligned} \bar{\mathbf{u}}^{(N_0)} &= \bar{\mathbf{u}}^{(N_i)} + \sum_{j=i_1}^{i-1} \delta \mathbf{u}_{N_j}^{N_{j+1}} + \delta \mathbf{u}_{N_{i_1}}^{N_0} \\ &= \underbrace{\bar{\mathbf{u}}^{(N_i)}}_{(i)} + \underbrace{\delta \mathbf{u}_{N_{i_1}}^{N_{i_1}}}_{(ii)} + \underbrace{\delta \mathbf{u}_{N_{i_1}}^{N_0}}_{(iii)}. \end{aligned} \quad (6.42)$$

In this decomposition, the first term (i) is associated to the large scales which resolved at level  $i$ . The second one (ii) is related to *intermediate scales*, *i.e.* to scales which are not resolved at level  $i$ , but which are resolved at the finer levels  $j$  considered during the current cycle  $i_1 \leq j < i$ . Finally, term (iii) is associated to the small scales resolved only at levels  $l$  that are finer than the finest level of the current cycle,  $0 \leq l < i_1$ .

At level  $i$ , the evolution equation (6.37) for  $\bar{\mathbf{u}}^{(N_i)}$  can be rewritten as:

$$\begin{aligned} \frac{\partial \bar{\mathbf{u}}^{(N_i)}}{\partial t} + P_{N_i} B \left( \bar{\mathbf{u}}^{(N_i)}, \bar{\mathbf{u}}^{(N_i)} \right) &= -\nu A \bar{\mathbf{u}}^{(N_i)} \\ &\quad - P_{N_i} B_{int} \left( \bar{\mathbf{u}}^{(N_i)}, \delta \mathbf{u}_{N_{i_1}}^{N_{i_1}} + \delta \mathbf{u}_{N_{i_1}}^{N_0} \right). \end{aligned} \quad (6.43)$$

This equation is solved at each level, using the quasi-static approximation. In practice, the non-linear interaction term is computed using the last com-

puted values of the intermediate scales (details)  $\delta \mathbf{u}_{N_{i_1}}^{N_{i_1}}$  during the current cycle, and the value of the small scales  $\delta \mathbf{u}_{N_{i_1}}^{N_0}$  computed at the end of the previous cycle. At the end of each cycle, these small scales are refreshed by projecting them onto an approximate inertial manifold (see [Foias *et al.*, 1988] for instance), and the cycling parameters  $i_1$ ,  $i_2$ , and  $n_V$  are adapted according to one of the methods detailed in the next section.

### 6.2.2.5 Dynamic estimation of the parameters $i_1$ , $i_2$ and $n_V$

Several methods have been proposed to adapt dynamically the cycling parameters in time:

- In the first version of the algorithm [Dubois *et al.*, 1990], the truncation order associated with the coarsest resolution level considered for the current cycle,  $N_{i_2}$ , was defined by comparing the kinetic energy of the large and small scales,  $\left| \bar{\mathbf{u}}^{(N_i)} \right|_2$  and  $|\delta \mathbf{u}_{N_i}^N|_2$ , respectively. The finest resolution level truncation order  $N_{i_1}$  was obtained by comparing  $\left| \frac{\partial}{\partial t} \bar{\mathbf{u}}^{(N_i)} \right|_2$  and  $\left| \frac{\partial}{\partial t} \delta \mathbf{u}_{N_i}^N \right|_2$ .
- In a later version [Dubois *et al.*, 1993], the definition of the coarsest level ( $i_2$ ) has been modified and based on the comparison of  $|\delta \mathbf{u}_{N_i}^N|_2$  with the accuracy of the numerical scheme used for time integration.
- While the two first versions use an arbitrary value of the number of V-cycles  $n_V$ , a modification was performed in [Dubois and Temam, 1993] to give an estimate of this parameter using the viscous relaxation time at the finest level  $i_1$ .
- In [Debussche *et al.*, 1995], the truncation order at the coarsest level,  $N_{i_2}$ , is defined by comparing the enstrophy contained at large and small scales, *i.e.*  $\left\| \bar{\mathbf{u}}^{(N_i)} \right\|$  and  $\|\delta \mathbf{u}_{N_i}^N\|$ , respectively. The finest level was defined by comparison of the large and small scales kinetic energy,  $\left| \bar{\mathbf{u}}^{(N_i)} \right|_2$  and  $|\delta \mathbf{u}_{N_i}^N|_2$ .

Thanks to these possible methods, some 2D simulations were conducted (simple analytical flows and 2D isotropic turbulence were considered). In order to perform three-dimensional computations (homogeneous isotropic turbulence), Dubois and coworkers derive in [Dubois *et al.*, 1998] and [Dubois and Jauberteau, 1998] an improved version of the algorithm, in which the determination of the cycling parameters is based on the control of the errors due to the quasi-static approximation.

In [Dubois *et al.*, 1998], some useful error estimates were provided. Let us consider one cycle of the algorithm, which consists in  $n_V$  V-cycles between the two levels  $i_1$  and  $i_2$ , during a time interval  $[t_1, t_2]$ , with  $t_2 = t_1 + 2(i_2 - i_1)n_V \Delta t$ , where  $t_1$  is time at the beginning of the cycle and  $\Delta t$  denotes the timestep.

At every level  $i \in [i_1, i_2]$ , the error induced on the large scales  $\bar{\mathbf{u}}^{(N_i)}$  by the use of the quasi-static approximation of the non-linear interaction terms (I) and (II) is shown to be smaller than  $\epsilon_1$ :

$$\epsilon_1 = 2(i_2 - i_1)n_V \Delta t^2 \max_{t \in [t_1; t_2]} \left| \frac{\partial}{\partial t} P_{N_i} B_{int} \left( \bar{\mathbf{u}}^{(N_i)}(t), \delta \mathbf{u}_{N_i}^{N_{i_1}}(t) + \delta \mathbf{u}_{N_{i_1}}^{N_0}(t) \right) \right|_2. \quad (6.44)$$

The error done on the intermediate scales  $\delta \mathbf{u}_{N_i}^{N_{i_1}}$  is smaller than  $\epsilon_2$ :

$$\epsilon_2 = (2(i - i_1) + 1) \Delta t \max_{t \in [t_1; t_2]} \left| \frac{\partial}{\partial t} \left( \delta \mathbf{u}_{N_i}^{N_{i_1}}(t) + \delta \mathbf{u}_{N_{i_1}}^{N_0}(t) \right) \right|_2. \quad (6.45)$$

Finally, the error committed on the small scales  $\delta \mathbf{u}_{N_{i_1}}^{N_0}$  by projection on an approximate inertial manifold is smaller than  $\epsilon_3$ :

$$\epsilon_3 = 2(i_2 - i_1) \Delta t \max_{t \in [t_1; t_2]} \left| \frac{\partial}{\partial t} \delta \mathbf{u}_{N_{i_1}}^{N_0}(t) \right|_2. \quad (6.46)$$

It can be remarked that error terms  $\epsilon_2$  and  $\epsilon_3$  are of first order in time. The maximum errors done on the large and intermediate scales,  $\epsilon_1$  and  $\epsilon_2$ , are shown to decrease as  $i$  decreases, *i.e.* the error decreases for finer levels.

On the basis of these estimates, the authors propose the following dynamic procedure to estimate the parameters  $i_1$ ,  $i_2$  and  $n_V$ :

- (1) The maximum targeted error on kinetic energy is evaluated as  $\epsilon_k = \epsilon_r \left| \bar{\mathbf{u}}^{(N)} \right|_2$ , where  $\epsilon_r$  denotes a non-dimensional parameter associated to the relative error on kinetic energy.
- (2) The coarser resolution level  $i_2$  is chosen to be the coarsest level  $i \in [1, M]$  such that it minimizes the error on the scales associated with  $\delta \mathbf{u}_{N_i}^{N_{i_2}}$ , kept frozen during on timestep:

$$\frac{\epsilon_k}{\left| \frac{\partial}{\partial t} \delta \mathbf{u}_{N_i}^N \right|_2} \geq Tol_2 \Delta t \quad (6.47)$$

where  $Tol_2$  is a user-defined tolerance parameter<sup>11</sup>.

<sup>11</sup>In their studies, the authors recommend to use some values of the order of unity for  $Tol_2$ . In practice, they use  $Tol_2 \simeq 1$  or 2.

- (3) The finest resolution level  $i_1$  is then chosen to be the finest level  $i \in [1, i_2 - 2]$  (at least three levels are considered in one cycle) such that the error on the small scales is minimal, *i.e.* such that, according to (6.46):

$$\frac{\epsilon_k}{\left| \frac{\partial}{\partial t} \delta \mathbf{u}_{N_i}^N \right|_2} \geq 2(i_2 - i) Tol_1 \Delta t \quad (6.48)$$

where  $Tol_1$  is another tolerance parameter ( $\simeq 1$  or  $2$ ). This condition accounts for the fact that at level  $i_1$ , the small scales are kept frozen during  $2(i_2 - i_1)$  timesteps.

- (4) The coarse resolution level  $i_2$  is modified if necessary, in order to consider only a (user-defined) maximum number of resolution levels during the cycle:

$$i_2 = \max(i_2, i_1 + \Delta_{level}) \quad (6.49)$$

where  $\Delta_{level}$  is in practice taken around five.

- (5) The number of V-cycles to be performed in the global cycle is estimated to minimize the error on the largest scales, using (6.44) as:

$$n_V \simeq \frac{\epsilon_k}{2(i_2 - i_1) \Delta t^2 \left| \frac{\partial}{\partial t} P_{N_{i_2}} B_{int} \left( \bar{\mathbf{u}}^{(N_{i_2})}, \delta \mathbf{u}_{N_{i_2}}^N \right) \right|_2}. \quad (6.50)$$

Thanks to this dynamic evaluation of the parameters  $i_1$ ,  $i_2$  and  $n_V$ , the cycling algorithm described in Sec. 6.2.2.4 can then be applied.

Dubois, Jauberteau and Temam applied their approach to the simulation of 2D analytical flows (see for instance [Dubois *et al.*, 1990]). In [Dubois *et al.*, 1993] and [Debussche *et al.*, 1995], the case of 2D isotropic homogeneous turbulence was considered, and then 3D calculations of isotropic homogeneous turbulence were carried out in [Dubois *et al.*, 1998], with a grid resolution varying between  $64^3$  and  $256^3$  in this last case. The extension of the method to the bi-periodic plane channel flow is discussed in [Dubois *et al.*, 1999].

### 6.2.3 Dynamic Global Multilevel LES

This method is a particular case of the global multilevel LES method developed by Terracol *et al.* [Terracol *et al.*, 2001; Terracol *et al.*, 2003] which has already been presented in Sec. 5.4.2, and in which the integration time devoted to the resolved scales at a given level was an arbitrary parameter. In order to increase the efficiency of the method when dealing with strongly

unsteady flows, the authors derived an improved, dynamic version of the algorithm. This temporal self-adaptive procedure has been designed in order to control the time variation of the frozen details at a given level and to ensure that it will remain lower than a given arbitrary threshold when integrating on some coarser levels. This threshold has to be chosen such that the time variation of the details can be considered as negligible. While the original developments were carried out in the case of compressible flows, the incompressible formalism will be presented below. In practice, the threshold parameter  $\epsilon_{max}$  is defined at each resolution level  $n$  as the maximum acceptable value for the relative time variation of the kinetic energy<sup>12</sup> of the small scales associated with the wavenumber range  $[\kappa_{n+1}; \kappa_n]$ .

At the beginning of each V-cycle of the algorithm, the self-adaptive procedure provides an estimation of the number of integration levels, and of the integration time that can be used at each level. It consists of three main steps:

- (1) The time  $T_{QS}$  during which the quasi-static approximation will remain valid at the finest representation level is first estimated :

$$T_{QS} \left\| \frac{\partial}{\partial t} \delta k^{(1)} \right\|_2 / \left\| k^{(1)} \right\|_2 \leq \epsilon_{max} \quad (6.51)$$

where  $\| \cdot \|_2$  is the  $\mathcal{L}_2$ -norm, and  $k^{(n)}$  is the kinetic energy of the resolved field at level  $n$ :

$$k^{(n)} = \frac{1}{2} \bar{\mathbf{u}}^{(n)} \otimes \bar{\mathbf{u}}^{(n)}. \quad (6.52)$$

Finally,  $\delta k^{(n)} = k^{(n)} - k^{(n+1)}$  denotes the kinetic energy associated to the scales in the wavenumber range  $[\kappa_{n+1}; \kappa_n]$ .

The maximum time of validity of the quasi-static approximation at the finest level is obtained from relation (6.51):

$$T_{QS} = \epsilon_{max} \left\| k^{(1)} \right\|_2 / \left\| \frac{\partial}{\partial t} \delta k^{(1)} \right\|_2. \quad (6.53)$$

To compute the time derivative in Eq. (6.53), the authors use a simple backward Euler formula. Given the value of  $T_{QS}$ , the maximum number of levels  $N$  that can be considered is estimated such that at least one time step will be performed at each coarse level (the time step  $\Delta t_n$  at

---

<sup>12</sup>In the compressible case, the total energy (including the pressure contribution) was utilized.

level  $n$  is estimated so that the CFL number is constant at each level). The following relation has therefore to be satisfied:

$$\sum_{l=2}^N \Delta t_l \leq T_{QS}. \tag{6.54}$$

Assuming a constant aspect ratio  $r$  in each space direction for two successive grid levels, the time step at each level  $n \geq 2$  is  $\Delta t_n = r^{n-2} \Delta t_2$ . This yields:

$$\sum_{l=2}^N r^{(l-2)} \leq \frac{T_{QS}}{\Delta t_2}. \tag{6.55}$$

This relation finally leads to:

$$r^{(N-1)} \leq (r-1) \frac{T_{QS}}{\Delta t_2} + 1. \tag{6.56}$$

This relation is satisfied by taking the following value for the maximum<sup>13</sup> number of levels  $N$ :

$$N = 1 + \mathcal{I} \left( \frac{\log((r-1)T_{QS}/\Delta t_2 + 1)}{\log(r)} \right) \tag{6.57}$$

where  $\mathcal{I}$  denotes the integer part.

- (2) The second step is then to derive the values of the integration times  $\Delta T_n$  at each level, which may consist in several time steps  $\Delta t_n$ . This is performed in order to ensure the validity of the quasi-static approximation. For any level  $n > 1$ , it is therefore imposed that the time variation of the smallest resolved scales at level  $n - 1$  remains negligible during time integration on levels  $l \geq n$ . This condition is enforced by the following relation:

$$\left( \sum_{l=n}^N \Delta T_l \right) \left\| \frac{\partial}{\partial t} \delta k^{(n-1)} \right\|_2 / \left\| k^{(n-1)} \right\|_2 \leq \epsilon_{max}. \tag{6.58}$$

---

<sup>13</sup>As highlighted by the authors, in practice it is necessary to limit the value of  $N$  to avoid the use of too coarse grids on which it would not look realistic to perform a numerical simulation.

This relation leads to the definition of the following upper triangular system with unknowns  $\Delta T_n, n = 2..N$ :

$$\left( \sum_{l=n}^N \Delta T_l \right) = \epsilon_{max} \left\| k^{(n-1)} \right\|_2 / \left\| \frac{\partial}{\partial t} \delta k^{(n-1)} \right\|_2, \quad n = 2..N. \quad (6.59)$$

This system can be solved in a trivial way. However, it is not ensured that all the values of the integration times obtained with this procedure are positive.

The following procedure was then proposed by the authors to avoid negative values of the integration times to be obtained: the system (6.59) is first solved recursively from  $n = N$  to  $n = 2$ . If at a given level  $l$  a negative value of  $\Delta T_l$  occurs, then the integration time at the coarsest grid level  $N$  is reduced by one time step:  $\Delta T_N \leftarrow \Delta T_N - \Delta t_N$ . If the resulting value of  $\Delta T_N$  is negative, then the maximum number of levels is also reduced:  $N \leftarrow N - 1$ . The resolution process is then started again from level  $N - 1$  to level 2. At the end of this resolution process, the values of  $\Delta T_n, n = 2..N$  are finally not necessary some solutions of the system (6.59), but the inequality (6.58) is satisfied, with strictly positive values for the integration time at each level.

- (3) Finally, the number of time steps to be performed at each level is simply computed as:

$$N_{it}^{(n)} = \mathcal{I} \left( \frac{\Delta T_n}{\Delta t_n} \right). \quad (6.60)$$

If the value obtained at a given level  $n$  is equal to zero, it is reseted to one, and the time step at this level is then set to  $\Delta T_n$ .

The only arbitrary parameter involved in the method is the threshold  $\epsilon_{max}$ . Numerical experiments show that the influence of this parameter is quite large. Typical alues for this parameter range from  $10^{-5}$  to  $10^{-2}$ ,  $\epsilon_{max} = 10^{-3}$  yielding satisfactory results in almost all considered flows.

As an illustration, Figs. 6.4 and 6.5 display results obtained in a plane channel flow, for a value of the skin-friction Reynolds number of  $Re_\tau = 590$ . For the multilevel simulations reported here (up to three grid levels were considered), the generalized multilevel model described in Sec. 5.4.2.2 is used on the coarse levels, while the dynamic Smagorinsky model is retained at the finest level. Two values of the threshold parameter  $\epsilon_{max}$  have been considered,  $1 \times 10^{-4}$  and  $5 \times 10^{-4}$ , respectively. The results are compared to the DNS data of Moser *et al.* [Moser *et al.*, 1999], to some fine monolevel

LES results obtained with the dynamic Smagorinsky model, and to those obtained with a three-level simulation using an imposed integration time of one time step at each level ( $\Delta T_n = \Delta t_n$ ). It is observed that the use of the dynamic cycling strategy leads to some result which are in very good agreement with fine monolevel results. As was also highlighted by the authors, the results are in this case better than those obtained with the imposed cycling procedure, while a higher saving in CPU time<sup>14</sup> is obtained with  $\epsilon_{max} = 5 \times 10^{-4}$ , thus indicating a better repartition of the integration times at each level.

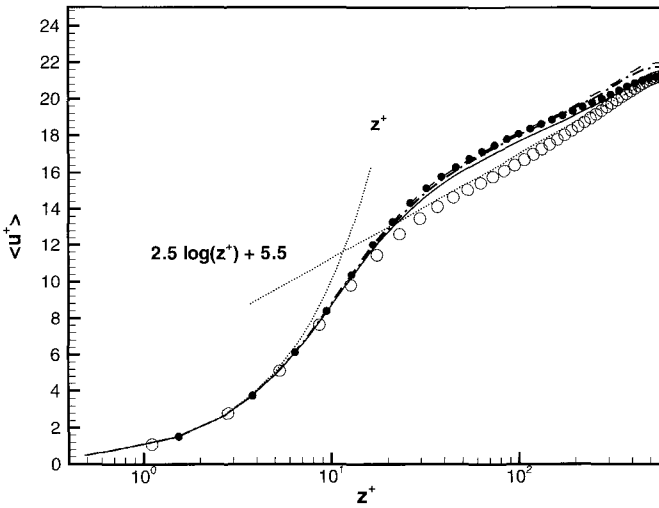


Fig. 6.4 Mean streamwise velocity profiles for the plane channel flow simulations at  $Re_\tau = 590$ . Open circles: DNS (Moser *et al.*, 1999); Filled circles: fine monolevel LES (dynamic Smagorinsky model); Dashed line: three-level simulation with  $\Delta T_n = \Delta t_n$ ; Solid line: two-level simulation with  $\epsilon_{max} = 1 \times 10^{-4}$ ; Dash-dotted line: three-level simulation with  $\epsilon_{max} = 5 \times 10^{-4}$ . From [Terracol, Sagaut and Basdevant, 2003] with permission of Elsevier.

### 6.3 Adaptive Wavelet-based Methods: CVS, SCALES

Adaptive wavelet bases have recently been used to build Navier–Stokes solvers. These methods appear as natural candidates for the design of self-

<sup>14</sup>A CPU gain factor of more than five in comparison with the fine monolevel LES was reported in that case.

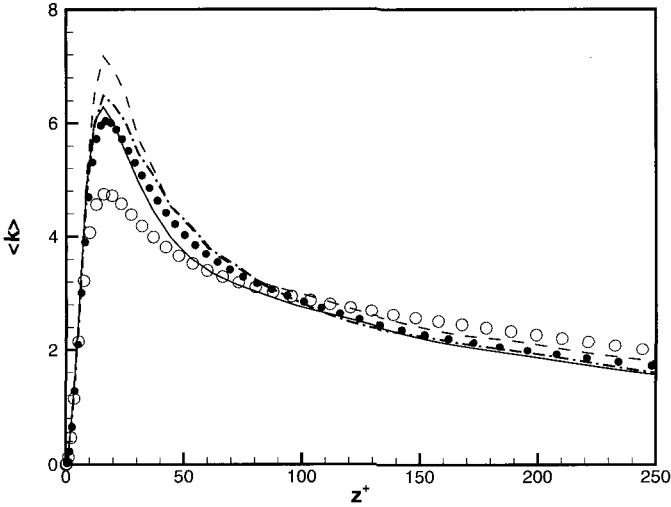


Fig. 6.5 Resolved turbulent kinetic energy profiles for the plane channel flow simulations at  $Re_\tau = 590$ . Open circles: DNS (Moser *et al.*, 1999); Filled circles: fine monolevel LES (dynamic Smagorinsky model); Dashed line: three-level simulation with  $\Delta T_n = \Delta t_n$ ; Solid line: two-level simulation with  $\epsilon_{max} = 1 \times 10^{-4}$ ; Dash-dotted line: three-level simulation with  $\epsilon_{max} = 5 \times 10^{-4}$ . From [Terracol, Sagaut and Basdevant, 2003] with permission of Elsevier.

adaptive multilevel techniques. The most advanced ones for turbulence direct and large eddy simulation are discussed in this section.

### 6.3.1 Wavelet decomposition: brief reminder

Wavelet are basis functions of particular interest within the multiresolution framework, since they are localized in both the physical and wave number spaces. A solution field  $\mathbf{u}$  defined in a  $n$ -dimension space is formally decomposed as

$$\mathbf{u}(\mathbf{x}) = \sum_{l \in L_0} c_l^0 \phi_l^0(\mathbf{x}) + \sum_{j=0}^{+\infty} \sum_{m=1}^{2^n-1} \sum_{k \in \mathcal{K}^{m,j}} d_k^{m,j} \psi_k^{m,j}(\mathbf{x}) \quad (6.61)$$

where  $\phi_l^0(\mathbf{x})$  and  $\psi_k^{m,j}(\mathbf{x})$  are  $n$ -dimensional scaling functions and wavelets of different families (loop over  $m$ ) and levels of resolution (loop over  $j$ ), respectively. Coefficients of the projection are  $c_l^0$  and  $d_k^{m,j}$ , while  $\mathcal{K}^{m,j}$  denotes the set of all degrees of freedom. Scaling function coefficients  $c_l^0$  are

related to the averaged values of  $u$ , while the wavelet coefficients represent the details of the field at different level of resolution. By definition, wavelet functions have a zero mean.

There are several families of wavelets, whose details will not be recalled here. The interested reader is referred to [Mallat, 1997] for an extensive presentation. Let us recall that most advanced results dealing with turbulence simulation have been obtained using second generation wavelets [Sweldens, 1998; Vasilyev and Bowman, 2000], which are well suited to deal with complex geometries and arbitrary boundary conditions.

Considering that the turbulent solution is composed of both coherent and random fluctuations, it is natural to separate them. The wavelet decomposition makes this operation very easy. Following Donoho [Donoho, 1994], the wavelet de-noising procedure consists in setting to zero wavelet coefficient that are below an arbitrary threshold,  $\epsilon$ . This non-linear, solution-dependent procedure is proved to be optimal to eliminate Gaussian white noise. The de-noised or coherent part of  $\mathbf{u}$ , referred to as  $\mathbf{u}_>$ , is expressed as

$$\mathbf{u}_>(\mathbf{x}) = \sum_{l \in L_0} c_l^0 \phi_l^0(\mathbf{x}) + \sum_{j=0}^{+\infty} \sum_{m=1}^{2^n-1} \sum_{\substack{k \in \mathcal{K}^{m,j} \\ |d_k^{m,j}| > \epsilon}} d_k^{m,j} \psi_k^{m,j}(\mathbf{x}). \quad (6.62)$$

The incoherent part is of course defined as  $\mathbf{u}_< \equiv (\mathbf{u} - \mathbf{u}_>)$ . This coherent/incoherent splitting of the solution does not a priori correspond to the classical decomposition between large and small scales, since coherent (resp. incoherent) motion is observed at all scales. This fact is illustrated in Fig. 6.6 which displays the turbulent kinetic energy spectra of the velocity fields associated to different wavelet levels.

An interesting property is that each scaling function coefficient and each wavelet coefficient is uniquely associated with a single grid point (indices  $l$  and  $k$ ). As a consequence, the wavelet thresholding operation is equivalent to selecting “active” grid nodes for the simulation.

Discarding small scales has several consequences: it is proved to violate the divergence-free constraint on the velocity field, and it yields a reconstruction error which varies linearly with respect to the threshold  $\epsilon$  for sufficiently smooth field:

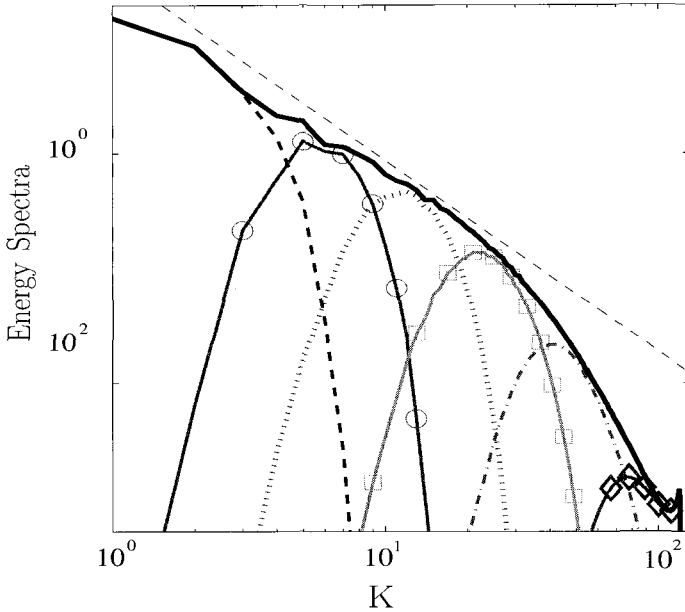


Fig. 6.6 Turbulent kinetic energy spectra of velocity field in isotropic turbulence (computed on a  $256^3$  grid). Solid line: full energy spectrum. dashed line without symbol: energy spectrum of the velocity field at wavelet level 1; solid line with circle: level 2; dotted line without symbol: level 3; solid line with squares: Level 4; dash-dot line: Level 5; solid line with diamonds: Level 6. From [Goldstein and Vasilyev, 2004] with permission of American Institute of Physics.

$$\|\mathbf{u} - \mathbf{u}_>\| \leq C\epsilon \quad (6.63)$$

where  $C$  is a constant of order unity.

### 6.3.2 Coherency diagram of a turbulent field

#### 6.3.2.1 Introduction to the coherency diagram

We now address the way the wavelet decomposition can be used to obtain a significant gain in terms of computational effort. As mentioned above, basic wavelet de-noising aims at separating coherent and incoherent motion, without any direct link with scale separation. Crossing wavelet thresholding and scale separation Vasilyev and coworkers [Goldstein and Vasilyev, 2004; De Stefano, Goldstein and Vasilyev, 2005; Goldstein, 2004] introduced the

Coherency Diagram of turbulent field, which is displayed in Fig. 6.7. It illustrates the fact that all possibilities arise in a turbulent field: coherent/incoherent motion occurs at resolved/unresolved scales.

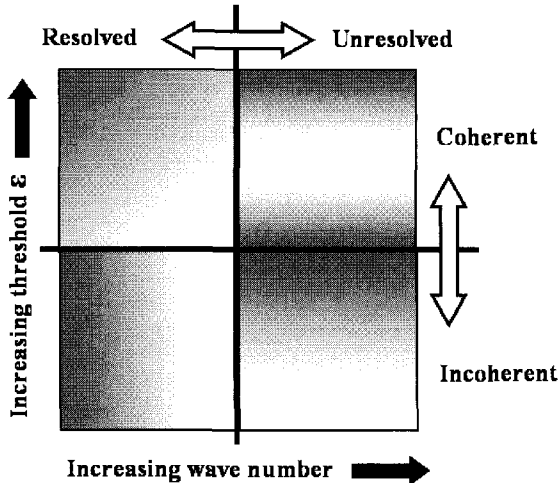


Fig. 6.7 Coherency diagram of a turbulent flow, showing the double decomposition according to the scale (as in usual Large-eddy Simulation) and the coherency (as interpreted from the wavelet threshold).

Usual simulation techniques are illustrated in Fig. 6.8, and are not sensitive to the coherent/incoherent character of the fluctuations, since both parts are simulated.

Let us now discuss some observed properties of the removed field using the wavelet thresholding.

- (1) Setting  $\epsilon = 0$  leads to a static wavelet basis, in which all degrees of freedom are kept active, leading to a full cost direct numerical simulation. Since all degrees of freedom are used, all scales are resolved, and the closure issue is not relevant.
- (2) Setting the threshold to an “optimal” value  $\epsilon = \epsilon_{\text{opt}}$  (discussed in Sec. 6.3.2.2) leads to an almost perfect split of the solution between the coherent motion and its Gaussian noise component. Unresolved motion is nearly purely Gaussian. The closure problem will consist in modeling the interactions between the resolved scales and a background white noise.

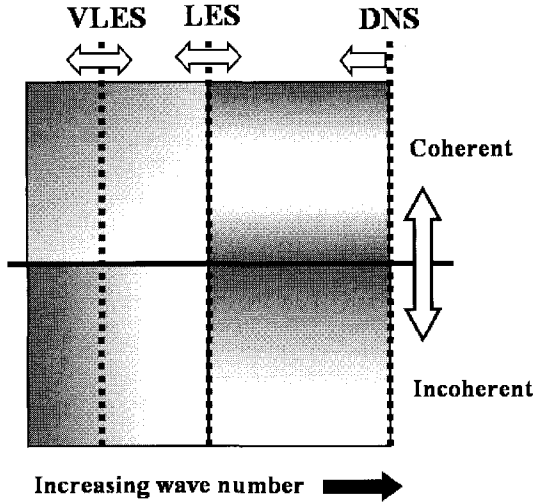


Fig. 6.8 Coherency diagram of usual simulation techniques which do not account for the coherency. All scales are considered, even if they correspond to incoherent, nearly Gaussian motion.

(3) Setting  $\epsilon > \epsilon_{opt}$  yields a higher cost reduction since more wavelet coefficients are discarded, but the unresolved motion now includes a part of the coherent motion, in the sense that it is not a pure white noise anymore. The closure problem is a priori different from the previous one, since the nature of the unresolved motion has changed.

On the grounds of these considerations, several types of simulations can be distinguished, which are listed in Table 6.1. Corresponding coherency diagrams are displayed in Fig. 6.9. Pure Direct Numerical Simulation will not be discussed, since it does not imply any specific problem.

Table 6.1 Different types of adaptive wavelet-based simulation techniques.

Technique name	threshold value	Section
DNS	$\epsilon = 0$	not discussed
<u>W</u> avelet <u>D</u> NS	$0 < \epsilon \ll \epsilon_{opt}$	6.3.3
<u>C</u> oherent <u>V</u> ortex <u>S</u> imulation	$\epsilon \approx \epsilon_{opt}$	6.3.4
<u>S</u> tochastic <u>C</u> oherent <u>A</u> daptive <u>L</u> arge <u>E</u> ddy <u>S</u> imulation	$\epsilon \gg \epsilon_{opt}$	6.3.5

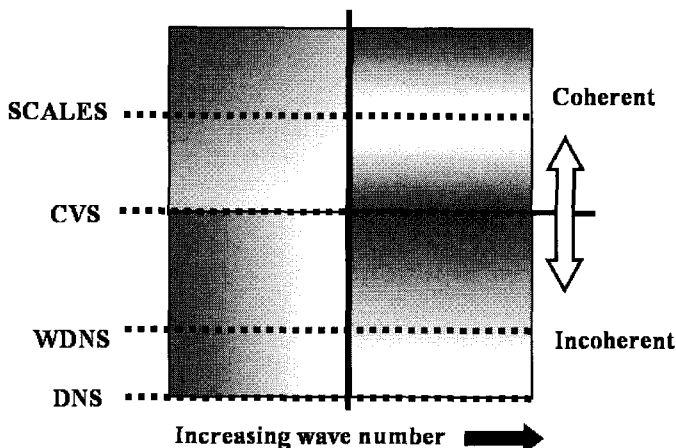


Fig. 6.9 Coherency diagram of adaptive-wavelet based simulation techniques which do not explicitly account for a cutoff wave number.

### 6.3.2.2 Threshold value and error control

The last important point is the evaluation of the optimal threshold  $\epsilon_{\text{opt}}$ . The question is twofold: on which variable should the wavelet decomposition be applied? And what is the thresholding value? Farge and coworkers [Farge, Schneider and Kevlahan, 1999; Farge, Pellegrino and Schneider, 2001; Farge *et al.*, 2003] apply the wavelet decomposition to the vorticity field, and set  $\epsilon_{\text{opt}}$  equal to the variance of the full instantaneous field in isotropic turbulence. This criterion approximates the theoretical criterion which says that the threshold value is equal to the variance of the Gaussian white noise component, which is not known in practical cases. Still considering isotropic turbulence, Vasilyev and coworkers [Goldstein and Vasilyev, 2004; De Stefano, Goldstein and Vasilyev, 2005; Goldstein, 2004] propose to decompose the velocity field and to choose  $\epsilon_{\text{opt}}$  so that the projection error norm  $\text{Err}_{\Pi}(h_r, \lambda) = \|u - u_h\|_{\mathcal{M}}$  will be minimized while guarantying a significant data compression, where  $\|u - u_h\|_{\mathcal{M}}$  is defined as the  $L_{\infty}$ -error scaled by the standard deviation  $\sigma$  between the probability density function (pdf) of the subgrid field and a Gaussian pdf with the same mean variance:

$$\|\mathbf{u} - \mathbf{u}_h\|_{\mathcal{M}} \equiv \sigma \|\text{pdf}(\mathbf{u}_<) - \text{pdf}(\text{Gaussian})\|_{\infty} \quad (6.64)$$

Here,  $\mathbf{u}_h$  is represented by the computed coherent field  $\mathbf{u}_>$  while incoherent part of the (unknown) exact solution is replaced by the ideal random Gaussian noise.

The authors observed using direct numerical simulation data that the optimal value of the threshold yields a 90 % compression when the filter is applied to the vorticity field (*i.e.* only the higher 10 % of the wavelet decomposition coefficients are kept active) and a 99.5 % compression when the velocity field is considered. The difference in the data compression originates in the fact that the vortical events are more coherent than the velocity fluctuations. Therefore, WDNS and DNS methods can be interpreted as dynamic basis methods based on a priori error estimate, the error being defined by Eq. (6.64).

Analyses conducted in [De Stefano, Goldstein and Vasilyev, 2005; Goldstein and Vasilyev, 2004] show that net average effect of unresolved scales on resolved ones in isotropic turbulence is a net drain of energy. This is consistent with the physical picture that the main dynamic mechanism is the forward kinetic energy cascade from large toward small scales, and that the randomness of small scales is higher than that of the large ones. This increasing chaotic character at higher wave numbers was coined by McComb as the *local chaos hypothesis* and used to define a scale separation operator in [Mc Comb, Hunter and Johnston, 2001]. A fine analysis also reveals that the net drain effect is mostly due to coherent unresolved motion, since the mean energetic effect of a Gaussian white noise is theoretically null. But it is important to note that this does not mean that incoherent motion has no energy exchanges with coherent events: it just means that the net balance is zero. This result is the cornerstone of the modelling strategies used in the different simulation techniques presented below. It also enables another interpretation of the WDNS and CVS methods: since the subgrid net energy transfer is zero, the resolved kinetic energy equation in WDNS and CVS is exact. More precisely, the resolution error  $\text{Err}_r(h_r, \lambda)$  associated with the resolved kinetic energy equation is null, the projection error and the discretization being still present. The choice of  $\epsilon_{\text{opt}}$  in WDNS and CVS can therefore be reinterpreted as an *a priori* control on the resolution error on resolved kinetic energy.

Analyzing kinetic energy transfers rather than the pdf of the subgrid field, Vasilyev and coworkers [Goldstein and Vasilyev, 2004; De Stefano,

Goldstein and Vasilyev, 2005; Goldstein, 2004] found that the optimal data compression on the velocity field is 95% (in place of the 99.5 % given above). This lower value is to be preferred to get a more robust control on the error committed on the kinetic energy. The probability density function of the subgrid dissipation in isotropic turbulence computed from SCALES with a 95% compression factor is shown in Fig. 6.10. It is observed that 99.5 % of the total subgrid dissipation is due to 5 % of the subgrid modes, which are the coherent part of the subgrid motion.

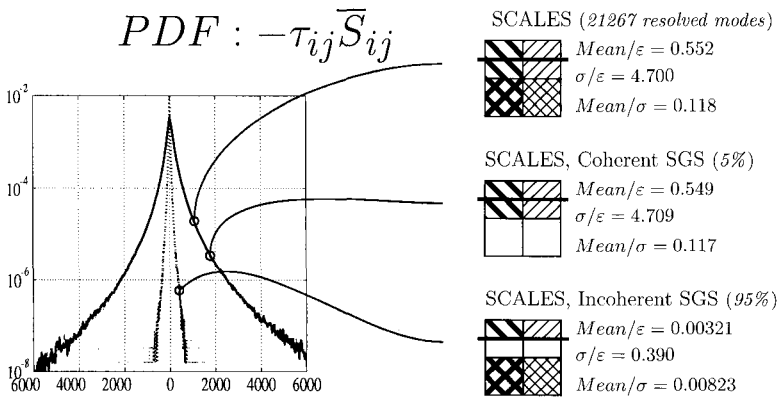


Fig. 6.10 SCALES subgrid scale dissipation in isotropic turbulence: probability density functions of the subgrid dissipation is decomposed into its coherent and incoherent components for a compression factor equal to 95%. From [Goldstein and Vasilyev, 2004] with permission of American Institute of Physics.

### 6.3.3 Adaptive Wavelet based Direct Numerical Simulation

Adaptive wavelet DNS is characterized by a very small threshold value compared with  $\epsilon_{opt}$ . As a consequence, all discarded events are pure white noise and have a zero net mean energy exchange with the resolved modes. As a consequence, unresolved modes are neglected and no model is introduced to account for them. The reconstruction error is assumed to very small. Nevertheless, a significant gain in terms of computational cost with respect with DNS on static grid can be obtained, depending on the flow under consideration.

### 6.3.4 Coherent Vortex Capturing method

The CVS method, proposed by Farge, Schneider and coworkers [Farge, Schneider and Kevlahan, 1999; Farge, Pellegrino and Schneider, 2001; Farge *et al.*, 2003; Schneider *et al.*, 2005], is defined by  $\epsilon = \epsilon_{\text{opt}}$ . Unresolved motion is therefore a random white noise, without mean kinetic exchange with the resolved modes. As in classical large-eddy simulation, it is assumed here that energy transfers are of primary importance to describe intermodal turbulent dynamics, and that interactions which do not lead to a net energy exchange can be neglected. As a consequence, no model is introduced in the CVS method for the unresolved scales. This is illustrated looking at the governing equations for CVS. Using the vorticity transport equation as a starting point

$$\frac{\partial \omega}{\partial t} + \mathbf{u} \cdot \nabla \omega = \omega \cdot \nabla \mathbf{u} + \nu \nabla^2 \omega, \quad \omega = \nabla \times \mathbf{u} \quad (6.65)$$

and applying the wavelet filter discussed above, one obtains the following equation for the coherent vorticity field

$$\frac{\partial \omega_{>}}{\partial t} + \mathbf{u}_{>} \cdot \nabla \omega_{>} = \omega_{>} \cdot \nabla \mathbf{u}_{>} + \nu \nabla^2 \omega_{>} + \tau_{\text{CVS}} \quad (6.66)$$

where the pseudo subgrid forcing term is defined as

$$\tau_{\text{CVS}} = (\mathbf{u}_{>} \cdot \nabla \omega_{>} - (\mathbf{u} \cdot \nabla \omega)_{>}) + ((\omega \cdot \nabla \mathbf{u})_{>} - \omega_{>} \cdot \nabla \mathbf{u}_{>}). \quad (6.67)$$

The governing equations of the CVS method are obtained neglecting  $\tau_{\text{CVS}}$  in Eq. (6.66). Efficiency and accuracy of the CVS approach is assessed comparing it to the traditional Direct Numerical Simulation approach. Such a comparison is provided in Fig. 6.11 which displays a comparison between the instantaneous vorticity fields in a plane mixing layer flow. The fields are observed to be quasi-identical, showing the the basic assumption dealing with the possibility to neglect the subgrid term if the wavelet threshold is carefully chosen is correct.

An important point which must be reminded is that the wavelet thresholding technique and the usual LES low-pass filter yield very different resolved and subgrid fields. This difference is illustrated in Fig. 6.12, which presents the resolved and unresolved fields for LES and CVS in isotropic turbulence. It is observed that, in the CVS approach, the resolved field

contains (as expected) almost all coherent structures, while the subgrid motion is still coherent in the usual LES case.

### 6.3.5 Stochastic Coherent Adaptive Large Eddy Simulation

The last method discussed in this section is the SCALES method [Goldstein and Vasilyev, 2004; De Stefano, Goldstein and Vasilyev, 2005; Goldstein, 2004; Goldstein, Vasilyev and Kevlahan, 2004; Goldstein, Vasilyev and Kevlahan, 2005], in which the threshold factor is taken larger than  $\epsilon_{\text{opt}}$ . As mentioned above, the net energy exchange is significant since some coherent modes are filtered out and a model for the unresolved scales is now required to recover satisfactory results.

The governing equations for the SCALES method are

$$\frac{\partial \bar{\mathbf{u}}^{>\epsilon}}{\partial t} + \nabla \cdot (\bar{\mathbf{u}}^{>\epsilon} \otimes \bar{\mathbf{u}}^{>\epsilon}) = -\nabla \bar{p}^{>\epsilon} + \nu \nabla^2 \bar{\mathbf{u}}^{>\epsilon} - \nabla \cdot \bar{\boldsymbol{\tau}}^{>\epsilon} \quad (6.68)$$

where  $\bar{\phi}^{>\epsilon}$  denotes the resolved part of the dummy variable  $\phi$  for the selected value of the threshold  $\epsilon$ . The subgrid stress tensor is defined as

$$\bar{\boldsymbol{\tau}}^{>\epsilon} \equiv \overline{\mathbf{u} \otimes \mathbf{u}}^{>\epsilon} - \bar{\mathbf{u}}^{>\epsilon} \otimes \bar{\mathbf{u}}^{>\epsilon} \quad (6.69)$$

and is formally similar to the usual subgrid tensor, the scale separation operator being replaced by the wavelet filtering operator.

Since the emphasis is put on the resolved kinetic energy balance, it is proposed in [Goldstein, 2004] to use a functional model defined as a generalized Smagorinsky model:

$$\bar{\boldsymbol{\tau}}^{>\epsilon} = -2\nu_{\text{scales}} \bar{\mathbf{S}}^{>\epsilon}, \quad \bar{\mathbf{S}}^{>\epsilon} = \frac{1}{2} (\nabla \bar{\mathbf{u}}^{>\epsilon} + \nabla^T \bar{\mathbf{u}}^{>\epsilon}) \quad (6.70)$$

where the eddy viscosity is defined as

$$\nu_{\text{scales}} = C_S \epsilon^2 |\bar{\mathbf{S}}^{>\epsilon}|. \quad (6.71)$$

The quadratic scaling of  $\nu_{\text{scales}}$  with respect to  $\epsilon$  was checked to be correct using DNS data base in isotropic turbulence for a field compression over the range of 78.5 % to 99.95 % in [Goldstein, 2004]. The constant  $C_S$  can be determined empirically or adjusted using a Germano-type dynamic procedure.

The test filter introduced in the usual Germano identity is obtained within the adaptive wavelet framework by considering another wavelet filter with a larger threshold value. Using a twice larger threshold value, the subgrid tensor at the test filter level is

$$\overline{\tau}^{>2\epsilon} = \overline{\overline{\mathbf{u}} \otimes \overline{\mathbf{u}}}^{>\epsilon^{>2\epsilon}} - \overline{\mathbf{u}}^{>\epsilon} \otimes \overline{\mathbf{u}}^{>\epsilon} \tag{6.72}$$

and the Germano identity reads

$$\overline{\tau}^{>2\epsilon} = \overline{\tau}^{>\epsilon^{>2\epsilon}} + \underbrace{\left( \overline{\overline{\mathbf{u}} \otimes \overline{\mathbf{u}}}^{>\epsilon^{>2\epsilon}} - \overline{\mathbf{u}}^{>\epsilon} \otimes \overline{\mathbf{u}}^{>\epsilon} \right)}_{\mathcal{L}^\epsilon}. \tag{6.73}$$

This expression is straightforwardly deduced from Eq. (4.15), since the Germano identity is a general relation which does not depend upon specific features of the scale separation operator. Using exactly the same procedure as in usual large-eddy simulation, the dynamic constant is evaluated as

$$C_S = \frac{\mathcal{L}_{ij}^\epsilon M_{ij}^\epsilon}{M_{ij}^\epsilon M_{ij}^\epsilon} \tag{6.74}$$

with

$$M^\epsilon = 2\epsilon^2 \overline{|\overline{S}^{>\epsilon}| \overline{|\overline{S}^{>\epsilon^{>2\epsilon}}|} - 2(2\epsilon)^2 \overline{|\overline{S}^{>2\epsilon}| \overline{|\overline{S}^{>2\epsilon}}|. \tag{6.75}$$

As in other implementations, the dynamic procedure must be regularized to prevent numerical problems. All techniques developed within the usual large-eddy simulation framework can be used in a straightforward manner, including the scale-dependent Lagrangian procedure proposed by Meneveau (see Sec. 4.2.3). It is worth noting that almost all subgrid models derived within the traditional scale-separation framework can be extended within this new wavelet-based framework (e.g. [Hoffman, 2002]).

The SCALES approach is illustrated in Fig. 6.13, which displays the results in decaying isotropic turbulence at a Taylor-scale-based Reynolds number equal to 72 with a dynamic Smagorinsky model. An excellent agreement with filtered DNS data is observed, assessing the efficiency of the method.

## 6.4 DNS and LES with Optimal AMR

All methods presented above are based on *a priori* error estimates, *i.e.* on models of the error. Since these models are not exact, the robustness and the accuracy of the error control cannot be guaranteed and the efficiency of the method is case-dependent. To obtain a more robust error control, it is necessary to use an *a posteriori* error estimate, which will account for errors really committed during the simulation.

The most mature technique within the DNS/LES framework is certainly the one developed by Hoffman [Hoffman and Johnson, 2004; Hoffman, 2003; Hoffman, 2004a; Hoffman, 2004b; Hoffman, 2005a; Hoffman, 2005b], which will be retained as generic example in this section.

### 6.4.1 Error definition: surfacic versus volumic formulation

Hoffman applies his technique to the computation of the mean aerodynamic forced exerted on a solid body. Therefore, the error estimate is directly tied to the goal of the simulation and the grid will be optimized to recover the best prediction of the drag (or the lift). It is important noting that the optimality is intrinsically related with a given error estimate: the best grid for drag computation is *a priori* not the optimal one for heat transfer or aeroacoustic sources predictions.

The usual definition of the mean drag of an immersed solid body with boundary  $\Gamma_0$  over a time interval  $I = [0, T]$  is

$$F(\sigma(\mathbf{u}, p)) \equiv \frac{1}{T} \int_I \int_{\Gamma_0} (\sigma \cdot \mathbf{n}) \cdot \phi \, dS \, dt \quad (6.76)$$

where  $\sigma(\mathbf{u}, p)$ ,  $\mathbf{n}$  and  $\phi$  are respectively the stress tensor, normal outward unit vector to the body surface and the vector along which the aerodynamic force is to be computed. This expression is localized on the solid boundary, and is not well suited for the definition of an optimal control strategy since it permits to compute the drag or the lift but not to track the sources of errors into the flow. It must therefore be replaced by another formulation, which will make it possible to estimate the role of each control cell within the computational domain to the error committed on the aerodynamic forces. Such a formulation must therefore appear as a volumic integral.

Before describing this new formulation, let us emphasize the fact that the very powerful idea used here is that the grid will be refined in regions

of the flow where the error arises, which are not necessarily the places where the error is observed. This point is illustrated considering the plane mixing layer flow, which is known to behave as a *noise amplifier*: due to its mean flow properties, all perturbations are amplified as they are advected downstream (see Fig. 6.14). Therefore, a small error committed at the upstream location A will result in a large error at the downstream location B. A local error estimate at point B will lead to a grid refinement in the vicinity of B, resulting in a small error reduction, while a non-local a posteriori error estimate will make it possible to “kill” the error source by refining the grid around A, leading to a much more significant error reduction.

Multiplying the momentum equation by a test function  $\Phi$  and integrating by part, Hoffman derives the following Galerkin-type formulation for the drag of a surface-mounted obstacle in a channel flow

$$F(\sigma(\mathbf{u}, p)) \equiv \frac{1}{T} \int_I (\langle \dot{\mathbf{u}} + \nabla \cdot (\mathbf{u} \otimes \mathbf{u}), \Phi \rangle + \langle p, \nabla \cdot \Phi \rangle + 2\nu \langle S(\mathbf{u}), S(\Phi) \rangle + \langle \nabla \cdot \mathbf{u}, \Theta \rangle) dt \quad (6.77)$$

where  $\dot{\mathbf{u}} = \frac{\partial \mathbf{u}}{\partial t}$ ,  $S(\mathbf{u}) = \frac{1}{2}(\nabla \mathbf{u} + \nabla^T \mathbf{u})$  and

$$\langle \mathbf{u}, \mathbf{v} \rangle \equiv \int_{\Omega} \mathbf{u}(\mathbf{x}) \mathbf{v}(\mathbf{x}) dV \quad (6.78)$$

where  $\Omega$  denotes the full computational domain occupied by the fluid. The function  $\Phi$  extends the function  $\phi$  and is defined in the whole domain  $\Omega$ , and  $\Theta$  is another test function introduced to get an accurate control on the incompressibility constraint. It must be noted that, for the sake of simplicity, boundary terms arising from solid boundaries of the channel have been neglected. This is achieved taking  $\Phi = \mathbf{0}$  on these boundaries. The relation (6.77) is written using the exact solution field  $(\mathbf{u}, p)$ . Now considering the discrete computed solution  $(\mathbf{u}_h, p_h)$ , one obtains the following formula for the drag prediction

$$F_h(\sigma(\mathbf{u}_h, p_h)) \equiv \frac{1}{T} \int_I (\langle \dot{\mathbf{u}}_h + \nabla \cdot (\mathbf{u}_h \otimes \mathbf{u}_h), \Phi \rangle + \langle p_h, \nabla \cdot \Phi \rangle + 2\nu \langle S(\mathbf{u}_h), S(\Phi) \rangle + \langle \nabla \cdot \mathbf{u}_h, \Theta \rangle + \text{SGS}(h, \mathbf{u}_h, p_h, \Phi, \Theta)) dt \quad (6.79)$$

where the additional term  $\text{SGS}(h, \mathbf{u}_h, p_h, \Phi, \Theta)$  accounts for the contribution of the subgrid model, if any.<sup>15</sup> The volumic error of drag (or lift, depending on the definition of  $\phi$ ) to be minimized will therefore be defined as

$$\text{Err}(h_r, \lambda) = |F(\sigma(\mathbf{u}, p)) - F_h(\sigma(\mathbf{u}_h, p_h))|. \quad (6.80)$$

### 6.4.2 *A posteriori error estimation and optimization loop*

The next step of the method consists in deriving an *a posteriori* estimate from Eq. (6.80). Since the exact solution  $(u, p)$  is not available, another formulation must be found. This is done introducing the following linearized dual problem, whose solution is  $(\phi, \theta)$ :

$$-\frac{\partial \phi}{\partial t} - \mathbf{u} \cdot \nabla \phi = \nabla \theta + \nu \nabla^2 \phi - \nabla \mathbf{u}_h \cdot \phi \quad (6.81)$$

$$\nabla \cdot \phi = 0. \quad (6.82)$$

This linear problem is a convection-diffusion-reaction problem where the convection by the exact velocity field  $\mathbf{u}$  acts backward in time. The approximated discrete computed solution is noted  $(\phi_h, \theta_h)$ . It is obtained in practice replacing  $\mathbf{u}$  by its computed approximation  $\mathbf{u}_h$  and solving the resulting equation. After some algebraic manipulations, one obtains the following new expression for the drag error:

$$|F(\sigma(\mathbf{u}, p)) - F_h(\sigma(\mathbf{u}_h, p_h))| = \left| \sum_{i=1, N} \text{Err}_h(i) + \sum_{i=1, N} \text{Err}_r(i) \right| \quad (6.83)$$

where  $N$  is the number of cell in the computational domain. The control-cell localized discretization error  $\text{Err}_h(i)$  and resolution error  $\text{Err}_r(i)$  are defined within the  $i$ th cell as

---

<sup>15</sup>It is worth noting that if the Implicit LES approach is used, this term is related to a specific part of the numerical error tied to a dissipative/regularizing operator such as an artificial viscosity term.

$$\begin{aligned} \text{Err}_h(i) = & \frac{1}{T} \int_I (\langle \dot{\mathbf{u}}_h + \nabla \cdot (\mathbf{u}_h \otimes \mathbf{u}_h), (\phi_h - \Phi) \rangle_i + \langle p_h, \nabla \cdot (\phi_h - \Phi) \rangle_i \\ & + 2\nu \langle S(\mathbf{u}_h), S(\phi_h - \Phi) \rangle + \langle \nabla \cdot \mathbf{u}_h, (\theta_h - \Theta) \rangle_i) dt \end{aligned} \quad (6.84)$$

$$\text{Err}_r(i) = \frac{1}{T} \int_I \text{SGS}(h, \mathbf{u}_h, p_h, \Phi, \Theta)_i dt \quad (6.85)$$

where the indice  $i$  denotes operator localized within the computational cell number  $i$ . Equations (6.84) and (6.85) provide a practical estimate for both discretization and modeling error in each cell. A very interesting feature is that this method makes it possible to control them separately. The modelling error can be analyzed more deeply. Recalling that  $\text{SGS}(h, \mathbf{u}_h, p_h, \Phi, \Theta)_i$  is associated to the weak form of the modelled subgrid term  $\mathcal{F}_{\text{LES}}$

$$\text{SGS}(h, \mathbf{u}_h, p_h, \Phi, \Theta)_i = \langle \mathcal{F}_{\text{LES}}, \Phi \rangle_i \quad (6.86)$$

it is seen that taking  $(\Phi, \Theta) = (\phi_h, \theta_h)$  in Eq. (6.85) one obtains an error estimate dealing with the subgrid force (in weak form), while taking  $(\Phi, \Theta) = (\mathbf{u}_h, p_h)$  one recovers an estimation on the error on the kinetic energy dissipation. These two choices obviously lead to different control strategies.

Further refining the definition of  $\text{SGS}(h, \mathbf{u}_h, p_h, \Phi, \Theta)_i$  also makes it possible to change the interpretation of the control problem. In the derivation of the error term given above, the target solution is the drag associated with the exact, full turbulent solution  $\mathbf{u}$ , which includes all scales since no turbulence model contribution appears in the exact drag definitions given by Eqs. (6.76) and (6.77). The optimal AMR algorithm will therefore converge toward the DNS solution, and the projection error  $\text{Err}_\Pi$  is also decreased. It is possible to change the target solution and to define it as the ideal filtered solution, *i.e.* as the LES solution with an exact subgrid model. This is done redefining  $\text{SGS}(h, \mathbf{u}_h, p_h, \Phi, \Theta)_i$  as follows:

$$\begin{aligned} \text{SGS}(h, \mathbf{u}_h, p_h, \Phi, \Theta)_i &= \langle \nabla \cdot \tau_{\text{LES}} - \mathcal{F}_{\text{LES}}, \Phi \rangle_i \\ &= \langle \tau_{\text{LES}}, S(\Phi) \rangle_i - \langle \mathcal{F}_{\text{LES}}, \Phi \rangle_i \end{aligned} \quad (6.87)$$

where boundary terms have been neglected and  $\tau_{LES}$  is the *exact* subgrid tensor. This quantity is not available in practice, and Hoffman uses a subgrid model with very high correlation coefficient with the true subgrid tensor in place of it. In this case, the projection error is neither taken into account and will nor be reduced.

The Optimal Adaptive Mesh Refinement DNS/LES algorithm can be written as follows

- (1) Solve Navier–Stokes equation (primal problem) in  $\Omega$  over the time interval  $I$  and store the unsteady solution  $(\mathbf{u}_h, p_h)$  over this interval.
- (2) Solve the linear dual problem (6.81) over  $\Omega \times I$  using the stored values of  $(\mathbf{u}_h, p_h)$  to get  $(\phi_h, \theta_h)$ . Compute the errors  $Err_h(i)$  and  $Err_r(i)$  on the fly.
- (3) If  $|\sum_{i=1,N} Err_h(i) + \sum_{i=1,N} Err_r(i)| \leq \epsilon$ , where  $\epsilon$  is an arbitrary error threshold, then stop. Else:
- (4) Refine the grid in a fraction of cell with largest  $Err_h(i) + Err_r(i)$  and go to (1).

### 6.4.3 Numerical results

Hoffman's optimal AMR-LES technique is illustrated considering the incompressible flow around a cylinder at a cylinder-diameter-based Reynolds number equal to 3900. The simulation is carried out following the Implicit Large-Eddy Simulation technique using a stabilized finite element method, in which the stabilization term plays the role of the subgrid model. The topology of the flow is illustrated in Fig. 6.15 which displays the instantaneous positive streamwise vorticity isosurfaces. The three-dimensional character of the turbulent flow is remarked. The final adapted grid for cylinder drag computation is displayed in Fig. 6.16. It is worth noting that the grid is not refined homogeneously within the boundary layer at the cylinder surface, showing that the optimal grid may be very different from usual computational grids on this configuration. The effect of the grid refinement on the computed drag coefficient is shown in Fig. 6.17. It is observed that a converged value is reached after a few grid optimization steps. The evolution of both error components as function of grid evolution is plotted in Fig. 6.18. It is worth noting that the discretization error overwhelms the modelling error after the second grid refinement step.

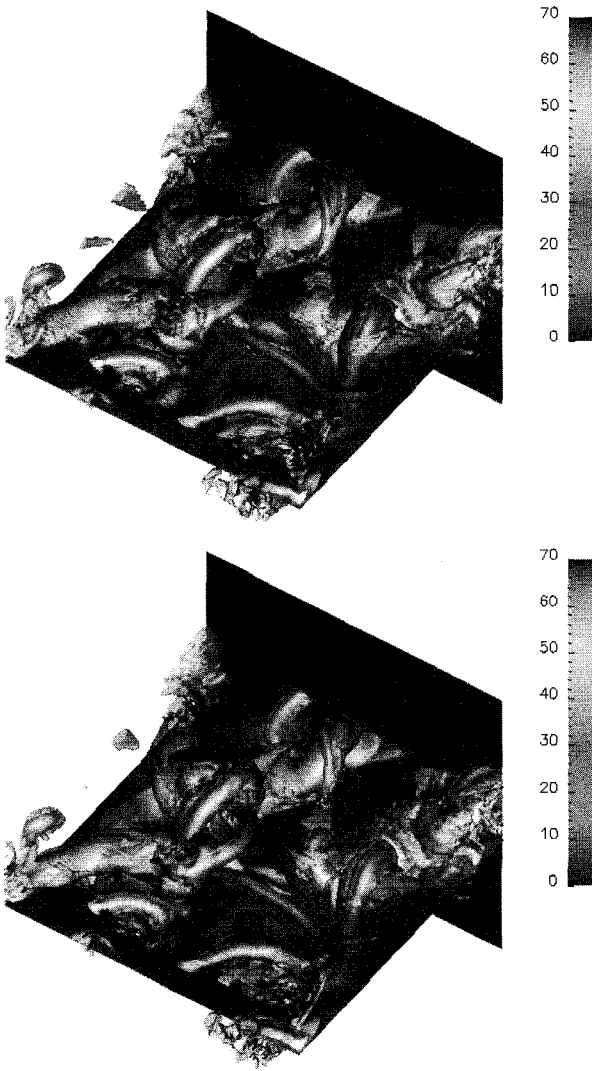


Fig. 6.11 Comparison between DNS (top) and CVS (bottom). Iso-surfaces of the vorticity modulus colored by the spanwise vorticity at  $t = 18 \frac{\delta^0}{\Delta U}$ . From [Schneider *et al.*, 2005] with permission of Cambridge University Press.

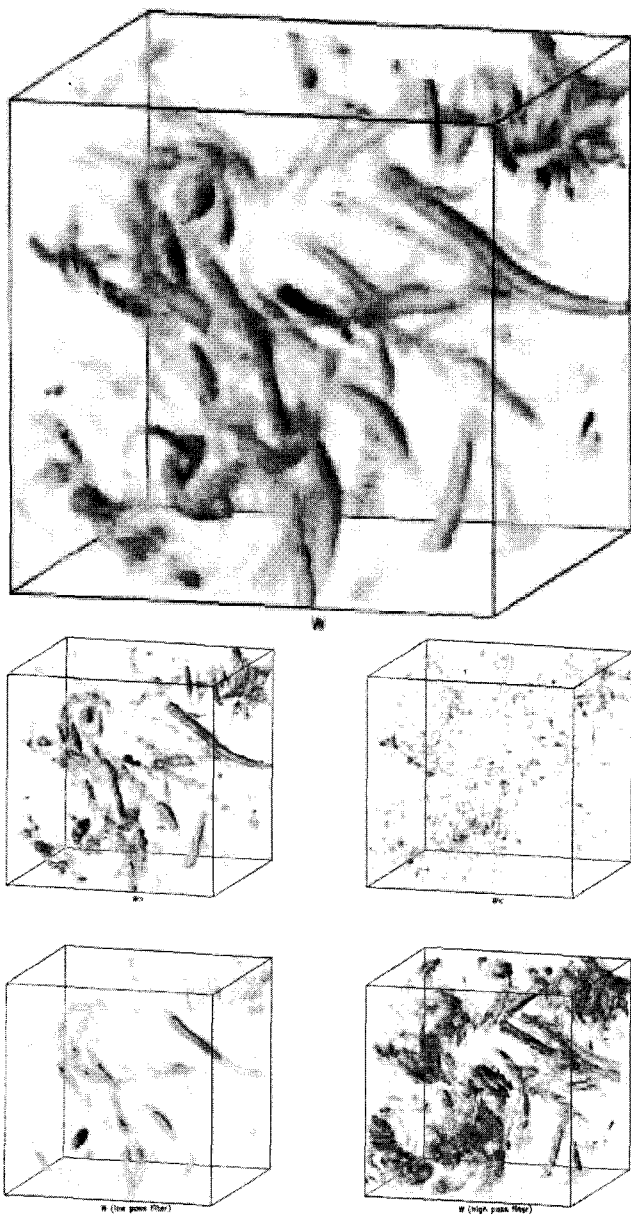


Fig. 6.12 Resolved/unresolved field decomposition in isotropic turbulence. Top: full instantaneous field. Bottom: left: resolved field, right: unresolved field, top: CVS, bottom: LES. From [Farge et al., 2003] with permission of American Institute of Physics.

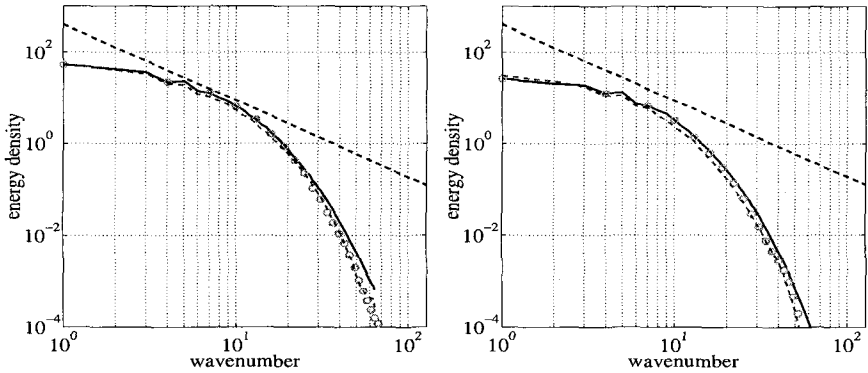


Fig. 6.13 Energy spectra in decaying isotropic turbulence for SCALES with dynamic Smagorinsky model (dashed line) at time  $t=0.08$  (left) and  $t=0.16$  (right). For comparison the DNS (solid line) and the filtered DNS (circles) are shown. A  $\kappa^{-5/3}$  straight dashed black line is shown to indicate the inertial range. From [Goldstein, Vasilyev and Kevlahan, 2004] with permission of American Institute of Physics.

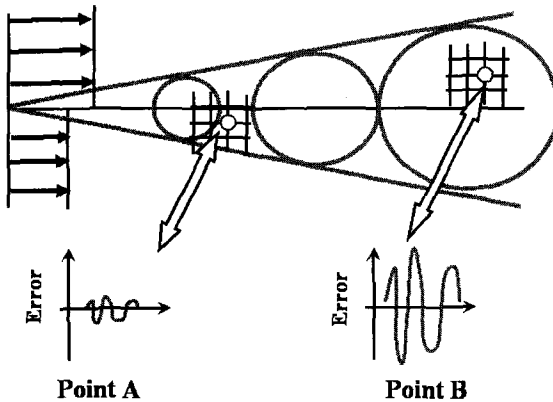


Fig. 6.14 Schematic view of the error growth in a plane mixing layer flow. The error committed at point A is amplified as it is advected downstream toward point B. The computational grid in the vicinity of A and B is illustrated.

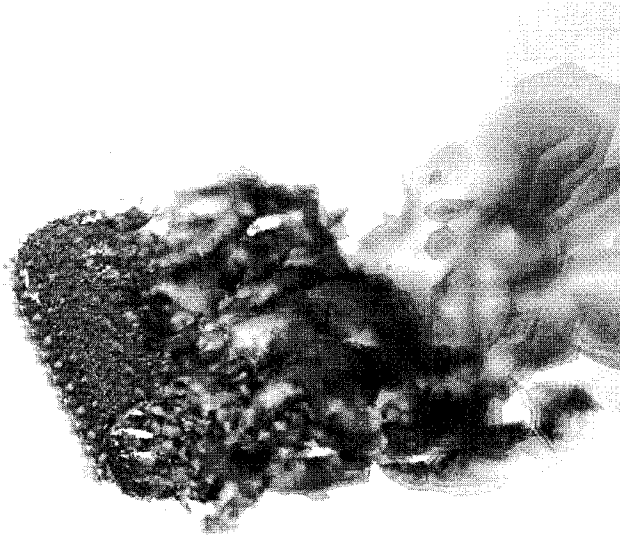


Fig. 6.15 Large-eddy simulation of the flow around a circular cylinder using an optimal AMR technique: instantaneous positive streamwise vorticity surface. Courtesy of J. Hoffman, Chalmers University, Sweden.

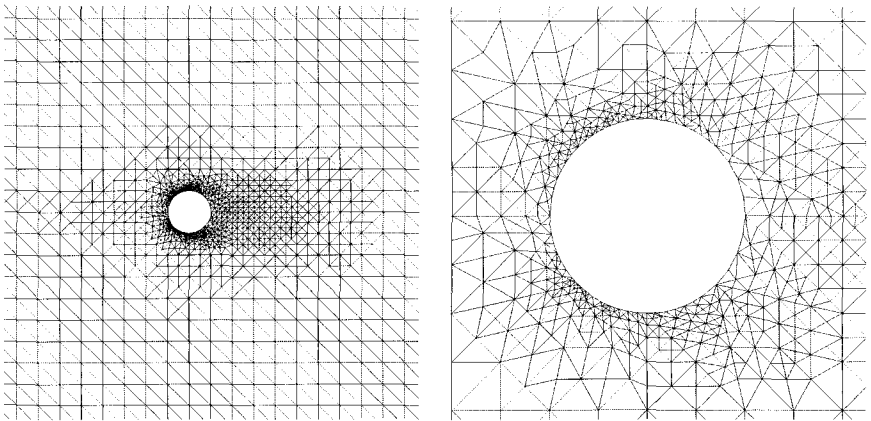


Fig. 6.16 Large-eddy simulation of the flow around a circular cylinder using an optimal AMR technique: views of the final optimized grid. Courtesy of J. Hoffman, Chalmers University, Sweden.

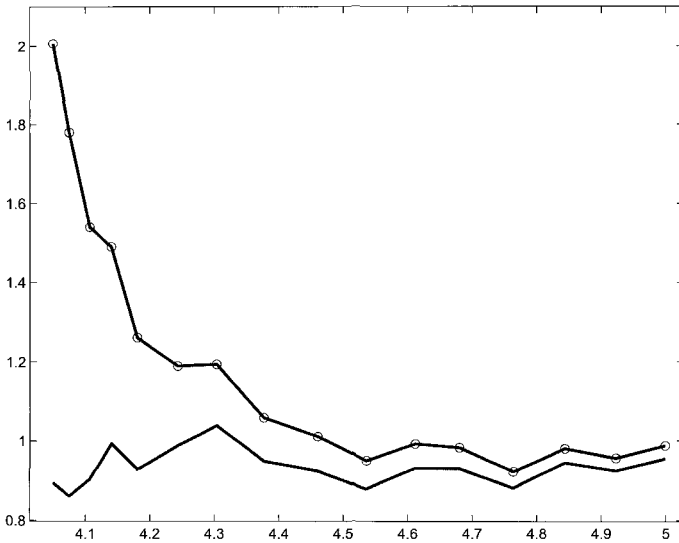


Fig. 6.17 Large-eddy simulation of the flow around a circular cylinder using an optimal AMR technique: drag coefficient as a function of the number of mesh points ( $\log_{10}$ ). Two different ways to compute the drag are considered: with (no symbol) or without (symbol) the contribution from the stabilization term coming from the finite element method. It is observed that the converged values of the drag are the same, but that the first estimation yields better predictions on coarse grids. Courtesy of J. Hoffman, Chalmers University, Sweden.

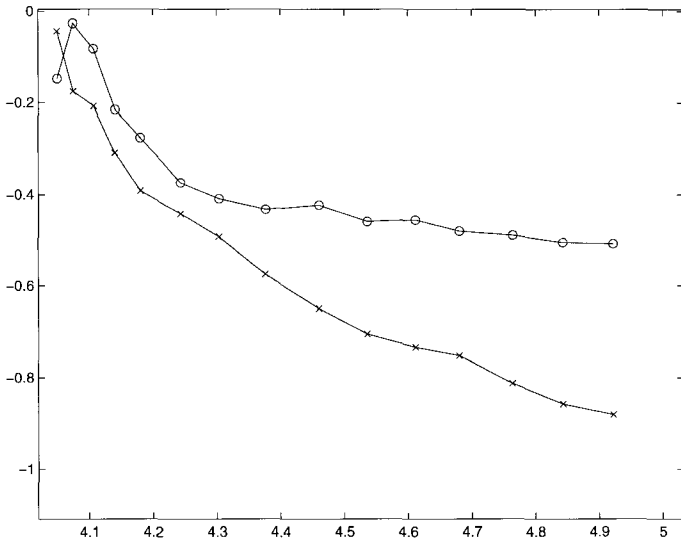


Fig. 6.18 Large-eddy simulation of the flow around a circular cylinder using an optimal AMR technique: error estimates on the drag coefficient as function of the number of grid points ( $\log_{10}$ ). Crosses: modeling/stabilization error; Circles: discretization error. Courtesy of J. Hoffman, Chalmers University, Sweden.

This page is intentionally left blank

## Chapter 7

# Global Hybrid RANS/LES Methods

This chapter is devoted to hybrid strategies that merge RANS and LES approaches. Non-zonal approaches like “universal methods” - which are able to switch automatically from one method to the other one result in a change in terms of frequency and wave numbers resolutions - are fully discussed in the following sections.

### 7.1 Bridging between Hybrid RANS/LES Methods and Multiscale Methods

All hybrid RANS/LES methods described below are fundamentally defined as a merging between a RANS-type eddy-viscosity model and a LES-type subgrid viscosity model. We analyze here this approach with the purpose of identifying the scale-separation operator associated with these hybrid methods, and we show that they can be recast within the framework of multiscale models.

#### 7.1.1 *Concept: the effective filter*

Most global hybrid RANS/LES methods are defined in a semi-heuristic way without any reference to a corresponding generalized scale separation operator that will give an explicit definition of both resolved and unresolved scales.

To give a meaningful insight into the hybrid RANS/LES approach, it is necessary to identify the way unresolved scales are filtered out in practical simulations. An important remark is that, in almost all published works, no explicit scale separation operator is applied to the computed solution during the simulation. Therefore, all the information related to the theoretical

scale separation operator (convolution filter, statistical average) is carried by the model used to account for the unresolved scales.

Let us introduce the following non-linear conservation law

$$\frac{\partial \mathbf{u}}{\partial t} + \nabla \cdot F(\mathbf{u}, \mathbf{u}) = 0 \quad (7.1)$$

to discuss the properties of the scale separation operator which are really applied to the exact solution in practical simulations of turbulent flows. Here,  $\mathbf{u}$  is the exact solution and  $F(\cdot, \cdot)$  is a non-linear flux. Let us now consider the governing equations for the large scales (*i.e.* the governing averaged or filtered equations):

$$\frac{\partial \bar{\mathbf{u}}}{\partial t} + \nabla \cdot F(\bar{\mathbf{u}}, \bar{\mathbf{u}}) = \underbrace{\left( F(\bar{\mathbf{u}}, \bar{\mathbf{u}}) - \overline{F(\mathbf{u}, \mathbf{u})} \right)}_{\tau_{\text{true}}} \quad (7.2)$$

where the resolved part of the solution is defined as

$$\bar{\mathbf{u}} = \mathcal{F}(\mathbf{u}) \quad (7.3)$$

with  $\mathcal{F}$  an arbitrary scale separation operator (see Chapter 2). Let us now write the practical problem, *i.e.* the one which is solved on the computer, like follows

$$\frac{\partial \mathbf{u}_h}{\partial t} + \nabla \cdot F(\mathbf{u}_h, \mathbf{u}_h) = \mathcal{M}(\mathbf{u}_h) \quad (7.4)$$

where  $\mathbf{u}_h$  and  $\mathcal{M}$  are the computed solution and the turbulence/subgrid model used, respectively.

The important fact here is that the computed solution,  $\mathbf{u}_h$ , is solution of the theoretical governing equation (7.2) if and only if the model is exact<sup>1</sup>:  $\mathcal{M}(\mathbf{u}_h) = \tau_{\text{true}}$ . Since this condition is never satisfied, one can easily see that

$$\mathbf{u}_h \neq \bar{\mathbf{u}} = \mathcal{F}(\mathbf{u}). \quad (7.5)$$

As a consequence,  $\mathcal{F}$  is not the relevant scale separation operator to define  $\mathbf{u}_h$ .

---

<sup>1</sup>The numerical errors are not taken into account here for the sake of clarity.

Therefore, the problem arises of finding the scale separation operator  $\mathcal{G}$  such that

$$\left( F(\tilde{\mathbf{u}}, \tilde{\mathbf{u}}) - \widetilde{F(\mathbf{u}, \mathbf{u})} \right) = \mathcal{M}(\mathbf{u}_h), \quad \tilde{\mathbf{u}} \equiv \mathcal{G}(\mathbf{u}). \quad (7.6)$$

Since it is the filter really experienced by the computed solution,  $\mathcal{G}$  is referred to as the *effective filter*. Identifying the effective filter is a complex inverse problem, and there is no theoretical evidence that it is well-behaved from a mathematical point of view. Since the effective filter is intrinsically tied to the turbulence model  $\mathcal{M}$  and that practical turbulence models do not perform equally well on different flow families, it is expected that the definition of  $\mathcal{G}$  will be both model- and flow-dependent.

### 7.1.2 Eddy viscosity effective filter

Magnient [Magnient *et al.*, 2001b; Magnient, 2001a] carried out the analysis of the effective filter associated with several subgrid viscosity models in the case of isotropic turbulence in the limit of vanishing molecular viscosity. The strategy adopted here was to identify the transfer function of the effective filter by looking at the resolved energy spectrum. It is worth noting that such a procedure provides us with an approximate evaluation of the effective filter, since it relies on the energy spectrum only. It is possible to develop a similar identification procedure using higher-order statistical moments or probability density functions.

It is first recalled that, in the case where a sharp cutoff filter with cutoff length  $\bar{\Delta}$  is considered, the filtered solution exhibits an inertial range obeying the Kolmogorov -5/3 law for the energy spectrum up to the cutoff wavenumber  $\kappa \equiv \pi/\bar{\Delta}$ :

$$E(\kappa) = K_0 \varepsilon^{2/3} \kappa^{-5/3}. \quad (7.7)$$

This spectrum shape is recovered if the subgrid model is such that the resolved kinetic energy balance is correctly enforced, meaning that both the global amount of energy transfer toward unresolved scales and the scale distribution of this energy drain are enforced in a proper way. This is for example the case when using the Smagorinsky subgrid viscosity model, which is defined as

$$\nu_t = (C_S \bar{\Delta})^2 |\bar{S}| \quad (7.8)$$

where  $C_S$  is an arbitrary constant. The kinetic energy drain experienced by the resolved motion due to the non-linear interactions with subgrid scales is

$$\varepsilon = \bar{\mathbf{u}} \cdot \mathcal{M} = (C_S \bar{\Delta})^2 |\bar{S}|^3. \quad (7.9)$$

This last relation shows that, setting the subgrid model constant  $C_S$  to the appropriate value, one can enforce in the simulation the same kinetic energy drain as the theoretical one. In the case of the sharp cutoff filter in the limit of vanishing molecular viscosity, one obtains  $C_S \simeq 0.18$ , and numerical experiments show that the expected kinetic energy spectrum is recovered using this value<sup>2</sup>. Equation (7.8) also reveals that by changing  $C_S$  one can enforce an arbitrary length scale in the subgrid model, resulting in a change in the energy dissipation, and therefore leading to a new resolved kinetic energy spectrum shape.

Defining the effective filter as the application which transforms the theoretical kinetic energy spectrum into the computed one, one can easily see that changing the subgrid length scale (and consequently the subgrid dissipation), one modifies the effective filter. These changes have been analyzed for two subgrid models, namely the Smagorinsky model and the one-equation on kinetic energy proposed by Schumann [Magnient *et al.*, 2001b]. It is recalled that, in the Schumann model, the subgrid viscosity is defined as

$$\nu_t = (C_S \bar{\Delta}) \sqrt{k} \quad (7.10)$$

where  $k$  is the subgrid kinetic energy.

Magnient and coworkers show that both the cutoff length and the mathematical form of the effective filter depend on the length scale which appears in the eddy viscosity and the subgrid viscosity definition:

- (1) Taking the usual empirical value of the constant of both models (Smagorinsky model and Schumann model), an inertial range with a  $-5/3$  slope is recovered up to the cutoff wave number associated with the

---

<sup>2</sup>In practice, the Kolmogorov spectrum is recovered if the numerical method does not introduce spurious energy dissipation and if  $\bar{\Delta} = 2\Delta x$ , where  $\Delta x$  is the mesh size.

Nyquist wave number of the computational mesh. In terms of effective filter, this can be analyzed interpreting the effective filter as a sharp cutoff filter with a cutoff wave number equal to  $k_c = \pi/\overline{\Delta}$ :

$$\mathcal{G}(x) = \begin{cases} 1 & x \leq 1 \\ 0 & \text{otherwise} \end{cases}, \quad x = \frac{k}{k_c}. \quad (7.11)$$

- (2) Taking higher values of the constants appearing in the eddy viscosity models, *i.e.* multiplying  $C_S$  in Eqs. (7.10) and (7.8) by a factor  $r > 1$ , one observes very different behaviors:

$$\mathcal{G}(x) = \begin{cases} (1 + x^4)^{-2/3} & x \leq 1 \\ 0 & \text{otherwise} \end{cases} \quad (7.12)$$

for the Smagorinsky model, and

$$\mathcal{G}(x) = \begin{cases} e^{\frac{1+x}{2}(5-\frac{4.4}{r})} & x \leq 1 \\ 0 & \text{otherwise} \end{cases} \quad (7.13)$$

for the Schumann model.

Therefore, tuning the constant in the subgrid viscosity models induces a change in both the cutoff length and the mathematical expression of the filter. As a consequence, RANS/LES models which are based on a local change in characteristic length scales in the definition of the turbulent viscosity also induce a change in the local effective filter, leading to a local change in the resolution of the solution and the definition of a multi-scale/multiresolution approach.

### 7.1.3 Global hybrid RANS/LES methods as multiscale methods

Since hybrid RANS/LES models rely on the merging of different turbulent viscosities with different built-in characteristic scales, switching from one definition to another one or interpolating between the two values is therefore equivalent to switching from one effective filter to another one or to defining a new effective scale separation operator. This change in the built-in scales of the model for the unresolved scales being performed locally in space, the global hybrid methods can therefore be interpreted as multiresolution

methods, in which the resolution in terms of wave number is increased in regions with low eddy-viscosity levels and decreased in regions with high viscosity levels. Global hybrid RANS/LES methods have therefore aroused the turbulence modelling community interest as discussed in the following sections.

## 7.2 Motivation and Classification of RANS/LES Methods

During the last decades, most of the numerical efforts in the field of applied aerodynamics have been focused on the simulation of nominal operational configurations. As a consequence of the rules of design, most practical configurations exhibit only limited separated flow areas and smooth gradients regions. Therefore, steady methodologies for turbulent flow prediction are able to handle these flowfields with a sufficient degree of accuracy. New industrial needs in aerodynamics concern for example the control of noise as well as the capability to predict dynamic loads so that the simulation of 3D unsteady turbulent flows is now required (see discussions by Spalart and Bogue [Spalart and Bogue, 2003], Deck *et al.* [Deck *et al.*, 2005]). Indeed, this need is becoming an especially pressing issue since a wide range of unsteady phenomena that have serious implications in terms of achievable performance, acoustic environment or safety has to be considered, and therefore requires to be accurately predicted as soon as possible in the design cycle of flight vehicles or cars (see Fig. 7.1).

Direct Numerical Simulations (DNS) are the most straightforward approaches to the solution of unsteady turbulent flows since the governing equations are discretized directly and solved numerically. One can obtain an accurate three-dimensional and time-dependent description of the flow completely without resorting to any modelling assumptions. Unfortunately, turbulent flows encountered in engineering applications exhibit such a wide range of excited length and time scales (shock wave, boundary and free shear layers) at high Reynolds number ( $\approx 10^5 - 10^8$ ) that DNS are still beyond our capabilities (see the discussion on the resolution requirements for LES and DNS in Chapter 1). However, DNS are a very useful tool for the study of transitional and turbulent flow physics like the definition of spatial relations between flow variables or dynamics of turbulent eddies. More recently, DNS have also been used to study strategies to control turbulence thanks to active or passive devices but are not a realistic possibility in most cases of practical importance.

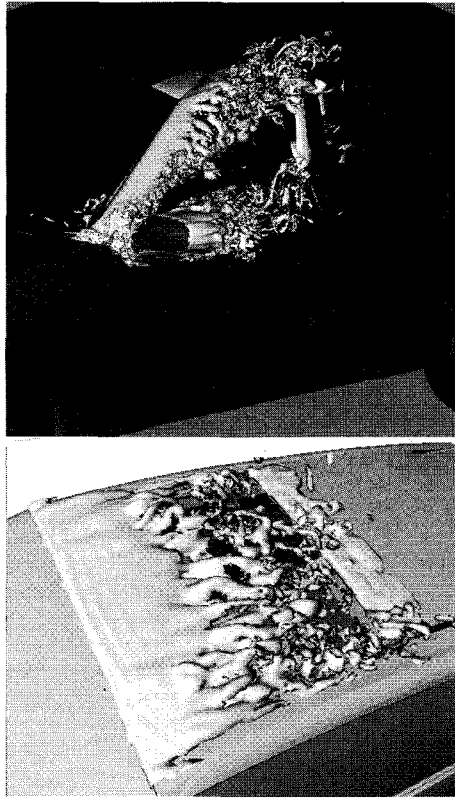


Fig. 7.1 Turbulent structures and approximate acoustic sources computation on a car. External components such as the side-view mirror (upper-part), sun-roof (lower-part) directly excite the panels which transmit noise to the driver ears. Courtesy of D. Ricot, Renault, France.

For these reasons, high Reynolds number separated flows have been traditionally predicted by solving the Unsteady Reynolds Averaged Navier Stokes (URANS) equations. This approach has experienced very different fortunes: URANS can give fairly good results in complex industrial geometries like flows around airliners but can meet tremendous problems when applied to simple geometries exhibiting massive separation like a base flow. This comes mainly from the fact that dominant eddies in massively separated flows are highly geometry-dependent and have not much in common with the standard eddies of the thin shear flows classical RANS turbulence models are designed to model.

On the other hand, the potential accuracy of LES is generally well-acknowledged. In practical engineering problems, the high cost of LES arises because of the resolution required in the boundary layers which dramatically raises the range of scales beyond affordability. For instance, Spalart *et al.* [Spalart *et al.*, 1997] reported as an estimate that for a wing, full LES will not be tractable until the year 2045, even assuming that wall modelling has been achieved. It is also worth remembering that from an engineering point of view, a LES of a complete wing would give too much information in some “useless” regions such as the leading edge or pressure side where traditional RANS modelling is often sufficient.

The recognition of this conflict between RANS and LES makes it very appealing to combine the fine-tuned RANS modelling in the attached boundary layers with the accuracy of LES in the separated regions. This motivation is supported by Germano’s [Germano, 1999] analysis. His work is based on the fact that RANS and LES equations are formally identical but with fundamentally different characteristic length scales. Let us recall that one of the earliest appearances of hybrid RANS/LES method is found in the seminal paper by Schumann [Schumann, 1975]. He developed a wall-model to supplement the SGS model in the near wall region. Little attention was paid to the subject until the more recent papers of Speziale [Speziale, 1997] and Spalart *et al.* [Spalart *et al.*, 1997] which have definitively led to breakthrough of hybrid RANS/LES simulations in industrial applications. Inspired by them, the development of hybrid RANS/LES approaches has received increasing attention among turbulence modelling specialists, CFD code developers and industrial CFD engineers. Indeed, recent years have added new intermediate strategies, coined as “URANS”, “TRRANS”, “PANS”, “SDM”, “OES”, “LNS”, “VLES”, “DES”, “XLES”, “SAS”, “Blending methods”, “zonal (and non-zonal) approaches”, “RANS/LES coupling”, “embedded LES”.

The purpose of this chapter is to help the reader to find a route through the jungle of publications covering both established and emerging approaches in the field of hybrid RANS/LES methods. Many of the methods discussed in this chapter are relatively new and the associated terminology is still evolving. The aforementioned strategies are compared in Fig. 7.2 in terms of their major capabilities (e.g. level of resolved physics), computational power requirement and readiness for industrial applications.

The effect of grid refinement on the solution constitutes the first important criteria to categorize unsteady methods [Spalart, 2000a]. As a matter of fact, in some strategies (referred to as “Unsteady Statistical Approaches”

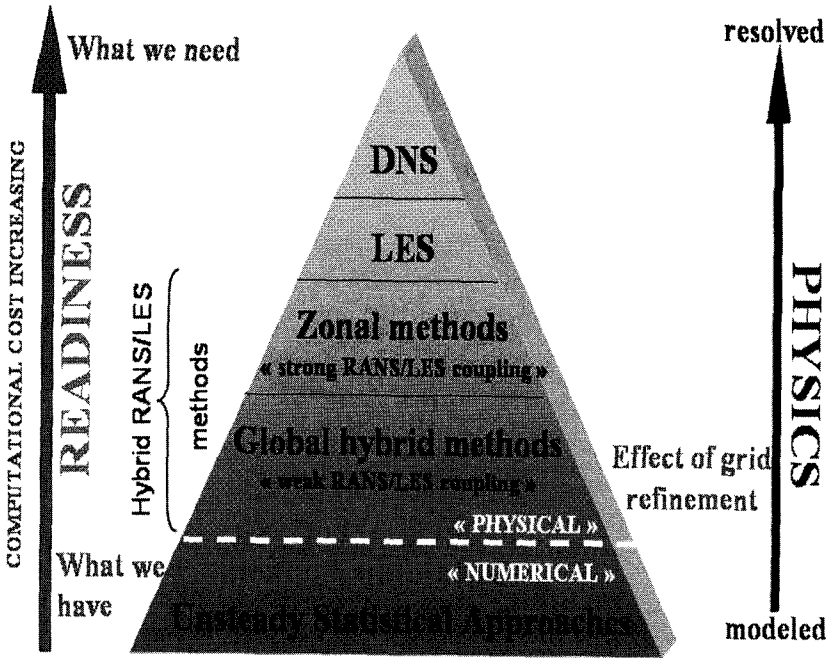


Fig. 7.2 Classification of unsteady approaches according to levels of modelling and readiness.

in Fig. 7.2), grid refinement aims at numerical accuracy. In other words, “numerical” means that grid refinement does not add any new physics to the solution. This class of methods is discussed in Sec. 7.3.

In contrast, in hybrid RANS/LES methods the aim of grid refinement is to enrich turbulence physics (labelled “physical” instead of “numerical”). Following the example of LES, grid refinement weakens the role of the modelled eddies, e.g. the smallest resolved eddies match the grid spacing<sup>3</sup>.

Hybrid methods can be, broadly speaking, categorized into two major classes corresponding to global and zonal hybrid methods respectively. Global hybrid RANS/LES approach relies on a single set of model equations and a continuous treatment at the RANS/LES interface. The decrease of eddy viscosity farther away from solid walls allows eddies to develop rapidly

<sup>3</sup>Spalart [Spalart, 2000a] defined LES as a simulation in which the turbulence model is tuned to the grid spacing and RANS as the opposite.

but no turbulent fluctuations are reconstructed at the RANS/LES interface. Therefore, this class of methods will also be referred to as “weak RANS/LES coupling” in the following and is discussed in Sec. 7.4.

Conversely, zonal hybrid methods are based on a discontinuous treatment at the RANS/LES interface where the LES content has to be explicitly reconstructed to account for the very large differences in the frequency spectrum between RANS and LES regions. This second strategy will be referred to as “strong RANS/LES coupling” and discussed separately in Chapter 8.

The motivation behind these different approaches will be given and illustrated for generic and technical flows. A summary is presented in Sec. 7.5.

### 7.3 Unsteady Statistical Modelling Approaches

Nowadays, steady RANS (sometimes referred to as SRANS) methods are routinely used for engineering applications and will not be discussed here. The ever increasing computational power has shifted attention to the Unsteady RANS (URANS) approaches which still constitutes the backbone for industry. Therefore the ability of this class of methods to handle unsteady flows is discussed in Sec. 7.3.1. The Semi-Deterministic Method (SDM) which aims at simulating the coherent motion is presented in Sec. 7.3.2.

Afterwards, we distinguish between URANS and LES depending on whether the eddy viscosity is sensitized to a filter width or grid spacing  $\Delta$  or not. In other words, modelled stresses in a RANS approach do not scale with the grid spacing as they do in LES. Unfortunately, the border between URANS and LES appears much less clear in the light of two recent proposals of Menter, Kuntz and Bender [Menter *et al.*, 2003] and Travin *et al.* [Travin *et al.*, 2004]. These authors offer intriguing alternatives to URANS solutions with LES-like behavior which are respectively presented in Sec. 7.3.3 and Sec. 7.3.4.

#### 7.3.1 Unsteady RANS approach

The most commonly used approaches to predict unsteady turbulent flows of industrial interest are based on Reynolds stress modelling. We have seen in Chapter 2 that Reynolds averaging is based on the idea that the flow can be decomposed into a mean flow and fluctuations (see Eq. 2.8). To make the most of this notion when performing time-dependent RANS calculations,

we defined the scale separation operator as a time-average over a time interval  $T$ . This averaging time  $T$  has to be larger than the characteristic time scale of turbulence  $\tau$  and smaller than the characteristic period  $\theta$  for the time evolution of the mean properties. From a mathematical point of view, this amounts to say that we apply a low-pass filter to the turbulent field with  $\frac{1}{T}$  representing the cut-off frequency.

Therefore, this URANS approach can be successfully used in cases where the flow is forced to be unsteady because of unsteady boundary conditions (such as body motion) e.g. in flowfield characterized by a separation of time scale (or spectral gap) between the unsteadiness of the mean field and turbulence. A typical example is given by a small-amplitude forced oscillation of a vehicle so that the flow remains fully attached or slightly separated. This type of motion is used for the numerical (and experimental) prediction of the damping derivative coefficients (see Fig. 7.3).

This URANS approach, sometimes referred (Hanjalić and Kenjerš [Hanjalić and Kenjeres, 2000]) to as TRANS (Transient-Reynolds-Averaged Navier–Stokes) can also yield interesting predictions for certain situations of unsteady separated flows when turbulence is not the driving phenomenon of flow instabilities. An example is provided by rotating stall which is generally the first instability encountered in multi-stage compressors, before surge. This three-dimensional phenomenon is characterized by one or more cells of stalled flow which rotate at a fraction of the rotor speed. URANS can give useful predictions for this complex phenomenon as recently showed by Gourdain *et al.* [Gourdain *et al.*, 2005] (see Fig. 7.4).

In the case of unsteady flows with a pronounced periodic character, the scale separation operator based on phase-averaging given by Eq. (2.31) can also be used. The resulting system of equations is sometimes named PANS which stands for Phase-Averaged Navier–Stokes equations. The phase averaging is theoretically grounded if pseudo-periodic components exist in the flow, for instance when boundary conditions impose flow unsteadiness. This situation arises for example in turbomachinery applications when rotor/stator interactions are taken into account or in flow around an helicopter blade.

Nevertheless, we have already seen that the URANS and PANS systems are formally equivalent and from now on, we designate them to as unsteady statistical methods instead of distinguishing URANS and PANS.

As an example, we consider that the flow around an helicopter blade is submitted to periodic forcing imposed by the the angular velocity of the rotor. The unsteady statistical approach is well-suited here since the

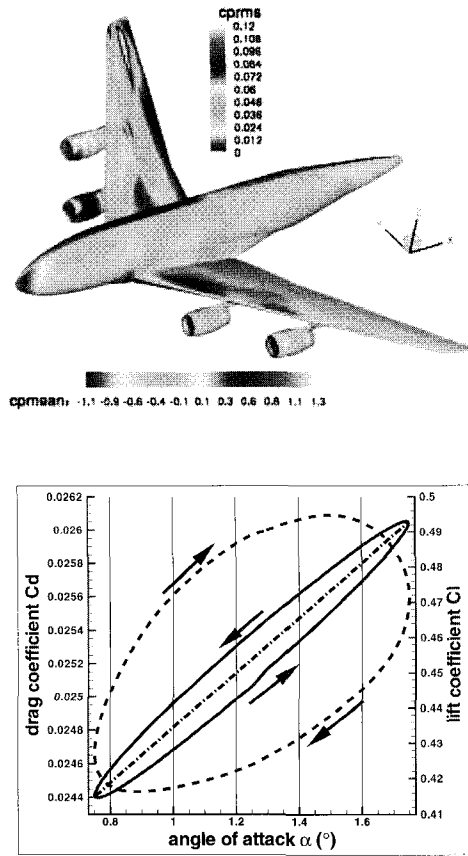


Fig. 7.3 URANS computation of a small amplitude forced oscillation. Top: time averaged pressure coefficient and pressure fluctuation coefficient on airplane. The grid contains  $8.10^6$  nodes for a half-configuration and requested less than 20 CPU hours (on a single NEC-SX6 processor) to complete a loop. Bottom: Lift coefficient (solid line) and drag coefficient (dashed line) evolution. The need for unsteady computations for accurate predictions of the lift and drag coefficients is highlighted by the elliptic shape of these aerodynamic coefficient versus angle of attack. Indeed, a series of steady computations allows only the linear curve to be obtained. Courtesy of V. Brunet, ONERA, France.

flow is naturally forced to be unsteady due to the periodic motion imposed by the rotor and this forcing easily provides a phase locking of the flow. Renaud *et al.* [Renaud *et al.*, 2005] performed an unsteady calculation using the  $k - \omega$  turbulence model [Wilcox, 1988b] with SST correction [Menter,

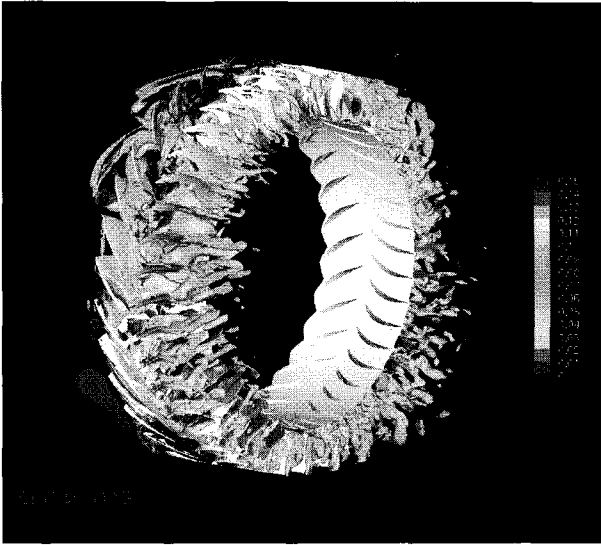


Fig. 7.4 Entropy flow field during rotating stall. Note the different stall cells emanating between the blades and propagating in the whole compressor. The simulation was performed on 4 processors of a NEC-SX6 super-computer on a  $N_{xyz} = 31 \cdot 10^6$  nodes grid. 3800 CPU hours and 29.5 Giga-bytes of memory storage (by using the one-equation Spallart-Allmaras turbulence model) were necessary to simulate 15 revolutions of the rotor. Courtesy of N. Gourdain, ONERA, France.

1994] around a complete helicopter configuration. A view of the body fitted grids around each blade of the four blades of the helicopter model and the background grid around the fuselage is presented Fig. 7.5.

The unsteady approach is needed to perform a quantitative analysis of the unsteady pressure fluctuations generated by the blades passage on the tail boom (see Fig. 7.6).

### 7.3.2 *The Semi-Deterministic Method of Ha Minh*

Following the idea proposed by Reynolds and Hussain, in the form suggested by the experimental results of Cantwell and Coles, the Semi-Deterministic Method (SDM) of Ha Minh and Kourta [Ha Minh and Kourta, 1993] (see also [Ha Minh, 1999]) is based on the decomposition of physical variables

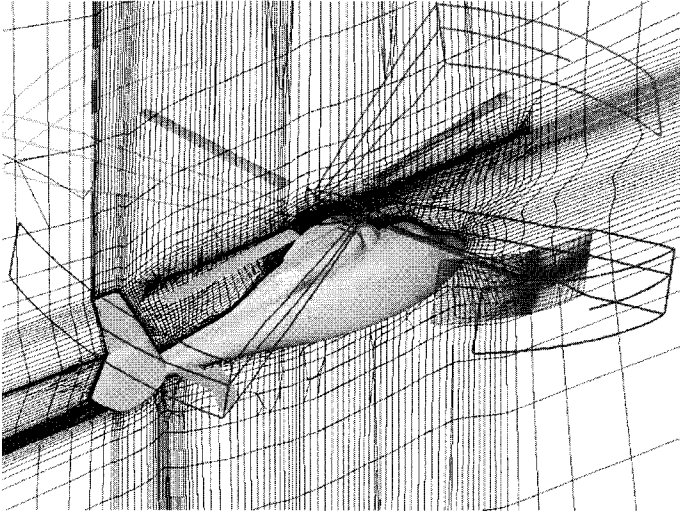


Fig. 7.5 Computational grid around a complete helicopter (every other grid point in all direction is shown). The total number of grid points has been limited to  $N_{xyz} = 9.1 \times 10^6$  points using the Chimera technique to reproduce the motion of the blade. The CPU cost to simulate a rotor revolution was less than 140 hours on a single processor of a NEC-SX6 super-computer. Courtesy of T. Renaud, ONERA, France.

into a coherent and incoherent part.<sup>4</sup>

$$f = f_{coherent} + \underbrace{f''}_{\text{chaotic turbulence}} \quad (7.14)$$

This approach can also be found in the literature under the appellation Organized Eddy Simulation (OES) since Braza [Braza, 2000] considers that in many situations, the flow is simultaneously organized (coherent motion) and chaotic (incoherent motion). The SDM approach consists in splitting the energy spectrum (see Fig. 7.7) into a discrete part regrouping all the organized modes or coherent modes of the flow (e.g. distinct frequency peaks of the spectrum) and a continuous part which corresponds to the chaotic or incoherent part of motion.

The time averaging procedure is obviously not relevant in the extraction of the coherent motion. The coherent part of the spectrum is predictable

<sup>4</sup>The criterion of distinction of the structures to be predicted from those to be modelled is their physical nature and not their size as in the case of LES.

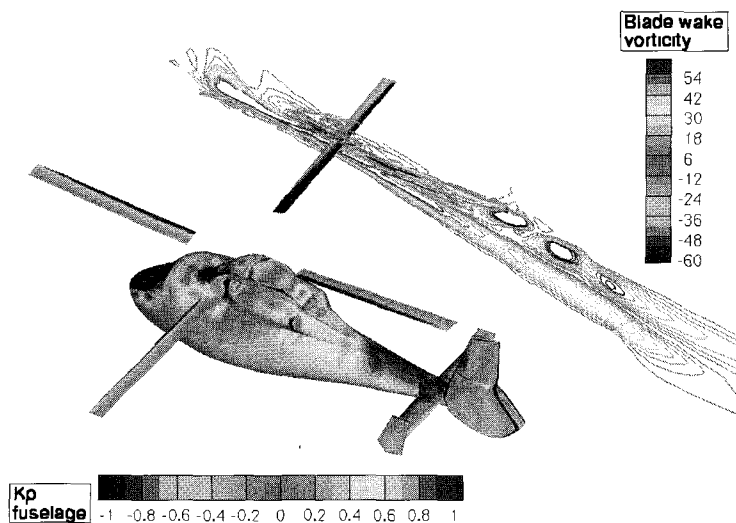


Fig. 7.6 Instantaneous pressure distribution on the fuselage and blades. The Mach number characteristic to forward flight is equal to  $M_\infty = 0.044$ . The blade wake vorticity is plotted at the same instant in a radial section of the retreating side. Courtesy of T. Renaud, ONERA, France.

by solving the phase-averaged Navier–Stokes equations ( $f_{coherent} = \bar{f} + \tilde{f}$  where  $\tilde{f}$  is periodic) and the remaining incoherent part can be modelled by a conventional one-point RANS closure. The nature of the small-scale stochastic fluctuations is believed to be universal and similar to the traditional turbulence concept. Although, the form of the equations of motion is formally similar to the one obtained by considering the Unsteady Reynolds Averaged Navier Stokes (URANS) equations, the time and length scales of the turbulent part are not the same as in flows in statistical equilibrium. If we consider the energy spectrum of the flow at any point of the flow domain, it appears that the turbulent energy of the steady (RANS) closure (with  $f = \bar{f} + f'$ ) is the sum of the analogous one for phase-averaging SDM closure (with  $f = \bar{f} + \tilde{f} + f''$ ) with the energy of  $\tilde{f}$ . As a consequence, the SDM energy should be smaller than the RANS one, and corresponding turbulent viscosities should also satisfy this inequality. This constitutes the main difference with the classical URANS approach since in the framework of an SDM simulation, the turbulence model has to be modified to take into account the coherent (or organized) structures which are not modelled but resolved.

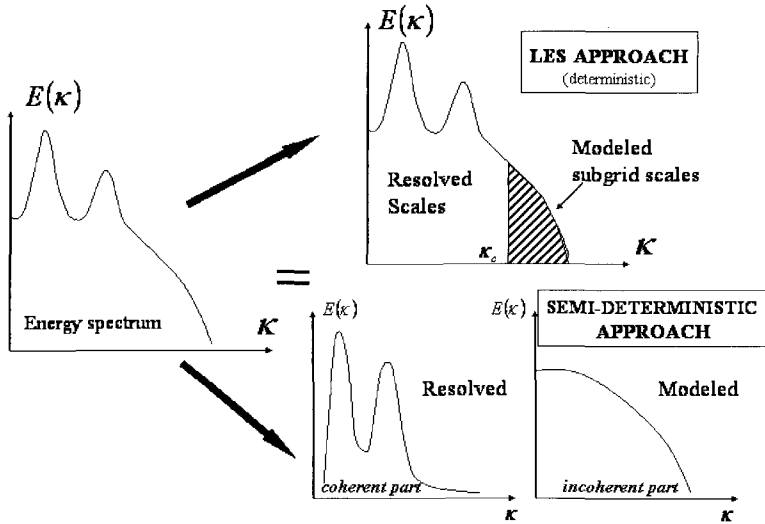


Fig. 7.7 Sketch of Spectrum decomposition according to the Semi-Deterministic Approach.

For example, adopting the relation  $\nu_t = C_\mu \frac{k^2}{\varepsilon}$  used in a two-equation  $k - \varepsilon$  turbulence model, Ha Minh proposed to reduce the values of  $C_\mu$ , thus decreasing the eddy viscosity to build the SDM. For example, for the backward facing step case, he obtains as optimal value  $C_\mu = 0.05$ .

Bastin *et al.* [Bastin *et al.*, 1997] used the SDM approach to investigate plane mixing layers at convective Mach numbers 0.19, 0.33 and 0.52 (*i.e.* quasi-incompressible cases and cases where compressibility effects are significant). They performed calculations with  $C_\mu$  taken equal to its standard 0.09 value and with  $C_\mu = 0.05$ . They observed no apparent modification of the coherent structure development and the mean flow is unchanged except that self-similarity is reached further downstream with  $C_\mu = 0.05$  than for  $C_\mu = 0.09$ . They have shown that decreasing  $C_\mu$  essentially results in shifting the energy balance between coherent and incoherent motion, the energy of the coherent structures being increased. The authors finally retained the value  $C_\mu = 0.05$ .

The OES approach has also been used to compute the unsteady flow around a NACA0012 profile at 20 degrees angle of attack. Braza [Braza, 2000] showed the ability of the  $k - \varepsilon$  model to properly predict the highly separated flow and the vortex shedding mode in the wake by taking  $C_\mu =$

0.02. This evaluation was made through *a posteriori* quantification of the turbulent energy and dissipation fields calculated with a Reynolds Stress Model (RSM). She deduced the  $C_\mu$  value by the classical relation  $\nu_t = C_\mu \frac{k^2}{\varepsilon}$  by adopting *a posteriori* the Boussinesq relation.

From the aforementioned applications, it is observed that firstly the value of  $(C_\mu)_{SDM}$  lies in the range  $[0.02 - 0.05]$  and secondly that this value is applied in the whole flowfield even for attached boundary layers. Indeed, the value of  $C_\mu = 0.09$  comes from scaling of flows in statistical equilibrium and plays a key role in determining the slope of the logarithmic law (see for example [Cousteix, 1989]) since the constants of the model  $C_{\varepsilon_1}$ ,  $C_{\varepsilon_2}$ ,  $\sigma_\varepsilon$  and  $C_\mu$  are linked to the von Kármán constant  $K$  according to:

$$\frac{1}{K^2} = \frac{1}{(C_{\varepsilon_1} - C_{\varepsilon_2}) \sigma_\varepsilon \sqrt{C_\mu}}. \quad (7.15)$$

Therefore, Deprés [Deprés, 2003] used a “zonal-SDM” approach which consists in retaining the standard value  $C_\mu = 0.09$  in attached boundary layers while separated flows are predicted by taking  $C_\mu = 0.02$ . This approach was then used to investigate an axisymmetric base flow extended by an emergence of lower diameter. Figure 7.8 displays an instantaneous snapshot of the coherent (or organized) structures obtained with this method. This picture clearly shows the roll-up of toroidal eddies which are progressively destabilized in the vicinity of the confluence area. After the break-up of these toroidal eddies, the main structures appear to be mainly longitudinal eddies. The spectrum of pressure fluctuations on the afterbody (see Fig. 7.9) displays a sharp peak at Strouhal number  $St_D = fD/U$ , based on the diameter of the main body and free-stream velocity, equal to 0.2. Hence, the near wake flow is characterized by a global unsteadiness and the periodicity is attributed to the periodicity of the large scale turbulent structures. It can be noted from Fig. 7.9 that the coherent part of the motion is well reproduced by the SDM approach while the high frequency fluctuations (incoherent part) are not reproduced. However, the amplitude of the coherent motion tends to be overestimated. This feature has also been observed by Bastin *et al.* [Bastin *et al.*, 1997].

These authors observed that the amplitude of the coherent structures, e.g. the ratio of the coherent fluctuation to the total turbulence level, depends on the choice of the viscosity constant  $C_\mu$ . Kourta [Kourta, 1999] used a flow-dependent  $C_\mu$  value based on the time scale ratio of the turbulence to the phase averaged strain  $\eta$  and on the time scale ratio of the

turbulence to the phase averaged rotation  $\xi$  as follows:

$$C_\mu(\eta, \xi) = \frac{2}{3} \cdot \frac{1}{A_1 + \eta + \gamma_1 \xi} \quad (7.16)$$

with

$$\eta = \frac{\langle k \rangle S}{\langle \epsilon \rangle}, \quad \xi = \frac{\langle k \rangle \Omega}{\langle \epsilon \rangle}, \quad A_1 = 1.25, \quad \gamma_1 = 0.9 \quad (7.17)$$

where  $S$  and  $\Omega$  denote the magnitude of strain and vorticity, respectively. Kourta applied this method to simulate vortex shedding in solid rocket nozzles by solving the phase averaged Navier Stokes equations for axisymmetric non-swirling flow. Here again, the frequency characteristic of the vortex shedding was well reproduced but the levels of pressure fluctuations associated to this phenomenon were overestimated. Kourta [Kourta, 1999] argued that this overestimation is partly due to the axisymmetry assumption which seems inadequate in this case exhibiting coherent structures. Indeed, an axisymmetrical or two-dimensional computation accounts for the role of time but not for three-dimensional effects leading to an “overcoherent” simulation since the vorticity has only one component normal to the computational plane.

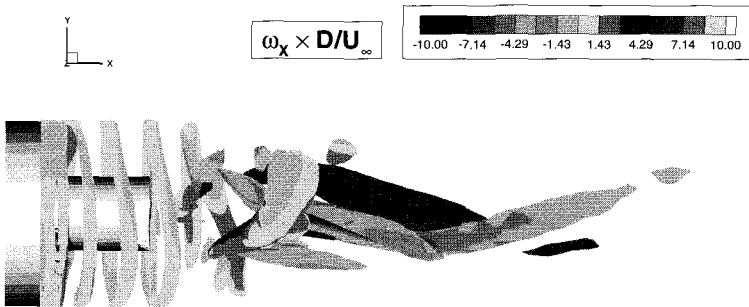


Fig. 7.8 Coherent structures over an axisymmetric afterbody using a Semi-Deterministic Approach. Courtesy of D. Deprés, ONERA, France.

Within the SDM framework, grid refinement aims at improving the numerical accuracy and does not add any new physics to the solution since the method is independent of any explicit filtering operation in the computational plane. In other words, there is no reason why an SDM calculation would require a finer grid than the one required for a grid converged RANS

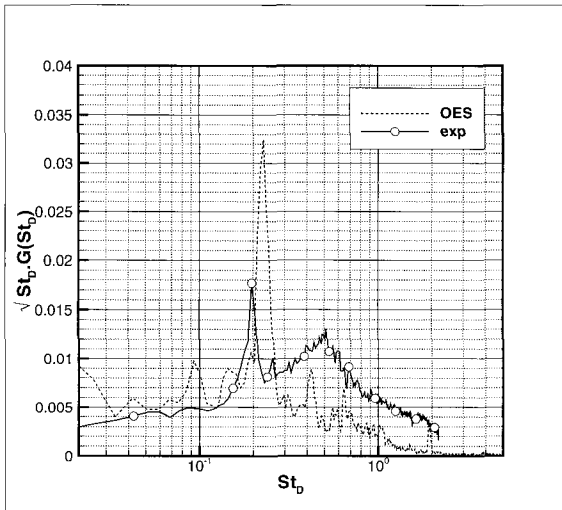


Fig. 7.9 Pressure spectra on the rear body using a Semi-Deterministic Approach. Courtesy of D. Deprés, ONERA, France.

calculation. As an example, Deprés [Deprés, 2003] performed an SDM simulation on a 800,000 points grid whereas Deck and Garnier [Deck and Garnier, 2004] used a 5 million points grid to perform a zonal-DES (see Sec. 7.4.6) and a LES on the same configuration. Nevertheless, the effect of grid refinement in the framework of unsteady statistical approaches is far from being fully understood (see Sec. 7.3.3).

The semi-deterministic approach can be considered as an hybrid approach as it combines “resolved” (or coherent) and “modelled” (or incoherent) Reynolds stresses. Nevertheless, it is important to outline that modelled stresses do not scale with the grid spacing as they do in LES. Therefore, the SDM (or OES) does not fall (according to our terminology introduced Sec. 7.2) into the category of RANS/LES approach.

### 7.3.3 The Scale Adaptive Simulation

Anticipating discussions developed in Sec. 7.4.4, let us say that DES relies on the comparison of the turbulent length-scale computed from the turbulence model and the local grid spacing. The decrease of eddy viscosity allowing a LES-like resolution of the turbulence field is entirely supplied by the grid dependent destruction term in DES mode (see Eq. (7.69) or

Eq. (7.105)). Thus an alternative to standard DES, which avoids the explicit dependency in the RANS region is the Scale Adaptive Simulation (SAS) approach recently proposed by Menter, Kuntz and Bender [Menter *et al.*, 2003].

Menter [Menter, 1997] showed that a destruction term for the eddy viscosity can be formulated without any explicit dependency with respect to the distance to the wall  $d_w$ . His model was originally derived in order to demonstrate the connection between one- and two-equation models and relies on a single transport equation for the eddy viscosity. More precisely, the model is derived from the two-equation  $k - \varepsilon$  model under the equilibrium assumption that the turbulent production  $P_k$  is equal to the dissipation rate  $\varepsilon$ . Assuming further that the diffusion coefficients in the underlying  $k - \varepsilon$  model are identical  $\sigma_k = \sigma_\varepsilon$ , the high-Reynolds number form of Menter's model (referred to as KE1E) reads as:

$$\frac{D\nu_t}{Dt} = \underbrace{c_1 \nu_t S}_{\text{Production}} + \underbrace{\nabla \cdot \left( \frac{\nu_t}{\sigma} \nabla \nu_t \right)}_{\text{Diffusion}} - \underbrace{c_2 \left( \frac{\nu_t}{L_{vK}} \right)^2}_{\text{Destruction}} \quad (7.18)$$

where  $c_1$ ,  $c_2$  and  $\sigma$  are modelling constants derived from those appearing in the underlying  $k - \varepsilon$  model. What is important here is that the destruction term is based on the *von Kármán* length scale, which acts as an integral length scale in boundary layer regions. For a simple boundary layer, the *von Kármán* length scale,  $L_{vK}$  is defined as:

$$L_{vK} = K \left| \frac{\frac{\partial u}{\partial y}}{\frac{\partial^2 u}{\partial y^2}} \right| \quad (7.19)$$

where  $u$  is the velocity parallel to the wall and  $y$  is the wall-normal coordinate. One can notice that  $L_{vK}/K$  is equal to the distance normal to the wall in the logarithmic layer region. It is worth noting that this expression for the dissipation length scale arises naturally in the derivation of a single model for the  $k - \varepsilon$  eddy viscosity using equilibrium assumptions. For general multi-dimensional calculations, an invariant formulation can be given:

$$L_{vK} = K \sqrt{\frac{S \cdot S}{\left( \frac{\partial S}{\partial x_j} \cdot \frac{\partial S}{\partial x_j} \right)}}. \quad (7.20)$$

To avoid the singularity of  $\frac{1}{L_{vK}}$  appearing in Eq. (7.18) in the case of a vanishing mean strain-rate, Menter *et al.* (2003) use the following invariant formulation of the *von Kármán* length scale:

$$L_{vK-SAS} = K \sqrt{\frac{\frac{\partial u_i}{\partial x_j} \frac{\partial u_j}{\partial x_i}}{\frac{\partial^2 u_l}{\partial x_m^2} \frac{\partial^2 u_m}{\partial x_l^2}}} \quad (7.21)$$

and propose the following modification of the KE1E model:

$$\begin{aligned} \tilde{L}_{vK-SAS} &= \max \left( L_{vK-SAS}, C_{SAS} \tilde{\Delta} \right) \\ \text{with } \tilde{\Delta} &= \min (\Delta x, \Delta y, \Delta z) \quad C_{SAS} = 0.6 \end{aligned} \quad (7.22)$$

where  $C_{SAS}$  is a model constant. The fraction of grid spacing  $C_{SAS} \tilde{\Delta}$  is required as a tolerance<sup>5</sup>. Furthermore when assuming source-term equilibrium, one obtains the following form of the eddy viscosity in LES mode:

$$\nu_t = \frac{c_1}{c_2} L_{vk-SAS}^2 S. \quad (7.24)$$

It turns out that  $L_{vk-SAS}$  introduces a dynamical behavior into the model. The SAS formulation was initially based on a one-equation model and has since been extended to more advanced models. As an example, Menter and Ergorov [Menter and Egorov, 2004; Menter and Egorov, 2005] adapted the SAS concept to the  $k - \omega$  model and simulated the flow around a cylinder for a Reynolds number based on the diameter equal to  $3.6 \times 10^6$ . Turbulent structures down to the grid limit (similar to those typically observed in LES simulations) are clearly observed in the wake of the cylinder (see Fig. 7.10). However, the SAS model handles the attached boundary layer in RANS mode making it reminiscent to global hybrid RANS/LES models. More precisely,  $L_{vK}$  automatically distinguishes stable and unstable flow regions. The concept was thus called *Scale - Adaptive Simulation* or SAS as the model adjusts automatically to the resolved field.

---

<sup>5</sup>Initially, to avoid the singularity caused by vanishing mean-strain rate, the destruction term was written as:

$$c_2 \min \left[ \left( \frac{\nu_t}{L_{vK}} \right)^2, (\nabla \nu_t)^2 \right]. \quad (7.23)$$

Menter *et al.* (2003) showed that this modification reduces the ability of the model to adjust the length scale to resolved turbulent eddies. Indeed, the term  $(\nabla \nu_t)^2$  can become very small since the diffusion term in the equation may produce small eddy viscosity gradients.

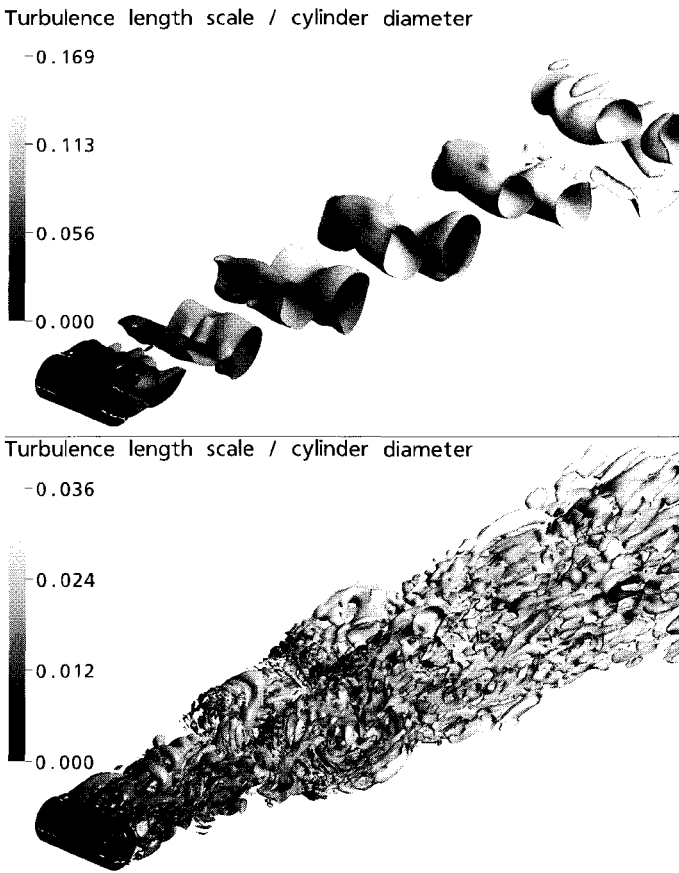


Fig. 7.10 Comparison of SST-URANS (top) and SST-SAS(bottom) solutions for cylinder in crossflow. The grid consists of  $3.18 \times 10^6$  nodes. In LES regions, the turbulent structures break down to the grid size  $L_{vK} \approx \Delta$ . Courtesy of F. Menter and Y. Egorov, ANSYS, Germany.

According to our classification (see Sec. 7.2), SAS can be considered as a URANS model since no explicit filter or grid size dependence appears in the formulation (except as a numerical tolerance for  $L_{vK}$ ). Nevertheless, this method is capable of resolving turbulent structures in highly separated flows, e.g. in flows which rapidly develop strong instabilities. SAS obviously “feels” the grid but a deeper understanding of the role played by the grid spacing and the numerical differentiation is needed.

### 7.3.4 The Turbulence-Resolving RANS approach of Travin *et al.*

The TRRANS model is based on a slight modification of the  $k - \omega$  model presented in Sec. 7.4.4.5 and can be formulated as a multiplier to the destruction term in the  $k$  equation:

$$D_k^{TRRANS} = \underbrace{(C_\mu \omega k)}_{D_k^{RANS} \equiv \varepsilon_{RANS}} \cdot F_{TRRANS} \quad (7.25)$$

with

$$F_{TRRANS} = \max \left( \left( \frac{S}{C_{TRRANS} \Omega} \right)^2, 1. \right) \quad (7.26)$$

where  $S$  and  $\Omega$  are respectively the magnitudes of strain and vorticity. The only new constant of the model is  $C_{TRRANS}$  which is larger than 1.

Therefore, in thin shear layers ( $S \approx \Omega$ ) as well as inside vortices ( $S \ll \Omega$ ), the TRRANS model is identical to the original RANS model. In contrast, in strain-dominated flow regions where  $S \gg \Omega$ , it can be noted from Eq. (7.26) that the model increases the dissipation of  $k$  which in turn results in a drop of eddy viscosity. At this stage, it is worth remembering that decreasing the eddy viscosity levels does not necessarily lead to a LES behavior.

The constant  $C_{TRRANS}$  was calibrated on the basis of Comte-Bellot and Corrsin [Comte-Bellot and Corrsin, 1971] data dealing with the kinetic energy spectrum of Decaying Homogeneous Isotropic Turbulence. The numerical procedure used to compute  $C_{TRRANS}$  was the same as the one used by Shur *et al.* [Shur *et al.*, 1999] and Strelets [Strelets, 2001] to determine the  $C_{DES}$  constants of the SA and SST models. The selected value of  $C_{TRRANS} = 1.25$  provides the best fit of the spectral slope in the inertial range near the cut-off wave number. It is particularly intriguing to note that their model yields a decay of energy following the “-5/3 law” up to the cut-off frequency. Up to now and to the author’s knowledge, this mechanism is still unknown.

Travin *et al.* also simulated three other flows with TRRANS: a NACA0012 airfoil with  $\alpha = 45$  deg. angle of attack, a circular cylinder and a backward facing step. For instance, they compared on a same grid the turbulence resolving capabilities of URANS, DES and TRRANS based on  $k - \omega$  turbulence model on the NACA0012. Figure 7.12 shows that the

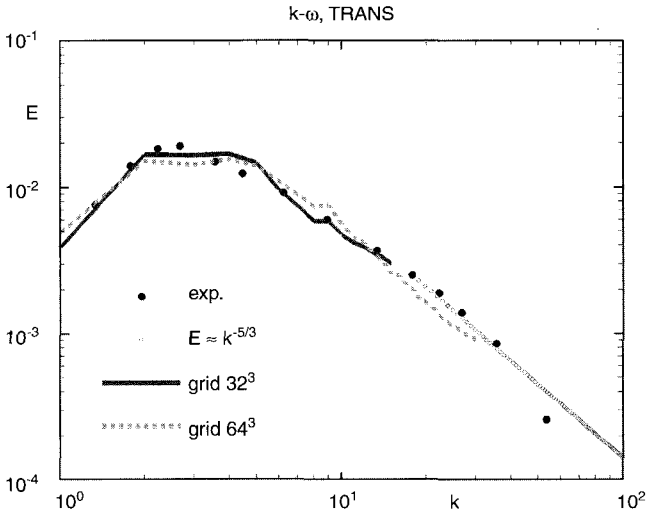


Fig. 7.11 Comparison of  $k - \omega$  TRRANS predictions of the DHIT energy spectra with the experimental data. Courtesy of M. Strelets, NTS, Russia.

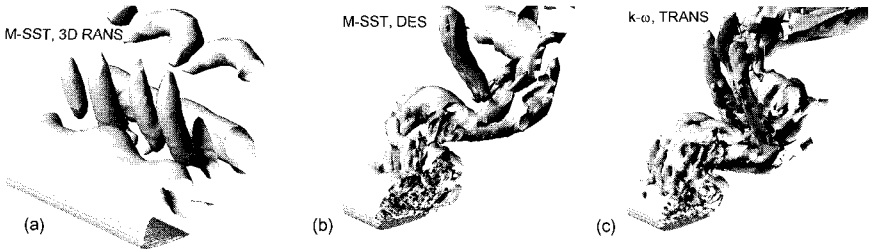


Fig. 7.12 NACA0012 airfoil at 45 deg. angle of attack. Swirl isosurfaces in the airfoil: a)  $k - \omega$  SST 3D URANS ( $L - z = 4c$ ) b)  $k - \omega$  SST-DES ( $L - z = c$ ) c)  $k - \omega$  TRRANS ( $L - z = c$ ). Courtesy of A. Travin, NTS, Russia.

level of resolved structures is quite similar between TRRANS and DES and obviously superior to URANS.

Similar conclusions were obtained on the flow around a circular cylinder. In addition, the response of TRRANS to grid refinement is of LES type e.g. smaller structures are resolved as the grid is refined. Therefore, Travin *et al.* named their model as a Turbulence Resolving Reynolds Averaged Navier–Stokes (TRRANS) approach. On the other hand, TRRANS unlike DES

failed to support unsteadiness in the backward facing step flow which is generally a good candidate for hybrid RANS/LES methods.

Conversely to DES (see Eq. (7.94)), the TRRANS modification is not sensitive to grid spacing and therefore preserves the RANS spirit of the model, making it reminiscent to SAS (see Sec. 7.3.3). The main difference is that TRRANS uses a non-dimensional ratio between first derivatives of the velocity fields whereas SAS derives the *von Kármán* length scale,  $L_{vK}$  from a ratio to first and second order derivatives (see Eq. (7.21)).

In conclusion, the ability of TRRANS to act in a LES-like fashion in certain flow regions does therefore raise questions concerning the URANS concept as a whole.

## 7.4 Global Hybrid Approaches

Most RANS models perform well for flows similar to the ones for which they are tuned like attached boundary layers. However, it seems to be generally well-acknowledged that the accurate prediction of massive separation is beyond the capabilities of “classical” URANS approaches. Nevertheless, massively separated flows are populated by large turbulent scales which can be accurately resolved by LES at affordable (CPU) cost, e.g., without a prohibitive the need for a grid resolution. Conversely, doing accurate predictions of wall-bounded flows with LES is still a challenging task. The primary obstacle to practical use of LES for realistic engineering flows which involve wall boundary-layers at high Reynolds number remains computational resources. Indeed, LES aims at capturing the scales of motion responsible for turbulence production which impose severe demands on the grid resolution near solid-walls. Hybrid RANS/LES was proposed to alleviate this grid resolution problem in the near-wall region.

Global (or non-zonal) RANS/LES strategies rely on a single set of equations that blends into a generalized model RANS and LES models. This hybrid approach is expected to act in RANS mode near the wall and transition to LES where desired. Several hybrids proposals have been made, which are presented below:

- (1) Very Large Eddy Simulation (VLES) , see Sec. 7.4.1
- (2) Limited Numerical Scales (LNS), see Sec. 7.4.2

- (3) Explicit blending of the RANS and LES methods, see Sec. 7.4.3
- (4) Detached Eddy Simulation (DES), see Sec. 7.4.4

The continuous treatment or smooth transition between RANS and LES modes raises the important issue of “grey-area” where the model cannot respond either as RANS or LES. This topic is discussed separately in Sec. 7.4.5 and some solutions to overcome this “grey-area” drawback are presented in Sec. 7.4.6.

#### 7.4.1 The Approach of Speziale

Speziale [Speziale, 1997; Speziale, 1998] was an early contributor in the development of hybrid RANS/LES closures. In his approach, the turbulent stresses are computed by damping the Reynolds stresses in regions where the grid spacing,  $\Delta$ , approaches the Kolmogorov length scale  $L_K$ , that is:

$$\tau = \alpha \cdot \tau^{\text{RANS}} \quad (7.27)$$

in which

$$\alpha = \left[ 1 - \exp\left(-\frac{\beta\Delta}{L_K}\right) \right]^n \quad (7.28)$$

where  $\beta$  and  $n$  are some modelling (unspecified) parameters,  $\Delta$  some representative mesh spacing (see Table 7.1) and  $L_K$  is the Kolmogorov length scale:

$$L_K = \frac{\nu^{\frac{3}{4}}}{\varepsilon^{\frac{1}{4}}}. \quad (7.29)$$

Speziale’s approach allows us to merge the RANS and LES methodologies which are classically treated as separated approaches. Indeed, in the limit as  $\frac{\Delta}{L_K} \rightarrow 0$ , all relevant scales are resolved, *i.e.* the subgrid scales vanish completely (e.g.  $\tau \equiv \mathbf{0}$ ) leading to a Direct Numerical Simulation.

The regular RANS behavior is recovered (e.g.  $\tau \equiv \tau^{\text{RANS}}$ ) at the other limit as  $\frac{\Delta}{L_K} \rightarrow \infty$  as the mesh becomes coarse or the Reynolds number becomes extremely large. Between these two limits, Speziale considers the simulation as a Very Large Eddy Simulation (VLES)<sup>6</sup>, that is an LES (the

---

<sup>6</sup>The acronym VLES has been used in the literature to refer to very different approaches going from URANS to LES. Indeed, following a conventional LES practice, the effect of the subgrid scale eddies is mainly to dissipate turbulent energy with negligible contribution to the Reynolds stresses. Hunt and Nixon [Hunt and Nixon, 1995] used the

eddy viscosity depending on the grid spacing  $\Delta$ ), where the preponderance of the turbulent kinetic energy is unresolved.

It can be noted that any trusted RANS model can be blended following this approach, although Speziale recommended the use of a two-equation RANS model with non-equilibrium effects incorporated via an explicit algebraic stress model.

However, a number of issues were never completely specified by Speziale, such as the definition of the crucial parameters  $\beta$  and  $n$  as well as the choice of the damping function given by Eq. (7.28). Further developments of Speziale's Kolmogorov length scale dependent blending have been pursued by several authors (see for instance [Sandberg and Fasel, 2004]). As an example, Zhang *et al.* [Zhang *et al.*, 2000] conserved the ratio  $\frac{\Delta}{L_K}$  to switch from RANS to LES mode via the contribution function:

$$\alpha = \left[ 1 - \exp \left( \frac{-5 \max(0, \Delta - 2L_K)}{NL_K} \right) \right]^n \quad (7.30)$$

where  $n$  and  $N$  are user-defined constants ( $n = 1$  in their study). This function is slightly different from the original form proposed by Speziale (see Eq. (7.28) since the grid spacing is compared to  $N$  times the Kolmogorov length scale ( $N$  is taken in the range 1000-2000 in their wall-jet application). This approach has been named new Flow Simulation Methodology (FSM) by the authors but falls into the category of VLES introduced by Speziale. Other forms of the contribution function  $\alpha$  and different choices of the length scale are given by Fasel *et al.* [Fasel *et al.*, 2002].

At this stage, it is important to point out that properly reaching both the DNS and RANS limits does not guaranty that the corresponding approach provides a correct LES mode. Since the original function proposed by Speziale compares grid spacing with the Kolmogorov scale, it reduces the RANS stresses significantly only in regions where the grid resolution approaches the one required for DNS. The knowledge of Kolmogorov's length scale is not strictly needed to ensure that the correct DNS behavior is reached in the limit of vanishing grid spacing and there are many possible choices of such blending functions (partly indicated by the

---

acronym VLES to define a LES in which the cutoff is placed close into the inertial range, *i.e.* when a non-negligible part of the total kinetic energy is contained in the modelled scales. Although, such a simulation cannot resolve the full range of turbulent scales, it is able to resolve the "very large eddies" to account for their non-linear interaction with the mean flow. Nevertheless, Hunt and Nixon's work should be classified as LES and not as an hybrid RANS/LES method.

free modelling parameters in Eq. (7.28)). In addition, when the Reynolds number tends to infinity (*i.e.*  $L_K \rightarrow 0$ , the model proposed by Speziale gives systematically a RANS behavior since  $\tau \equiv \tau^{\text{RANS}}$  according to Eq. (7.28). In other words, the grid spacing has no influence anymore on the eddy viscosity and an LES subgrid scale can not be reached as fine as the grid is. Surprisingly, this feature received little attention in the literature. Therefore, Magnient [Magnient, 2001a] suggested an hybrid approach that not only depends on  $\frac{\Delta}{L_K}$  but also on the ratio  $\frac{L_{\text{RANS}}}{\Delta}$  where  $L_{\text{RANS}}$  is a characteristic length scale, in a RANS sense, of the large structures. Assuming  $L_{\text{RANS}} \gg L_K$ , Magnient postulates that the influence of both ratio  $\frac{\Delta}{L_K}$  and  $\frac{\Delta}{L_{\text{RANS}}}$  is statistically uncorrelated and suggests the following form of the hybrid eddy viscosity:

$$\nu_t = \nu_t^{\text{RANS}} f\left(\frac{\Delta}{L_{\text{RANS}}}\right) g\left(\frac{\Delta}{L_K}\right). \quad (7.31)$$

The contribution function  $g$  is similar to Speziale's function (see Eq. (7.28). In the framework of a Very Large Eddy Simulation, *e.g.*  $L_K \ll \Delta$ , Magnient postulates  $g \approx 1$  and chooses a  $k - \varepsilon$  model to determine  $\nu_t^{\text{RANS}}$ :

$$\nu_t \propto \frac{k^2}{\varepsilon} f\left(\frac{\Delta}{L_{\text{RANS}}}\right), \quad L_{\text{RANS}} \propto \frac{k^{\frac{3}{2}}}{\varepsilon} \quad (7.32)$$

In classical LES, one can show by simple dimensional analysis [Sagaut, 2005] that the subgrid scale viscosity can be expressed as a function of the filter width and the dissipation rate of the resolved scales:

$$\nu_t \propto \Delta^{\frac{4}{3}} \varepsilon^{\frac{1}{3}}. \quad (7.33)$$

Under the equilibrium assumption, the kinetic energy dissipation rate is constant and the following relation between a RANS and a LES model can be established:

$$\frac{\nu_t}{\Delta^{\frac{4}{3}}} = \frac{\nu_t^{\text{RANS}}}{L_{\text{RANS}}^{\frac{4}{3}}} \quad (7.34)$$

yielding to<sup>7</sup>:

$$f\left(\frac{\Delta}{L_{RANS}}\right) = \frac{\Delta^{\frac{4}{3}}}{L_{RANS}^{\frac{4}{3}}}. \quad (7.36)$$

Finally, Magnient obtains the following expression of the eddy viscosity:

$$\nu_t = C_e \Delta^{\frac{4}{3}} \varepsilon^{\frac{1}{3}}, \quad C_e = 0.0966 \quad (7.37)$$

where  $k$  and  $\varepsilon$  are determined using a classical  $k - \varepsilon$  RANS model. It is also worth remembering that Eq. (7.37) is not aimed at the treatment of wall bounded flows. He used the above model to simulate a temporal evolving mixing layer and observed that this new model derived from a  $k - \varepsilon$  RANS model gives results similar to those obtained with classical LES. Magnient concluded that his approach is not fully satisfactory since the constants of the RANS turbulence model need to be recalibrated to perform a Very Large Eddy Simulation. This last remark has also been advocated for Semi-Deterministic or Organized Eddy Simulation (see Sec. 7.3.2).

## 7.4.2 Limited Numerical Scales (LNS)

### 7.4.2.1 General idea of LNS

A variant of VLES, LNS (Limited Numerical Scales) has been introduced by Batten *et al.* [Batten *et al.*, 2000; Batten *et al.*, 2002] as a mean of closure for Speziale's [Speziale, 1997; Speziale, 1998] approach (see Sec. 7.4.1). The LNS achieves this goal by re-defining Speziale's latency parameter  $\alpha$  (see Eq. 7.28), with the following ratio of effective-viscosity norms:

$$\alpha = \frac{\min [(LV)_{LES}, (LV)_{RANS}]}{(LV)_{RANS}} \quad (7.38)$$

where  $(LV)$  is the length-scale/velocity scale product of some LES subgrid scale model, and  $(LV)_{RANS}$  is the corresponding product for the given

---

<sup>7</sup>A similar rescaling law for computing the subgrid viscosity was proposed by Zajczkowski and Peltier [Zajczkowski and Peltier, 2001]. Following inertial range arguments, they suggest computing the subgrid viscosity  $\nu_t^{LES}$  from the RANS eddy viscosity  $\nu_t^{RANS}$  as:

$$\nu_t^{LES} = f\left(\frac{\Delta}{L_{RANS}}\right) \nu_t^{RANS} \quad \text{with} \quad f\left(\frac{\Delta}{L_{RANS}}\right) \nu_t^{RANS} = \left(\frac{\Delta}{L_{RANS}}\right)^2. \quad (7.35)$$

RANS model. The  $\alpha$  parameter is envisioned to play a strong role in the blending strategy since the length scale/velocity scale product is a primary parameter that has strong influence on the eddy viscosity amplitude. It is also worthwhile to note from Eq. (7.38) that no additional closure coefficient is required. In the case where consistent models are assumed for both LES and RANS stress tensors, the latency factor simply selects the shear-stress of minimum magnitude. When fine grid regions are encountered by the LNS method, due to the scaling of the predicted Reynolds-stress tensor by  $\alpha$ , the eddy viscosity is instantaneously decreased to the levels implied by the underlying sub-grid model.

#### 7.4.2.2 Example of application

Any trusted RANS turbulence model can be combined with any pre-existing SGS model. As an example, assuming a linear Boussinesq closure, the definition (7.38) implies that the eddy viscosity simply gets multiplied by  $\alpha$ :

$$\nu_t = \alpha \nu_t^{RANS}, \quad 0 \leq \alpha \leq 1. \quad (7.39)$$

From Eq. (7.38), the latency parameter  $\alpha$  can be expressed as:

$$\alpha = \min \left\{ \frac{\nu_t^{LES}}{\nu_t^{RANS} + \epsilon}, 1 \right\} \quad (7.40)$$

where  $\nu_t^{RANS}$  and  $\nu_t^{LES}$  are respectively the RANS eddy viscosity and the SGS viscosity and  $\epsilon$  some small parameter,  $\mathcal{O}(10^{-20})$ , to allow  $\alpha \rightarrow 0$  without singularities in low Reynolds number regions. Note that the LNS formulation contains no additional (empirical) constant beyond those appearing in the baseline RANS and LES models.

As an example, the ‘‘LNS hybridization’’ of a  $k - \epsilon$  turbulence model with the conventional Smagorinsky SGS model yields:

$$\alpha = \min \left\{ \frac{C_{Smag} \Delta^2 S k^2}{C_\mu \epsilon} + \epsilon, 1 \right\}. \quad (7.41)$$

Batten *et al.* defined  $\Delta$  as a measure for the local Nyquist grid wavelength but other definitions gathered in Table 7.1 have been advocated by several authors (see for example Spalart *et al.* 1997, Bush and Mani 2001).

Table 7.1 Definitions of the filter width.  $\Delta t$  is the computational time step,  $|\bar{\mathbf{u}}|$  the local fluid velocity relative to the mesh and  $k$  represents the turbulent kinetic energy.

$\Delta$	Comments
$\Delta_1 = (\Delta x \Delta y, \Delta z)^{\frac{1}{3}}$	classical filter width for LES
$\Delta_2 = \max(\Delta x, \Delta y, \Delta z)$	most widely used definition for global hybrids
$\Delta_3 = 2 \max(\Delta x, \Delta y, \Delta z)$	smallest wave length that can be supported at any orientation to the local mesh
$\Delta_4 = \max(\Delta x, \Delta y, \Delta z,  \bar{\mathbf{u}} \Delta t)$	accounts for both space and time filtering
$\Delta_5 = \max(\Delta x, \Delta y, \Delta z,  \bar{\mathbf{u}} \Delta t, \sqrt{k}\Delta t)$	may be problematic since initial values for $k$ can force permanent RANS behavior whatever the grid spacing and time step are

### 7.4.3 Blending methods

#### 7.4.3.1 General idea of blending methods

As already mentioned, Schumann [Schumann, 1975] was an early contributor in the development of hybrid models. He proposed a wall-model which relates linearly the mean shear stresses to the mean velocity component of the first-off-wall grid point. Nevertheless, Schumann's proposal applied only to the lower section of the boundary layer whereas global RANS/LES methods aim at treating the entire boundary layer with a RANS model.

The blending approach was then revisited by Baggett [Baggett, 1998] who expressed the SGS tensor as a function of the subgrid scale viscosity  $\nu_t^{LES}$  and the eddy viscosity  $\nu_t^{RANS}$  provided by a RANS model:

$$\tau_{ij} - \frac{1}{3}\tau_{kk}\delta_{ij} = - [(1 - \Gamma(y))\nu_t^{LES} + \Gamma(y)\nu_t^{RANS}] \bar{S}_{ij} \quad (7.42)$$

where  $\Gamma(y)$  is a blending function between the RANS and LES descriptions of the flow. When the blending function equals unity, the hybrid model acts in RANS mode whereas the LES component is recovered when  $\Gamma$  is zero. Although  $\Gamma(y)$  depends on the distance to the wall  $y$ , Baggett indicates that the blending function should be parameterized by the ratio  $\Delta/L_\varepsilon$  where  $L_\varepsilon$  is an estimate of the turbulent integral dissipation length and  $\Delta$  is a measure of the filter width.

Further developments in the use of a flow-dependent blending function between RANS and LES regions have been made by Fan *et al.* [Fan *et al.*, 2001; Fan *et al.*, 2002]. Indeed, the intended use of every hybrid methodol-

ogy is to make the model acting in RANS mode for attached wall-bounded flow regions and switching into LES formulation in separated flow regions<sup>8</sup>. This scenario is quite similar to what Menter [Menter, 1994] faced in his work to hybrid the  $k - \varepsilon/k - \omega$  RANS models.<sup>9</sup>

Following ideas borrowed from Menter (see eq. (7.43)), Fan *et al.* suggested using a blending function to shift the RANS model near the solid wall to a subgrid LES model further away for both the Turbulent Kinetic Energy (TKE) and viscosity:

$$\begin{aligned} [\text{hybrid RANS/LES TKE equation}] &= \Gamma \cdot [\text{RANS TKE equation}] \\ &+ (1 - \Gamma) [\text{LES TKE equation}] \end{aligned} \quad (7.45)$$

$$\begin{aligned} [\text{LES/RANS hybrid viscosity}] &= \Gamma \cdot [\text{RANS eddy viscosity}] \\ &+ (1 - \Gamma) [\text{LES SGS viscosity}] \end{aligned} \quad (7.46)$$

where  $\Gamma$  is a flow-dependent blending function in the hybrid RANS/LES simulation designed to yield a value of 1 in the attached boundary layer

---

<sup>8</sup>Hamba [Hamba, 2001] adopted an opposite route by applying LES in the near-wall layer whereas the standard  $k - \varepsilon$  model is solved in the outer region away from the wall. Nevertheless, the author concluded that such an approach is less efficient than the more common strategies with RANS application near the wall.

<sup>9</sup>Menter [Menter, 1994] developed a single RANS model that combines the best features of both  $k - \varepsilon$  and  $k - \omega$  model RANS model. More precisely, his model is designed to retain the robustness and accuracy of the Wilcox  $k - \omega$  model [Wilcox, 1988b] for wall bounded viscous regions while enforcing the  $k - \varepsilon$  model away from the solid surfaces to avoid the undesirable dependance of the  $k - \omega$  model to free stream values of  $\omega_\infty$ . To achieve this goal, Menter linearly combined both RANS models as follows:

$$[\text{Menter's hybrid model}] = F_1 \cdot [k - \omega \text{ model}] + (1 - F_1) [k - \varepsilon \text{ model}] \quad (7.43)$$

where  $F_1$  is a blending function designed to yield a value of 1 near solid surfaces and to fall rapidly to 0 in the outer region of the boundary layer. The following functional form for  $F_1$  was designed to meet these criteria:

$$F_1 = \tanh(\eta^4), \quad \eta = \max\left(\frac{L^{RANS}}{d_w}, \frac{C_d L^{RANS}}{k^{\frac{1}{2}} d_w^2} 500\nu\right), \quad L^{RANS} = \frac{k^{\frac{1}{2}}}{C_\mu \omega} = \frac{k^{\frac{3}{2}}}{C_\mu \varepsilon} \quad (7.44)$$

where  $d_w$  denotes the distance to the closest wall. The first argument compares the RANS turbulence length scale with the distance to the nearest wall. This ratio is equal to one in the logarithmic portion of the boundary layer and approaches zero near the edge of the boundary layer. The second term is designed to ensure that  $\Gamma$  does not go zero in the laminar sublayer.

and to transition rapidly to zero further away. It can also be noted from Eq. (7.46) that any trusted RANS model can be blended with any pre-existing SGS model<sup>10</sup>.

### 7.4.3.2 Applications

As an example, Fan *et al.* [Fan *et al.*, 2002] used Menter's [Menter, 1994]  $k - \omega$  model near the wall and a one-equation subgrid model away from walls. They modified the kinetic energy equation<sup>11</sup> and the eddy-viscosity respectively as follows:

$$\frac{Dk}{Dt} = P_k - \left[ \underbrace{\Gamma (C_\mu k \omega)}_{\varepsilon_{RANS}} + (1 - \Gamma) c_d \underbrace{\frac{k^{3/2}}{\Delta}}_{\varepsilon_{LES}} \right] + \text{diffusion} \quad (7.47)$$

$$\nu_t = \underbrace{\Gamma \frac{k}{\omega}}_{\nu_t^{RANS}} + (1 - \Gamma) \underbrace{c_S \sqrt{k} \Delta}_{\nu_t^{LES}} \quad (7.48)$$

where  $P_k$  is the turbulence kinetic energy production term (approximated by  $P_k = \nu_t \Omega^2$  where  $\Omega$  is the magnitude of vorticity),  $\varepsilon$  the dissipation of  $k$  and  $C_\mu$  a constant appearing in Menter's model.  $\Delta$  is a measure of the grid spacing and  $c_S$  and  $c_d$  are model coefficients.  $c_S$  was chosen as 0.1 in their study while  $c_d$  was taken to 0.01 and 0.1 in two simulations. The blending function  $\Gamma$  is a modification of the one initially used by Menter (see Eq. 7.44):

$$\Gamma = \tanh(\eta^4) \quad \text{with} \quad \eta = \frac{1}{\omega} \max \left( \frac{\sqrt{k}}{C_\mu d_w}, 500 \frac{\nu}{d_w^2} \right). \quad (7.49)$$

<sup>10</sup>The use of transport equations for the turbulent quantities is not fundamental here. For example, Kawai and Fujii [Kawai and Fujii, 2004] blended the Baldwin Lomax zero equation turbulence model [Baldwin and Lomax, 1978] with the Smagorinsky [Smagorinsky, 1963] SGS model thanks to a weighting function of inner and outer regions in the boundary layer.

<sup>11</sup>The modification in the  $k$  equation consists here in rewriting (and increasing) the dissipative term which appears to be a conventional hybrids practice. Indeed, similar modifications are performed in DES (see Sec. 7.4.4.5) and XLES (see Sec. 7.4.4.6). Alternate proposals have been suggested by Basu *et al.* [Basu *et al.*, 2005] by reducing directly the modelled TKE.

It can be noted that in the limit of balancing subgrid production and dissipation ( $\Gamma = 0$ )<sup>12</sup>, the model returns a Smagorinsky type eddy viscosity:

$$\nu_t = c_S \sqrt{\frac{c_S}{c_d}} \Delta^2 \Omega \quad (7.52)$$

with a lower constant value  $c_S \sqrt{\frac{c_S}{c_d}} = 0.1$  (with  $c_d = 0.1$ ) and a higher constant value  $c_S \sqrt{\frac{c_S}{c_d}} = 0.31$  with  $c_d = 0.01$  (to be compared with  $C_{Smag}=0.18$ ).

Fan *et al.* [Fan *et al.*, 2002] used their model to simulate a shock wave/boundary layer interaction of Mach number 3 flow over a 20 degree compression corner. This test case exhibiting thin layer separation is a very difficult test case for hybrid models since no clear separation between regions modelled through RANS and LES is apparent. Their results indicated that the axial extent of the separated area is not well reproduced, mainly due to a too severe loss of modelled turbulent energy. Nevertheless, their approach allows a subsequent shift to an LES mode in the outer part of the recovering boundary layer. Improvements [Fan *et al.*, 2003] were obtained by imposing an appropriate unsteady approach boundary layer showing that treatment of LES inflow sections is also a critical issue for global hybrid RANS/LES methods.

Baurle *et al.* [Baurle *et al.*, 2003] indicate that the blending function given by Eq. (7.49) always forces an LES treatment away from walls even if the mesh is too coarse to support resolved LES eddies, resulting in lower Reynolds stress modelled compared to those provided by the RANS model.<sup>13</sup> To overcome this important problem, the authors

---

<sup>12</sup>It is worth noting that the combination of Eqs 7.47 and 7.48 in the limit  $\Gamma = 0$  yields a one equation model for the transport of the subgrid viscosity:

$$\frac{D\nu_t}{Dt} = \frac{c_S}{2} (c_S \Delta^2 \Omega^2 - c_d k) + \text{diffusion} \quad (7.50)$$

where the turbulent kinetic energy acts as a destruction term in Eq. 7.50. In addition, by neglecting the variation of the filter width  $\Delta$ , one can obtain the following relation between the equations of  $k$  and  $\nu_t$ :

$$\frac{D\nu_t}{Dt} = \frac{\nu_t}{2k} \frac{Dk}{Dt}. \quad (7.51)$$

<sup>13</sup>This important issue encountered in any hybrid RANS/LES approach can be attributed to a “grey-area” between the RANS and LES region (Spalart *et al.* [Spalart *et al.*, 1997]) and was later called Modelled-Stress-Depletion (MSD) by Spalart *et al.* [Spalart *et al.*, 2005a] (see Sec.7.4.5).

redefined the blending function using ideas borrowed from the LNS approach (see Sec. 7.4.2):

$$\Gamma = \max(\tanh(\eta^4, \tilde{\alpha}_{LNS})) \quad (7.53)$$

where

$$\tilde{\alpha}_{LNS} = E \left[ \min \left( \frac{\nu_t^{LES}}{\nu_t^{RANS}}, 1. \right) \right] \quad (7.54)$$

where  $E[x]$  is the integer part of  $x$ .

The parameter  $\tilde{\alpha}_{LNS}$  ensures that the RANS turbulence model is selected if the SGS viscosity  $\nu_t^{LES}$  is greater than the RANS eddy viscosity  $\nu_t^{RANS}$ . Further developments of this blending approach have been pursued by several authors. As an example Xiao, Edwards and Hassan [Xiao *et al.*, 2004] compared the behavior of several blending functions that are either geometry dependent or explicitly dependent of the grid:

$$\Gamma_{vK} = \tanh \left( \frac{L_{vK}}{\alpha_1 \lambda} \right)^2, \quad \Gamma_{d_w} = \tanh \left( \frac{d_w}{\alpha_1 \lambda} \right)^2, \quad \Gamma_{\Delta} = \tanh \left( \frac{L_{RANS}}{\alpha_2 \Delta} \right)^2 \quad (7.55)$$

where  $L_{vK}$  is the *von Kármán* length scale (see Sec. 7.3.3),  $d_w$  the distance to the wall,  $\lambda$  is proportional to the Taylor microscale,  $\alpha_1$  and  $\alpha_2$  are arbitrary constants and  $L_{RANS}$  is the integral turbulent length scale contained in the turbulence model. The authors indicate that  $\Gamma$  has to be a non-decreasing function as the distance from the nearest wall increases, thus re-introducing a certain degree of geometry dependence. The constants of the model  $\alpha_1 = 25$  and  $\alpha_2 = 5$  were chosen such that the blending function  $\Gamma = 1/2$  in the log-law region. These authors then simulate a shock wave/boundary layer interaction over a 20 and 25 degree compression corner. Minor differences between the aforementioned blending functions were observed except concerning the skin friction coefficient. These authors obtained the best results (when compared with the available experimental data) with the blending function  $\Gamma_{vK}$  based on the *von Kármán* length scale which is “explicitly independent” of the grid.

### 7.4.4 Detached-Eddy Simulation

#### 7.4.4.1 General idea

Among hybrid strategies, the approach that has probably drawn most attention in the recent time frame is the Detached Eddy Simulation (DES) which was proposed by Spalart *et al.* [Spalart *et al.*, 1997] and has since gone through various stages of refinement. This modelling strategy was suggested as a response to the conflict between the unaffordable computational cost of a true wall-bounded layer LES and the inability of classical RANS methods to treat properly industrial high Reynolds number flows with massive separation. The approach was given the name Detached Eddy Simulation since the small structures “attached” to the wall would be modelled in RANS mode whereas the larger ones populating the separated regions and wakes, *i.e.* “detached” to the wall, would be resolved.

The DES idea was first proposed in 1997 using a simple modification of the Spalart-Allmaras [Spalart and Allmaras, 1992; Spalart and Allmaras, 1994] RANS model and a more global definition of the technique was given somewhat later by Travin *et al.* [Travin *et al.*, 2000] as follows:

*A Detached-Eddy Simulation is a three-dimensional unsteady numerical solution using a single turbulence model, which functions as a sub-grid-scale model in regions where the grid density is fine enough for a large-eddy simulation, and as a Reynolds-averaged model in regions where it is not.*

From the above definition, a DES model can be obtained from a RANS model by an appropriate modification of the length scale  $L_{RANS}$ , which is explicitly or implicitly involved in any RANS turbulence model<sup>14</sup>. The new DES length scale may be defined as:

$$L_{DES} = \min(L_{RANS}, C_{DES}\Delta) \quad (7.56)$$

where  $C_{DES}$  is a modelling parameter to be determined and  $\Delta$  is based on the largest dimension of the local grid cell:

$$\Delta = \max(\Delta_x, \Delta_y, \Delta_z). \quad (7.57)$$

The use of the maximum grid extension is physically justified as it controls which wavelengths can be resolved and the eddy-viscosity level.

---

<sup>14</sup>The Prandtl-Kolmogorov assumption states  $\nu_t \propto \mathcal{U}\mathcal{L}$  where  $\mathcal{U}$  is the characteristic velocity scale and  $\mathcal{L}$  the length scale of the energy-containing structures.

More precisely, in the attached boundary layer, due to the significant grid anisotropy ( $\Delta_x \approx \Delta_z \gg \Delta_y$ ) typical of the grid in this flow region, in accordance with Eq. (7.56),  $L_{DES} = L_{RANS}$ , and the model reduces to the standard RANS model. Otherwise, once a field point is far enough from walls *i.e.* ( $L_{RANS} < C_{DES}\Delta$ ), the eddy viscosity becomes grid-dependent and the model acts as a subgrid scale version of the RANS model. This initial formulation of DES was later referred to as DES97 by Spalart *et al.* [Spalart *et al.*, 2005a].

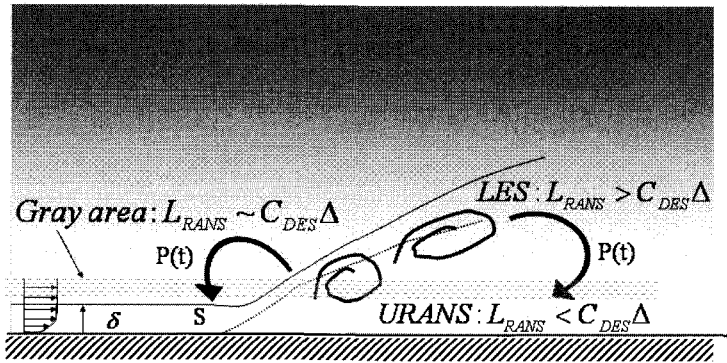


Fig. 7.13 Sketch of RANS and LES regions in a DES approach.

Figure 7.13 shows a “natural” treatment of separation by DES in the sense that the entire boundary layer of thickness  $\delta$  upstream of separation is handled by the RANS model (*i.e.*  $\delta < C_{DES}\Delta$ ). Note that attached boundary layers are affected by the unsteady pressure field and are thus treated in URANS mode.

It is important to stress that the switch from RANS to LES mode is fixed by the grid according to Eq. (7.56). A violation of the inequality  $\delta < C_{DES}\Delta$  may occur due to the use of a very fine grid in both  $x$  and  $z$  directions. The region corresponding to  $L_{RANS} \approx C_{DES}\Delta$  was recognized as potentially delicate and is called “grey-area” by the authors of DES because it is not exactly clear what happens in this region since the solution is neither “pure” RANS nor “pure” LES. This important problem faced in all

hybrid RANS/LES simulations is discussed in further details in Sec. 7.4.5 and a visualization of this RANS/LES interface in the case of boundary layer separation is provided in Fig. 7.14.

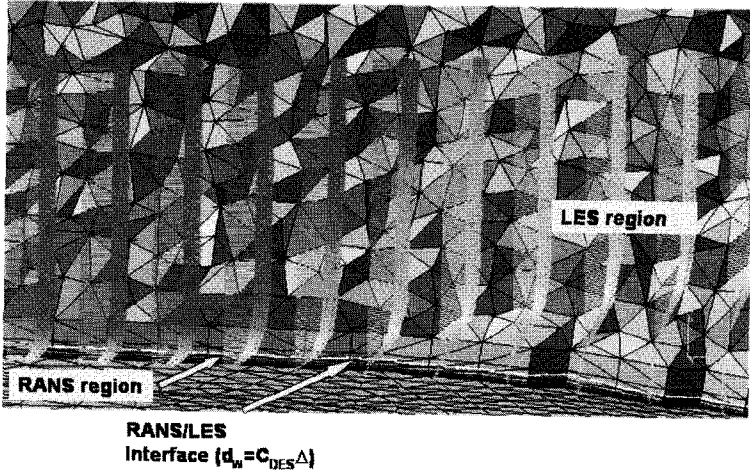


Fig. 7.14 RANS/LES interface location in the vicinity of separation on an unstructured grid. Note that the boundary layer upstream separation has no LES content. Courtesy of J. Forsythe, Cobalt Solutions LLC, USA.

#### 7.4.4.2 DES based on the SA model

The DES model was originally based on the Spalart-Allmaras [Spalart and Allmaras, 1992; Spalart and Allmaras, 1994] RANS model which solves one transport equation for the eddy viscosity. In the following, a brief description of the model is given since different implementation strategies are encountered in the literature depending mainly on the treatment of the RANS damping functions in LES mode. For the sake of clarity, the transition terms are omitted and the standard model reads as:

$$\frac{D\tilde{\nu}}{Dt} = \underbrace{c_{b1}\tilde{S}\tilde{\nu}}_{\text{Production}} + \underbrace{\frac{1}{\sigma} [\nabla \cdot ((\nu + \tilde{\nu})\nabla\tilde{\nu}) + c_{b2}(\nabla\tilde{\nu})^2]}_{\text{Diffusion}} - \underbrace{c_{w1}f_w \left(\frac{\tilde{\nu}}{d_w}\right)^2}_{\text{Destruction}}. \quad (7.58)$$

The eddy viscosity is defined as

$$\nu_t = \tilde{\nu} f_{v1}. \quad (7.59)$$

In order to ensure that  $\tilde{\nu}$  equals  $Ky\tau$  in the log layer, in the buffer layer and in the viscous sublayer, a damping function  $f_{v1}$  is defined as:

$$f_{v1} = \frac{\chi^3}{\chi^3 + c_{v1}^3} \quad \text{with} \quad \chi = \frac{\tilde{\nu}}{\nu}. \quad (7.60)$$

The vorticity magnitude  $S$  is modified such that  $\tilde{S}$  maintains its log-layer behavior ( $\tilde{S} = \frac{y\tau}{Ky}$ ):

$$\tilde{S} = \sqrt{2\Omega_{ij}\Omega_{ij}} f_{v3} + \frac{\tilde{\nu}}{K^2 d_w^2} f_{v2}, \quad \Omega_{ij} = \frac{1}{2} \left( \frac{\partial \tilde{u}_i}{\partial x_j} - \frac{\partial \tilde{u}_j}{\partial x_i} \right) \quad (7.61)$$

which is accomplished with help of the functions<sup>15</sup>:

$$f_{v2} = 1 - \frac{\chi}{1 + \chi f_{v1}}, \quad f_{v3} = 1. \quad (7.63)$$

In order to obtain a faster decay of the destruction term in the outer region of the boundary layer, a function  $f_w$  is introduced:

$$f_w(g) = g \left( \frac{1 + c_{w3}^6}{g^6 + c_{w3}^6} \right)^{1/6}, \quad g = r + c_{w2} (r^6 - r), \quad r = \frac{\tilde{\nu}}{\tilde{S} K^2 d_w^2} \quad (7.64)$$

where  $g$  acts as a limiter that prevents large values of  $f_w$ . Both  $r$  and  $f_w$  are equal to 1 in the log-layer and decrease in the outer region. Constants of the model are:

---

<sup>15</sup>Note that  $\tilde{S}$  can become negative which may disturb  $r$  and results in numerical blinking. Therefore, Spalart proposed an other possibility to define the  $f_v$ 's functions:

$$\tilde{f}_{v2}(\chi) = \left( 1 + \frac{\chi}{c_{v2}} \right)^{-3} \quad \tilde{f}_{v3}(\chi) = \frac{(1 + \chi f_{v1})(1 - \tilde{f}_{v2})}{\chi} \quad c_{v2} = 5. \quad (7.62)$$

Now  $\tilde{S} \geq 0$  since the modified  $f_{v2}$  function remains positive along the wall and  $\tilde{f}_{v3}$  differs notably from 1 in the close vicinity of solid walls. It has been observed (Deck *et al.* [Deck *et al.*, 2002a]) that modified functions ( $\tilde{f}_{v2}, \tilde{f}_{v3}$ ) shifts laminar-turbulent transition backward but do not modify the steady-state solution.

$$c_{b1} = 0.1355, \quad c_{b2} = 0.622, \quad \sigma = \frac{2}{3}, \quad K = 0.41$$

$$c_{w1} = \frac{c_{b1}}{K^2} + \frac{1 + c_{b2}}{\sigma}, \quad c_{w2} = 0.3, \quad c_{w3} = 2, \quad c_{v1} = 7.1. \quad (7.65)$$

What is important here is that the model is provided with a destruction term for the eddy viscosity that contains  $d_w$ , the distance to the closest wall. This term when balanced with the production term, adjusts the eddy viscosity to scale with local deformation rate  $\tilde{S}$  producing an eddy viscosity given by

$$\tilde{\nu} \sim \tilde{S} d_w^2. \quad (7.66)$$

Following these arguments, Spalart *et al.* suggested to replace  $d_w$  with a new length  $\tilde{d}$  given by

$$\tilde{d} = \min(d_w, C_{DES}\Delta). \quad (7.67)$$

Postulating a local equilibrium between production and destruction<sup>16</sup> at the high Reynolds number limit, the balance between these terms yields:

$$c_{b1} S \nu_t = c_{w1} f_w^{DES} \left( \frac{\nu_t}{C_{DES}\Delta} \right)^2 \quad (7.68)$$

leading to

$$\nu_t = \frac{c_{b1}}{c_{w1} f_w^{DES}} C_{DES}^2 \Delta^2 S \quad (7.69)$$

$f_w^{DES}$  can be determined by noticing from Eqs. (7.64) and (7.69) that:

$$r^{DES} = \frac{\nu_t}{SK^2 C_{DES}^2 \Delta^2} = \frac{c_{b1}}{f_w^{DES} c_{w1} K^2} \quad (7.70)$$

and then solving the following equation for  $f_w^{DES}$ :

$$f_w^{DES} = g(f_w^{DES}) \left( \frac{1 + c_{w3}^6}{g(f_w^{DES})^6 + c_{w3}^6} \right)^{1/6}. \quad (7.71)$$

The physically acceptable root of this equation [Strelets, 2002] is given by

$$f_w^{*DES} = 0.424. \quad (7.72)$$

<sup>16</sup>Like many turbulence models which contain cross diffusion terms of the turbulent variables, the Spalart Allmaras model contains a non-conservative diffusion term  $\frac{c_{b2}}{\sigma} (\nabla \tilde{\nu})^2$  (see Eq 7.58) that acts as a positive source term in the  $\tilde{\nu}$  equation and does not favor the decrease of eddy viscosity in LES mode.

Following a conventional LES practice, Shur *et al.* [Shur *et al.*, 1999] calibrated the constant  $C_{DES}$  on the basis of the data of Comte-Bellot and Corrsin [Comte-Bellot and Corrsin, 1971] on the spectrum of Decaying Homogeneous Isotropic Turbulence (DHIT). Their numerical approximations used to calibrate  $C_{DES}$  are based on a centered fourth order difference scheme for the advective fluxes and a second order accurate backward scheme for time integration. They adjusted the constant  $C_{DES}$  to provide the best fit of the resolved energy spectra to the experimental ones, with a special care to the correct spectral slope in the inertial range near cut-off number. The authors recommended the value:

$$C_{DES} = 0.65. \quad (7.73)$$

Finally, the already mentioned relation  $\tilde{\nu} \sim \tilde{S} d_w^2$  becomes

$$\nu_t = C_{DES}^2 \underbrace{\frac{c_{b1}}{c_{w1} f_w^*}}_{\tilde{C}_S^2=0.20^2} \Delta^2 < S > \quad (7.74)$$

which is analogous to the well-known Smagorinsky model and the equivalent constant  $\tilde{C}_S$  appearing in the eddy viscosity can be compared to the constant appearing in the Smagorinsky model  $C_{Smag} = 0.18$ . Note that DES also provides a dynamic SGS model in a sense.

Some authors (Spalart [Spalart, 2001], Travin *et al.* [Travin *et al.*, 2000], Aupoix *et al.* [Aupoix *et al.*, 2001]), highlight that the comparison with Smagorinsky's model cannot be performed completely since we do not know exactly if the grid size  $\Delta$  is really the cut-off scale. It is only known to be of the order of  $\Delta$  and a set of "filtered equations" is not available.

#### 7.4.4.3 Possible extensions of standard SA-DES

Breuer *et al.* [Breuer *et al.*, 2003] showed that in practice, replacing  $d_w$  by  $\tilde{d}$  in every equation of the RANS model can lead to unexpected distribution of eddy viscosity. Indeed the damping function of the RANS model may interpret the low eddy viscosity levels typical of resolved LES regions as closeness to the wall with corresponding fast non-linear drop of subgrid viscosity. Therefore, they suggest to disable the near wall functions in the low Reynolds terms only in the LES mode of DES:

$$f_{v1} = 1 \quad f_{v2} = 0 \quad f_w = 1. \quad (7.75)$$

This choice is also motivated by the RANS behavior of the  $f$  functions farther away from the wall. Note that these modifications will theoretically modify the value of the additional model constant  $C_{DES} = 0.65$  which was calibrated by Shur *et al.* [Shur *et al.*, 1999] using isotropic turbulence with the original near wall functions. Indeed, Eq. (7.75) implies:

$$f_w^{*DES} = 1 \quad (7.76)$$

and the equivalent constant becomes  $\tilde{C}_S = 0.13$ . However the resulting slight modification of  $C_{DES}$  should not be crucial [Spalart, 2000a]. It is worth recalling that Shur *et al.* [Shur *et al.*, 1999] calibrated  $C_{DES}$  by using high-order centered difference and variations of  $C_{DES}$  can also be attributed to differences in numerical dissipation when using second-order upwind differences<sup>17</sup>.

However, Eq. (7.75) may lead to a discontinuity of  $\nu_t$  at the RANS/LES interface due to the discontinuity of  $f_w$  compared to its RANS value. Therefore, an alternative proposal that prevents activation of the low Reynolds terms in LES mode has been made by Shur *et al.* [Shur *et al.*, 2003] (see also [Spalart *et al.*, 2005a]) by introducing a threshold function based on  $\nu_t/\nu$  in the definition of the length scale:

$$L_{DES} = \min \left( L_{RANS}, \Psi \left( \frac{\nu_t}{\nu} \right) C_{DES} \Delta \right). \quad (7.77)$$

Indeed, due to the  $f_{v1}$  and  $f_{v2}$  functions (see Eqs. (7.60) and (7.63)), the equivalent Smagorinsky constant in the SA-DES model turns out to be a function of subgrid eddy-viscosity  $\tilde{C}_S \left( \frac{\nu_t}{\nu} \right)$  which is virtually constant for  $\nu_t/\nu \geq 15$  (e.g.  $f_{v1} = 1$ ) but drops quickly to zero when  $\nu_t/\nu < 10$  (e.g.  $f_{v1} = 0$  at the wall)<sup>18</sup>. The new function  $\Psi \left( \frac{\nu_t}{\nu} \right)$  ensures that at equilibrium

<sup>17</sup>Note that taking  $C_{DES} = 0$  brings the method very close from Implicit LES (ILES).

<sup>18</sup>Indeed, Eq. (7.68) has been written by postulating a local equilibrium between production and destruction *in the high Reynolds number limit*. but in practice, the balance between these terms yields:

$$c_{b1} \left( S + \frac{\tilde{\nu}}{K^2 C_{DES}^2 \Delta} f_{v2} \right) \tilde{\nu} = c_{w1} f_w^{*DES} \left( \frac{\tilde{\nu}}{C_{DES} \Delta} \right)^2. \quad (7.78)$$

Due to the definition of the eddy viscosity (see Eq. 7.59), one can show that:

$$\nu_t = \frac{f_{v1} c_{b1} C_{DES}^2}{c_{w1} f_w^{*DES} - \frac{c_{b1}}{K^2} f_{v2}} = \underbrace{(\varphi C_{DES})^2}_{\tilde{C}_S^2 \left( \frac{\nu_t}{\nu} \right)} \Delta^2 S \quad \text{with} \quad \varphi \equiv \varphi \left( \frac{\nu_t}{\nu} \right). \quad (7.79)$$

the model reduces to  $\tilde{C}_{DES} \equiv \text{constant}$  and is defined by:

$$\Psi^2 = \min \left[ 100, \frac{1 - \frac{c_{b1}}{c_{w1} K^2 f_w^* f_{v2}}}{f_{v1}} \right] \quad (7.80)$$

where  $\Psi$  is limited to ensure reasonable behavior in the DNS limit  $\nu_t < \nu/100$ . Note that  $\Psi$  becomes quite strong for subgrid eddy viscosity less than  $10\nu$  whilst  $\Psi = 1$  at high Reynolds number (e.g.  $\nu_t \gg \nu$  and  $f_{v2} = 0$ ,  $f_{v1} = 1$ ) and thus does not require any re-calibration of  $C_{DES}$ . This modification has been successfully applied to the DHIT problem and to the NACA0012 at 60 angle of attack (see [Shur *et al.*, 2003]).

#### 7.4.4.4 Examples

Among the global hybrid methods, the DES approach currently has the widest experience, and published calculations concern both generic and technical flows. For instance, Constantinescu and Squires [Constantinescu and Squires, 2004] performed calculations of sub and supercritical flows over a sphere, Travin *et al.* [Travin *et al.*, 2000] performed DES past a circular cylinder, Forsythe *et al.* [Forsythe *et al.*, 2003] reported DES predictions of the flow over an *F-15E* fighter at 65° angle of attack (see Figs. 7.15 and 7.16), Deck *et al.* [Deck *et al.*, 2002b] evaluated unsteady loads due to separated flows over space launcher configurations, Kumar and Loth [Kumar and Loth, 2001] as well as Mogili *et al.* [Mogili *et al.*, 2005] performed iced-wing simulations and the F/A-18 Tail buffet was investigated by Morton *et al.* [Morton *et al.*, 2004].

#### 7.4.4.5 DES based on the $k - \omega$ model

As already mentioned in Sec. 7.4.4.1, the DES-SA link is not fundamental and Strelets [Strelets, 2001] introduced a DES model based on Menter's [Menter, 1994] Shear Stress Transport (STT) model. The driving length scale for the Spalart-Allmaras model is the distance to the closest wall,  $d_w$  and the DES procedure is straightforward. In two-equation RANS turbulence models, the length scale  $L_{RANS}$  appears in different terms which

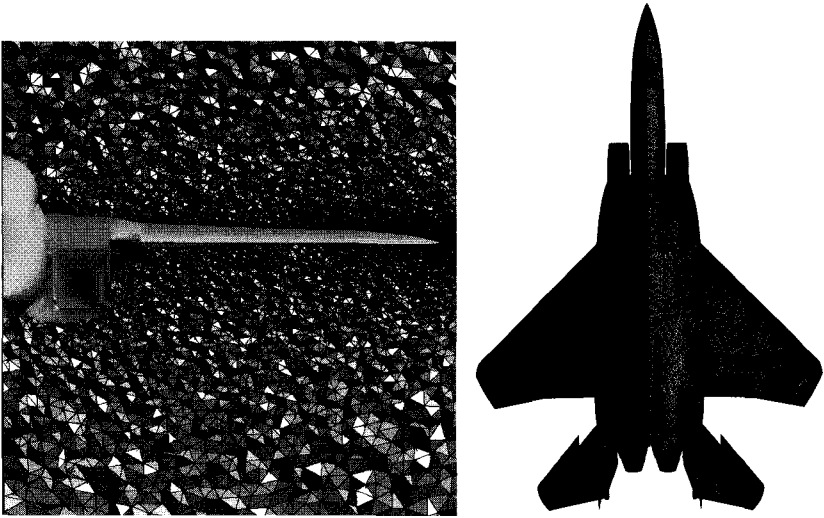


Fig. 7.15 Unstructured computational mesh near aircraft surface. The finest DES grid has approximately  $2.2 \times 10^5$  faces on the aircraft and  $10 \times 10^6$  cells (mixed tetrahedrons and prisms) whereas  $2.85 \times 10^6$  cells are used for the coarse grid. Courtesy of J. Forsythe, Cobalt Solutions LLC, USA.

provides a freedom of choice [Yan *et al.*, 2005] regarding specific terms where this length scale should be replaced by the DES length scale  $L_{DES}$  in accordance with Eq. (7.56).

As an example, the  $k$  and  $\omega$  transport equation read:

$$\frac{Dk}{Dt} = P^k - \underbrace{\varepsilon}_{D^k} + \nabla \cdot ((\nu + \nu_k \sigma_t) \nabla k) \quad (7.81)$$

$$\frac{D\omega}{Dt} = P^\omega - D^\omega + \nabla \cdot ((\nu + \nu_\omega \sigma_t) \nabla \omega) + (1 - F_1) CD_{k-\omega}$$

where  $P^k$  (respectively  $P^\omega$ ),  $D^k = \varepsilon$  (respectively  $D^\omega$ ) are the production and destruction terms of  $k$  (respectively  $\omega$ ) and  $CD_{k-\omega}$  the cross diffusion term of  $k$  and  $\omega$ , which are defined by:

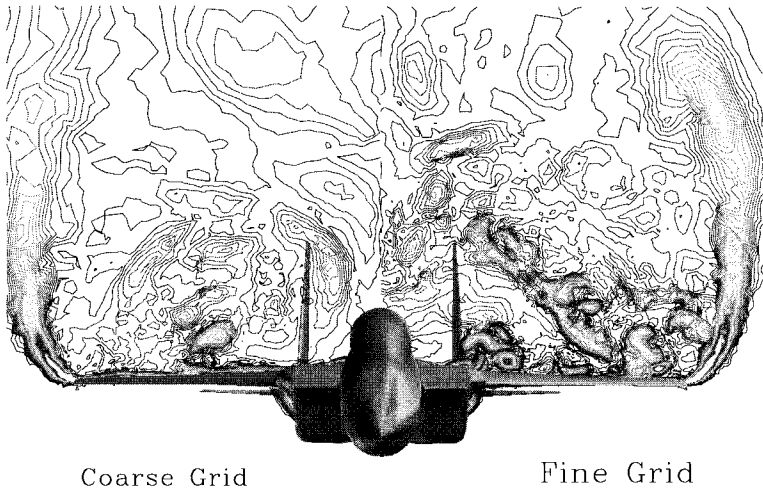


Fig. 7.16 Vorticity contours along a section of the aircraft (Coarse-grid results in the left half part and fine-grid DES predictions in the right-half part. The free stream Mach number is equal to 0.3 resulting in a chord-based Reynolds number of  $13.6 \times 10^6$ . Note the ability of DES in its LES mode to resolve turbulent features, e.g. geometry-dependent eddies over the aircraft. Moreover, a wider range of scales is captured with mesh refinement. Courtesy of J. Forsythe, Cobalt Solutions LLC, USA.

$$P^k = \tau_{\mathbf{R}} : \mathbf{S} \quad (7.82)$$

$$D^k = C_{\mu} \omega k \quad (7.83)$$

$$P^{\omega} = \frac{\gamma}{\nu_t} P^k \quad (7.84)$$

$$D^{\omega} = \beta \omega^2 \quad (7.85)$$

$$CD_{k-\omega} = 2 \frac{\sigma_{\omega}^2}{\omega} \nabla k \cdot \nabla \omega \quad (7.86)$$

where  $\tau_{\mathbf{R}}$  is the tensor of the Reynolds stresses and  $\mathbf{S}$  is the mean strain tensor. The eddy viscosity is defined as:

$$\nu_t = \phi_{SST} \frac{k}{\omega} \quad (7.87)$$

$\phi_{SST}$  limits the turbulent shear stress to  $a_1 k$  where  $a_1 = 0.31$  and is defined by:

$$\phi_{SST} = \frac{a_1}{\max(a_1\omega, \frac{\Omega}{\omega}F_2)}, \quad F_2 = \tanh(arg_2^2) \quad (7.88)$$

$$arg_2 = \max\left(\frac{2\sqrt{k}}{0.09\omega d_w}, \frac{400\nu}{\omega d_w^2}\right), \quad C_{D\omega} = \max(CD_{k-\omega}; 10^{-20}) \quad (7.89)$$

$\Omega$  is the magnitude of vorticity,  $d_w$  the distance to the wall whereas  $F_1$  defined by:

$$F_1 = \tanh(arg_1^4), \quad arg_1 = \min\left(\max\left(\frac{\sqrt{k}}{0.09\omega d_w}, \frac{500\mu}{\omega d_w^2}\right), \frac{4\sigma_{\omega_2}k}{C_{D\omega}d_w^2}\right) \quad (7.90)$$

is a switching function that determines the value of the model constant (see also Sec.7.4.3). For instance, if  $\phi_1$  represents a generic constant of the  $k-\omega$  model and  $\phi_2$  represents the same for the  $k-\varepsilon$  equations, the model constants used in Eqs. 7.82 are determined by:

$$\phi = F_1\phi_1 + (1 - F_1)\phi_2. \quad (7.91)$$

Constants of the model are:

$$\begin{aligned} \sigma_{k1} = 0.85, \quad \sigma_{\omega_1} = 0.5, \quad \beta_1 = 0.075, \quad a_1 = 0.31 \\ \sigma_{k2} = 1.0., \quad \sigma_{\omega_2} = 0.856, \quad \beta_2 = 0.0828, \quad C_\mu = 0.09 \\ \gamma = \frac{\beta}{C_\mu} - \frac{\sigma_\omega K^2}{C_\mu}, \quad K = 0.41. \end{aligned} \quad (7.92)$$

In the SST model, the turbulent length scale is given by:

$$L_{k-\omega}^{RANS} = \frac{k^{\frac{1}{2}}}{C_\mu\omega}. \quad (7.93)$$

One can notice that this length scale can be expressed in several terms in the above equations. The DES modification suggested by Strelets [Strelets, 2001] replaces the length scale  $L_{k-\omega}^{RANS}$  by:

$$L_{k-\omega}^{DES} = \min(L_{k-\omega}^{RANS}, C_{DES}\Delta) \quad (7.94)$$

only in the dissipative term for the kinetic energy equation:

$$D_k^{DES} = \frac{k^{\frac{3}{2}}}{L_{k-\omega}^{DES}}. \quad (7.95)$$

Since Menter's SST model is based on a blending of  $k-\varepsilon$  and  $k-\omega$ , Strelets calibrated the model by running both the  $k-\varepsilon$  and  $k-\omega$  DES models on isotropic turbulence. This lead to:

$$C_{DES}^{k-\omega} = 0.78, \quad C_{DES}^{k-\varepsilon} = 0.61. \quad (7.96)$$

Strelets [Strelets, 2001] compared the ability of DES models based respectively on the Spalart-Allmaras and  $k-\omega$  models to predict the aerodynamic coefficients for the NACA0012 airfoil (see Fig. 7.17) at several angles of attack (see Fig. 7.12 for a visualization of the flowfield over the airfoil at a  $45^\circ$  angle of attack). The author observed that there are much less disparities between the two DES models than between the same two models in URANS mode.

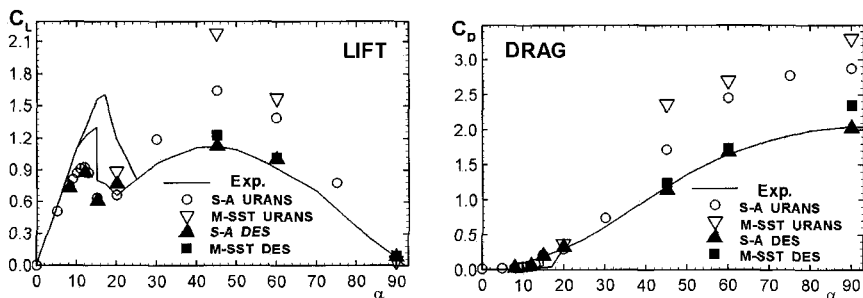


Fig. 7.17 Lift and drag coefficient for NACA0012 airfoil : comparison of URANS and DES predictions with experimental data. Note that beyond stall, URANS suffers from a very large drag and lift excess (especially for  $\alpha \geq 30^\circ$ ) whereas both DES-SST and DES-SA are in fair agreement with experiment. Courtesy of M. Strelets, NTS, Russia.

#### 7.4.4.6 Extra-Large Eddy Simulation (XLES)

Kok *et al.* [Kok *et al.*, 2004] attached importance to the precise SGS model employed in the LES mode of the hybrid approach and outlined that the DES models do not include a clearly defined SGS model. As an example, it has been seen in Sec. 7.4.4.2 that in DES-SA, the model returns a Smagorinsky-like model only if, in the high-Reynolds number limit, local equilibrium is assumed between the production and destruction terms of the eddy viscosity. The same remark holds for the DES-SST where a local equilibrium assumption in both the  $k$  and  $\omega$  equations has to be assumed. This assumption for both production and dissipation of  $k$  seems unlikely

to appear simultaneously in situations far-from-equilibrium regimes like massively separated flows (see Chapter 3)

Bush and Mani [Bush and Mani, 2001] proposed an hybrid RANS/LES model where the  $k - SGS$  model [Schumann, 1975] is recovered in LES mode without making an equilibrium assumption. They applied the basic idea of DES (see Eq. (7.67)) to all turbulent variables. Inspired by them, an alternative proposal to DES-SST by Kok *et al.* [Kok *et al.*, 2004] consists in a modification of the turbulent length scale in the dissipation term of  $k$  but also in the eddy viscosity expression. The formulation named X-LES (Extra Large Eddy Simulation) consists of a decomposition of a RANS  $k - \omega$  TNT [Kok, 2000] turbulence model and a  $k - SGS$  model. The differences between the RANS and the SGS model lies in the modelling of the eddy viscosity and the dissipation of the turbulent kinetic energy for which different length scales are used:

$$\nu_t = L_{RANS} k^{\frac{1}{2}}, \quad \varepsilon = C_\mu \frac{k^{\frac{3}{2}}}{L_{RANS}}, \quad L_{RANS} = \frac{k^{\frac{1}{2}}}{\omega} \quad (7.97)$$

for the RANS model and

$$\nu_t = C_1 \Delta k^{\frac{1}{2}}, \quad \varepsilon = C_2 \frac{k^{\frac{3}{2}}}{\Delta}, \quad L_{LES} = C_1 \Delta \quad (7.98)$$

for the SGS model.

Similarly to Eq. (7.67), the XLES formulation is obtained by replacing the length scales in the eddy viscosity by a composite length scale:

$$L_{XLES} = \min(L_{RANS}, C_1 \Delta) \quad (7.99)$$

so that

$$\nu_t = L_{XLES} k^{\frac{1}{2}} \quad \text{and} \quad \varepsilon = C_\mu \frac{k^{\frac{3}{2}}}{L_{XLES}} \quad (7.100)$$

or

$$\nu_t = \min \left( \underbrace{\frac{k}{\omega}}_{\nu_t^{RANS}}, \underbrace{C_1 k^{\frac{1}{2}} \Delta}_{\nu_t^{LES}} \right) \quad (7.101)$$

and

$$\varepsilon = \max \left( \underbrace{C_\mu k \omega}_{\varepsilon_{RANS}}, \underbrace{C_2 \frac{k^{3/2}}{\Delta}}_{\varepsilon_{LES}} \right). \quad (7.102)$$

Where  $C_1 = 0.06$  was calibrated in LES mode with a DHIT simulation and  $C_2 = C_\mu/C_1$  in order to make  $\nu_t$  and  $\varepsilon$  switch simultaneously. In addition, the production, destruction and diffusion terms are modified *via* the eddy viscosity. The flow solutions are dynamically divided into RANS and LES regions. In regions where  $L_{RANS} > C_1 \Delta$ , XLES is in LES mode and the original  $k$ -equation SGS model is applied whereas approaching a solid wall,  $L_{RANS}$  goes to zero and thus the model acts in RANS mode.

It can also be noted that the eddy viscosity defined by Eq. (7.101) is very close from the one provided by LNS (see Eq. (7.39)) which takes the minimum between the RANS eddy viscosity and the SGS viscosity. The XLES approach falls also into the category of DES due to the definition of the XLES length scale (see Eq. (7.99)). Equations (7.102) and (7.101) can also be compared to those provided by the blending methods (see Eqs. (7.47) and (7.48)) except that the shift from RANS to LES is achieved through a smoother blending function rather than with the *min* function within XLES. This illustrates again how these approaches are close to each other. Therefore, the important issue of “grey-area” discussed in Sec. 7.4.5 faces any hybrid RANS/LES method.

#### 7.4.5 Grey Area-Grid Induced Separation (GIS)

Detached Eddy Simulation is well understood in thin boundary layers where the model acts in RANS mode, and in regions of massive separation where the model acts as a subgrid scale version of the RANS model. However, standard DES introduces a significant dependency into the RANS part of the simulation. Indeed, in its intended use, attached boundary layers are treated entirely in pure RANS mode and, according to Eq. (7.67), the simulation requires a near wall grid spacing in tangential directions that is larger than the boundary layer thickness at that location ( $\Delta_x \approx \Delta_z > \delta$ , see Fig. 7.18a). The other extreme is the LES grid with  $\Delta_x < \delta$  (see Fig. 7.18c) since the model acts in LES mode with wall-modelling very near the wall. Unfortunately, difficulties arise for “ambiguous” grids [Spalart, 2004] when the switching to LES mode occurs inside the boundary layer, e.g. when the

grid brings the  $\tilde{d} = C_{DES}\Delta$  branch of Eq. (7.67) to intrude the boundary layer (see Fig. 7.18b). The region corresponding to  $d \approx \Delta$  is called “grey-zone” by the authors of DES (Spalart *et al.* [Spalart *et al.*, 1997; Spalart, 2000b]) because it is not clear what exactly happens in this region in which the model needs to convert from fully modelled turbulence (attached boundary layer) to mostly resolved turbulence (massive separation).

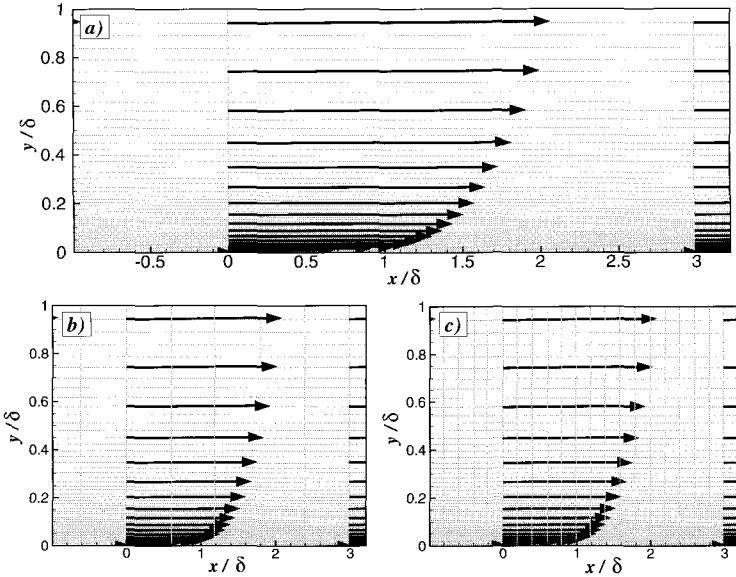


Fig. 7.18 Grid densities in a boundary layer: a) RANS ( $\Delta_x > \delta$ ); b) ambiguous spacing; c) LES ( $\Delta_x < \delta$ ). Assume  $\Delta_z \approx \Delta_x$  (adapted from Spalart, 2004).

The result is a weakened eddy viscosity, but not weak enough to allow LES eddies to form resulting in lower Reynolds stress levels compared to those provided by the RANS model. This was referred to as “Modelled-Stress-Depletion” (MSD) by Spalart *et al.* [Spalart *et al.*, 2005a] and is illustrated in Fig. 7.19. In addition, the depleted stresses decrease the skin friction coefficient and at worst may cause premature separation or “Grid-Induced Separation (GIS)” [Menter *et al.*, 2003].

Nikitin *et al.* [Nikitin *et al.*, 2000] used DES as a wall-layer model in calculations of plane channel flow with different grids exploring a wide range of Reynolds number ( $180 \leq Re_\tau \leq 8000$ ). Their calculations showed some

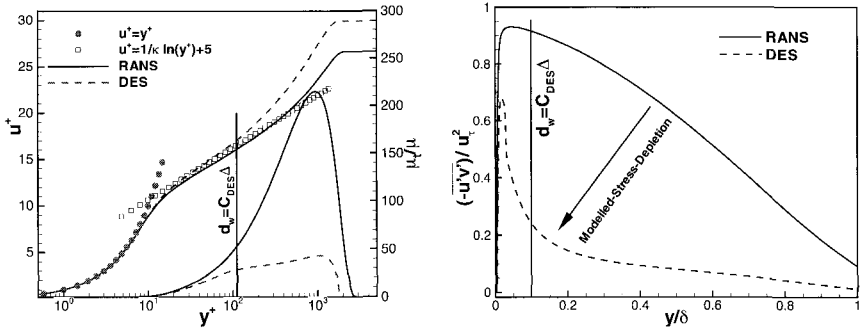


Fig. 7.19 Modelled-Stress-Depletion (MSD) in flat plate boundary layer;  $C_{DES}\Delta \approx 0.1\delta$ . Note that the DES peak eddy viscosity is reduced by about 75% and the skin friction by 20% over the RANS prediction.

promising results since the turbulence in the outer layer was sustained even in the grid areas not particularly refined ( $(\Delta_x^+)_{max} \approx 8000$ ). Moreover, these authors have shown that the velocity profiles have a “modelled” logarithmic layer near the wall (contained in the RANS model) and a “resolved” logarithmic layer in the core region of the channel since LES is performing, but the two layers have a mismatch of several wall units in  $U^+$ . This issue is called “log-layer mismatch (LLM)” by Spalart *et al.* [Spalart *et al.*, 2005a]. Furthermore, the skin friction coefficient was under-predicted by approximately 15% in most cases. The same under-prediction has also been observed by Caruelle and Ducros [Caruelle and Ducros, 2003] in the case of a DES calculation of a flat plate on a LES grid. This intermediate blending region within the DES approach was studied more deeply by Piomelli *et al.* [Piomelli *et al.*, 2003]. They performed LES of the flow in a plane channel at high Reynolds number by varying the location and extent of this blending layer. Their study shows that the “DES super-buffer layer” is characterized by very long eddies, with unphysically long time-scales. Improvements were obtained by reducing the value of  $C_{DES}$  to bring the outer-flow eddies closer to the wall. Similarly, in hybrid RANS/LES computations of channel flow, Baggett [Baggett, 1998] also observed too large streamwise structures compared with the expected size of the streaks populating the attached boundary layer. Therefore, Baggett suggested that hybrid RANS/LES methods may be inappropriate for the use of near-wall flow regions because they cannot maintain a physical near-wall cycle. He

argued that the outer flow is coupled to the wall through a physically incorrect buffer layer since the small scale perturbations from the buffer layer are responsible for the major part of the turbulence production. Piomelli *et al.* [Piomelli *et al.*, 2003] used backscatter forcing to introduce small fluctuations in the transition region with the object to generate resolved fluctuations. Peltier and Zajackowski [Peltier and Zajackowski, 2001] modelled the effects of these smaller scale eddies populating the buffer layer using an *ad hoc* white noise forcing. They showed that the core flow is able to extract energy from these fluctuations to organize turbulence eddies. The challenging topic of turbulence generation is discussed in Sec. 8.3.

At this stage, it is worthwhile to stress that grey areas are not specific to DES. Indeed, this issue arises as soon as global hybrid RANS/LES methods are employed since a transition zone exists in which the resolved, energy-containing eddies are gradually generated and grow. More precisely, one wonders how quickly the unsteady turbulent eddies develop after the model has switched from the RANS to the LES mode. This concern is of outstanding importance for the prediction of free shear layers since a delayed onset of resolved eddies may deteriorate the assessment of turbulent stresses due to a reduction of the unresolved turbulence level. Such situations may appear for flows displaying only weak instabilities.

To date, DES is the most widely used hybrid method and imperfections have just become visible earlier. Nevertheless, grey-areas need careful monitoring and some efforts have been done to try to overcome GIS drawback.

## 7.4.6 Solutions against GIS

### 7.4.6.1 Modifying the length scale

Some initial effort was applied against GIS with moderate success. One can notice from Eq. (7.67) that the location of the grey area depends both on the definition of the DES length scale and on  $C_{DES}$ . To keep the original value  $C_{DES} = 0.65$  calibrated on isotropic turbulence, Caruelle and Ducros [Caruelle and Ducros, 2003] introduced a second constant  $C_{DES2}$  only used for selecting the switch position so that:

$$\tilde{d} = C_{DES}\Delta \quad \text{if} \quad d_w > C_{DES2}\Delta. \quad (7.103)$$

The modified distance  $\tilde{d}$  is therefore discontinuous. This approach is nevertheless difficult to use in a predictive industrial context.

An alternative proposal has been suggested by Forsythe *et al.* [Forsythe

*et al.*, 2004] based on a function of  $d$  and  $C_{DES}\Delta$  that overshoots  $C_{DES}\Delta$  when they are nearly equal. More precisely, the authors modified the DES length scale according to the equation:

$$\tilde{d} = \min \left( C_{DES} \max \left( n^2 \frac{\Delta}{d_w} C_{DES} \Delta, \Delta \right), d_w \right) \quad (7.104)$$

where  $n$  is the ratio of the new RANS-LES interface height to the original height. In other words, the parameter  $n$  limits by how much  $\tilde{d}$  is allowed to exceed  $C_{DES}\Delta$ . The authors used the value  $n = 3$  to push the grey-area outside of the boundary layer. These proposals have to be viewed as a partial solution because further refinement will defeat them.

#### 7.4.6.2 Zonal-DES

For complex geometries, the design of the DES grid appears to be a dilemma for the user. On the one hand, the RANS part of the simulation requires a near wall grid spacing in tangential directions that is larger than the boundary layer thickness at that location to avoid GIS. On the other hand, there is no reason why a DES calculation would accept a coarser grid than an LES calculation (except in the boundary layer). Especially, a LES grid is locally refined in all directions since strongly anisotropic grids are inefficient [Spalart, 2001]. As a result, the grid is also refined in regions not intended to be handled by LES. This situation is practically unavoidable in structured grids where refinement is required in some region of high geometric curvature or in presence of thick boundary layers.

This dilemma has motivated the development of the zonal-DES approach [Deck, 2005b] where fully attached boundary layer regions are treated in RANS mode no matter how fine the grid is. That means that, following the example of RANS-LES coupling methods, the user has to select individual RANS and LES domains. The interest of this approach is that the user can focus his grid refinement on regions of interest (e.g. LES regions) without corrupting the boundary layer properties farther upstream or downstream. In addition, the use of special gridding strategies such as patching methods is straightforward with this multi-domain approach. As an example, zonal-DES has been recently used [Deck, 2005a] together with a patch-grid method to investigate the unsteady flowfield over a high-lift wing with deployed slat and flap (see Fig. 7.20). Indeed this flow exhibits large low speed areas, strong pressure gradients, confluence of boundary layers and wake, unsteadiness and three-dimensionality

on fairly large scales. Each of these can create a challenging issue for a hybrid RANS/LES approach (see Fig. 7.21) since a full-LES of this flow is unaffordable due to the wide range of excited scales.

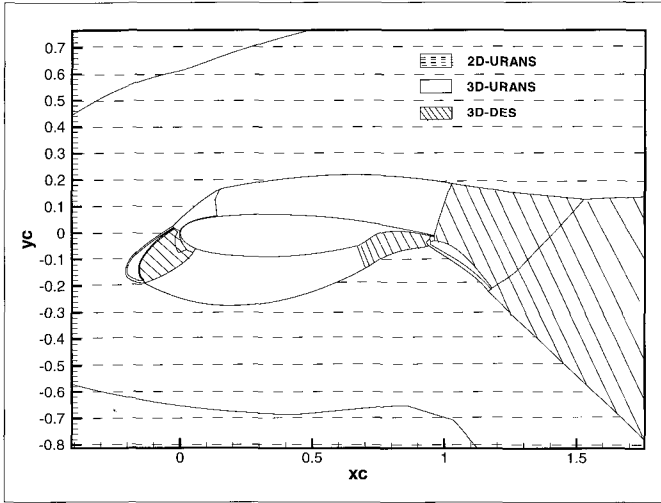


Fig. 7.20 Grid topology and zonal DES. The merging of the slat wake with the main body plays a key-role on the maximum lift coefficient  $CL_{max}$  evolutions. This merging is explicitly treated in URANS mode as well as the attached boundary layer on the main wing, slat and flap. Note also that three-dimensional computations are limited to a zone close to the airfoil where the flow is turbulent, whereas two-dimensional simulations are performed in the far-field (except in the wake).

This explicit character of the splitting of the flow zones differs from zonal RANS/LES coupling since no turbulent fluctuations are reconstructed at the interface (see Chapter 8). Similarly to other global hybrid methods, zonal-DES is well adapted to handle separated flows which develop rapidly strong instabilities which overwhelm the turbulence inherited from upstream boundary layers. This approach may be useful to treat real-life geometries with a very different level of sensitivity in different regions and has been used to investigate transonic buffet on supercritical airfoils [Deck, 2005b] and supersonic base flows [Simon *et al.*, 2006] as well as to assess unsteady loads over a wide range of flight vehicles including launcher-afterbodies, overexpanded nozzles and subsonic missile intake flows [Deck *et al.*, 2005].

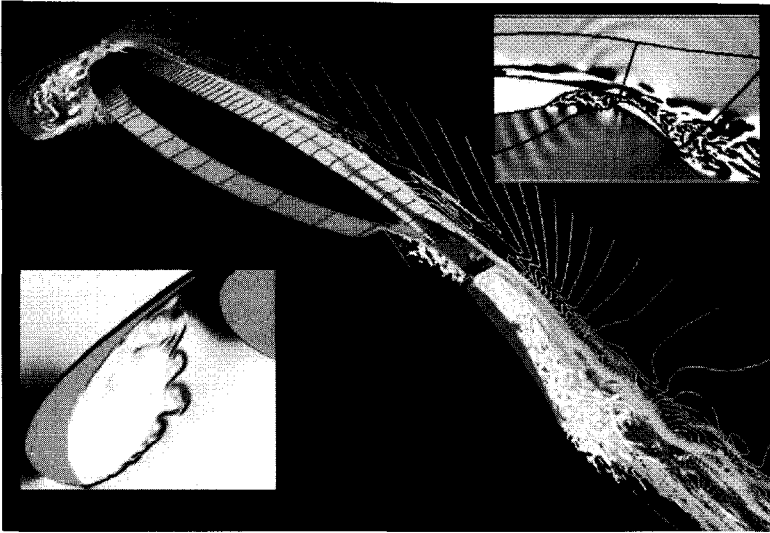


Fig. 7.21 Instantaneous flowfield on a High Lift Device wing using zonal-DES. The  $x - y$  grid has 250,000 points, and the spanwise grid has 31 points with  $\Delta z/c = 0.002$ . The time step is  $2.2 \times 10^{-5} c/U_\infty$ . The chord Reynolds number is  $1.8 \times 10^6$ . Note the self-exciting shear layers growing in the slat and flap covers as well as the propagation of pressure waves emanating from the main wings's trailing edge (Deck, 2005).

#### 7.4.6.3 Shielding the boundary layer-Delayed Detached Eddy Simulation

GIS is not specific to the SA-DES “version” of the model. Indeed, the DES modification of Strelets concerning the  $k - \omega$  model (see eq. (7.95)) can be formulated as a multiplier to the destruction (*i.e.* dissipation) term in the  $k$  equation:

$$\varepsilon = C_\mu \omega k \cdot F_{DES} \quad \text{with} \quad F_{DES} = \max \left( \frac{L_{k-\omega}^{RANS}}{C_{DES} \Delta}, 1 \right). \quad (7.105)$$

The main practical problem with this DES formulation is that there is no mechanism to prevent the limiter from becoming active in the attached portion of the boundary layer.

As the SST model is based on a zonal formulation, differentiating between the boundary layer and the rest of the field, Menter and Kuntz [Menter and Kuntz, 2004] proposed to use the blending functions  $F_1$  or  $F_2$

(see Eqs. (7.90) and (7.88)) to disable the DES limiter inside the boundary layer. They proposed the following modification for the SST-DES model:

$$\tilde{F}_{DES} = \max \left( \frac{L_{k-w}^{RANS}}{C_{DES}\Delta} (1 - f_d), 1 \right) \quad f_d \equiv F_1 \text{ or } F_2 \quad (7.106)$$

$f_d = 0$  recovers the formulation proposed by Strelets [Strelets, 2001], see Eq 7.105.  $F_1$  and  $F_2$  functions equal 1 in the boundary layer and fall to zero rapidly at the edge. Menter and Kuntz recommend the use of  $F_2$  which shields most of the boundary layer. In addition, they indicate that refinement of the surface grid below  $0.1\delta$ , where  $\delta$  is the boundary layer thickness, should be avoided.

Inspired by them, Spalart *et al.* [Spalart *et al.*, 2005a] redefined the DES length scale as follows:

$$\tilde{d} = d_w - f_d \max(0, d_w - C_{DES}\Delta) \quad (7.107)$$

where  $f_d$  is a shielding function designed to be 1 in the LES region and 0 elsewhere. Therefore setting  $f_d$  to 0 yields RANS ( $\tilde{d} = d_w$ ) no matter how fine the grid is, while setting it to 1 gives standard DES ( $\tilde{d} = \min(d_w, C_{DES}\Delta)$ ). The subscript “d” represents “delayed” and this new version of the technique is referred to as *DDES* for *Delayed DES*.

To achieve this goal, Spalart *et al.* [Spalart *et al.*, 2005a] proposed the following definition of  $f_d$  (similar to  $1 - F_2$ ):

$$f_d = 1 - \tanh \left( [8r_d]^3 \right) \quad (7.108)$$

with

$$r_d = \frac{\nu_t + \nu}{\sqrt{U_{i,j}U_{i,j}}K^2d_w^2}, \quad K = 0.41 \quad (7.109)$$

where  $\nu_t$  and  $\nu$  are respectively the eddy and molecular viscosity,  $U_{i,j}$  the velocity gradients and  $d_w$  the distance to the wall.  $r_d$  is a slightly modified version of the parameter  $r = \frac{\tilde{\nu}}{\bar{S}K^2d_w^2}$  appearing in the SA model (see Eq. (7.64)) which represent the ratio (squared) of the model integral length scale to the distance to the wall.

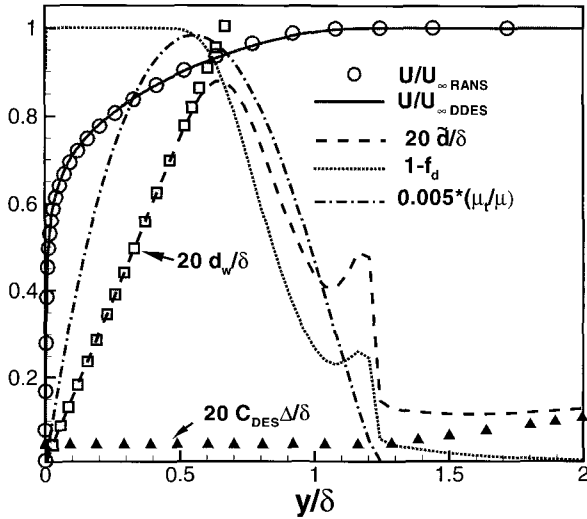


Fig. 7.22 DDES behavior in flat plate boundary layer with LES-like resolution ( $\Delta x^+ \approx 50, \Delta y^+ \approx 1, \Delta z^+ \approx 15$ ). Note that the modified length scale  $\tilde{d}$  follows the LES branch farther away from the wall than it would in DES97. More precisely, one can notice that  $\tilde{d} = d_w$  over more than half of the boundary layer thickness and at its peak, exceeds  $C_{DES}\Delta$  by more than an order of magnitude. The second peak near  $y/\delta \approx 1.1 - 1.2$  is due to the shear rate reaching zero at the edge of the boundary layer and entering  $r_d$ . However, it is not noticeably disturbing the eddy viscosity.

Figure 7.22 presents the evolution of  $1 - f_d$  near the wall and other quantities relevant to DDES on a very fine flat plate grid. This is a strong case since the ambiguous grid spacing penetrates deeply into the boundary layer. One can notice that DDES preserves the RANS velocity profile almost fully.

Although the new definition of  $\tilde{d}$  does not constitute a mere adjustment within DES, there is an essential change. Indeed, the DDES length scale does not depend only on the grid but depends also on the time-dependent eddy viscosity field. DDES has been exercised by several authors in different codes on subsonic and supersonic boundary layers with different grid refinements as well as on a backward facing step, a circular cylinder and on a single and multi-element airfoil. These successful tests showed that the RANS mode is maintained in thick boundary layers whilst maintaining LES content after separation.

## 7.5 Summary

This chapter summarizes a number of unsteady strategies ranging from unsteady statistical approaches that solve the averaged Navier–Stokes equations throughout the entire computational domain to global hybrid methods which are able to switch automatically from RANS to LES resulting in a change in the resolution in terms of frequency and wave numbers. The capabilities of these methods have been demonstrated and supported by a wide set of applications showing that the recent developments in hybrid RANS/LES are natural candidates for engineering applications.

Therefore, to provide some guidelines for using these methods for industrial turbulent flow modelling, let us introduce three categories of flows where steady-state calculations are not sufficient to properly describe the physical phenomena:

- *Category I:*

It consists of flows characterized by a scale separation between the unsteadiness of the mean field and turbulence. This kind of situation arises when boundary conditions impose flow unsteadiness. A generic example may be the case of a body motion like a small-amplitude forced oscillation of the vehicle so that the flow remains fully attached or slightly separated. This type of motion is used for the numerical (and experimental) prediction of the damping derivative coefficients. An other example may be the flow around an helicopter blade where the periodic forcing is imposed by the angular velocity of the rotor.

- *Category II:*

It includes massively separated flows characterized by a large scale unsteadiness dominating the time-averaged solution. This kind of flows are populated by energetic wake eddies, e.g. strong instabilities which overwhelm the turbulence inherited from upstream boundary layers. Many technical flows fall into that category like the flow behind a car, over an aircraft or airfoil at high angle of attack as well as in the unsteady wake developing on the leeward-side of buildings. Note from the above examples that the location of separation is triggered more or less by the geometry.

- *Category III:*

It categorizes flows that are quite sensitive to the Lagrangian history of the upstream or free-stream turbulence. As mentioned by Spalart [Spalart, 2000a], this kind of flows are rather submitted to convective

instabilities than to absolute instabilities (see [Huerre and Monkewitz, 1990]). This constitutes the main difference between flows of category II and III. A generic example is given by a shallow separation bubble on a smooth surface induced by a moderate adverse pressure gradient.

Although a universal method for industrial unsteady flows including of categories I, II and III will not be available in the near future, useful results for engineering applications can be obtained by adapting the level of modelling to the problem of interest. According to our classification of unsteady methods (see Fig. 7.2), the capabilities of unsteady statistical approaches, global and zonal hybrid RANS/LES methods are gathered in the following Table.

Family	Name of the method	Formulation	RANS/LES interface	Flows			
				I	II	III	
Unsteady statistical approaches $\nu_t = \nu_t(L_{RANS})$	URANS,PANS	same turbulence model as in RANS	/	+	-?	-	
	SDM, Ha Minh (1999) OES, Braza (2000)	turbulence model modified $\nu_t^{SDM} < \nu_t^{RANS}$	/	/	+?	-	
	TRRANS Travin <i>et al.</i> (2004)	$\epsilon_{TRRANS} = \epsilon_{RANS} \cdot F_{TRRANS}$ $F_{TRRANS} = \max \left[ \left( \frac{s}{\epsilon_{TRRANS} \Omega} \right)^2, 1 \right]$	no clear border	+	+?	-	
	SAS Menter <i>et al.</i> (2003)	turbulent length scale sensitized to $L_{vK}$	no clear border	+	+?	-	
Global hybrid methods $\nu_t = \nu_t(L_{RANS}, \Delta)$	VLES (FSM) Speziale (1997)	$\nu_t = \alpha \nu_t^{RANS}$ $0 \leq \alpha(L_\Delta/L_K) \leq 1$	no clear border	+ ~	+	-	
	LNS Batten <i>et al.</i>	$\alpha = \min \left( \frac{\nu_t^{LES}}{\nu_t^{RANS} + \epsilon}, 1 \right)$	flow dependent	+ ~	+	-	
	Blending methods Baurle <i>et al.</i> 2003	$\nu_t = \Gamma \nu_t^{RANS} + (1 - \Gamma) \nu_t^{LES}$ $\Gamma = \Gamma \left( \frac{L_\Delta}{L_{RANS}} \right)$	flow dependent	+ ~	+	-	
	DES type methods	DES Spalart (1997) Strelets (2001)	$\nu_t = U \times \mathcal{L}$ $\mathcal{L} = \min(L_{RANS}, L_\Delta)$	fixed (SA-DES) flow dependent (SST-DES)	+ ~	+	-
		XLES Kok <i>et al.</i> (2004)	similar to DES, DES limiter applied to all turbulent variables	flow dependent	+ ~	+	-
		Zonal DES Deck (2005a)	similar to DES,DES limiter overridden explicitly in selected zones	fixed	+ ~	+	-
		DDES Spalart <i>et al.</i> (2005)	$\mathcal{L} = L_{RANS} - f_d \max(0, L_{RANS} - L_\Delta)$ $f_d = \begin{cases} 0 & \forall L_\Delta \text{ in the TBL} \\ 1 & \text{in LES regions} \end{cases}$	flow dependent	+ ~	+	-
	Zonal hybrid methods	RANS/LES coupling Wall-Modelled LES NLDE	RANS and LES models applied separately LES content is explicitly reconstructed at the RANS/LES interface	fixed	- ~	+ ~	+

Table 7.2 Meanings of the grade used in the summary table. “limited interest” means that similar quality results can be obtained at lower computational cost by other methods

grade	reliability
+	well-adapted
+ ~	adapted but of limited interest
+?	may or not be adapted (e.g. case-dependent)
-?	limited and/or questionable accuracy
- ~	not adapted for practical reasons (CPU cost)
-	not-adapted

First of all, URANS has still its place and can be successfully used in complex industrial geometries where the flow is forced to be unsteady because of unsteady boundary conditions (flows of category I). The use of URANS methods to handle flows of category II like massive separation is less clear. This comes mainly from the fact that dominant eddies in massively separated flows are highly specific of the geometry and do not have much in common with the standard eddies of the thin shear flows that classical RANS are designed to model. The question whether a model can predict turbulent structures rests simply in the level of eddy viscosity provided by the turbulence model. Therefore OES (or SDM) may improve URANS predictions for that class of flows. The TRRANS and SAS models are difficult to classify since they obviously defy the traditional boundaries of URANS and LES. Indeed, we distinguished in Fig. 7.2 URANS and LES whether or not the eddy viscosity is sensitized to a filter width or grid spacing  $\Delta$ . TRRANS and SAS are not “explicitly” sensitized to grid spacing and therefore preserve the RANS spirit of the underlying model. Nevertheless these methods are capable of resolving turbulent structures down to the grid limit in highly separated flows. The ability of these methods to treat systematically flows of category II is not fully established. As an example, TRRANS has failed to support unsteadiness in the backward facing step flow which is normally a good candidate for hybrid RANS/LES methods. The border between the URANS and LES behaviors of these models is not clear but both methods are very young and a deeper understanding of the change in the resolution should also evolve.

Flows of category II represent an important class of flows of engineering interest. Therefore, in recent years, hybrid RANS/LES methods have become increasingly important among the turbulence modelling community. The main idea of these approaches is to apply LES in massively separated

flow regions and URANS in the attached boundary layers. We have seen in this chapter that all variants of this family are close to each other and rely mainly on a comparison of the integral turbulent length scale  $L_{RANS}$  provided by the RANS model and some representative of the mesh spacing  $\Delta$  or filter width (see Table 7.1). The cell size  $\Delta$  therefore controls which wavelength can be resolved as well as eddy viscosity levels. This decrease of eddy viscosity farther away from solid walls allows eddies to develop rapidly. Global (or non-zonal) RANS/LES strategies rely on a single set of model equations and a continuous treatment at the RANS/LES interface.

The definite differences between these hybrid RANS/LES methods rely on the choice of:

- (1) the continuous (or not) treatment of the eddy viscosity across the interface that is either fixed or flow dependent.
- (2) The underlying RANS and SGS model.

For example, the DES modification concerns only the source term(s) involved in the turbulence model<sup>19</sup> and the eddy viscosity remains continuous across the interface. Conversely, LNS takes the weaker between the RANS and subgrid viscosity. XLES like LNS defines a clear SGS model in the LES mode ( $k - SGS$  and Smagorinsky models for XLES and LNS respectively) whereas DES blends the concept of RANS and SGS. The necessity whether the precise determination of the SGS model employed by RANS/LES approaches is a key issue or not is still questionable. Indeed, we do not know if the grid extension spacing  $\Delta$  is really the cut-off scale and if a set of “filtered equations” is available. It would be fair to say that we solve the Navier–Stokes equations with a certain level of dissipation similar to that provided by a SGS model. Note that an eddy viscosity decrease can also compensate for numerical dissipation on coarse grids! Global hybrid RANS/LES has sometimes been presented as a “coarse-grid version of LES” (see [Spalart *et al.*, 2005a] for a discussion). This statement is not correct because there is no reason why a hybrid RANS/LES calculation would accept a coarser grid than an LES except, of course, in the boundary layer where the hybrid model acts in RANS mode. As for LES, the design of a correct (safe?) hybrid RANS/LES grid to handle complex geometries is a challenging task. The user has also to make decisions on the choice

---

<sup>19</sup>The DES formulation leads to a discontinuity in the gradient of the length scale that enters the destruction term of the turbulence model due to the min function employed in the Formula (7.67).

of the time-step and numerical schemes that may have serious implications [Strelets, 2001] on the final results (see Fig. 7.23).

Another critical issue that faces any hybrid RANS/LES method (and not only DES!) is the drawback of grey-areas in which the model needs to switch from fully modelled turbulence (in the attached boundary layer) to mostly resolved turbulence (within massive separation). The “automatic” switching from RANS to LES mode does not imply an instantaneous transformation of the resolution level and global hybrid approaches are not adapted to treat flows of category III. Grey areas need careful monitoring and some solutions to overcome this drawback have been presented in this chapter.

Global hybrid techniques combining RANS and LES modelling will constitute the basis of industrial tools in the mid-term and their domain of application is already quite interesting. The next foreseen challenge in applied numerical aerodynamics will be the capture of the boundary layer dynamics including transition and separation issues (e.g. flows of category III). This second class of hybrid methods is discussed separately in the next chapter.

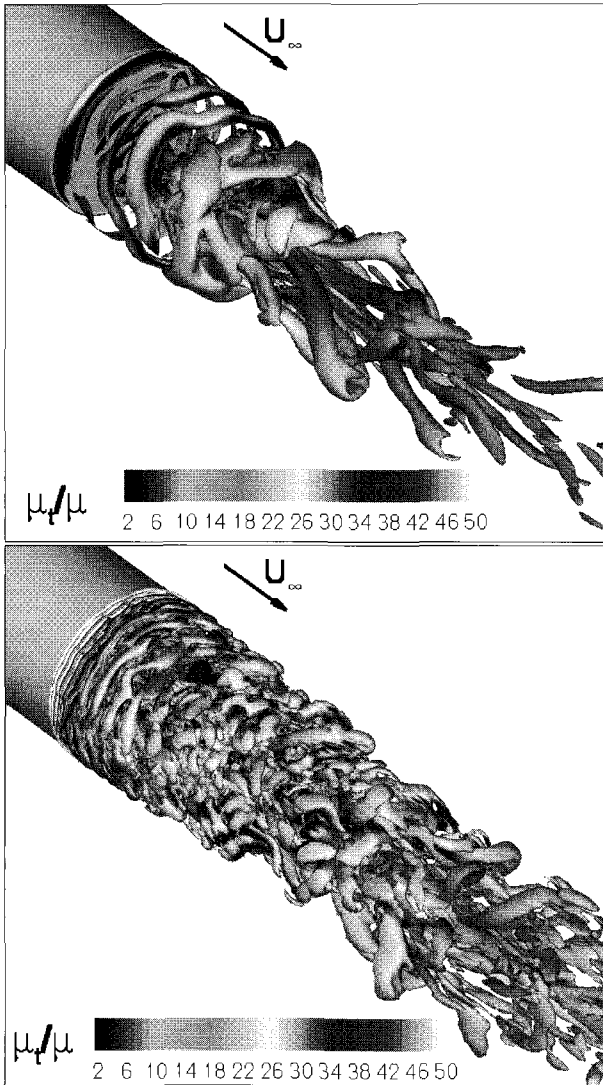


Fig. 7.23 Zonal-DES of a base flow. The same grid ( $N_{xyz} = 7.10^6$  nodes) and time-integration scheme are used in both calculations. Upper part: Roe's upwind scheme with *minmod* limiter; lower part: low-dissipative version of the AUSM scheme. Note the drastic effect of the spatial differentiating scheme (e.g. numerical dissipation) on the turbulence resolving capabilities (Deck, 2005).

## Chapter 8

# Zonal RANS/LES Methods

This chapter is devoted to the discussion of zonal couplings between RANS and LES methods via the definition of multiresolution/multidomain methods. The main problems including interfacing conditions as well as turbulence reconstruction are presented.

The global hybrid methods discussed above (see Chapter 7) are based on a continuous treatment of the flow variables (such as the velocity field) at the RANS and LES interface. These methods introduce a “grey-area” in which the solution is neither “pure” RANS nor “pure” LES since the switch from RANS to LES mode does not imply an instantaneous change in the resolution level. We thus qualified global methods as “weak RANS/LES coupling methods” since there is no mechanism to transfer the modelled turbulence energy into resolved turbulence energy. These global methods may not be adequate in situations where upstream or free-stream turbulence play a significant role, as well as in cases in which separation is not triggered by a geometric singularity.

The use of pre-defined “pure” RANS and “pure” LES zones in which classical RANS and LES models are utilized may alleviate this “grey-area” problem. Zonal hybrid methods are therefore based on a purely discontinuous treatment of the RANS/LES interface. The main difficulty is that information must be exchanged at the RANS/LES domain interface between two solutions with very different spectral contents. Thus, these methods fall into the category of “strong RANS/LES coupling methods”.

This change in the resolution raises the problem of determining the associated boundary conditions at the RANS/LES interface since those associated with the RANS governing equations can no longer be used to feed the LES solution. The problem of strong RANS/LES coupling is equivalent to a multi-resolution decomposition of the problem and can take several forms as illustrated in Fig. 8.1.

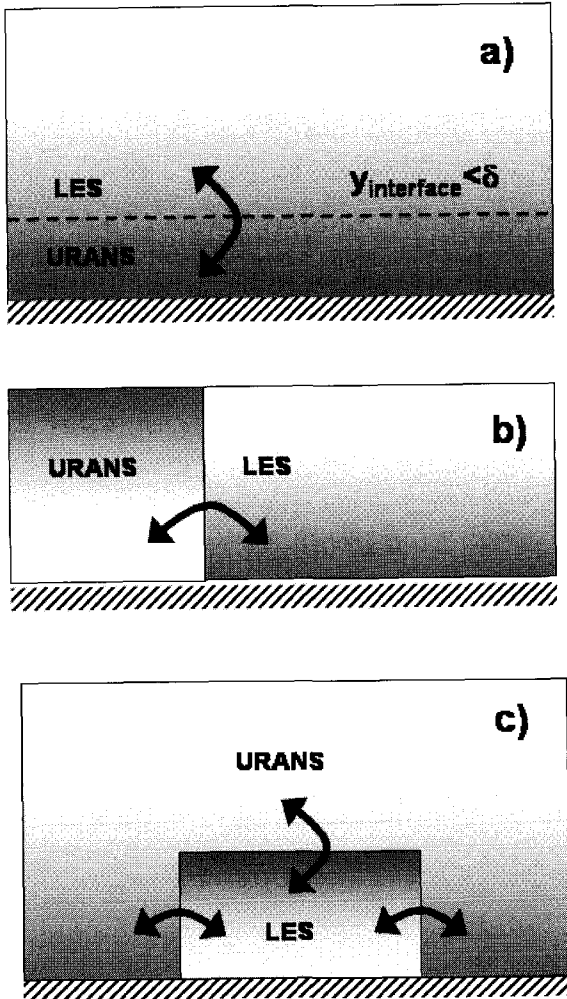


Fig. 8.1 Several configurations of RANS/LES coupling: a) Wall-Modelled LES b) Turbulent inflow condition c) embedded LES.

- Whilst global hybrids aim at covering the entire boundary layer in the URANS mode, zonal-hybrid methods aim at covering only the inner-part of the boundary layer. Consequently, LES content has to be generated in the outer part of the boundary layer. This first type of problem is sometimes referred to as Wall-Modelled LES [Spalart, 2000a].

- The second type of RANS/LES coupling aims at representing a turbulent inflow especially when a LES domain is located downstream a RANS domain. In this case, synthetic turbulent structures have to be generated to match statistical characteristics provided by the RANS side.
- The most general multi-domain/multi-resolution problem concerns the case where a local LES simulation is embedded into a global RANS simulation.

In all cases, the spatial derivatives across the RANS/LES interface of the averaged flowfield are discontinuous and synthetic turbulence must be generated at the inflow of the LES domain when it is located downstream a RANS region. Implementation of inflow conditions for LES is a serious and still open problem. Indeed, using the RANS field alone to generate inflow data for the LES domain cannot be sufficient: additional modelling which includes further assumptions on local length scales, time scales and energy distribution is required to recover an efficient inlet condition for LES.

This chapter is devoted to the presentation of zonal RANS/LES methods and is organized as follows. The RANS/LES interface problem and possible numerical treatments are discussed in Sec. 8.1. The main inflow data generation methods for zonal hybrids calculations like mapping techniques and synthetic turbulence reconstruction are presented respectively in Sec. 8.2 and Sec. 8.3.

## 8.1 Theoretical Setting of RANS/LES Coupling

### 8.1.1 *Full-variables approach*

One of the first attempts to derive a consistent discontinuous coupling between RANS and LES was suggested by Quéméré and Sagaut [Quéméré and Sagaut, 2002]. They derived a general framework for the definition of the exchange of information at the RANS/LES interface, which relies on the definition of some interface variables to construct a transfer operator at the interface.

For the sake of clarity, let us consider two domains  $\Omega^1$  and  $\Omega^2$  that are assumed to have different grid resolutions with a common boundary ( $\Gamma$ ). With reference to Chapter 2, the fine domain (LES) is noted  $\Omega^1$  and  $\Omega^2$  refers to the coarse one (RANS). Therefore, the characteristic cut-off length

scales satisfy the inequality  $\Delta^1 < \Delta^2$  (see Fig. 8.2). To distinguish variables related to the two domains,  $\bullet^1$  variables refer to the high resolution domain and  $\bullet^2$  variables to the low level resolution domain.

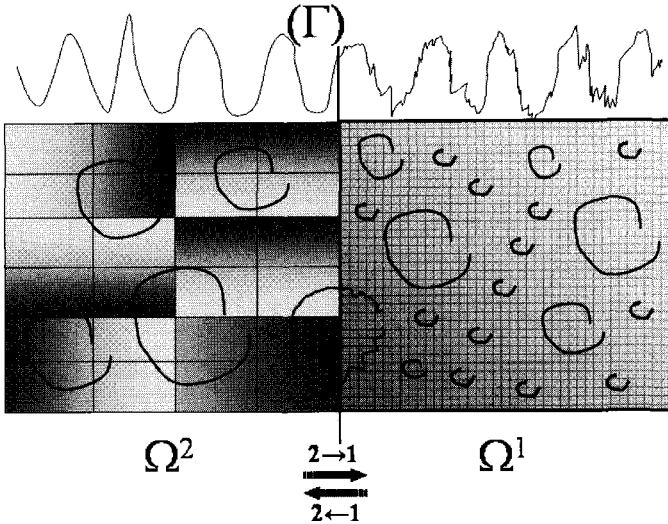


Fig. 8.2 Sketch of the multi-resolution problem.

The aerodynamic field in each domain is split into its respective filtered and fluctuating part:

$$\begin{aligned} \mathbf{u} &= \bar{\mathbf{u}}^{(1)} + \mathbf{u}'_1 \quad \text{on } \Omega^1 \\ \mathbf{u} &= \bar{\mathbf{u}}^{(2)} + \mathbf{u}'_2 \quad \text{on } \Omega^2. \end{aligned} \quad (8.1)$$

The difference between the filters involves a discontinuous behavior of the filtered variables and the fluctuating values at the interface which in turn affects the subgrid viscosity that accounts for the effect of the subgrid scales:

$$\bar{\mathbf{u}}^{(1)}|_{\Gamma} \neq \bar{\mathbf{u}}^{(2)}|_{\Gamma} \Rightarrow \mathbf{u}'_{1|\Gamma} \neq \mathbf{u}'_{2|\Gamma} \Rightarrow \nu_t^{(1)}|_{\Gamma} \neq \nu_t^{(2)}|_{\Gamma}. \quad (8.2)$$

Quéméré and Sagaut [Quéméré and Sagaut, 2002] proposed a coupling algorithm for an explicit time integration scheme associated to a cell-centered finite volume discretization. This coupling is performed by

reconstructing the Dirichlet values and the corresponding value of the sub-grid model in a row of ghost cells associated to each domain along the interface  $\Gamma$  (see Figs. (8.2) and (8.3)). Therefore, the coupling procedure acts directly on the computed variables and the modified fluxes at the interface are obtained directly from the reconstructed field at the interface. In this region, there exists a two-way coupling:

- a frequency restriction of the solution for the coarse domain  $\Omega^2$ :

$$\Omega^1 \rightarrow \Omega^2 : \quad \bar{\mathbf{u}}|_{\Gamma}^{(2)} = \mathcal{O}_{1 \rightarrow 2} \left( \bar{\mathbf{u}}|_{\Gamma}^{(1)} \right) \quad (8.3)$$

- a frequency enrichment of the solution for the fine domain:

$$\Omega^2 \rightarrow \Omega^1 : \quad \bar{\mathbf{u}}|_{\Gamma}^{(1)} = \mathcal{O}_{2 \rightarrow 1} \left( \bar{\mathbf{u}}|_{\Gamma}^{(2)} \right) \quad (8.4)$$

where  $\mathcal{O}_{1 \rightarrow 2}$  and  $\mathcal{O}_{2 \rightarrow 1}$  are respectively the restriction and enrichment operators at the interface<sup>1</sup>. From now on, we adopt the notations  $\bar{\mathbf{u}}_{RANS} = \bar{\mathbf{u}}^{(2)}$  (respectively  $\Omega^2 \equiv \Omega_{RANS}$ ) and  $\bar{\mathbf{u}}_{LES} = \bar{\mathbf{u}}^{(1)}$  (respectively  $\Omega^1 \equiv \Omega_{LES}$ ).

#### 8.1.1.1 Enrichment procedure from RANS to LES

The information provided by the RANS domain is used to derive some boundary conditions for the LES domain. This enrichment procedure characterized previously by the operator  $\mathcal{O}_{2 \rightarrow 1}$  (see Eq. (8.4)) can be interpreted as a de-filtering or de-convolution procedure in which high frequencies are generated. The basic idea proposed by Quéméré and Sagaut [Quéméré and Sagaut, 2002] consists in introducing the frequency complement  $\delta \mathbf{u}|_{R,L}$  which has to be added to the RANS (e.g. low frequency) signal to recover the LES (e.g. high frequency) signal:

$$\delta \mathbf{u}|_{R,L} = \bar{\mathbf{u}}_{LES} - \bar{\mathbf{u}}_{RANS}. \quad (8.5)$$

This quantity has to be computed in the ghost cells of the LES domain in order to get a reliable estimation of  $\bar{\mathbf{u}}_{LES}$  at this location. The particular treatment proposed by Quéméré and Sagaut can be described as follows. Let us first introduce (see Fig. 8.3):

- $\mathbf{x}_G$ : center of the ghost LES cell embedded into the RANS cell.

<sup>1</sup>It can be noted from Eqs 8.3 and 8.4 that  $\mathcal{O}_{1 \rightarrow 2} \circ \mathcal{O}_{2 \rightarrow 1} = \mathcal{O}_{2 \rightarrow 1} \circ \mathcal{O}_{1 \rightarrow 2} = Id$ , where  $Id$  is the identity operator.

- $\mathbf{x}_R$ : center of the last real cell of the LES domain facing the RANS/LES interface.

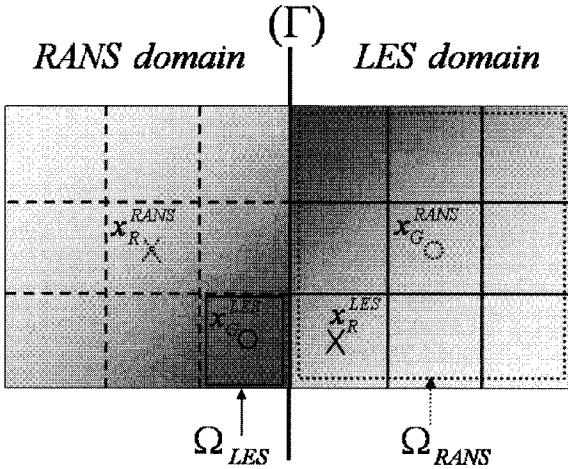


Fig. 8.3 Sketch of the information transfer between RANS and LES domains.

The reconstruction is obtained with the following formula:

$$\bar{\mathbf{u}}_{LES}(\mathbf{x}_G^{LES}, t) = \bar{\mathbf{u}}_{RANS}(\mathbf{x}_G^{LES}, t) + C\delta\mathbf{u}_{|_{R,L}}(\mathbf{x}_R^{LES}, t) \quad (8.6)$$

where

$$\delta\mathbf{u}_{|_{R,L}}(\mathbf{x}_R^{LES}, t) = \bar{\mathbf{u}}_{LES}(\mathbf{x}_R^{LES}, t) - \langle \bar{\mathbf{u}}_{LES}(\mathbf{x}_R^{LES}, t) \rangle_{\Omega} \quad (8.7)$$

where the value of the RANS field  $\bar{\mathbf{u}}_{RANS}$  at point  $\mathbf{x}_G^{LES}$  is obtained by interpolation of the RANS field<sup>2</sup>.  $C$  is a weighting factor that was empirically defined by Quéméré and Sagaut as the ratio of the characteristic length scales evaluated from the volume of the ghost cell and the first interior cell respectively. This procedure is similar to the one developed by these authors in the context of multidomain/multiresolution LES (see Sec. 5.5).

$\bar{\mathbf{u}}_{LES}(\mathbf{x}_R^{LES})$  is obtained directly in the LES domain. Finally,  $\langle \bar{\mathbf{u}}_{LES}(\mathbf{x}_R^{LES}) \rangle_{\Omega}$  represents an estimation of the RANS field at point  $\mathbf{x}_R^{LES}$ ,

<sup>2</sup>The RANS and LES domains are generally only partially coincident.

obtained by averaging the LES field over the volume  $\Omega$ . This volume is, according to the authors, case-dependent. In general, it is taken as an average over the homogeneous directions of the flow<sup>3</sup>.

The authors indicate that such a treatment is valuable only in the case of “lateral” or “outflow” boundaries. The generation of turbulent inflow conditions for the LES zone when it is located downstream a RANS domain is a particularly challenging issue and is discussed separately in Sec. 8.2 and Sec. 8.3.

### 8.1.1.2 Restriction procedure from LES to RANS

The restriction procedure characterized previously by the operator  $\mathcal{O}_{1 \rightarrow 2}$  (see Eq. (8.3)) may be interpreted as an averaging-operator (*i.e.* a low-pass filter) to remove the frequencies corresponding to turbulent fluctuations:

$$\bar{\mathbf{u}}_{RANS}(\mathbf{x}_G^{RANS}, t) = \langle \bar{\mathbf{u}}_{LES}(\mathbf{x}_R^{LES}, t) \rangle_{\Omega(t)}. \quad (8.8)$$

The treatment of the eddy viscosity is different if the RANS domain is located downstream or upstream of the LES domain. In the latter case, the feedback from the LES region to the RANS region is achieved by averaging the LES field to provide data for the RANS field boundary conditions whilst traditional RANS equations are solved for the turbulent variables and the eddy viscosity  $\nu_t$ .

In the case where the RANS zone is located downstream a LES domain, one has to reconstruct an eddy viscosity from the LES flowfield. As an example, the filtering process proposed by Nolin *et al.* [Nolin *et al.*, 2005] is divided into two steps. Firstly the solution from the LES side is filtered both in time and space as follows:

$$\langle \bar{\mathbf{u}}_{LES}(\mathbf{x}_R^{LES}, t) \rangle_{\Omega} = \frac{1}{\Omega_{RANS}} \int_{\Omega_{RANS}} \bar{\mathbf{u}}_{LES}(\xi, t) d\xi \quad (8.9)$$

where  $\Omega_{RANS}$  denotes the volume of the cell in the RANS domain and  $\bar{\mathbf{u}}_{LES}(\mathbf{x}, t)$  the space filtered aerodynamic field which in turn is time-filtered:

---

<sup>3</sup>The averaging procedure can also introduce time averaging (then noted  $\langle \bullet \rangle_{\Omega_{LES}, t}$ ) as in the works by Nolin *et al.* (2005), see Eq. (8.9).

$$\begin{aligned} \langle \bar{\mathbf{u}}_{LES}(\mathbf{x}_R^{LES}, t^n) \rangle_{\Omega, t} &= \frac{N-1}{N} \langle \bar{\mathbf{u}}_{LES}(\mathbf{x}_R^{LES}, t^{n-1}) \rangle_{\Omega, t} + \frac{1}{N} \langle \bar{\mathbf{u}}_{LES}(\mathbf{x}_R^{LES}, t^n) \rangle_{\Omega} \\ \bar{\mathbf{u}}_{RANS}(\mathbf{x}_G^{RANS}, t^n) &= \langle \bar{\mathbf{u}}_{LES}(\mathbf{x}_R^{LES}, t^n) \rangle_{\Omega, t} \end{aligned} \quad (8.10)$$

where the superscript  $\bullet^n$  refers to the instance  $t^n$  and  $N$  is the number of time-steps over which the fields are integrated. Nolin *et al.* introduced the twice-filtered field  $\bar{\mathbf{u}}_{RANS}(\mathbf{x}_G^{RANS}, t)$  into the RANS equations to obtain a linear system on  $\nu_t$ . In the framework of a finite volume formulation, the momentum conservation equation may be written as:

$$\oint_{\partial\Omega_{RANS}} 2\nu_t \mathbf{S} \cdot \mathbf{n} ds = \Omega_{RANS} \frac{\partial \bar{\mathbf{u}}_{RANS}}{\partial t} + \oint_{\partial\Omega_{RANS}} (\mathcal{F}^a - 2\nu \mathbf{S}) \cdot \mathbf{n} ds \quad (8.11)$$

where  $\mathbf{S}$  is the strain rate tensor,  $\mathbf{n} ds$  the surface vector of the cell interface and  $\mathcal{F}^a$  the inviscid flux tensor. Note that the system is overdetermined because the RANS eddy viscosity  $\nu_t$  appears in the three equations relative to the velocity components. In addition, Nolin *et al.* indicate that a robustness problem may arise if the system is projected onto a direction in which the velocity gradients are very small. Therefore, they solve the linear system for the wall tangent velocity component yielding the highest gradients. These authors applied their method to a conventional plane channel flow as well as to a more realistic airfoil flow case and outlined the importance of the twice-filtering operation applied to the LES field.

### 8.1.2 Perturbation approach: NLDE

This approach, referred to as NLDE for *Non-Linear Disturbance Equations*, was originally developed by Morris *et al.* [Morris *et al.*, 1997]. Here, the extension of this method to the case of a RANS/LES flow decomposition, as developed by Labourasse and Sagaut [Labourasse and Sagaut, 2002] is discussed. This hybrid RANS/LES technique represents a two-level particular case of the multilevel decomposition of the flow variables introduced in Sec. 2.5.1 as follows: here, the first (fine) representation level of the solution corresponds to the filtering approach, while the second one is related to an averaged representation of the flow. The following, two-level, decomposition is then considered:

$$\bar{\mathbf{u}}_{LES} = \bar{\mathbf{u}}_{RANS} + \delta \mathbf{u}_{R,L} \quad (8.12)$$

where, with reference to Chapter 2,  $\bar{\mathbf{u}}_{LES} = \bar{\mathbf{u}}^{(1)}$  corresponds to the finer representation level (LES),  $\bar{\mathbf{u}}_{RANS} = \bar{\mathbf{u}}^{(2)}$  to the coarser one, obtained by an averaging operator, and  $\delta\mathbf{u}_{R,L} = \delta\mathbf{u}^{(1)}$  is associated to turbulent fluctuations around the mean flow  $\bar{\mathbf{u}}_{RANS}$ , which can be computed with the LES approach. Here, it has been chosen to introduce these new notations instead of the more general ones  $\bar{\mathbf{u}}^{(1)}$ ,  $\bar{\mathbf{u}}^{(2)}$ , and  $\delta\mathbf{u}^{(1)}$ , for the sake of clarity and consistency with the general topic of this chapter. We can notice that this two-level decomposition of the filtered velocity field also introduces a triple decomposition of the original (full) velocity field  $\mathbf{u}$  as:

$$\mathbf{u} = \bar{\mathbf{u}}_{RANS} + \delta\mathbf{u}_{R,L} + \mathbf{u}' \quad (8.13)$$

where  $\mathbf{u}'$  is associated to the (unresolved) subgrid scales.

The aim of the NLDE approach is to reconstruct the turbulent fluctuations around the mean flow  $\bar{\mathbf{u}}_{RANS}$ , which is considered to be known. For this, some evolution equations have to be derived for the fluctuating field  $\delta\mathbf{u}_{R,L}$ . Remarking that this quantity represents the *detail* between the two representation levels of the solution, its evolution equation is a particular case of Eq. (2.58). The set of the Non-linear Disturbance Equations describing the evolution of the turbulent fluctuations  $\delta\mathbf{u}_{R,L}$  is then:

$$\begin{aligned} \nabla \cdot (\delta\mathbf{u}_{R,L}) &= 0 \\ \frac{\partial}{\partial t} \delta\mathbf{u}_{R,L} + \nabla \cdot (\delta\mathbf{u}_{R,L} \otimes \delta\mathbf{u}_{R,L} + \delta\mathbf{u}_{R,L} \otimes \bar{\mathbf{u}}_{RANS} + \bar{\mathbf{u}}_{RANS} \otimes \delta\mathbf{u}_{R,L}) \\ &= -\nabla \delta p_{R,L} + \nu \nabla^2 \delta\mathbf{u}_{R,L} - \nabla \cdot (\tau_{LES} - \tau_{RANS}) \end{aligned} \quad (8.14)$$

where, similarly to the velocity fluctuation  $\delta\mathbf{u}_{R,L}$ , the pressure fluctuation is defined as  $\delta p_{R,L} = \bar{p}_{LES} - \bar{p}_{RANS}$ .

It is interesting to remark that the perturbation momentum equation can be re-written as:

$$\begin{aligned} \frac{\partial}{\partial t} \delta\mathbf{u}_{R,L} + \nabla \cdot ((\delta\mathbf{u}_{R,L} + \bar{\mathbf{u}}_{RANS}) \otimes (\delta\mathbf{u}_{R,L} + \bar{\mathbf{u}}_{RANS})) \\ + \nabla \cdot (\delta p_{R,L} + \bar{p}_{RANS}) - \nu \nabla^2 (\delta\mathbf{u}_{R,L} + \bar{\mathbf{u}}_{RANS}) + \nabla \cdot (\tau_{LES}) \\ = \nabla \cdot (\bar{\mathbf{u}}_{RANS} \otimes \bar{\mathbf{u}}_{RANS}) + \nabla \bar{p}_{RANS} - \nu \nabla^2 \bar{\mathbf{u}}_{RANS} + \nabla \cdot (\tau_{RANS}) \end{aligned} \quad (8.15)$$

or, equivalently:

$$\begin{aligned}
& \frac{\partial}{\partial t} \delta \mathbf{u}_{R,L} + \nabla \cdot (\bar{\mathbf{u}}_{LES} \otimes \bar{\mathbf{u}}_{LES}) + \nabla \bar{p}_{LES} - \nu \nabla^2 \bar{\mathbf{u}}_{LES} + \nabla \cdot (\boldsymbol{\tau}_{LES}) \\
& = \nabla \cdot (\bar{\mathbf{u}}_{RANS} \otimes \bar{\mathbf{u}}_{RANS}) + \nabla \bar{p}_{RANS} - \nu \nabla^2 \bar{\mathbf{u}}_{RANS} + \nabla \cdot (\boldsymbol{\tau}_{RANS})
\end{aligned} \tag{8.16}$$

where the RHS depends only on the mean field computed by RANS. It is to be noted here that, according to the Reynolds-Averaged Navier–Stokes equations (see Eqs. (2.24)) detailed in Chapter 2, this term theoretically vanishes in the case of a steady mean flow. It is however recommended to compute explicitly this term, in order to account for some possible convergence and/or discretization<sup>4</sup> errors.

Several properties have been highlighted by Labourasse and Sagaut when implementing and testing this approach (some plane channel flow computations were first carried out by the authors, considering several choices for the mean flow and several sizes of the computational domain). The most interesting one is certainly the ability of the method to deal with reduced domain size, due to the fact that the perturbation formulation is less sensitive to the possible numerical errors arising at the domain boundaries. Following this idea, the authors have then proposed a zonal version of this method, which consists in reconstructing turbulent fluctuations around a mean flow in some numerical subdomain only, in which an accurate description of the flow unsteadiness is sought. This may be the case for instance at the trailing-edge of a wing or blade profile, for an accurate description of the wake. The configuration is therefore treated in its major part with the RANS approach (the steady approach is retained by the authors), while only small (reduced) parts of the computational domain are treated by the NLDE approach. This point is illustrated by Fig. 8.4 in the case of the flow around a NACA0012 profile, and where only the trailing-edge region is treated by three-dimensional NLDE (the overall configuration being treated by the 2D RANS approach) in order to get a description of the associated aeroacoustic sources.

The main point that has to be addressed is the coupling between the global RANS and the NLDE regions. The associated problem is the definition of some appropriate boundary conditions at the interfaces

---

<sup>4</sup>The numerical schemes used for RANS computations generally differ from those used for LES. Since the NLDE system has to be solved with some numerical schemes which are well-suited for LES computations, a mean field  $\bar{\mathbf{u}}_{RANS}$  which was well converged in time during a RANS computation can however lead to a non-negligible convergence error with a different scheme.

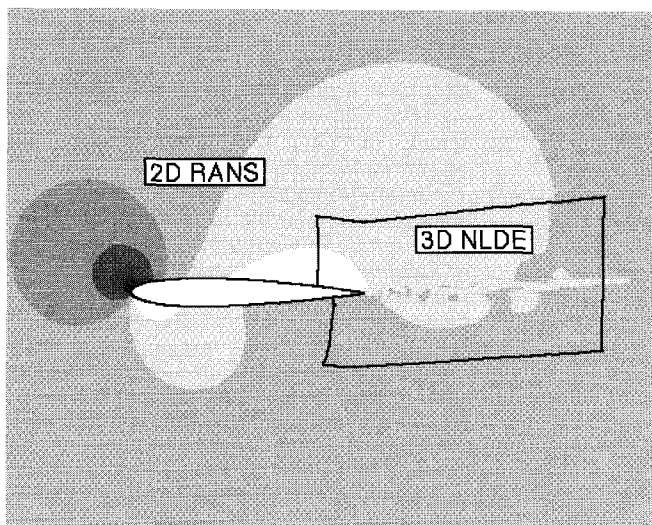


Fig. 8.4 Use of the zonal NLDE approach in a NACA0012 configuration (Terracol, 2005).

of the NLDE region. While the mean flow can be simply defined by taking directly the corresponding values of the aerodynamic field computed by RANS, a particular treatment is required for the turbulent fluctuations. In their works performed in the compressible flow case, Labourasse and Sagaut recommend the use of an extension of usual non-reflexive characteristic treatments [Thomson, 1987a; Thomson, 1987b; Poinso and Lele, 1991] to the perturbation formulation. This extension is detailed in [Sagaut *et al.*, 2003], and the resulting hybrid approach was applied successfully by the authors to the numerical simulation of some realistic industrial cases such as the trailing-edge region from a low-pressure turbine blade, or the slat cove region of a three-element high-lift wing profile.

However, as it is also highlighted by the authors, this numerical treatment does not allow to account for some turbulent flows at the inflow interface of the NLDE region. As it is the case for all the zonal RANS/LES approaches, a particular treatment has to be added to generate explicitly some turbulent fluctuations in such cases. A survey of some possible existing methodologies to generate appropriate turbulent fluctuations at the inflow of a NLDE (or more generally LES) region is carried out in Secs. 8.2

and 8.3 of the present chapter. It is to be noted that this point represents certainly the main challenge to be met to ensure the applicability of zonal RANS/LES approaches to the simulation of turbulent flows in general configurations.

## 8.2 Inlet Data Generation – Mapping Techniques

The URANS modelling approach is based on a scale separation (or spectral gap) between the unsteadiness of the mean field and the turbulent field (see Sec. 7.3). Therefore, the quantities being computed in (U)RANS are steady (or vary on a time scale much longer than the computational time step) and do so in a deterministic manner (rather than random) so that inlet quantities are well defined. In contrast, LES does not exhibit such a scale separation and thus requires a specific treatment to resolve large-scale turbulence in space and time.

In the LES mode of hybrid methods, the unsteady three-dimensional energy-carrying eddies are resolved. Hence, the velocity specified at the inflow of the computational domain should ideally represent the contribution of these eddies. For an incompressible flow, these structures can be characterized as a time dependent velocity vector function of two-space directions, satisfying a prescribed spectrum as well as given first and second order moments, along with the appropriate phase correlation between modes. This latter information is the most difficult to specify since it is related to the shape of the turbulent eddies, or in other words, to the structure of turbulence which is highly flow-dependent. Without this correct structural information, the calculation requires a transition region where the turbulent eddies evolve until the correct phase information is reached. Batten, Goldberg and Chakravarthy [Batten *et al.*, 2004] introduced the acronym of Large Eddy STimulation (LEST) to qualify the process that generates the large scale eddies needed to form the unsteady boundary condition at the RANS/LES interface.

The choice of the method to specify this inflow condition is problem dependent and various techniques can be used:

- generate inlet data from another precursor simulation, see Sec. 8.2.1
- dedicate a part of the computational domain to the use of a recycling methods, see Sec. 8.2.2
- superimpose synthetic fluctuation on the mean velocity profile, see Sec. 8.2.3.

The topic of inlet data generation is now growing rapidly and these methods are therefore discussed further in the following sections. The use of synthetic turbulence reconstruction is discussed separately in Sec. 8.3.

### 8.2.1 Precursor calculation

An accurate way to generate inlet data description consists in retrieving them from a precursor simulation. In practice, the velocity field in a plane normal to the streamwise direction is stored at each time step. The sequence of planes is then used as inflow data (e.g. unsteady Dirichlet conditions) for a separate calculation of the flow of interest (see Fig. 8.5). Despite its accuracy, this technique implies a heavy extra computational loads and is restricted to simple cases (see [Kaltenbach *et al.*, 1999] for an example of application).

A variant of this method for hybrid RANS/LES simulations has been developed by Schlüter, Pitsch and Moin [Schlüter *et al.*, 2004] in the case where an LES domain is located downstream of a RANS domain.

This method uses the mean velocity field from the RANS solution and adds turbulence extracted from a pre-generated database (referred to as *DB*) created by an auxiliary LES computation as follows:

$$u_{(i),LES}(t) = \bar{u}_{(i),RANS} + u'_{(i),DB}(t) \quad i = 1, 2, 3. \quad (8.17)$$

Turbulent fluctuations  $u'_{(i),DB}$  are extracted from the data base and then rescaled to match required statistics (e.g. mean velocity field and rms fluctuations) of the target RANS field as follows:

$$u_{(i),LES}(t) = \bar{u}_{(i),RANS} + [u_{(i),DB}(t) - \bar{u}_{(i),DB}] \frac{\sqrt{u'^2_{(i),RANS}}}{\sqrt{u'^2_{(i),DB}}}. \quad (8.18)$$

Indeed, taking the ensemble average of Eq. (8.18) leads to  $\bar{u}_{(i),LES} = \bar{u}_{(i),RANS}$  whereas subtracting  $\bar{u}_{(i),RANS}$  from both sides of Eq. (8.18) before taking the square and the ensemble average yields  $\overline{u'^2_{(i),LES}} = \overline{u'^2_{(i),RANS}}$ . It is also assumed that the axial components of the Reynolds tensor  $\overline{u'^2_{(i),RANS}}$  are known quantities. However, most RANS models do not compute the single components of the Reynolds stress tensor but more general turbulent quantities such as the turbulence kinetic energy  $k_{RANS}$ .

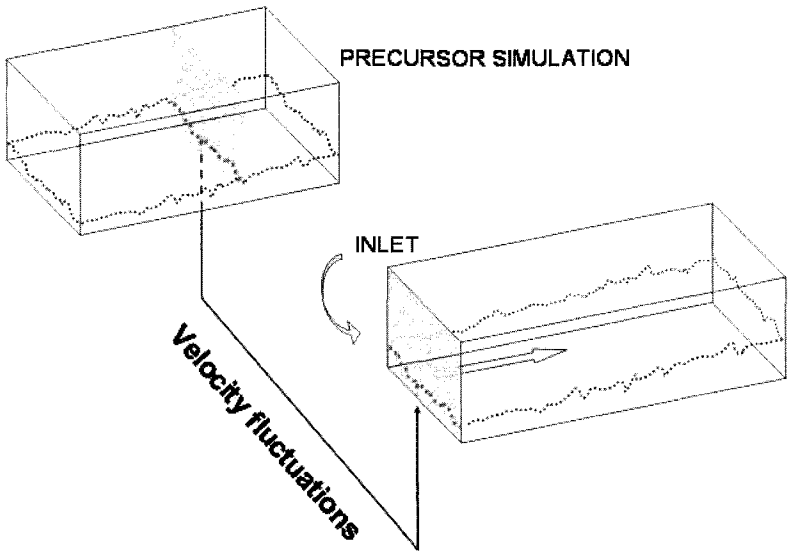


Fig. 8.5 Sketch illustrating a database lookup technique in which a previous computation is used to provide inlet data.

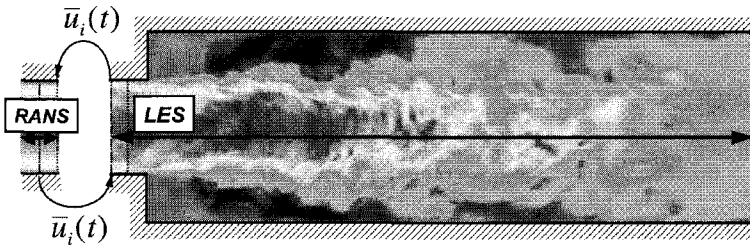


Fig. 8.6 Sketch illustrating the interface and boundary condition of an integrated RANS/LES. The inlet velocity profile in the RANS region are prescribed according to the available experimental data. The LES inflow boundary condition are obtained by the LES solver which provides the inflow velocity profiles that match the statistical properties yielded by the RANS velocity profile. Courtesy of J. Schlüter, CTR, USA.

Assuming homogeneous isotropic turbulence, the normal stresses of the Reynolds tensor can be recovered by:

$$\overline{u'^2}_{(i),RANS} = \frac{2}{3}k_{RANS}. \quad (8.19)$$

Schlüter *et al.* [Schlüter *et al.*, 2005] applied their method to simulate the complex flow path of an entire gas turbine. Compressor and turbine are computed in RANS mode and the combustor with LES (see figure 8.7).

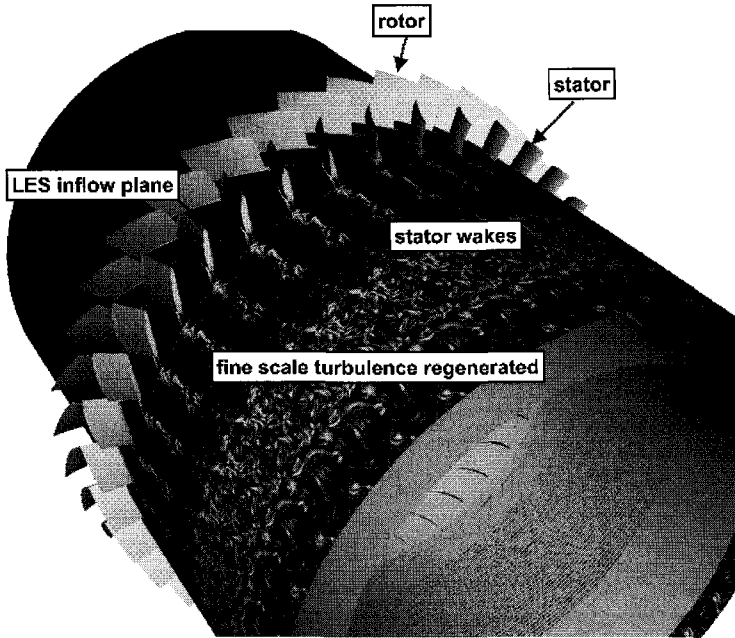


Fig. 8.7 Integrated RANS-LES of compressor/prediffuser. The vorticity distribution highlights the wakes of the stators in the RANS domain whereas the vorticity distribution in the LES domain is characterized by small scale turbulence. This small scale turbulence has been reconstructed explicitly using the LES inflow boundary condition. Courtesy of Jorg Schlüter, CTR, USA.

The precursor simulation is assumed to provide realistic scales but does not need to be, *a priori*, in the same configuration as the real LES calculation of interest. Schlüter, Pitsch and Moin [Schlüter *et al.*, 2004] outlined that the scaling of Eq. (8.18) is linear and that it is recommended to reproduce the expected inlet conditions as closely as possible in order to keep the

approximation in the bounds of validity of a linear approximation. Little is known about the effect of a scaling factor significantly different from unity that occurs when the database is very different from the target turbulent flow field. To get a better knowledge of this issue, Keating *et al.* [Keating *et al.*, 2004] created a database using a periodic simulation of a channel flow at a Reynolds number based on the channel half-height  $Re = 2280$ . This database was then rescaled to match first and second order statistics of channel flow at Reynolds number  $Re = 6900$ . Using a rescaling similar to that given by Eq. (8.18), the skin friction coefficient as well as the Reynolds shear stress were recovered ten boundary layer ( $10\delta$ ) thicknesses downstream from the inlet, whereas  $15\delta$  were necessary to recover the turbulent kinetic energy.

### 8.2.2 Recycling methods

For incompressible spatially developing boundary layers, Lund, Wu and Squires [Lund *et al.*, 1998] developed an approach where the simulation generates its own inflow conditions. Their method consists in taking a plane from a location several boundary layer thicknesses  $\delta$  downstream of the inflow. These data are then rescaled and reintroduced at the inflow (see Fig. 8.8). This assumes the accepted scaling laws for mean flow and fluctuations of the flat-plate boundary layer.

The idea is to decompose each flowfield into a mean and a fluctuating part and then apply the appropriate scaling law to each one separately. A velocity component  $u_i(x, y, z, t)$  is decomposed as the sum of an average in the spanwise direction and in time  $\bar{u}_i(x, y)$  and a time fluctuating part  $u'_i(x, y, z, t)$  according to:

$$u'_i(x, y, z, t) = u_i(x, y, z, t) - \bar{u}_i(x, y). \quad (8.20)$$

For the sake of simplicity, we denote the streamwise, wall-normal and spanwise velocity components by  $u_1, u_2, u_3$  and the corresponding coordinates are  $x, y, z$ .

In the recycling method, the inner and outer layers of the boundary layer are rescaled separately (index *re*) to account for the different similarity laws that are observed in these two regions. Both layers can be linked with those at the inflow (index *inf*) thanks to the following relations for the inner region:

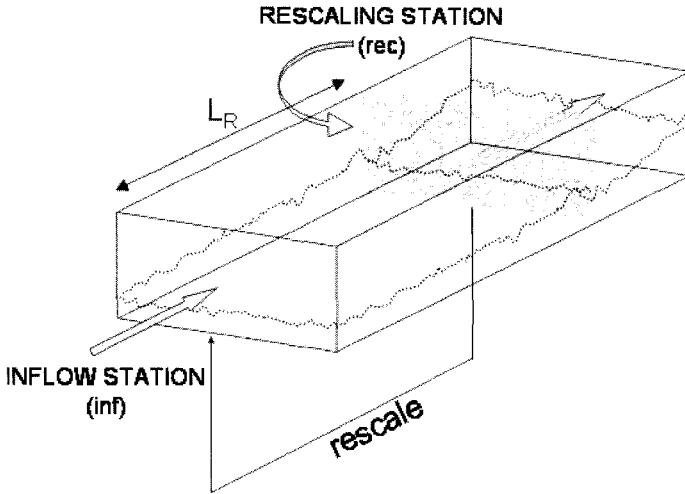


Fig. 8.8 Sketch illustrating a recycling technique in which data from an interior plane is mapped backwards to the inlet.

$$(\bar{u}_1^{inner})_{(inf)} = \beta (\bar{u}_1)_{(re)} (y_{(inf)}^+) \tag{8.21}$$

$$(\bar{u}_2^{inner})_{(inf)} = (\bar{u}_2)_{(re)} (y_{(inf)}^+) \tag{8.22}$$

$$(\bar{u}_3^{inner})_{(inf)} = 0 \tag{8.23}$$

$$(u_i^{\prime,inner})_{(inf)} = \beta (u_i^{\prime})_{(rec)} (y_{(inf)}^+, z, t) \tag{8.24}$$

and for the outer region:

$$(\bar{u}_1^{outer})_{(inf)} = \beta (\bar{u}_1)_{(re)} (\eta_{(inf)}) + (1 - \beta) U_\infty \tag{8.25}$$

$$(\bar{u}_2^{outer})_{(inf)} = (\bar{u}_2)_{(re)} (\eta_{(inf)}) \tag{8.26}$$

$$(\bar{u}_3^{outer})_{(inf)} = 0 \tag{8.27}$$

$$(u_i^{\prime,outer})_{(inf)} = \beta (u_i^{\prime})_{(rec)} (\eta_{(inf)}, z, t). \tag{8.28}$$

The rescaling factor  $\beta$  is the ratio of friction velocities respectively at the inlet station and at the recycled station:

$$\beta = \frac{u_{\tau,(inf)}}{u_{\tau,(re)}}. \tag{8.29}$$

In the above relations,  $y_{(inf)}^+$  and  $\eta_{(inf)}$  are the inner and the outer coordinates at the inlet stations:

$$y_{(inf)}^+ = \frac{y u_{\tau, (inf)}}{\nu} \quad \eta_{(inf)} = \frac{y}{\delta_{(inf)}}. \quad (8.30)$$

Complete velocity profiles valid over the entire inflow boundary layer are obtained by a weighted average of inner and outer profile<sup>5</sup>:

$$(u_i)_{(inf)} = \left[ (\bar{u}_i^{inner})_{(inf)} + (u_i^{\prime, inner})_{(inf)} \right] \cdot [1 - \mathcal{W}(\eta_{(inf)})] \\ + \left[ (\bar{u}_i^{outer})_{(inf)} + (u_i^{\prime, outer})_{(inf)} \right] \cdot \mathcal{W}(\eta_{(inf)}). \quad (8.31)$$

The weighting function  $\mathcal{W}$  is defined as:

$$\mathcal{W}(\eta) = \frac{1}{2} \left\{ 1 + \tanh \left[ \frac{4(\eta - b)}{(1 - 2b) + b} \right] / \tan(4) \right\} \quad (8.32)$$

where  $b = 0.2$  to provide a smooth transition at  $y/\delta = 0.2$ .

It has to be noted from Eqs. (8.29) and (8.30) that the rescaling operation requires the knowledge of the skin friction velocity  $u_{\tau}$  and the boundary layer thickness  $\delta$ , both at the rescaling station and the inlet plane. These quantities can be determined from the mean velocity profile at the rescaling station, but they must be specified at the inflow position. Lund *et al.* (1998) proposed to impose  $\delta$  at the inflow and to evaluate  $u_{\tau}$  as follows:

$$u_{\tau, (inf)} = u_{\tau, (re)} \left( \frac{\theta_{(re)}}{\theta_{(inf)}} \right)^{\frac{1}{2(n-1)}} \quad (8.33)$$

where  $\theta$  is the incompressible momentum thickness and the exponent  $n$  is set to 5<sup>6</sup>.

<sup>5</sup>Xiao *et al.* [Xiao *et al.*, 2003] rescale only the fluctuating components of velocity. In other words, the new profiles at the inlet are obtained by superimposing the recycled fluctuating component onto the mean component. This velocity profile remain fixed throughout the simulation and is extracted from an initial RANS calculation.

<sup>6</sup>Other solutions have been proposed in the literature (see Sagaut *et al.* [Sagaut *et al.*, 2004] for a review). As an example, Urbin and Knight [Urbin and Knight, 2001] derived from a power law  $U/U_{\infty} = (y/\delta)^{1/n}$ , the variables  $\beta$  and  $\delta_{(rec)}/\delta_{(inf)}$  as follows:

$$\beta = \left( \frac{\delta_{rec}}{\delta_{(inf)}} \right)^{\frac{1}{10}}, \quad \frac{\delta_{(rec)}}{\delta_{(inf)}} = \left( 1 + 0.27^{\frac{6}{5}} \frac{L_R}{\delta_{(inf)}} \mathcal{R}e_{(inf)}^{-\frac{1}{5}} \right)^{\frac{5}{6}} \quad (8.34)$$

where  $\mathcal{R}e_{(inf)}$  is the Reynolds number based on the inflow boundary layer thickness and  $L_R$  is the distance between inflow and recycle planes.

Spalart, Strelets and Travin [Spalart *et al.*, 2005b] proposed a simplified version of the rescaling method of Lund *et al.* [Lund *et al.*, 1998] which consists in rescaling the velocity field only in the wall-normal direction. Their interest is in keeping the distance from inflow plane to recycling plane as short as possible, so that differences in  $u_\tau$  are very slight. They also argue that the eddies in the inner-layer are re-generated rapidly, so that it is not essential to scale them exactly. Let the boundary layer thicknesses at the inflow station  $x = x_{(inf)}$  and rescaling station  $x = x_{(rec)}$  be  $\delta_{(inf)}$  and  $\delta_{(rec)}$ . Spalart *et al.* proposed the following single inflow condition for the velocity vector:

$$u(x_{(inf)}, y, z, t) = u\left(x_{(rec)}, y \frac{\delta_{(rec)}}{\delta_{(inf)}}, z + \eta_z, t\right) \quad (8.35)$$

where the spanwise shift  $\eta_z$  is introduced to keep turbulence at the inlet and recycling stations out of phase. In their DNS of an eddy break-up device in a boundary layer, the authors set the value of  $\eta_z$  equal to half the spanwise period and the recycling plane was located less than  $5 \delta$  downstream of the inflow plane.

The recycling approach has been successfully used in previous Direct and Large Eddy Simulation but not so many publications are devoted to its use in hybrid RANS/LES simulations.

Xiao *et al.* [Xiao *et al.*, 2003] used the  $k - \zeta$  (enstrophy) two-equation model [Robinson and Hassan, 1998] in the URANS region and blended it into a one equation model in the LES region (see also Sec. 7.4.3). Their approach differs from standard LES because of the existence of two additional RANS equations for  $k$  and  $\zeta$ . These authors derived new similarity laws to rescale the turbulent variable. Because  $u$  scales with  $u_\tau$  in both inner and outer regions, the turbulent kinetic energy  $k$  scales with  $u_\tau^2$  leading to:

$$\begin{aligned} (k^{inner})_{(inf)} &= \beta^2 (k^{inner})_{(rec)} \\ (k^{outer})_{(inf)} &= \beta^2 (k^{outer})_{(rec)}. \end{aligned} \quad (8.36)$$

Then, the eddy viscosity in the log layer is given by:

$$\nu_t = \chi u_\tau y \quad \text{with} \quad \chi = 0.41 \quad (8.37)$$

whereas the eddy viscosity provided by the  $k - \zeta$  RANS model reads as:

$$\nu_t = C_\mu \frac{k^2}{\nu \zeta} \quad \text{with} \quad C_\mu = 0.09. \quad (8.38)$$

Hence, Xiao *et al.* proposed (in the frame of compressible flow) the following scaling for the  $\zeta$  variable:

$$\begin{aligned} \left( \frac{\nu \nu_w \zeta}{u_\tau^4} \right)_{(inf)}^{inner} &= \left( \frac{\nu \nu_w \zeta}{u_\tau^4} \right)_{(rec)}^{inner} \\ \left( \frac{\delta \nu_w \zeta}{u_\tau^3} \right)_{(inf)}^{outer} &= \left( \frac{\delta \nu_w \zeta}{u_\tau^3} \right)_{(rec)}^{outer} \end{aligned} \quad (8.39)$$

It can be seen looking at Eqs. (8.36) and (8.39) that only the mean part of the turbulent quantities are rescaled and recycled. In a later work [Fan *et al.*, 2004], both mean and fluctuation parts of the turbulence quantities are rescaled according to:

$$\begin{aligned} \bar{\phi}_{(inf)}^{inner} &= \bar{\phi}_{(rec)} \left( y_{(inf)}^+ \right), & \bar{\phi}_{(inf)}^{outer} &= \bar{\phi}_{(rec)} \left( \eta_{(inf)} \right) \\ \phi'_{(inf)}{}^{inner} &= \phi'_{(rec)} \left( y_{(inf)}^+ \right), & \phi'_{(inf)}{}^{outer} &= \phi'_{(rec)} \left( \eta_{(inf)} \right) \end{aligned} \quad (8.40)$$

where  $\bar{\phi}$  and  $\phi'$  denote respectively the mean and time fluctuating parts of any turbulent quantity  $\phi$  ( $\phi = k$  and/or  $\omega$ , ...). The new profiles of the turbulent variables are obtained by an expression similar to Eq. (8.31).

The recycling-rescaling method was originally developed for flat plate boundary layers and it may face considerable problems in more complex geometries. In addition, it is to be noted that the main difficulty relative to recycling methods remains to initiate the recycling process. In general, a secondary turbulent boundary layer simulation has to be used to provide some appropriate perturbation. Moreover, such a process may introduce a non-physical recycling frequency ( $f_k = kU_\infty/L_R$  where  $L_R$  is the distance between inlet and recycling planes) due to the artificial streamwise periodicity introduced in the simulation, which depends on the location of the recycling planes (see for example [Kannepalli *et al.*, 2002]). These artificial periodicities can be broken by adding additional random noise at the inlet.

Spille-Kohoff and Kaltenbach [Spille-Kohoff and Kaltenbach, 2001] proposed a method which is a variant of the recycling-rescaling approach along with random inflow generation data but a number of control planes are placed a short distance downstream of the inlet. At each of these planes, a controller is introduced that amplifies the wall-normal velocity fluctuations through the use of body forces in the wall-normal momentum equation to match a target Reynolds shear stress provided by experiments or by a

RANS model.<sup>7</sup> Keating *et al.* [Keating *et al.*, 2004] successfully applied this forcing method including a control loop in the case of channel flow. Indeed, these authors obtained the correct Reynolds stresses within less than ten channel half-heights.

### 8.2.3 Forcing conditions

The main difference between global hybrid methods (see Sec. 7.4) and zonal methods is that global methods generally aim at covering the whole attached boundary layer (to avoid grey-area drawbacks, see Sec. 7.4.5) whereas zonal methods aim at covering only the inner-part of the boundary layer with URANS. This change of degree in the resolved equation within the boundary layer brings in the problem of the interface treatment between the inner-layer treated in RANS<sup>8</sup> and the outer one provided by LES. Hanjalić *et al.* [Hanjalić *et al.*, 2004] recalled that most hybrid methods suffer from the difficulty of reconciling the conditions on both sides of the RANS/LES interface and introduced the idea of “seamless coupling strategies” between URANS and LES. Nevertheless, the current experience of using weak RANS/LES coupling methods (see Sec. 7.4.5) shows that it is not enough just using RANS in the near-wall region in order to get good results in the LES region. In other words, additional conditions are needed at the interface.

Therefore, Dahlström and Davidson [Dahlstrom and Davidson, 2003], Dahlström [Dahlstrom, 2003], Davidson and Billson [Davidson and Billson, 2004] proposed to add instantaneous fluctuations to the momentum equations at the LES side of the interface to feed the LES region with

---

<sup>7</sup>Indeed, let us briefly recall for sake of simplicity the production term in the Reynolds shear-stress budget for a two-dimensional flow (see [Piquet, 1999] for a complete presentation):

$$\mathcal{P}_{u'v'} = -\overline{v'v'} \frac{\partial \bar{u}}{\partial y}. \quad (8.41)$$

One can notice from Eq. (8.41) that the decrease of the shear stress which in turn decrease the production of TKE is highly influenced by the decay of  $\overline{v'v'}$ . Therefore Spille-Kohoff and Kaltenbach [Spille-Kohoff and Kaltenbach, 2001] proposed to add a source term in the wall-normal momentum equation so that the Reynolds stress  $\overline{u'v'}$ ( $y$ ) reaches a prescribed profile. This source term acts simultaneously in several ( $x-z$ ) planes which are  $\mathcal{O}(1)\delta$  apart in the streamwise direction.

<sup>8</sup>Wall-layer modelling is still a serious problem for LES. An exhaustive review of existing wall-models is beyond the scope of this chapter but the reader can consult discussions in the papers by Piomelli and Ballaras [Piomelli and Balaras, 2003].

relevant turbulent structures. The RANS/LES interface is located in the inner part of the logarithmic region (*i.e.* around 30 and 60 wall units away from the wall, see Fig. 8.9). These fluctuations may be either synthesized (see Sec. 8.3) or taken from a DNS of a generic boundary layer (see Sec. 8.2.1) and are added as momentum sources in the cells adjacent to the RANS/LES interface. The forcing term has to mimic physical turbulent fluctuations and therefore should force the momentum equations to start to resolve large-scale turbulence. The source terms for the three momentum equations read as:

$$\mathcal{S}_u = -\gamma u'_a v'_a A_n, \quad \mathcal{S}_v = -\gamma v'_a v'_a A_n, \quad \mathcal{S}_w = -\gamma w'_a v'_a A_n \quad (8.42)$$

where  $A_n$  is the area of the LES cell facing the interface plane as illustrated in Fig. 8.9 and  $\gamma$  is a scaling function which is the ratio of the local modelled turbulent kinetic energy  $k_{RANS}$  and the turbulent kinetic energy of the added fluctuations  $k_{fluct} = \frac{1}{2} (\overline{u'_a{}^2} + \overline{v'_a{}^2} + \overline{w'_a{}^2})$  and  $\gamma$  is given by:

$$\gamma(x, y_{interface}, z, t) = c_\gamma \frac{k_{RANS}}{k_{fluct}}(x, y_{interface}, z, t) \quad (8.43)$$

where  $c_\gamma$  is an arbitrary constant taken as 0.4 and 1 by the authors. The RANS kinetic energy is provided by a one-equation model:

$$\frac{\partial k}{\partial t} + \frac{\partial}{\partial x_j} (\overline{u_j k}) = 2\nu_t \overline{S_{ij} S_{ij}} + \frac{\partial}{\partial x_j} \left[ (\nu + \nu_t) \frac{\partial k}{\partial x_j} \right] - C_\epsilon \frac{k^{\frac{3}{2}}}{\mathcal{L}}. \quad (8.44)$$

This model is used in both URANS and LES region (*i.e.* outer region  $y > y_{interface}$ ) and in the LES region where it corresponds to the subgrid-scale kinetic energy ( $k_{SGS}$ ). The turbulent length scale  $\mathcal{L}$  and eddy viscosity  $\nu_t$  are different in the two regions<sup>9</sup> (see Table 8.1).

<sup>9</sup>Note that no interface condition is used in the  $k$ -equation to ensure the continuity of the eddy viscosity at the interface. Conversely, Temmerman *et al.* [Temmerman *et al.*, 2004] computed dynamically the  $C_\mu$  coefficient appearing in the RANS turbulence model to yield a smoother transition between the URANS and LES regions since these authors used a  $k - \epsilon$  model in the URANS region coupled with a subgrid scale model in the LES region. With an eddy viscosity given by  $\nu_t^{RANS} = f_\mu C_\mu \frac{k^2}{\epsilon}$ , matching the subgrid scale eddy viscosity  $\nu_t^{LES}$  at the interface implies:

$$C_{\mu, interface} = \frac{\langle \nu_t^{LES} \rangle}{\langle f_\mu \frac{k^2}{\epsilon} \rangle} \quad (8.45)$$

where  $\langle \bullet \rangle$  denotes averaging over any homogeneous direction. The smooth transition from the traditional RANS value  $C_\mu = 0.09$  to the interface value  $C_{\mu, interface}$  is achieved

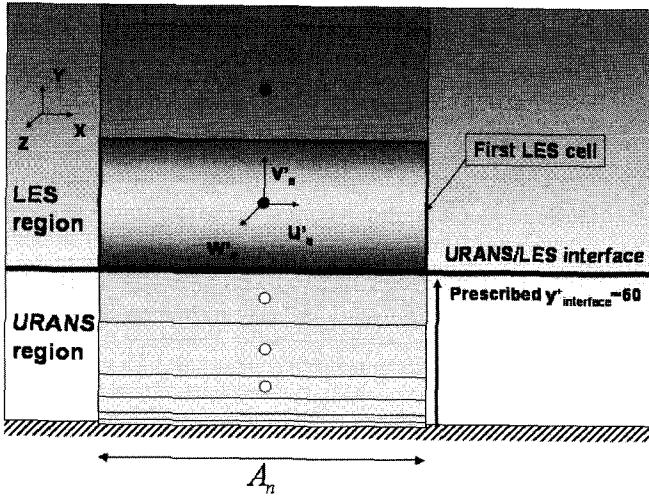


Fig. 8.9 Added fluctuations in a control volume in the LES cell adjacent to the URANS/LES interface. Adapted from Davidson and Billson (2004).

thanks to the empirical exponential function (see [Temmerman *et al.*, 2004]):

$$C_\mu = 0.09 + (C_{\mu,interface} - 0.09) \frac{1 - \exp(-y/\Delta)}{1 - \exp(-y_{interface}/\Delta)} \quad (8.46)$$

where  $\Delta = (\Delta x \Delta y \Delta z)^{\frac{1}{3}}$  and  $y_{interface}$  refers to the distance from the prescribed interface to the wall (see Fig. 8.9). At this stage, it is worthwhile to recall that the value  $C_\mu = 0.09$  plays a key role in determining the slope of the modelled logarithmic layer (contained in the RANS model) near the wall (see Eq. (7.15)). In other words, changing the standard value issued from scaling of flows in statistical equilibrium may corrupt the properties of the attached boundary layer (see Sec. 7.3.2) and raises the problem of Log-Layer-Mismatch (see Sec. 7.4.5) between the modelled inner-part of the log-layer and the resolved logarithmic layer provided by LES in the outer part of the boundary layer. In the case where no LES content is added in the outer part of the boundary layer, Temmerman *et al.*'s approach can be considered as a global hybrid approach (see Fig. 7.2) and therefore needs a careful monitoring of the grey-area (see Sec. 7.4.5).

Table 8.1 Parameters of the one equation model used by Davidson and Billson (2004) for both URANS and LES regions.  $d_w$  denotes the distance to the wall

	<i>URANS</i> ( $y < y_{interface}$ )	<i>LES</i> ( $y > y_{interface}$ )
$\mathcal{L}$	$2.5d_w \left[ 1 - \exp \left( -0.2k^{\frac{1}{2}} \frac{d_w}{\nu} \right) \right]$	$\Delta = (\Delta_x \Delta_y \Delta_z)^{\frac{1}{3}}$
$\nu_t$	$2.5k^{\frac{1}{2}} d_w \left[ 1 - \exp \left( -0.014k^{\frac{1}{2}} \frac{d_w}{\nu} \right) \right]$	$0.07k^{\frac{1}{2}} \Delta$
$C_\epsilon$	1	1.07

The fluctuations prescribed at the inlet interface are transformed along the streamwise evolution of the interface at each time-step using an assumption of “frozen turbulence” (*i.e.* Taylor’s hypothesis):

$$u'_{i,a}(x, y_{interface}, z, t) = u'_{i,a} \left( x_0, y_{interface}, z, M_S \left( t - \frac{x - x_0}{\langle \bar{u}_{interface} \rangle} \right) \right) \quad (8.47)$$

where  $x_0$  denotes the location of the inlet and  $\langle \bar{u}_{interface} \rangle$  the mean velocity component at the interface averaged both in time and over any homogeneous direction.  $M_S$  is a parameter that can be used to artificially increase the streamwise turbulent length scale of the added fluctuations.

Dahlström and Davidson [Dahlstrom and Davidson, 2003] used their method to simulate a fully developed channel flow and plane asymmetric diffuser flow. To generate the fluctuations needed in Eq. (8.42), a DNS of channel flow at  $Re_\tau = 500$  was used. Instantaneous data of the velocity components at plane  $x_0$  are stored on disk. These authors advocate that these DNS data can be used for forcing at the interface for a wide range of boundary layers since the inner structure of the log-law region depends only weakly on the Reynolds number. They found that the interface condition improves results considerable (velocity and turbulent kinetic energy profiles) compared to the case without forcing submitted to grey-area problems (see Sec. 7.4.5).

### 8.3 Turbulence Reconstruction for Inflow Conditions

The inflow methods relying on synthetic turbulence generations are based on the assumption that turbulence can be specified by using only low order statistics (mean velocity, spectra). An early proposal for the generation of synthetic turbulence was given in the paper by Kraichnan [Kraichnan,

1969] in his work on diffusion by a random velocity field. His proposal was based on a sum of Fourier modes and was limited to frozen isotropic turbulence. The topic of synthetic turbulence generation is now growing rapidly.

### 8.3.1 Random fluctuations

The simplest approach is to superimpose random noise on the inlet mean velocity profile. Nevertheless, one of the most significant aspect of turbulence is its spatial and temporal coherence in the long wave range quantified by the integral and Taylor scales (see Chapter 1). Indeed, the larger scale turbulent eddies initiate the cascade of turbulent kinetic energy from large to small scales. A random noise inlet condition suffers from a lack of correlation in both time and space. As a result, these random fluctuations lie usually in the high wave number part of the kinetic energy spectrum and are very quickly dissipated, without sustaining real turbulence. The flow relaminarizes quickly downstream the inlet plane (see [Schlüter *et al.*, 2004]). A further improvement might be a white noise signal that would reproduce the single point statistics.

### 8.3.2 Inverse Fourier transform technique

A classical approach for the generation of synthetic inflow data is to produce a velocity signal which has certain statistical properties (mean and fluctuating values, energy spectra).

To this end, the proposal of Lee, Lele and Moin [Lee *et al.*, 1992] is based on an inverse Fourier transform of the velocity field. For the sake of simplicity, we illustrate this approach by a one-dimensional example. Therefore, let us consider a discrete signal  $u_k$  in physical space. Its discrete Fourier transform defines uniquely the corresponding  $\hat{u}_n$  in the Fourier space:

$$u_k = \frac{1}{N} \sum_{n=0}^{N-1} \hat{u}_n \exp\left(2i\pi k \frac{n}{N}\right), \quad n = 0, \dots, N-1 \quad (8.48)$$

where  $\hat{u}_n$  are complex numbers which can be written as:

$$\hat{u}_n = |\hat{u}_n| \exp(i\Phi_n), \quad i^2 = -1 \quad (8.49)$$

where  $|\hat{u}_n|$  and  $\Phi_n \in [0; 2\pi]$  are respectively the modulus and the phase angle of the complex wave number  $\hat{u}_n$ . The Parseval relation which states

the conservation of the energy of the signal in both physical and Fourier space (thus providing a connection between  $|\hat{u}_n|$  and the energy spectrum  $E(n) = \frac{1}{2}u_n u_n^*$ ) yields:

$$\sum_{n=0}^{N-1} E(n) \equiv \frac{1}{2N} \sum_{n=0}^{N-1} |\hat{u}_n|^2 = \frac{1}{2} \sum_{k=0}^{N-1} |u_k|^2. \quad (8.50)$$

Consequently, if one chooses a random phase angle  $\Phi_n$  as well as a prescribed spectrum  $E(n)$ , an inverse Fourier transform of  $\hat{u}_n$  (with  $|\hat{u}_n| \equiv \sqrt{2E(n)}$ ) produces a velocity  $u_k$  with the prescribed spectrum  $E(n)$ . Note that the signal obtained from the above procedure is periodic in time. Therefore, Lee and coworkers modify the phase angle  $\Phi_n$  at a random instance by a small amount  $\Delta\Phi_n$  (sometimes referred to as *phase jittering technique*<sup>10</sup>). However, the extension of this method in the three-dimensional case is relatively complex<sup>11</sup>. Indeed, in three-dimensional turbulence, significant amounts of energy are transferred in both directions in terms of wave numbers and not so many experiments provide nowadays the three-dimensional energy spectrum. Therefore, Lee *et al.* used the following model spectrum:

$$E(\kappa) \sim \kappa^4 \exp\left(-2\left(\frac{\kappa}{\kappa_e}\right)^2\right), \quad \kappa = (\kappa_1^2 + \kappa_2^2 + \kappa_3^2)^{\frac{1}{2}} \quad (8.52)$$

where  $\kappa_e$  is the peak wave number in the energy spectrum which cannot be chosen uniquely.

As an example, Le, Moin and Kim [Le *et al.*, 1997] performed a DNS of a backward facing step flow at a Reynolds number of  $Re_h = 5100$  based on the step height  $h$  and inlet free-stream velocity. The time-dependent velocity described at the inflow consists of a mean velocity profile obtained from Spalart's [Spalart, 1988] boundary layer simulation to which random

<sup>10</sup>In Fourier space, one can also change the amplitude of the original energy spectrum  $E(\kappa)$ :

$$E(\kappa) \equiv E(\kappa)(1 + \epsilon) \quad (8.51)$$

where  $\epsilon$  is a random number of fixed magnitude, before performing the inverse Fourier transform of  $E(\kappa)$  to provide fresh data. Conversely to Lee *et al.*'s technique [Lee *et al.*, 1992], this method is referred to as an *amplitude jittering technique*. Both methods were compared by Chung and Sung [Chung and Sung, 1997]. These authors indicate that for wall bounded flows, *amplitude jittering* may be more efficient than *phase jittering* because flow structures (*i.e.* phase information) are not destroyed in the former.

<sup>11</sup>It can be noted that the use of the Fourier transform introduces some additional constraints since the grid has to be cartesian and equidistant.

fluctuations with given moments and spectra were superposed. These authors used the above method of Lee, Lele and Moin [Lee *et al.*, 1992] to generate velocity fluctuations at the inlet which ensures that the resulting inlet signal does not contain excessive small-scale motion (analogous to random numbers, see Sec. 8.3.1) and that the peak in the spectrum corresponds to well-resolved wavelength. However, Le, Moin and Kim [Le *et al.*, 1997] found that the flow loses its statistical characteristics some distance downstream of the inflow although Lee *et al.*'s procedure produces a set of stochastic inlet data that satisfies a prescribed set of second-order statistics. Finally, their calculation required an inlet domain with a length of ten step heights (e.g. a third of their total domain length) to recover the targeted turbulent characteristics. The authors attributed this transition to the structureless inlet turbulence which was a result of the randomized phase angles in Lee's *et al.* method (1992).

Instead of using the inverse Fourier transform, Klein, Sadiki and Janicka [Klein *et al.*, 2003] introduced a method which is based on digital filtering of random data that is able to reproduce a prescribed set of second order statistics as well as auto-correlation functions. Their method was shown to give satisfactory results in plane jet simulations.

### 8.3.3 Random Fourier modes synthesization

A time-space turbulent velocity field can also be generated using random Fourier modes. This basic idea was suggested by Kraichnan [Kraichnan, 1969] in 1969 and has since gone through various stages of refinement.

Davidson [Davidson, 2005] prescribed the time space velocity field as follows:

$$u'_i(x_j) = 2 \sum_{n=1}^N \hat{u}^n \cos(\kappa_j^n x_j + \phi^n) \sigma_i^n \quad (8.53)$$

where  $\hat{u}^n$ ,  $\kappa_j$ ,  $\phi^n$ ,  $\sigma_i^n$  are respectively amplitude, wave number vector, phase and direction of Fourier mode  $n$ .

The amplitude of each mode  $\hat{u}^n$  is given<sup>12</sup> by:

$$\hat{u}_n = \sqrt{E(|\kappa_j^n|) \Delta\kappa} \quad (8.54)$$

where the energy spectrum is taken as a modified *Von Kármán* spectrum:

---

<sup>12</sup>Note that the turbulent kinetic energy is given by  $k = \frac{1}{2} \sum_{n=1}^N (\hat{u}_n)^2$ .

$$E(\kappa) \equiv \frac{u_{rms}^2}{\kappa_e} \cdot \frac{(\kappa/\kappa_e)^4}{\left[1 + (\kappa/\kappa_e)^2\right]^{\frac{17}{6}}} \exp\left[-2\left(\frac{\kappa}{\kappa_K}\right)^2\right] \quad (8.55)$$

where  $\kappa_K = \epsilon^{\frac{1}{4}} \nu^{-\frac{3}{4}}$  is the Kolmogorov wave number and  $\kappa_\tau$  is the most energetic length scale (see Fig. 8.10). Davidson and Billson [Davidson and Billson, 2004] divided linearly the spectrum into 150 intervals.

The wave number vector components  $\kappa_j^n$  are chosen randomly on a sphere and the phase of each mode is chosen with uniform probability between  $0 \leq \phi^n \leq 2\pi$ . The direction of each mode  $\sigma_i^n$  is obtained under the incompressibility assumption since continuity requires:

$$\kappa_i^n \sigma_i^n \equiv 0 \quad \forall n \quad (8.56)$$

This procedure produces at each time step a set of stochastic inlet data that satisfies a prescribed spectrum but lacks temporal correlation. Therefore, Davidson [Davidson, 2005] introduced a time correlation at instant  $t^m$  through a linear interpolation of the running average (e.g. instant  $t^1$  to  $t^{m-1}$ ). To create correlation in time, new fluctuating velocity fields are computed as:

$$\left(\mathcal{U}'_i\right)^m = a \left(\mathcal{U}'_i\right)^{m-1} + b \left(u'_i\right)^m, \quad a = \exp\left(-\frac{\Delta t}{T_t}\right) \quad (8.57)$$

where  $t^m$  denotes instant  $m\Delta t$  where  $\Delta t$  is the computational time step and  $b = (1 - a^2)^{1/2}$ . The time correlation of  $\mathcal{U}'_i$  is equal to  $\exp\left(-\frac{\Delta t}{T_t}\right)$  where the time scale  $T_t$  is proportional to the turbulent time scale  $k/\epsilon$ .

The turbulent velocity field is finally prescribed as:

$$u_i(0, y, z, t) = U_i(y) + \left(\mathcal{U}'_i\right)^m \quad (8.58)$$

where the mean velocity field is set as  $U_2 = U_3 = 0$  and

$$U_1^+ = \begin{cases} y^+ & y^+ \leq 5 \\ -3.05 + 5 \ln(y^+) & 5 \leq y^+ \leq 30 \\ \frac{1}{\chi} \ln(y^+) + 5.2 & y^+ \geq 30. \end{cases} \quad (8.59)$$

Davidson [Davidson, 2005] applied this method for hybrid RANS/LES (see Eq. (8.44)) of channel flow at  $Re_\tau = 2000$  using different sets of length and time scales of the inlet fluctuations. He also evaluated the ability of the method in the case of periodic streamwise boundary conditions as well as in the case of inlet-outlet boundary conditions.

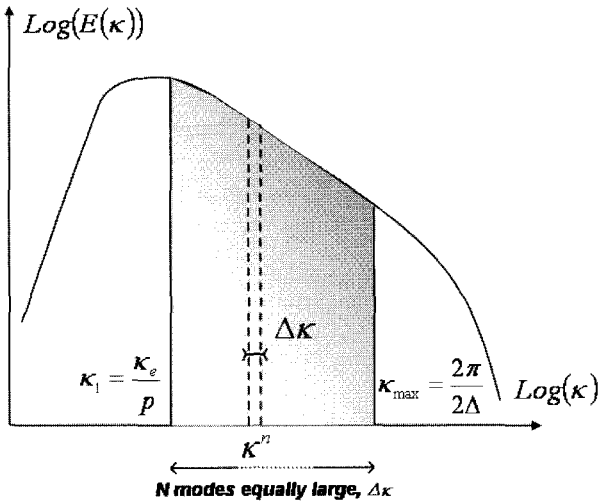
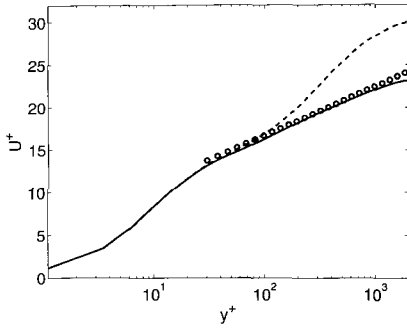


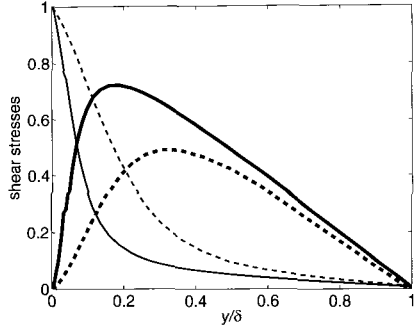
Fig. 8.10 Modified Von Kármán spectrum (the  $N$  modes are equally distributed). The largest wave number is given by the mesh resolution  $\kappa_{max} = 2\pi/2\Delta$  and smallest wave number is given by  $(\kappa_e/p)_{p \geq 1}$  where  $\kappa_e = \frac{9\pi}{55L_t}$ ,  $L_t = C \frac{k^{3/2}}{\epsilon}$ ,  $C = 3$ . The factor  $p$  is chosen greater than one to make the largest scale larger than those corresponding to  $\kappa_e$ .

The velocity profiles with and without forcing are presented in Fig. 8.11 in the case of periodic streamwise boundary conditions. One can notice that the agreement of hybrid RANS/LES with forcing is excellent whereas without forcing the velocity profile suffers Modelled-Stress-Depletion (see Sec. 7.4.5). In the case of inlet-outlet boundary conditions, Figs. 8.12 and 8.13 allow one to evaluate the effect of the time scale  $T_t$  since the turbulent length scale is set to  $L_t = 0.11\delta$ . It can be seen that in case with no time correlation, the resolved turbulence is dramatically reduced. Therefore, Davidson concluded that the time scale is as important as the length scale. Furthermore, he added that inlet and length scales should not be equal to the correct, physical values, but should be related to the grid.

Smirnov, Shi and Celik [Smirnov *et al.*, 2001] proposed the idea of a tensor scaling based on scaling transformations of the Reynolds stresses that allows to generate flowfield representing turbulent velocity fluctuations. Inspired by them, Batten, Goldberg and Chakravarthy [Batten *et al.*, 2004] introduced a simplified alternative to Smirnov *et al.*'s method to generate synthetic turbulence that is based on the superposition of sinusoidal modes with random frequencies and wave number with given spectra. Their



(a)  $\langle \bar{u} \rangle$  profiles.  $\circ$ :  $2.5 \ln(y^+) + 5.2$



(b) Shear stresses. Thick lines: resolved; thin lines: modelled.

Fig. 8.11 Mean velocities and shear stresses. Streamwise periodic boundary conditions. Solid lines: forcing with isotropic fluctuations with  $M_S = 0.25$ ; dashed lines: no forcing. Reynolds number  $Re_\tau = \frac{u_\tau \delta}{\nu} = 2000$ . Mesh  $32 \times 64 \times 32$  (streamwise, wall-normal, spanwise). Domain:  $4\pi \times 2 \times 2\pi$ . Grid spacing:  $(\Delta x^+, \Delta y^+, \Delta z^+) = (785, [1 - 292], 393)$  Courtesy of L. Davidson, Chalmers University of Technology, Sweden.

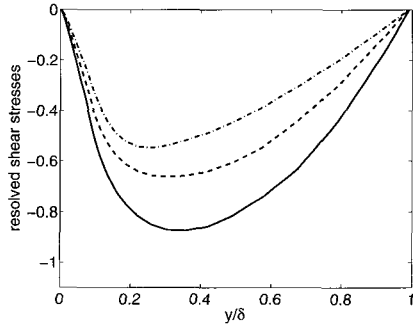
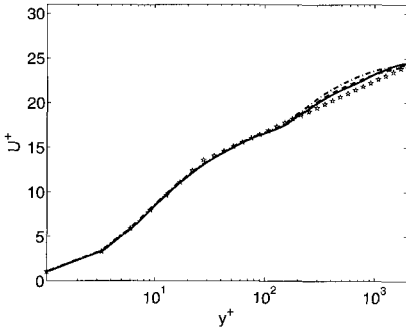


Fig. 8.12 Mean velocities and shear stresses. Inlet-outlet boundary conditions. Length scale:  $L_t = 0.11\delta$ . Time scale:  $T_t = 0.22\delta/u_\tau$ . Solid line:  $x/\delta = 7.3$ ; dashed line:  $x/\delta = 15.2$ ; dash-dotted line:  $x/\delta = 22.9$ . Mesh  $64 \times 64 \times 32$  (streamwise, wall-normal, spanwise). Domain:  $8\pi \times 2 \times 2\pi$ . Grid spacing:  $(\Delta x^+, \Delta y^+, \Delta z^+) = (785, [1 - 292], 393)$   $Re_\tau = 2000$ . Mean inlet velocity from log-law. Fluctuating velocities from isotropic synthetic turbulence with turbulent length scale  $L_t$  and time scale  $T_t$ . Courtesy of L. Davidson, Chalmers University of Technology, Sweden.

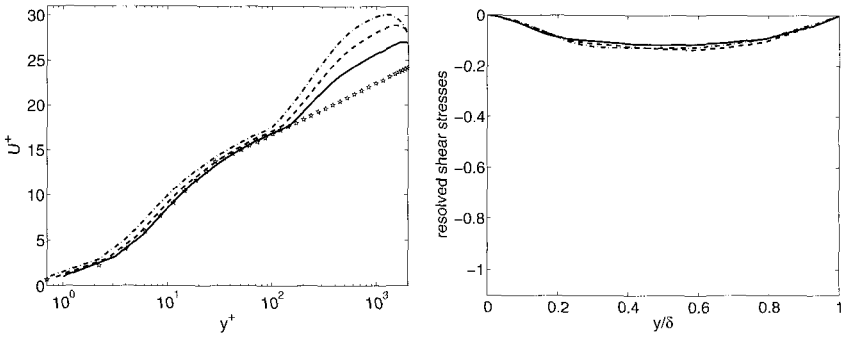


Fig. 8.13 Mean velocities and shear stresses. Inlet-outlet boundary conditions. Length scale:  $L_t = 0.11\delta$ . Time scale:  $T_t = 0$ . Solid line:  $x/\delta = 7.3$ ; dashed line:  $x/\delta = 15.2$ ; dash-dotted line:  $x/\delta = 22.9$ . Courtesy of L. Davidson, Chalmers University of Technology, Sweden.

reconstruction procedure requires, as input, the local Reynolds stress tensor  $\overline{u'_i u'_j}$  as well as the length and time scales of turbulence (denoted respectively as  $\mathcal{L}$  and  $\tau$ ) which can be extracted from the available RANS data. Indeed, the scales  $\mathcal{L}$  and  $\tau$  as well as the velocity scale  $\mathcal{U}$  can be calculated from the turbulent kinetic energy  $k$  and the turbulent dissipation rate  $\varepsilon$  as follows:

$$\mathcal{U} = \sqrt{2k}, \quad \tau = \frac{k}{\varepsilon}, \quad \mathcal{L} = \mathcal{U}\tau. \tag{8.60}$$

The synthetic turbulent fluctuation field  $u'_i$  is reconstructed by a tensor scaling:

$$u'_i = a_{ik} v_k \tag{8.61}$$

where  $a_{ik}$  is the Cholesky<sup>13</sup> decomposition of the local Reynolds stress

<sup>13</sup>The Cholesky factorization expresses a positive definite symmetric matrix as the product of a triangular matrix and its transpose :

$$\mathbf{A} = \mathbf{R}^t \mathbf{R} \tag{8.62}$$

where  $\mathbf{R}$  is an upper triangular matrix. As an example, Lund *et al.* [Lund *et al.*, 1998] proposed the following transformation:  $u_i = \bar{u}_i + a_{ij} v_j$  with  $\bar{v}_j = 0$ ,  $\overline{v_i v_j} = \delta_{ij}$  and  $a_{ij}$  reads:

$$(a_{ij}) = \begin{pmatrix} \sqrt{R_{11}} & 0 & 0 \\ R_{21}/a_{11} & \sqrt{R_{22} - a_{21}^2} & 0 \\ R_{31}/a_{11} & (R_{32} - a_{21}a_{31})/a_{22} & \sqrt{R_{33} - a_{31}^2 - a_{32}^2} \end{pmatrix}$$

$a_{ij}$  can be considered as a Cholesky decomposition of the correlation tensor  $R_{ij}$ .

tensor and  $v_k$  is an intermediate velocity field defined as a sum of  $N$  sines and cosines with random phases and amplitudes:

$$v_i(x_j, t) = \sqrt{\frac{2}{N}} \sum_{n=1}^N [p_i^n \cos(\tilde{\kappa}_j^n \tilde{x}_j + \omega^n \tilde{t}) + q_i^n \sin(\tilde{\kappa}_j^n \tilde{x}_j + \omega^n \tilde{t})] \quad (8.63)$$

where

$$\tilde{x}_j = 2\pi \frac{x_j}{\mathcal{L}} \quad ; \quad \tilde{t} = 2\pi \frac{t}{\tau} \quad ; \quad \omega^n = \mathcal{N}(1, 1) \quad (8.64)$$

are spatial coordinates normalized by the length and time scale of turbulence and  $\omega^n$  are the random frequencies taken from a normal distribution  $\mathcal{N}(\mu, \sigma)$  of mean  $\mu$  and standard deviation  $\sigma$ . The amplitude of cosines and sines are given by:

$$p_i^n = \epsilon_{ijk} \zeta_j^n \kappa_k^n, \quad q_i^n = \epsilon_{ijk} \zeta_j^n \kappa_k^n, \quad \zeta_i^n = \mathcal{N}(0, 1) \quad (8.65)$$

where  $\epsilon_{ijk}$  is the so-called alternator<sup>14</sup> and  $\tilde{\kappa}_j^n = \frac{U}{c^n}$  are modified wave numbers obtained by multiplying the wave numbers  $\kappa_i^n = \mathcal{N}(0, \frac{1}{2})$  taken from a normal distribution with variance  $\frac{1}{2}$ , by the ratio of the velocity scale  $U$  to  $c^n$  given:

$$c^n = \sqrt{\frac{3}{2} \frac{u'_l u'_m \kappa_l^n \kappa_m^n}{\kappa_k^n \kappa_k^n}} \quad (8.66)$$

$c^n$  is an anisotropic scale taken as a tensorially invariant measure in the direction of the modal wave vector  $\kappa^n$ . Although the wave numbers  $\kappa_i^n$  are distributed isotropically in a sphere, the additional tensor scaling given by eq (8.66) accounts for the anisotropy of the flow. Indeed, dividing the wave number  $\kappa_i^n$  by  $c^n$  tends to elongate wave numbers that are aligned with the largest component of the Reynolds-stress tensor. As an example, near the wall a larger  $\overline{u'_1 u'_1}$  implies a stronger correlation in the  $x$  direction and eddies are more elongated in  $x$ . Ideally, a Reynolds Stress Model (RSM) would provide the most accurate description of the Reynolds stress tensor. However, Batten *et al.* (2004) outlined that simpler model can be used. As an example, these authors used the cubic two-equation  $k - \epsilon$  model of Goldberg *et al.* [Goldberg *et al.*, 1999]. The situation may be more prob-

<sup>14</sup> $\epsilon_{ijk} = 1$  if  $\{i, j, k\}$  is an even permutation of  $\{1, 2, 3\}$ , to  $-1$  if  $\{i, j, k\}$  is an odd permutation of  $\{1, 2, 3\}$  and to  $0$  if  $\{i, j, k\}$  is not a permutation of  $\{1, 2, 3\}$ .

lematic if a one equation eddy viscosity model is used since the turbulent kinetic energy cannot be obtained directly from the model without additional modelling assumptions. Keating *et al.* [Keating *et al.*, 2004] tested the synthetic turbulence generation method proposed by Batten *et al.* on a channel flow at a Reynolds number based on the channel half-height equal to  $Re = 6900$ . The number of modes  $N$  (see Eq. (8.63)) used to generate the synthetic field was 200. They obtained synthetic turbulence with a realistic spectrum with significant energy content for scales larger than the integral length scale  $\mathcal{L}$ . However, a relatively long transition region (near  $20\delta$ ) was necessary to regenerate fully-developed turbulence.

### 8.3.4 Synthetic turbulence

Sandham, Yao et Lawal [Sandham *et al.*, 2003] proposed a different technique to perform a synthetic reconstruction of the typical structures present in turbulent boundary layers. Their method is based on a more deterministic approach to define specific disturbances with prescribed phase information into the inner- and outer-layer of the boundary layer. Indeed, the inner-layer is populated with low speed streaks while the outer layer is characterized by large-scale coherent structures. At the inflow, the streamwise and wall-normal (denoted as  $u_i^{\prime,inner}$ ,  $i = 1, 2$ ) components of the velocity fluctuations are used to represent lifted streaks of the inner-layer with a peak at a location of  $y_{p,1}^+ = 12$ . The outer layer fluctuations (denoted as  $u_i^{\prime,outer}$ ) represent three-dimensional vortices. The inner- and outer-layer fluctuations are given respectively by:

$$\begin{aligned} u_i^{\prime,inner} &= C_{i,1} y^+ \exp\left(-\left(\frac{y^+}{y_{p,1}^+}\right)^i\right) \sin(\omega_1 t) \cos(\beta_1 z + \Phi_1) \quad i = 1, 2 \\ u_i^{\prime,outer} &= \sum_{j=2}^4 C_{i,j} \left(\frac{y}{y_{p,j}}\right)^2 \exp\left(-\left(\frac{y}{y_{p,j}}\right)^2\right) \sin(\omega_j t) \cos(\beta_j z + \Phi_j) \end{aligned} \quad (8.67)$$

where  $j = 1, 2, 3, 4$  are mode indices,  $y^+$  is the normalized wall coordinate,  $\omega_j$  denotes the forcing frequencies,  $\beta_j$  and  $\Phi_j$  are the spanwise wave numbers and associated phase shifts, respectively, and  $C_{i,j}$  are constants. Note that three modes are used to represent the largest structures of the outer layer. The parameters  $\beta_j$  and  $\omega_j$  are chosen to match the typical sizes of

the coherent structures present in the boundary layer. Finally, the spanwise component  $u'_3$  is computed using the divergence free condition. In addition, a white noise was also added in the boundary layer zone with a maximum amplitude of 4% of the reference velocity.

Based on the method developed by Sandham *et al.* [Sandham *et al.*, 2003], Terracol [Terracol, 2005] use the following boundary layer model to reconstruct streamwise and wall normal components of the velocity fluctuations at the inflow:

$$u'_i = U_\infty \sum_{j=1}^4 C_{i,j} \left( \frac{y}{y_j^{max}} \right)^{n_j} \exp \left( - \left( \frac{y}{y_j^{max}} \right)^{n_j} \right) \cos(\beta_j z + \phi_j) \sin(\omega_j t)$$

$$i = 1, 2. \quad (8.68)$$

The first mode ( $j = 1$ ) provides a model for the near wall streaks, while higher-order modes ( $j > 1$ ) represent some larger structures encountered in the outer part of the boundary layer. The peak perturbation locations are respectively fixed to  $(y_j^{max})^+ = 12$  and  $(y_j^{max}) = (j - 1) \delta^*$  where  $\delta^*$  is the displacement thickness at the inflow location. The amplitude coefficients have been tuned to match typical turbulent boundary layer turbulent stress profiles. The exponent  $n_j$  has also been introduced to modify the envelope of the first mode, with  $n_1 = 1 - \frac{1}{6} (1 + \tanh[10(y - y_1^{max})])$  and  $(n_j)_{j>1} = 1$ . The values of each parameter used are detailed in Table 8.2. For this purpose, we introduce (in wall units) the spanwise spacing of the synthetic structures  $\lambda_z^+ = \frac{2\pi(u_\tau)}{\beta_j \mu}$  and their life times  $\tau^+ = \frac{2\pi(u_\tau)^2}{\omega_j \mu}$  where  $\mu$  denotes viscosity and  $u_\tau$  the skin-friction velocity at the inflow. Note however that these values are case-dependent.

The author evaluated the capabilities of different turbulence generation methods on the flow over a thin flat plate ended by a blunt trailing edge of thickness  $h$ . The Reynolds number based on the trailing edge thickness is  $Re_h = 10000$  and the Mach number is equal to 0.5.

Table 8.2 Analytical TBL parameters

$j$	$C_{1j} \frac{U_\infty}{u_\tau^{(in)}}$	$C_{2j} \frac{U_\infty}{u_\tau^{(in)}}$	$y_j^{max}$	$\lambda_z^+$	$\tau^+$	$\phi_j$
1	15.2	-5	$12 \mu / u_\tau^{(in)}$	100	100	0
2	5.6	-2.8	$\delta^*$	133	32	0.1
3	5.6	-2.8	$2\delta^*$	200	58	0.2
4	5.6	-2.8	$3\delta^*$	400	109	0.3

An initial LES on the whole configuration taking into account the boundary layer transition process was first performed to get a reference. In this initial calculation, the flat plate extends over  $60h$  and transition is located  $45h$  upstream of the trailing edge.

Then, a shorter computational domain located close to the trailing-edge has been considered since the streamwise extent of the flat plate region has been reduced to  $11h$ . On this reduced domain, Terracol [Terracol, 2005] performed three zonal LES calculations based on the NLDE approach (see Sec. 8.1.2). The first calculation (Zonal(a)) uses only the characteristic boundary treatment at inflow while the second one (Zonal(b)) takes advantage of an additional recycling treatment for the perturbation (see Sec. 8.2.2) and the third one (Zonal(c)) relies on the use of the analytical model given by Eq. (8.68).

For both zonal simulations accounting explicitly for turbulent fluctuations at the inflow (Zonal(b) and Zonal(c)), the author observes a very good behavior. The three-dimensional features of the flow are well reproduced, as shown in Fig. 8.14, where the near-wall streaky structures are correctly re-generated. Figure 8.15 shows that for these two simulations, the velocity profiles agree pretty well with the reference LES, for both the mean and fluctuations profiles. However, it appears clearly that the zonal simulation performed without the adjunction of inflow disturbances (Zonal(a)) fails to reproduce the flow correctly, leading to a strong underestimation of the friction and turbulent fluctuations.

The author also investigated the radiated acoustic field, by looking at the pressure spectrum above the trailing edge (see Fig. 8.16). It can be observed that the three zonal simulations provide a good representation of the main frequency peak, at a Strouhal number of  $St \simeq 0.24$ . However, it can also be observed that simulation “Zonal(b)” introduces some spurious energy in the high frequencies ( $St \simeq 1$ ). According to the author, this may be explained by the intrinsic nature of the recycling-based inflow condition, which introduces naturally its own recycling frequency in the flowfield. Based on this observation, the analytical inflow condition (simulation “Zonal(c)”) was finally retained to perform other calculations<sup>15</sup>.

---

<sup>15</sup>In [Terracol, 2005], the author presented some first zonal simulations of the flow in the vicinity of the blunted trailing-edge of a NACA0012 airfoil, for a significant value of the chord-based Reynolds number ( $Re_c = 2.86 \times 10^6$ ).

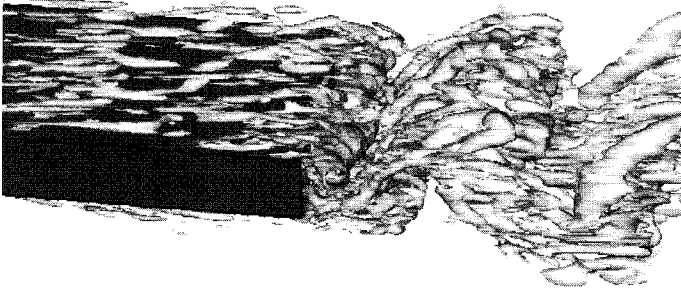


Fig. 8.14 3D view of the flow close to the trailing edge (simulation “Zonal(c)”). Terracol (2005).

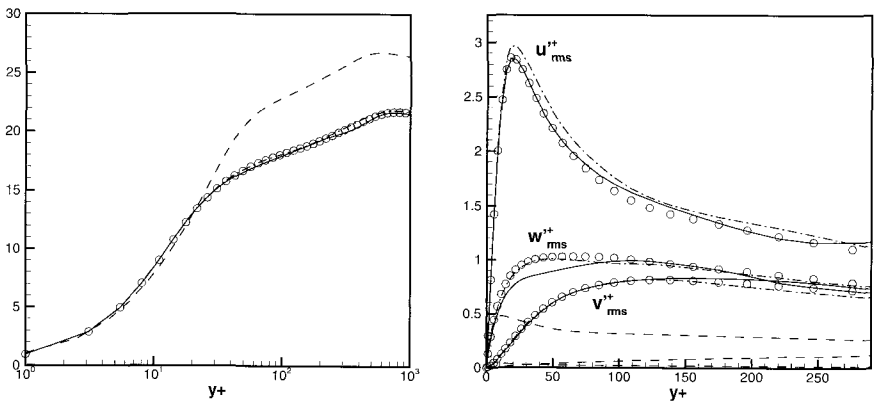


Fig. 8.15 Mean streamwise (left) and rms (right) velocity profiles. Symbols: reference LES; dashed line: Zonal(a); dash-dotted line: Zonal(b); solid line: Zonal(c). Terracol (2005).

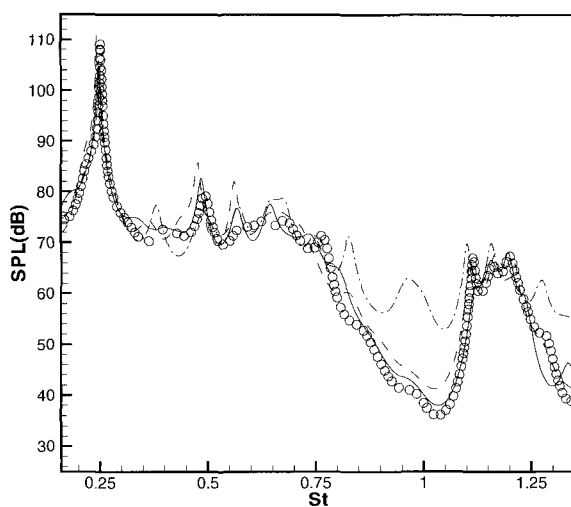


Fig. 8.16 Pressure spectrum at  $10h$  above the trailing edge. Symbols: reference LES; dashed line: Zonal(a); dash-dotted line: Zonal(b); solid line: Zonal(c). Terracol (2005).

This page is intentionally left blank

# Bibliography

- Adams, N. A. (1999). Advances in direct deconvolution modeling of subgrid-scales for flows with discontinuities. *Annual Research Briefs, Center for Turbulence Research*, 317–327.
- Adams, N. A. (2000a). Direct simulation of the turbulent boundary layer along a compression ramp at  $M=3$  and  $Re_\theta = 1685$ . *J. Fluid Mech.*, 420:47–83.
- Adams, N. A. (2000b). Deconvolution methods for large-eddy simulation. *Proceedings of the ECCOMAS 2000 congress, Barcelona*.
- Adams, N. A. and Leonard, A. (1999). Deconvolution of subgrid-scales for the simulation of shock-turbulence interaction. In *Direct and Large-Eddy Simulation III*, 201–212. Kluwer Academic Publishers.
- Angot, P., Caltagirone, J., and Khadra, K. (1992). Une méthode adaptative de raffinement local : la correction du flux à l'interface (in french). *C. R. Acad. Sci. Paris, série I*, 315:739–745.
- Aupoix, B., Guenot, D., and Sagaut, P. (2001). ATAC: Amélioration des modèles de turbulence pour prévoir l'écoulement dans la tuyère et sur l'arrière corps. *Onera, RT No.64/00144 DAFE/DMAE*.
- Baggett, J. (1998). On the feasibility of merging les with rans for the near-wall region of attached turbulent flows. *CTR Annual Research Briefs, Technical Rept, 267-277, Center for Turbulence Research, Stanford Univ, Stanford, CA*.
- Baldwin, B. and Lomax, H. (1978). Thin layer approximation of algebraic model for separated flows. *AIAA Paper 78-0257*.
- Bardina, J., Ferziger, J. H., and Reynolds, W. C. (1980). Improved turbulence models based on large eddy simulation of homogeneous, incompressible, turbulent flows. *AIAA paper 80-1357*.
- Barenblatt, G.I. (1996). *Scaling, self-similarity, and intermediate asymptotics*. Cambridge University Press, UK
- Bastin, F., Lafon, P., and Candel, S. (1997). Computation of jet mixing noise due to coherent structures: the plane jet. *Journal of Fluid Mechanics, vol.335, 261-304*.
- Basu, D., Hamed, A., and Das, K. (2005). DES and Hybrid RANS/LES models for unsteady separated turbulent flow predictions. *AIAA Paper 05-0503*,

- 43rd AIAA Aerospace Sciences Meeting and Exhibit, Reno, Nevada, Jan.
- Batten, P., Goldberg, U., and Chakravarthy, S. (2000). Sub-Grid turbulence modeling for unsteady flow with acoustic resonance. *AIAA Paper 00-0473*, 38th AIAA Aerospace Sciences Meeting and Exhibit, Reno, Nevada.
- Batten, P., Goldberg, U., and Chakravarthy, S. (2002). LNS-An Approach Towards Embedded LES. *AIAA Paper 02-0427*, 40th AIAA Aerospace Sciences Meeting and Exhibit, Reno, Nevada.
- Batten, P., Goldberg, U., and Chakravarthy, S. (2004). Interfacing Statistical Turbulence Closures with Large-Eddy-Simulation. *AIAA J.*, vol.42, No.3, 485-492, March.
- Baurle, R. A., Tam, C., Edwards, J. R., and Hassan, H. A. (2003). Hybrid Simulation Approach for Cavity Flows: Blending, Algorithm, and Boundary Treatment Issues. *AIAA J.*, vol.41, No.8, 1481-1480.
- Berger, M. (1982). *Adaptive Mesh Refinement for Partial Differential Equations*. PhD thesis.
- Berger, M. and Colella, P. (1989). Local adaptive mesh refinement for shock hydrodynamics. *J. Comput. Phys.*, 82:64-84.
- Berger, M. and Olinger, J. (1984). Adaptive mesh refinement for hyperbolic partial differential equations. *J. Comput. Phys.*, 53:484-512.
- Bertoglio, J.P. and Jeandel, D. (1986). A simplified spectral closure for inhomogeneous turbulence: application to the boundary layer, *Proc. Fifth Turbulent Shear Flows Conference*
- Besnard, D., Harlow, F.H., Rauenzahn, R.M. and Zemach, C. (1990). Spectral transport model for turbulence, Los Alamos National Laboratory Report LA-11821-MS
- Boersma, B., Kooper, M., Nieuwstadt, F., and Wesseling, P. (1997). Local grid refinement in large-eddy simulations. *J. Eng. Math.*, 32:161-175.
- Bou-Zeid, E., Meneveau, C. and Parlange, M. (2005). A scale-dependent Lagrangian dynamic model for large eddy simulation of complex turbulent flows. *Phys. Fluids* 17, 025105 (18 pages)
- Braza, M. (2000). The Direct Numerical Simulation at the Service of Turbulence Modelling Methodologies for Unsteady Aerodynamic Flows. *Proceedings of the ECCOMAS 2000 congress, Barcelona*.
- Breuer, M., Jovicic, N., and Mazaev, K. (2003). Comparison of DES, RANS and LES for the separated flow around a flat plate at high incidence. *International Journal for Numerical Methods in Fluids*, vol.41, 357-388.
- Burton, G. and Dahm, W. (2005a). Multifractal subgrid-scale modeling for large-eddy simulation. I model development and *a priori* testing. *Phys. Fluids*, 17(7):075111.
- Burton, G. and Dahm, W. (2005b). Multifractal subgrid-scale modeling for large-eddy simulation. II backscatter limiting and *a posteriori* evaluation. *Phys. Fluids*, 17(7):075112.
- Bush, R. and Mani, M. (2001). A two-equation large eddy stress model for high sub-grid shear. *AIAA Paper 01-2561*, 15th AIAA Computational Fluid Dynamics Conference, Anaheim, USA, June.
- Caltagirone, J., Khadra, K., and Angot, P. (1995). Sur une méthode de raffine-

- ment local multigrille pour la résolution des équations de navier-stokes (in french). *C. R. Acad. Sci. Paris, série IIB*, 320:295–302.
- Cambon, C., Jeandel, D. and Mathieu, J. (1981). Spectral modeling of homogeneous non isotropic turbulence, *J. Fluid Mech.* 104, 247–262
- Cantwell, B. and Coles, D. (1983). An experimental study of entrainment and transport in the turbulent wake of circular cylinder. *Journal of Fluid Mechanics*, vol.136, 321–374.
- Carati, D. and Vanden Eijnden, E. (1997). On the self-similarity assumption in dynamic models for large-eddy simulations. *Phys. Fluids* 9 (7), 2165–2167
- Carati, D. and Wray, A. A. (2000). Time filtering in large eddy simulation. *Proceedings of the Summer Program 2000, Center for Turbulence Research*, 263–270.
- Caruelle, B. and Ducros, F. (2003). Detached-Eddy Simulation of Attached and Detached Boundary Layers. *International Journal of Computational Fluid Dynamics*, vol.No.17, No.6, 433–451.
- Chassaing, P. (2000). Turbulence en mécanique des fluides. Analyse du phénomène en vue de sa modélisation à l’usage de l’ingénieur. (In french). *Cépenduès-Editions*.
- Chung, Y. and Sung, H. (1997). Comparative study of inflow conditions for spatially evolving simulation. *AIAA Journal*, vol.35, No.2, 269–274.
- Clark, R. A., Ferziger, J. H., and Reynolds, W. C. (1979). Evaluation of subgrid-scale models using an accurately simulated turbulent flow. *J. Fluid Mech.*, 91:1–16.
- Clark, T. and Zemach, C. (1995). A spectral model applied to homogeneous turbulence, *Phys. Fluids* 7 (7), 1674–1694
- Comte-Bellot, G. and Corrsin, S. (1971). Simple eulerian time correlation of full- and narrow-band velocity signals in grid-generated “isotropic” turbulence. *Journal of Fluid Mechanics*, vol.48, 273–337.
- Constantinescu, G. and Squires, K. (2004). Numerical investigations of flow over a sphere in the subcritical and supercritical regimes. *Physics of Fluids*, vol.16, No.5, 1449–1466.
- Cousteix, J. (1989). Turbulence et Couche limite. *Cepandues-Editions*.
- Cui, G., Zhou, H., Zhang, Z. and Shao, L. (2004). A new dynamic subgrid eddy viscosity model with application to turbulent channel flow. *Phys. Fluids* 16(8), 2835–2842
- Dahlstrom, S. (2003). *Large Eddy Simulation of the Flow Around a High Lift Airfoil*. PhD thesis, Dpt of Thermo and Fluid Dynamics, Chalmers University of Technology, Goteborg, Sweden.
- Dahlstrom, S. and Davidson, L. (2003). Hybrid LES-RANS with additional conditions at the matching region. In K. Hanjalić, Y. Nagano, and M.J. Tummers, editors. *Turbulence Heat and Mass Transfer 4*, 689–696, New York, Wallingford (UK), 2003, begell house, inc.
- Dakhoul, Y. and Bedford, K. (1986a). Improved averaging method for turbulent flow simulation. part 1: theoretical development and application to burger’s transport equation. *Int. J. Numer. Methods Fluids*, 6:49–64.
- Dakhoul, Y. and Bedford, K. (1986b). Improved averaging method for turbu-

- lent flow simulation. part 2: calculations and verification. *Int. J. Numer. Methods Fluids*, 6:65–82.
- Davidson, L. (2005). Hybrid LES-RANS: Inlet Boundary Conditions. *Proceedings of the 3rd National Conference on Computational Mechanics - MekIT'05, 7-22*, Eds. B. Skallerud and H.I. Andersson, Trondheim, Norway, May 11-12.
- Davidson, L. and Billson, M. (2004). Hybrid LES-RANS Using Synthetized Turbulence For Forcing At the Interface. *Proceedings of the European Congress on Computational Methods in Applied Sciences and Engineering, Jyväskylä, Finland, July 24-28*.
- Davidson, P. (2004). Turbulence. An introduction for scientists and engineers. *Oxford university press*.
- Debussche, A., Dubois, T., and Temam, R. (1995). The nonlinear galerkin method : a multi-scale method applied to the simulation of homogeneous turbulent flows. *Theoret. Comput. Fluid Dynamics*, 7(4):279–315.
- Deck, S. (2005a). Zonal Detached-Eddy Simulation of the flow around a High-Lift Configuration. *AIAA J.*, 43(11):2372–2384.
- Deck, S. (2005b). Numerical simulation of transonic buffet over a supercritical airfoil. *AIAA J.*, 43(7):1566–1566.
- Deck, S., Champigny, P., Garnier, E., Guillen, P., Thepot, R., and Vuillerme, A. (2005). Numerical Simulations of Flow Induced Unsteady Loads on Flight Vehicles. *RTO-MP-AVT-123 Symposium, paper 6, Budapest, Hungary, April*.
- Deck, S., Duveau, P., d’Espiney, P., and Guillen, P. (2002a). Development and application of spalart allmaras one equation turbulence model to three-dimensional supersonic complex configurations. *Aerospace Science and Technology, Vol. 6, No. 3, 171-183*.
- Deck, S. and Garnier, E. (2004). Detached and Large Eddy Simulation of Unsteady Side Loads over an Axisymmetric Afterbody. *5<sup>th</sup> European Symposium on Aerothermodynamics for Space Vehicles, Cologne, Germany, Nov*.
- Deck, S., Hallard, R., and Guillen, P. (2002b). Detached Eddy Simulation applied to Space Launcher Configurations. *EuroMech Colloquium 440 Aerodynamics and Thermochemistry of High Speed Flows, Marseille, France*.
- Deprés, D. (2003). *Analyse physique et modélisation des instationnarités dans les écoulements d’arrière-corps transoniques*. PhD thesis, Université de la Méditerranée Aix-Marseille II.
- De Stefano, G., Goldstein, D.E., and Vasilyev, O.V. (2005). On the role of subgrid-scale coherent modes in large-eddy simulation. *J. Fluid Mech.* 525, 263–274
- Domaradzki, J. and Loh, K. (1999). The subgrid-scale estimation model in the physical space representation. *Phys. Fluids*, 11(8):2330–2342.
- Domaradzki, J. and Saiki, E. (1997). A subgrid-scale model based on the estimation of unresolved scales of turbulence. *Phys. Fluids*, 9(7):2148–2164.
- Domaradzki, J. and Yee, P. (2000). The subgrid-scale estimation model for high Reynolds number turbulence. *Phys. Fluids*, 12(1):193–196.
- Donoho, D.L. (1994). De-noising by soft-thresholding. *IEEE Transf. Inf. Theory* 41, 613–627

- Dubief Y., D. F. (2000). On coherent-vortex identification in turbulence. *Journal of turbulence*, vol. 1, (11), 1-22.
- Dubois, T., Domaradzki, J., and Honein, A. (2002). The subgrid-scale estimation model applied to large eddy simulations of compressible turbulence. *Phys. Fluids*, 14(5):1781-1801.
- Dubois, T. and Jauberteau, F. (1998). A dynamic multilevel model for the simulation of the small structures in three-dimensional homogeneous isotropic turbulence. *J. Scient. Comp.*
- Dubois, T., Jauberteau, F., and Temam, R. (1993). Solution of the incompressible navier-stokes equations by the nonlinear galerkin method. *J. Scient. Comp.*, 8(2):167-194.
- Dubois, T., Jauberteau, F., and Temam, R. (1998). Incremental unknowns, multilevel methods and the numerical simulation of turbulence. *Comput. Methods Appl. Mech. Engrg.*, 159:123-189.
- Dubois, T., Jauberteau, F., and Temam, R. (1999). *Dynamic Multilevel Methods and the Numerical Simulation of Turbulence*. Cambridge University Press.
- Dubois, T., Rosier, C., and Temam, R. (1990). A nonlinear galerkin method for the navier-stokes equations. *Comput. Methods Appl. Mech. Engrg.*, 80:245-260.
- Dubois, T. and Temam, R. (1993). Separation of scales in turbulence using the nonlinear galerkin method. In Habashi, W. and Hafez, M., editors, *Advances in Computational Fluid Dynamics*.
- Ducros, F., Comte, P., Lesieur, M. (1996). Large-eddy simulation of transition to turbulence in a boundary layer developing spatially over a flat plate. *J. Fluid Mech.* 326, 1-36
- Fan, T. C., Xiao, X., Edwards, J. R., Hassan, H. A., and Baurle, R. A. (2004). Hybrid Large-Eddy/Reynolds-Averaged Navier-Stokes Simulations of Shock-Separated Flows. *AIAA Journal of Spacecraft and Rockets*, vol.41, No.6, 897-906.
- Fan, T. C., Tian, M., Edwards, J. R., Hassan, H. A., and Baurle, R. A. (2001). Validation of a Hybrid Reynolds-Averaged/Large-Eddy Simulation Method for Simulating Cavity Flows. *AIAA Paper 01-2929, 31st AIAA Fluid Dynamics Conference and Exhibit, Anaheim, CA, June*.
- Fan, T. C., Xiao, X., Edwards, J. R., and Baurle, R. A. (2002). Hybrid LES/RANS Simulation of a Shock Wave/Boundary Layer Interaction. *AIAA Paper 02-0431, 40th AIAA Aerospace Sciences Meeting and Exhibit, Reno, Nevada, Jan*.
- Fan, T. C., Xiao, X., Edwards, J. R., Hassan, H. A., and Baurle, R. A. (2003). Hybrid LES/RANS Simulation of a Mach 3 Shock Wave/Boundary Layer Interaction. *AIAA Paper 03-0080, 41st AIAA Aerospace Sciences Meeting and Exhibit, Reno, Nevada, Jan*.
- Farge, M., Kevlahan, N., Perrier, V., and Goirand, E. (1996). Wavelets and turbulence. *Proc. IEEE*, 84(4):639-669.
- Farge, M., Pellegrino, G. and Schneider, K. (2001). Coherent vortex extraction in 3D turbulent flows using orthogonal wavelets. *Phys. Rev. Lett.* 87(5), 054501

- Farge, M., Schneider, K. and Kevlahan, N. (1999). Non-Gaussianity and coherent vortex simulation for two-dimensional turbulence using an adaptive orthogonal wavelet basis. *Phys. Fluids* 11 (8), 2187–2201
- Farge, M., Schneider, K., Pellegrino, G., Wray, A. and Rogallo, R.S. (2003). Coherent vortex extraction in three-dimensional homogeneous turbulence: comparison between CVS-wavelet and POD-Fourier decompositions. *Phys. Fluids* 15 (10), 2886–2896
- Fasel, H., Seidel, J., and Wernz, S. (2002). A methodology for simulation of complex turbulent flows. *Journal of Fluids Engineering*, Vol. 124, 933–942.
- Foias, C., Manley, O., and Temam, R. (1988). Modelling of the interaction of small and large scale eddies in two-dimensional turbulent flows. *Math. Mod. and Num. Anal. (M2AN)*, 22(1):93–114.
- Forsythe, J., Fremaux, C., and Hall, R. (2004). Calculation of Static and Dynamic Stability Derivatives of the F/A-18E in abrupt Wing Stall Using RANS and DES. *ICCFD3, Toronto, Canada, July*.
- Forsythe, J., Squires, K., Wurtzler, K., and Spalart, P. (2003). Detached Eddy Simulation of the F-15E at high alpha. *Journal of Aircraft*, vol.40, No.3, 193-200.
- Garnier, E., Mossi, M., Sagaut, P., Comte, P., and Deville, M. (1999). On the use of shock-capturing schemes for Large-Eddy Simulation. *J. Comput. Phys.*, 153:273–311.
- Germano, M. (1986). A proposal for a redefinition of the turbulent stresses in the filtered Navier-Stokes equations. *Phys. Fluids*, 29(7):2323–2324.
- Germano, M. (1992). Turbulence: the filtering approach. *J. Fluid Mech.*, 238:325–336.
- Germano, M. (1999). From RANS to DNS: Towards a bridging model. In N.D. Sandham and L.Kleiser, editors, *Direct and Large-Eddy Simulation III, ERCOFTAC series, Kluwer academic publishers*, 225-236.
- Germano, M., Piomelli, U., Moin, P., and Cabot, W. H. (1991). A dynamic subgrid-scale eddy viscosity model. *Phys. Fluids A*, 3:1760–1765.
- Germano, M. (1996). A statistical formulation of the dynamic model. *Phys. Fluids* 8 (2), 565–570
- Germano, M. (1998). Fundamentals of large-eddy simulation. (Advanced Turbulent Flows Computations, Peyret and Krause eds.), CISM Courses and Lectures 395, 81–130
- Germano, M. (2001). Ten years of the dynamic model. (Modern simulation strategies for turbulent flow, Geurts ed.), Edwards, 173–190
- Geurts, B. J. (1997). Inverse modeling for large-eddy simulation. *Phys. Fluids*, 9(12):3585–3587.
- Ghosal, S., Lund, T.S., Moin, P. and Akselvoll, K. (1995). A dynamic localization model for large-eddy simulation of turbulent flows. *J. Fluid Mech.* 286, 229–255
- Ghosal, S. and Moin, P. (1995). The basic equations for the large-eddy simulation of turbulent flows in complex geometries. *J. Comput. Phys.*, 118:24–37.
- Gleize, V. (1994). Simulation numérique d'écoulements turbulents compressibles hors d'équilibre à l'aide de schémas à échelles multiples, PhD Thesis, Univ.

- of Aix-Marseille II, (in French)
- Gleize, V., Schiestel, V. and Couaillier, V. (1996). Multiple scale modeling of turbulent nonequilibrium boundary layer flows, *Phys. Fluids* 8 (10), 2716–2732
- Goldberg, U., Peroomian, O., Palaniswamy, S., and Chakravarthy, S. (1999). Anisotropic  $k - \epsilon$  Model for Adverse Pressure Gradient Flow. *AIAA Paper 99-0152, 39th AIAA Aerospace Sciences Meeting and Exhibit, Reno, Nevada, Jan.*
- Goldstein, D.E. (2004). Stochastic coherent adaptive large eddy simulation method, PhD Thesis, University of Colorado, Boulder.
- Goldstein, D.E. and Vasilyev, O.V. (2004). Stochastic coherent adaptive large eddy simulation method. *Phys. Fluids* 16(7), 2497–2513
- Goldstein, D.E., Vasilyev, O.V. and Kevlahan, N.K.R. (2004). Adaptive LES of 3D decaying isotropic turbulence. *Proceedings of the 2004 Summer Program, Center for Turbulence Research, 111–122*
- Goldstein, D.E., Vasilyev, O.V. and Kevlahan, N.K.R. (2005). CVS and SCALES simulation of 3D isotropic turbulence. *Journal of Turbulence*, submitted
- Gourdain, N., Burguburu, S., and Leboeuf, F. (2005). Rotating stall and analysis in an axial compressor. *ISABE Conference and Exhibit, paper 2205-1138, Munchen, Germany, Sept.*
- Ha Minh, H. (1999). La modélisation statistique de la turbulence: ses capacités et ses limitations. *Comptes-Rendus de l'Académie des Sciences de Paris, 327, Série 2b: 343-358.*
- Ha Minh, H. and Kourta, A. (1993). Semi-Deterministic Turbulence Modelling for Flows Dominated by Strong Organized Structures. *9th Turbulent Shear Flows Symposium, Kyoto, 10.5-1. 10.5-6.*
- Haller, G. (2005). An objective definition of a vortex. *Journal of Fluid Mechanics, vol.525, 1-26.*
- Hamba, F. (2001). An attempt to combine Large-Eddy Simulation with the  $k - \epsilon$  model in a channel flow calculation. *submitted to Theoretical and Computational Fluid Dynamics, Vol 14, 323-336.*
- Hanjalić, K., Hadžiabdić, M., Temmerman, L., and Leschziner, M. (2004). Merging LES and RANS Strategies: Zonal or Seamless Coupling? *In R. Friedrich et al. editors, Direct and Large-Eddy Simulation V, Kluwer academic publishers, 451-464.*
- Hanjalić, K. and Kenjeres, P. (2000). Reorganization of turbulence structure in magnetic rayleigh-bénard convection: a t-rans study. *Journal of Turbulence, vol.1, (8), 1-22, (<http://jot.iop.org>).*
- Hanjalic, K., Launder, B.E. and Schiestel, R. (1980). Multiple-time-scale concepts in turbulent shear flows, *Turbulent Shear Flows, Vol. 2*, Bradbury, L., Durst, F., Launder, B.E., Schmidt, F.W. and Whitelaw, J.H. editors, Springer, New-York, 36–49
- Harten, A. (1983). High resolution scheme for hyperbolic conservation laws. *Journal of Computational Physics, vol.49, 357-393.*
- Harten, A. (October 1994). Multiresolution representation and numerical algorithms : a brief review. ICASE Report No 94-59.

- Hinze, J.O. (1959). Turbulence. An introduction to its mechanism and Theory. *Mc Graw Hill*.
- Hinze, J.O. (1987). Turbulence, 2nd edition. McGraw-Hill publishing Company, New-York.
- Hoffman, J. (2002). Dynamic subgrid modelling for time dependent convection-diffusion-reaction equations with fractal solutions. *Int. J. Numer. Meth. Fluids* 40, 583–592
- Hoffman, J. (2003). Adaptive DNS/LES: a new agenda in CFD. Chalmers Finite Element Center preprint 2003-23. Chalmers University of Technology
- Hoffman, J., Johnson, C. (2004). Computability and adaptivity in CFD. Encyclopedia of Computational Mechanics, Stein, E., de Horz, R. and Hughes, T.J.R. eds, John Wiley & Sons
- Hoffman, J. (2004a). Efficient computation of mean drag for the subcritical flow past a circular cylinder using adaptive DNS/LES. *Int. J. Numer. Anal. Modeling* 1 (1), 1–18
- Hoffman, J. (2004b). On duality based a posteriori error estimation in various norms and linear functionals for LES. *SIAM J. Sci. Comput.* 26 (1), 178–195
- Hoffman, J. (2005a). Weak uniqueness of the Navier–Stokes equations and adaptive turbulence simulation. Proceedings of the 12th Leslie Fox prize.
- Hoffman, J. (2005b). Computation of the mean drag for bluff body problems using adaptive DNS/LES. *SIAM J. Sci. Comput.* , in press
- Holmen, J., Hughes, T.J.R., Oberai, A. and Wells, G. (2004). Sensitivity of the scale partition for variational multiscale large-eddy simulation of channel flow. *Phys. Fluids* 16(3), 824–827
- Huerre, P. and Monkewitz, P. (1990). Local and global instabilities in spatially developing flows. *Annual Review of Fluid Mechanics*, 22:473-537.
- Hughes, T.J.R. (1995). Multiscale phenomena: Green’s function, the Dirichlet-to-Neumann formulation, subgrid scale models, bubbles and the origin of stabilized methods. *Comput. Methods Appl. Mech. Engrg.* 127, 387–401
- Hughes, T.J.R., Feijoo, G.R., Mazzei, L. and Quincy, J.B. (1998). The variational multiscale method - a paradigm for computational mechanics. *Comput. Methods Appl. Mech. Engrg.* 166, 2–24
- Hughes, T.J.R., Mazzei, L. and Jansen, K.E. (2000). Large eddy simulation and the variational multiscale method. *Comput. Visual Sci.* 3, 47–59
- Hughes, T.J.R., Mazzei, L., Oberai, A.A. and Wray, A.A. (2001). The multiscale formulation of large-eddy simulation: decay of homogeneous isotropic turbulence. *Phys. Fluids* 13(2), 505–512
- Hughes, T.J.R., Oberai, A.A. and Mazzei, L. (2001). Large-eddy simulation of turbulent channel flows by the variational multiscale method. *Phys. Fluids* 13(6), 1784–1799
- Hughes, T.J.R., Scovazzi, G. and Franca, L.P. (2004). Multiscale and stabilized methods. (Encyclopedia of Computational Mechanics, Stein, E., de Borts, E. and Hughes, T.J.R. editors), John Wiley & Sons, Ltd.
- Hughes, T.J.R. and Stewart, J. (1996). A space-time formulation for multiscale phenomena. *J. Comput. Appl. Math.* 74, 217–229

- Hughes, T.J.R., Wells, G. and Wray, A. (2004). Energy transfers and spectral eddy viscosity in large-eddy simulations of homogeneous isotropic turbulence: comparison of dynamic Smagorinsky and multiscale models over a range of discretizations. *Phys. Fluids* 16 (11), 4044–4052
- Hunt, D. and Nixon, D. (1995). A very Large Eddy Simulation of an Unsteady Shock Wave/Turbulent Boundary Layer Interaction. *AIAA Paper 95-2212, 26th AIAA Fluid Dynamics Conference, San Diego, California, 19-22 June.*
- Hunt, J., Wray, A., and Moin, P. (1988). Eddies, stream, and convergence zones in turbulent flows. *Center for Turbulence Research, Report CTR-S88.*
- Hussain, A. and Reynolds, W. (1970). The mechanics of an organized wave in turbulent shear flow. *Journal of Fluid Mechanics, vol.41 (2), 241-258.*
- Jeandel, D., Brison, J.F. and Mathieu, J. (1978). Modeling methods in physical and spectral space, *Phys. Fluids* 21(2), 169–182
- Jeanmart, H. and Winckelmans, G. (2002). Comparison of recent dynamic subgrid-scale models in turbulent channel flow. Proceedings of the Summer program - Center for Turbulence Research, 105–116
- Jouhaud, J.C., Montagnac, M. and Tourette, L. (2005). A multigrid adaptive mesh refinement strategy for 3D aerodynamic design. *Int. J. Numer. Method Fluids*.47, 367–385
- Kaltenbach, H., Fatica, M., Mittal, R., Lund, T., and Moin, P. (1999). Study of flow in a planar asymmetric diffuser using large(eddy simulation. *Journal of Fluid Mechanics, vol.390, 151-185.*
- Kaneda, Y., Ishihara, T., Yokokawa, M., Itakura, K., and Uno, A. (2003). Energy dissipation rate and energy spectrum in high resolution direct numerical simulations of turbulence in a periodic box. *Physics of Fluids, vol.15, No.2, L21-24.*
- Kannepalli, C., Arunajatesan, S., and Dash, S. (2002). RANS/LES methodology for supersonic transverse jet interactions with approach flow. *AIAA Paper 02-1139, 40th AIAA Aerospace Sciences Meeting and Exhibit, Reno, Nevada, Jan.*
- Kawai, S. and Fujii, K. (2004). Computational Study of a Supersonic Base Flow Using LES/RANS Hybrid methodology. *AIAA Paper 04-0068, 42th AIAA Aerospace Sciences Meeting and Exhibit, Reno, Nevada, Jan.*
- Keating, A., Piomelli, U., Balaras, E., and Kaltenbach, H. (2004). *apriori* and *aposteriori* tests of inflow conditions for large-eddy simulation. *Physics of Fluids, vol.16, No. 12, 4696-4712.*
- Kim, S.W. (1991). Calculation of divergent channel flows with a multiple-time-scale turbulence model, *AIAA J.* 29(4), 547–554
- Kim, S.W. and Chen, C.P. (1989). A multiple-time-scale turbulence model based on variable partitioning of the turbulent kinetic energy spectrum, *Numer. Heat Transfer/B* 16, 193–211
- Klein, M., Sadiki, A., and Janicka, J. (2003). A digital filter based generation of inflow data for spatially developing direct numerical or large eddy simulations. *Journal of Computational Physics, vol.186, 652-665.*
- Kok, J. (2000). Resolving the dependence on freestream values for the  $k - \omega$  turbulence model. *AIAA Journal, vol.38, No.7, 1292-1295.*

- Kok, J., Dol, H., Oskam, H., and van der Ven, H. (2004). Extra-Large Eddy Simulation of massively separated flows. *AIAA Paper 04-0264, 42th AIAA Aerospace Sciences Meeting and Exhibit, Reno, Nevada, Jan.*
- Koobus, B. and Farhat, C. (2004). A variational multiscale method for the large eddy simulation of compressible turbulent flows on unstructured meshes - application to vortex shedding, *Comput. Methods Appl. Mech. Engrg.* 193, 1367–1383
- Kourta, A. (1999). Computation of vortex shedding in rocket motors using time-dependent turbulence model. *AIAA Journal of Propulsion and Power, vol.15, No.3, 390-400.*
- Kraichnan, R. (1969). Diffusion by a random velocity field. *Physics of Fluids, vol.13, No.1, 22-31.*
- Kravchenko, A. and Moin, P. (2000). Numerical studies of flow over a circular cylinder at  $re_d = 3900$ . *Phys. Fluids*, 12(2):403–417.
- Kravchenko, A., Moin, P., and Moser, R. (1996). Zonal embedded grids for numerical simulation of wall-bounded turbulent flows. *J. Comput. Phys.*, 127:412–423.
- Kravchenko, A., Moin, P., and Shariff, K. (1999). B-Spline Method and Zonal Grids for Simulations of Complex Turbulent Flows. *J. Comput. Phys.*, 151:757–789.
- Kumar, S. and Loth, E. (2001). Detached Eddy Simulation of an iced airfoil. *AIAA Paper 01-0678, 39th AIAA Aerospace Sciences Meeting and Exhibit, Reno, Nevada, Jan.*
- Labourasse, E. (2002). *Reconstruction des fluctuations turbulentes par une approche hybride RANS/SGE (in french)*. PhD thesis, Université de Paris VI.
- Labourasse, E. and Sagaut, P. (2002). Reconstruction of turbulent fluctuations using a hybrid RANS/LES approach. *J. Comput. Phys.*, 182:301–336.
- Laporta, A. (1995). Etude spectrale et modélisation de la turbulence inhomogène, PhD Thesis, Ecole Centrale de Lyon, (in French)
- Le, H., Moin, P., and Kim, J. (1997). Direct numerical simulation of turbulent flow over a backward-facing step. *Journal of Fluid Mechanics, vol.330, 349-374.*
- Lee, S., Lele, S., and Moin, P. (1992). Simulation of spatially evolving turbulence and the applicability of Taylor's hypothesis in compressible flow. *Physics of Fluids A 4, 1521-1530.*
- Lele, S. K. (1994). Compact finite difference schemes with spectral-like resolution. *J. Comput. Phys.*, 103:16–42.
- Leonard, A. (1974). Energy cascade in large-eddy simulations of turbulent fluid flows. *Adv. in Geophys. A*, 18:237–248.
- Léonard, S., Terracol, M., and Sagaut, P. (2005a). A wavelet-based adaptive mesh refinement method for large eddy simulation. 35th AIAA Fluid Dynamics Conference.
- Léonard, S., Terracol, M., and Sagaut, P. (2005b). A wavelet-based adaptive mesh refinement method for large eddy simulation. *submitted to J. Comput. Phys.*
- Lesieur, M. (1990). Turbulence in Fluids. 2nd revised version. *Kluwer Academic*

*Publishers.*

- Levasseur, V., Sagaut, P., Chalot, F. and Davroux, A. (2005b). An entropy-variable based VMS/GLS method for the simulation of compressible flows on unstructured grids. *Comput. Methods Appl. Mech. Engrg.* in press
- Lilly, D.K. (1992). A proposed modification of the Germano subgrid-scale closure method. *Phys. Fluids A* 4(3), 633–635
- Loh, K. and Domaradzki, J. (1999). The subgrid-scale estimation model on nonuniform grids. *Phys. Fluids*, 11(12):3786–3792.
- Lund, T., Wu, X., and Squires, K. (1998). Generation of Turbulent Inflow Data for Spatially-developing Boundary Layer Simulations. *Journal of Computational Physics*, vol.No.140, 233-258.
- Magnient, J. C. (2001a). *Simulation des grandes échelles (SGE) d'écoulements de fluide quasi incompressibles*. PhD thesis, Université de Paris Sud.
- Magnient, J. C., Sagaut, P., Deville, M. (2001b). A study of built-in-filter for some eddy viscosity models in large-eddy simulation. *Phys. Fluids*, 13(5):1440–1449.
- Mallat, S. (1997). A wavelet tour of signal processing. Academic Press, New York
- Manhart, M. (1999). Direct numerical simulation of turbulent boundary layers on high performance computers. In *High Performance Computing in Science and engineering*. Springer Verlag.
- Manhart, M. and Friedrich, R. (1999). Towards DNS of turbulent boundary layers. In *Direct and Large-Eddy Simulation III*, 429–440. Kluwer Academic Publishers.
- Mary, I. (2003). Large eddy simulation of vortex breakdown behind a delta wing. *Int. J. Heat and Fluid Flow*, 24:596–605.
- Mary, I. and Nolin, G. (2004). Zonal grid refinement for large eddy simulation of turbulent boundary layers. AIAA paper 2004-0257.
- Mc Comb, W.D., Hunter, A. and Johnston, C. (2001). Conditional model-elimination and the subgrid-modeling problem for isotropic turbulence. *Phys. Fluids* 13(7), 2030-2044
- Mc Cormick, S. (1989). Multilevel adaptive methods for partial differential equations. SIAM, Frontiers in applied mathematics series Vol. 6.
- Mc Cormick, S. (1992). Multilevel projection methods for partial differential equations. SIAM, CBSM series Vol. 62.
- Mc Cormick, S. F. (1994). Multilevel adaptive methods for elliptic eigenproblems: a two-level convergence theory. *SIAM J. Numer. Anal.*, 31(6):1731–1745.
- Meneveau, C. and Lund, T.S. (1997). The dynamic Smagorinsky model and scale-dependent coefficients in the viscous range of turbulence. *Phys. Fluids* 9(12), 3932–3934
- Meneveau, C., Lund, T.S., and Cabot, W.H. (1996). A Lagrangian dynamic subgrid-scale model of turbulence. *J. Fluid Mech.* 319, 353–385
- Menter, F. (1994). Two-equation Eddy-viscosity turbulence models for engineering applications. *AIAA J.*, vol.32, No. 8, 1598-1605.
- Menter, F. (1997). Eddy viscosity transport equations and their Relation to the  $k - \epsilon$  model. *ASME Journal of Fluid Engineering*, Vol 119, 876-884, Dec. 1997.

- Menter, F. and Egorov, Y. (2004). Revisiting the turbulent scale equation. *Proc. IUTAM Symposium, One hundred years of boundary layer research, Göttingen, Germany.*
- Menter, F. and Egorov, Y. (2005). A Scale-Adaptive Simulation Model using Two-Equation Models. *AIAA Paper 05-1095, 43rd AIAA Aerospace Sciences Meeting and Exhibit, Reno, Nevada, Jan.*
- Menter, F. and Kuntz, M. (2004). Adaptation of eddy-viscosity turbulence models to unsteady separated flow behind vehicles. *Symp. "The aerodynamics of heavy vehicles: trucks, buses and trains." Monterey, USA, Dec. 2-6, 2002. R.Mc-Callen, F.Browand and J. Ross, eds. Springer.*
- Menter, F., Kuntz, M., and Bender, R. (2003). A Scale-Adaptive Simulation Model for Turbulent Flow Predictions. *AIAA Paper 03-0767, 41th AIAA Aerospace Sciences Meeting and Exhibit, Reno, Nevada, Jan.*
- Mitran, S. (2001). A comparison of adaptive mesh refinement approaches for large eddy simulation. In Liu, C., Sakell, L., and Beutner, T., editors, *DNS/LES progress and challenges, third AFOSR International Conference, Columbus, Ohio.*
- Mogili, P., Thompson, D., Choo, Y., and Addy, H. (2005). RANS and DES Computations for a Wing with Ice Accretion. *AIAA Paper 05-1372, 43rd AIAA Aerospace Sciences Meeting and Exhibit, Reno, Nevada, Jan.*
- Monin, A. S. and Yaglom, A. M. (1971). *Statistical Fluids Mechanics: Mechanics of turbulence.* MIT press.
- Morinishi, Y. and Vasilyev, O. (2002). Vector level identity for dynamic subgrid scale modeling in large eddy simulation. *Phys. Fluids* 14(10), 3616–3623
- Morris, P. J., Long, L. N., Bangalore, A., and Wang, Q. (1997). A parallel three-dimensional computational aeroacoustics method using nonlinear disturbance equations. *J. Comput. Phys.*, 133:56–74.
- Morton, S., Cummings, R., and Kholodar, D. (2004). High Resolution Turbulence Treatment of F/A-18 Tail Buffet. *AIAA Paper 04-1676, 45th AIAA/ASME/ASCE/AHS/ASC Structures Structural Dynamics and Material Conference, Palm Spring, Ca, USA, April.*
- Moser, R., Kim, J., and Mansour, N. (1999). Direct numerical simulation of turbulent channel flow up to  $Re_\tau = 590$ . *Phys. Fluids*, 11(4):943–945.
- Mossi, M. and Sagaut, P. (2003). Numerical investigation of fully developed channel flow using shock-capturing schemes. *Computers and Fluids*, 32:249–274.
- Munts, E.A., Hulshoff, S.J. and de Borst, R. (2004). A space-time variational multiscale discretization for LES. 34th AIAA Fluid Dynamics Conference, AIAA Paper 2004-2132
- Nolin, G., Mary, I., and Ta-Phuoc, L. (2005). RANS eddy viscosity reconstruction from LES flow field for turbulent boundary layers. 35th AIAA Fluid Dynamics Conference & Exhibit.
- Nikitin, N., Nicoud, F., Wasistho, B., Squires, K., and Spalart, P. (2000). An approach to wall modeling in large eddy simulation. *Physics of Fluids, vol.12, 1629-1631.*
- Orszag, S. (1970). Analytical theories of turbulence, *J. Fluid Mech.* 41 (2), 363–

386

- Parpais, S. (1997). Développement d'un modèle spectral pour la turbulence inhomogène, PhD Thesis, Ecole Centrale de Lyon, 159p. (in French)
- Parpais, S., Touil, H., Bertoglio, J.P. and Michard, M. (1999). A spectral closure for inhomogeneous turbulence applied to the computation of the intake stroke in a car engine, *Proc. Fourth Int. Symp. Eng. Turb. Modelling and Meas.*
- Peltier, L. and Zajaczkowski, F. (2001). Maintenance of the near-wall cycle of turbulence for hybrid RANS/LES of fully-developped channel flow. *Proceedings of the third AFOSR Int. Conf. on DNS/LES, Arlington, edited by C.Liu, L. Sakell and T. Beutner, Greyden press, Columbus, OH, 5-9 August, 829-834.*
- Perrier, V., Philipovitch, T., and Basdevant, C. (1995). Wavelet spectra compared to fourier spectra. *J. Math. Phys.*, 36(3):1506-1519.
- Piomelli, U. (1993). High Reynolds number calculations using the dynamic subgrid-scale stress model. *Phys. Fluids A*, 5(6):1484-1490.
- Piomelli, U. and Balaras, E. (2003). Cwall-layer models for large-eddy simulations. *Annual Review of Fluid Mechanics*, 34:349-374.
- Piomelli, U., Balaras, E., Squires, K., and Spalart, P. (2003). Interaction of the inner and outer layers in Large Eddy Simulations with wall-layer models. *International Journal of Heat and Fluid Flows*, Vol. 24, pp 538-550.
- Piquet, J. (1999). Turbulent Flows-Models and Physics. *Springer.*
- Poinsot, T. J. and Lele, S. (1991). Boundary conditions for direct simulations of compressible viscous flows. *J. Comput. Phys.*, 101:104-129.
- Porté-Agel, F., Meneveau, C. and Parlange, M.B. (2000). A scale-dependent dynamic model for large-eddy simulation: application to a neutral atmospheric boundary layer. *J. Fluid Mech.* 415, 261-284
- Pouquet, A., Lesieur, M., André, J.C., Basdevant, C. (1975). Evolution of high Reynolds number two-dimensional turbulence, *J. Fluid Mech.* 72, 305-319
- Pruett, C. (2000). Eulerian time-domain filtering for spatial large-eddy simulation. *AIAA journal*, 38(9):1634-1642.
- Pruett, C., Gatski, T., Grosch, C., and Thacker, W. (2003). The temporally filtered Navier-Stokes equations: properties of the residual stresses. *Phys. Fluids*, 15(8):2127-2140.
- Quéméré, P. and Sagaut, P. (2002). Zonal multidomain RANS/LES simulations of turbulent flows. *Int. J. Numer. Meth. Fluids*, 40:903-925.
- Quéméré, P., Sagaut, P., and Couaillier, V. (2001). A new multi-domain/multi-resolution method for large-eddy simulation. *Int. J. Numer. Meth. Fluids*, 36:391-416.
- Quirk, J. J. (1994). *An Adaptive Grid Algorithm for Computational Shock Hydrodynamics.* PhD thesis.
- Renaud, T., Le Pape, A., and Benoit, C. (2005). Unsteady Euler and Navier-Stokes computations of a Complete Helicopter. 31<sup>st</sup> *European Rotorcraft Forum, Florence, ITALY, Sept.*
- Robinson, D. and Hassan, H. (1998). Further Development of the  $k-\zeta$ (Enstrophy) Turbulence Closure Model. *AIAA J.*, vol.36, No.10, 1825-1833.

- Rubinstein, R. (2000). Formulation of a two-scale model of turbulence, ICASE Report No. 2000-5
- Rüde, U. (1993). Mathematical and computational techniques for multilevel adaptive methods. SIAM, Frontiers in applied mathematics series Vol. 13.
- Sagaut, P. (2005). Large-eddy simulation for incompressible flows, 3rd edition. Springer, Berlin.
- Sagaut, P., Comte, P., Ducros, F. (2000). Filtered subgrid-scale models. *Phys. Fluids* 12(1), 233–236
- Sagaut, P., Garnier, E., Tromeur, E., Larcheveque, L., and Labourasse, E. (2003). Turbulent Inflow Conditions for LES of supersonic and subsonic wall bounded flows. *AIAA Paper 03-0068, 41th AIAA Aerospace Sciences Meeting and Exhibit, Reno, Nevada, Jan.*
- Sagaut, P., Garnier, E., Tromeur, E., Larcheveque, L., and Labourasse, E. (2004). Turbulent Inflow Conditions for Large-Eddy-Simulation of Compressible Wall-Bounded Flows. *AIAA J.*, vol.42, No.3, 469-477, March.
- Sagaut, P., Labourasse, E., Quéméré, P. and Terracol, M. (2000). Multiscale approaches for unsteady simulation of turbulent flows. *Int. J. Nonlinear Sciences and Numerical Simulation* 1(4), 285–298
- Sagaut, P. and Levasseur, V. (2005a). Sensitivity of spectral variational multiscale methods for large-eddy simulation, *Phys. Fluids* 17, 035113
- Sandberg, R. and Fasel, H. (2004). Application of a new Flow Simulation Methodology for Supersonic Axisymmetric Wakes. *AIAA Paper 04-0067, 42nd AIAA Aerospace Sciences Meeting and Exhibit, Reno, Nevada, USA, Jan.*
- Sandham, N., Yao, Y., and Lawal, A. (2003). Large-eddy simulation of transonic turbulent flow over a bump. *International Journal of Heat and Fluid Flows*, 24:584–595.
- Schiestel, R. (1987). Multiple-time-scale modeling of turbulent flows in one point closure, *Phys. Fluids* 30, 722–731
- Schiestel, R. (1983a). Multiple scale concept in turbulence modelling. Part I: Multiple-scale model for turbulence kinetic energy and mean square of passive scalar fluctuations, *J. Mécanique Théorique et Appliquée* 2(3), 417–449 (in French)
- Schiestel, R. (1983b). Multiple scale concept in turbulence modelling. Part II: Reynolds stresses and turbulent fluxes of a passive scalar, algebraic modelling and simplified model using Boussinesq hypothesis, *J. Mécanique Théorique et Appliquée* 2(4), 601–628 (in French)
- Schlatter, P., Stolz, S., and Kleiser, L. (2004). LES of transitional flows using the approximate deconvolution model. *International Journal of Heat and Fluid Flows*, 25(3):549–558.
- Schlüter, J., Pitsch, H., and Moin, P. (2004). Large,Eddy Simulation Inflow Conditions for Coupling with Reynolds-Averaged Flow Solvers. *AIAA J.*, vol.42, No.3, 478-484, March.
- Schlüter, J., Wu, X., Kim, S., Alonso, J., and Pitsch, H. (2005). Integrated simulations of a compressor/combustor assembly of a gas turbine engine. *ASME GT-2005-68204, ASME turbo expo 2005 land sea and air, June.*
- Schneider, K., Farge, M., Pellegrino, M., and Rogers, M. (2005). Coherent vortex

- simulation of 3D turbulent mixing layers using orthogonal wavelets. *J. Fluid Mech.*, 534, 39–66
- Schumann, U. (1975). Subgrid scale model for finite difference simulations of turbulent flows in plane channels and annuli. *Journal of Computational Physics*, vol.18, 376–404.
- Scott Collis, S. (2001). Monitoring unresolved scales in multiscale turbulence modeling. *Phys. Fluids* 13(6), 1800–1806
- Scott Collis, S. (2002). Multiscale methods for turbulence simulation and control. Rice University report, 93 pages.
- Scotti, A. and Meneveau, C. (1999). A fractal model for large-eddy simulation of turbulent flows. *Physica D*, 127:198–232.
- Shah, K. B. and Ferziger, J. H. (1995). A new non-eddy viscosity subgrid-scale model and its application to channel flow. *Annual Research Briefs, Center for Turbulence Research*, 73–90.
- Shao, L., Bertoglio, J.P., Cui, G.X., Zhou, H.B. and Zhang, Z.S. (2003). Kolmogorov equation for large eddy simulation and its use for subgrid modeling. (Proceedings of the 5th ERCOFTAC Workshop on Direct and Large Eddy Simulation, Kluwer)
- Shur, M., Spalart, P., Strelets, M., and Travin, A. (1999). Detached-eddy simulation of an airfoil at high angle of attack. *4th Int. Symposium on Eng. Turb. Modelling and Measurements.*, Elsevier, Corsica, May 24–26.
- Shur, M., Spalart, P., Strelets, M., and Travin, A. (2003). Modification of SA Subgrid Model in DES Aimed to Prevent Activation of the low-RE terms in LES mode. *DES Workshop held at the University of St.-Petersburg, Russia, July*.
- Simon, F., Deck, S., Guillen, P., and Sagaut, P. (2006). RANS-LES Simulations of Supersonic Base Flows. *AIAA paper 2006-0898, 44th AIAA Aerospace Sciences Meeting and Exhibit, Reno, Nevada, Jan.*
- Sjögreen, B. and Yee, H. C. (2004). Multiresolution wavelet based adaptive numerical dissipation control for high order methods. *J. Sc. Comp.*, 20(2):211–255.
- Smagorinsky, J. (1963). General circulation experiments with the primitive equations. *Monthly Weather Review*, 91(3):99–164.
- Smirnov, A., Shi, S., and Celik, I. (2001). Random flow generation technique for large eddy simulations and particle-dynamics modeling. *Journal of Fluids Engineering*, Vol. 123, 359–371, June.
- Spalart, P. (1988). Direct simulation of a turbulent boundary layer up to  $\mathcal{R}_\theta = 1480$ . *Journal of Fluid Mechanics*, vol.187, 61–98.
- Spalart, P. (2000a). Strategies for turbulence modelling and simulations. *International Journal of Heat and Fluid Flows*, Vol. 21, pp 252–263.
- Spalart, P. (2000b). Trends in turbulence treatments. *AIAA Paper 00-2306, Fluids 2000, Denver, CO, USA*.
- Spalart, P. (2001). Young-person’s guide to detached eddy simulation grids. *NASA, Technical Report CR-2001-211032, July*.
- Spalart, P. (2004). Topics in Detached Eddy Simulation. *ICCFD3, Toronto, Canada, July*.

- Spalart, P. and Allmaras, S. (1992). A one equation turbulence model for aerodynamic flows. *AIAA Paper 92-0439*.
- Spalart, P. and Allmaras, S. (1994). A one equation turbulence model for aerodynamic flows. *La Recherche Aéropatiale*, 5-21.
- Spalart, P. and Bogue, D. (2003). The role of CFD in aerodynamics, off-design. *Aeronautical Journal*, June.
- Spalart, P., Deck, S., Shur, M., Squires, K., Strelets, M., and Travin, A. (2005a). A New Version of Detached-Eddy Simulation, Resistant to Ambiguous Grid Densities. *submitted to Theoretical and Computational Fluid Dynamics, revised*.
- Spalart, P., Jou, W., Strelets, M., and Allmaras, S. (1997). Comments on the feasibility of LES for wings and on a hybrid RANS/LES approach. *Proceedings of the 1st AFOSR Int. Conf. on DNS/LES, Ruston, 137-147*.
- Spalart, P., Strelets, M., and Travin, A. (2005b). Direct Numerical Simulation of Large-Eddy-Break-Up Devices in a Boundary Layer. *Int. Symp. Eng. Turb. Modelling and Measurements VI, Sardiani, W. Rodi, ed., May*.
- Speziale, C. (1997). Turbulence Modeling for Time-Dependant RANS and VLES: A Review. *AIAA Paper 97-2051, June*.
- Speziale, C. (1998). Turbulence Modeling for Time-Dependant RANS and VLES: A Review. *AIAA J., vol.36, No.2, 173-184*.
- Spille-Kohoff, A. and Kaltenbach, H. (2001). Generation of turbulent inflow data with a described shear-stress profile. *Proceedings of the third AFOSR Int. Conf. on DNS/LES, Arlington, edited by C.Liu, L. Sakell and T. Beutner, Greyden press, Columbus, OH, 5-9 August, 137-147*.
- Stolz, S. and Adams, N. (1999). An approximate deconvolution procedure for large-eddy simulation. *Phys. Fluids*, 11(7):1699-1701.
- Stolz, S., Adams, N., and Kleiser, L. (2001a). An approximate deconvolution model for large-eddy simulation with application to incompressible wall-bounded flows. *Phys. Fluids*, 13(4).
- Stolz, S., Adams, N., and Kleiser, L. (2001b). An approximate deconvolution model for LES of compressible flows and its application to shock-turbulence interaction. *Phys. Fluids*, 13(10).
- Strelets, M. (2001). Detached Eddy Simulation of Massively Separated Flows. *AIAA Paper 01-0879, 39th AIAA Aerospace Sciences Meeting and Exhibit, Reno, Nevada, Jan*.
- Strelets, M. (2002). private communication.
- Sullivan, P., Mc Williams, J., and Moeng, C. (1996). A grid nesting method for large-eddy simulation of planetary boundary-layer flows. *Boundary-Layer Meteorol.*, 80:167-202.
- Sweldens, W. (1998). The lifting scheme: a construction of second generation wavelets. *SIAM J. Math. Anal.* 29, 511-546
- Temmerman, L., Hadziabdić, M., Leschziner, M., and Hanjalić, K. (2004). A hybrid two-layer URANS-LES approach for Large Eddy Simulation at high Reynolds numbers. *International Journal of Heat and Fluid Flows*, in press.
- Tennekes, H. and Lumley, J. (1974). First course in turbulence. *The MIT Press, Cambridge, Massachusetts, and London, England, 3rd edition*.

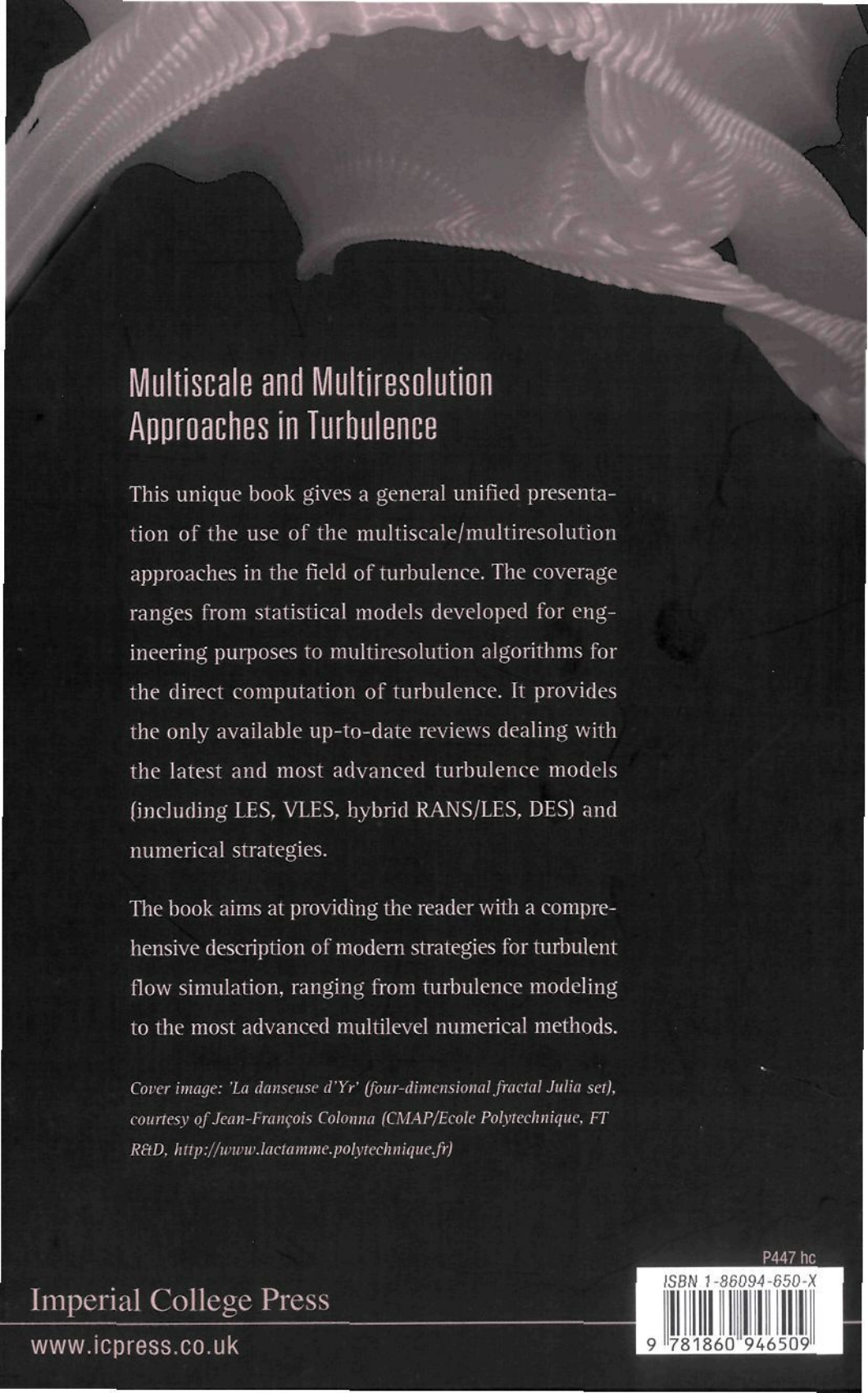
- Terracol, M. (2001). Méthodes multineveau pour la simulation des grandes échelles des écoulements turbulents compressibles (in french). PhD thesis, Université de Paris 13.
- Terracol, M. (2005). A zonal RANS/LES approach for noise sources prediction. *Int. Symp. Eng. Turb. Modelling and Measurements VI, Sardinia, W. Rodi, ed., May*.
- Terracol, M. and Sagaut, P. (2003). A multilevel-based dynamic approach for sugrid-scale modeling in large-eddy simulation. *Phys. Fluids*, 15(12):3671–3682.
- Terracol, M., Sagaut, P., and Basdevant, C. (2001). A multilevel algorithm for Large Eddy Simulation of turbulent compressible flows. *J. Comput. Phys.*, 167(2):439–474.
- Terracol, M., Sagaut, P., and Basdevant, C. (2003). A time self-adaptive multilevel algorithm for large-eddy simulation. *J. Comput. Phys.*, 184(2):339–365.
- Terracol, M., Sagaut, P. and Basdevant, C. (2000). Une méthode multineveau pour la simulation des grandes échelles des écoulements turbulents compressibles. *C. R. Acad. Sci. Paris, Série II.b* 328, 81–86 (in French)
- Thomson, K. W. (1987a). Time dependant boundary conditions for hyperbolic systems. *J. Comput. Phys.*, 68:1–24.
- Thomson, K. W. (1987b). Time dependant boundary conditions for hyperbolic systems, II. *J. Comput. Phys.*, 89:439–461.
- Touil, H. (2002). Modélisation spectrale de la turbulence inhomogène anisotrope, PhD Thesis, Ecole Centrale de Lyon, 123p. (in French)
- Travin, A., Shur, M., Strelets, M., and Spalart, P. (2000). Detached-Eddy Simulations past a circular cylinder. *Int. J. Flow Turbulence and Combustion*, vol. 23, 293–313).
- Travin, A., Shur, M., and Spalart, P., Strelets, M. (2004). On URANS Solutions With LES-like Behavior. *Proceedings of the European Congress on Computational Methods in Applied Sciences and Engineering, Jyväskylä, Finland, July 24–28*.
- Urbin, G. and Knight, D. (2001). Large-Eddy Simulation of a Supersonic Boundary Layer Using an Unstructured Grid. *AIAA J.*, vol.39, No.7, 1288–1295.
- Vasilyev, O.V. and Bowman, C. (2000). Second generation wavelet collocation method for the solution of partial differential equations. *J. Comput. Phys.* 165, 660–693
- Vasilyev, O. V., Lund, T. S., and Moin, P. (1998). A general class of commutative filters for les in complex geometries. *J. Comput. Phys.*, 146:82–104.
- Voke, P. (1989). Multiple mesh simulation of low reynolds number turbulent channel flow. In C. Taylor, P. G. and Sani, R., editors, *Numerical Methods in Laminar and Turbulent Flow*, volume 6, 1567–1577.
- Voke, P. (1990). Multiple mesh simulation of turbulent flow. Report QMW EP-1082 - University of London.
- Vreman, A. (2003). The filtering analog of the variational multiscale method in large-eddy simulation. *Phys. Fluids* 15(8), L61–L64
- Wei, T. and Willmarth, W. W. (1989). Reynolds-number effects on the structure

- of a turbulent channel flow. *J. Fluid Mech.*, 204:57.
- Wesseling, P. (1991). *An introduction to multigrid methods*. John Wiley & sons.
- Wilcox, D.C. (1988a). Reassessment of the scale-determining equation for advanced turbulence models, *AIAA J.* 26(11), 1299–1310
- Wilcox, D.C. (1988b). Multiscale model for turbulent flows, *AIAA J.* 26(11), 1311–1320
- Winckelmans, G.S. and Jeanmart, H. (2001). Assessment of some models for LES without/with explicit filtering. (Direct and large-eddy simulation IV, Geurts, Friedrich and Métais eds.), Kluwer, 55–66
- Xiao, X., Edwards, J. R., and Hassan, H. A. (2004). Blending Functions in Hybrid Large-Eddy/Reynolds-Averaged Navier-Stokes Simulations. *AIAA J.*, vol.42, No.12, 2508-2515.
- Xiao, X., Edwards, J. R., Hassan, H. A., and Baurle, R. A. (2003). Inflow Boundary Conditions for Hybrid Large Eddy/Reynolds Averaged Navier-Stokes Simulations. *AIAA J.*, vol.41, No.8, 1463-1489.
- Yan, J., Mockett, C., and Thiele, F. (2005). Investigation of Alternative Length Scale Substitutions in Detached-Eddy Simulation. *Flow Turbulence and Combustion*, vol. 74, 85-102).
- Zajaczkowski, F. and Peltier, L. (2001). Energy-containing-range modeling of fully-developed channel flow using a hybrid RANS/LES technique. *Proceedings of the third AFOSR Int. Conf. on DNS/LES, Arlington, edited by C.Liu, L. Sakell and T. Beutner, Greyden press, Columbus, OH, 5-9 August, 823-828.*
- Zang, Y., Street, R., and Koseff, J. (1993). A dynamic mixed subgrid-scale model and its applications to turbulent recirculating flows. *Phys. Fluids A*, 5(12):3186–3196.
- Zhang, H., Bachman, C., and Fasel, H. (2000). Application of a new methodology for simulations of complex turbulent flows. *AIAA Paper 00-2535, Fluids 2000, Denver, CO, USA.*

# Index

- Adaptive grid, 178
- Adaptive Mesh Refinement (AMR), 165
- Approximate Deconvolution Model (ADM), 128, 134
- Blending, 244, 250
- Coherency diagram, 198
- Cycling methods, 151
- Deconvolution, 126
- Delayed Detached Eddy Simulation (DDES), 274
- Detached-Eddy Simulation (DES), 237, 244, 251, 254
- Details, 37, 41
- Direct Numerical Simulation (DNS), 45
- Ensemble average, 26
- Ergodicity, 27
- Error estimate, 175, 207
- Extra Large Eddy Simulation (XLES), 251, 265, 266
- Filtered Navier–Stokes equations, 33
- Filtering approach, 46
- Flow Simulation Methodology (FSM), 245
- Generalized multilevel closure, 161
- Germano identity, 93, 160, 161
- Global multigrid methods, 148, 151
- Global RANS/LES methods, 219
- Grey area, 244, 255, 267
- Grid-Induced Separation (GIS), 267, 268, 270, 273
- Hierarchical decomposition, 35
- Hybrid RANS/LES approach, 48, 219, 226, 277
- Implicit Large Eddy Simulation (ILES), 33
- Inlet data generation, 294, 306
- Integral scale, 9
- Interpolation operators, 149
- Kolmogorov scale, 12
- Large Eddy Simulation (LES), 31, 46
- Large Eddy STimulation (LEST), 294
- Leonard decomposition, 34
- Limited Numerical Scales (LNS), 243, 247, 267
- Local multigrid methods, 149
- Low-pass filter, 31
- Modelled-Stress-Depletion (MSD), 252, 268, 269
- Multidomain methods, 149, 163
- Multifractal, 141
- Multigrid, 146

- Multilevel decomposition, 36
- Multilevel LES approach, 46, 153
- Multilevel Navier–Stokes equations, 39
- Multilevel subgrid closures, 156
- Multimesh, 152
- Multiscale decomposition, 38
- Multiscale statistical approach, 46
  
- Non-Linear Disturbance Equations (NLDE), 41, 290
  
- Organized Eddy Simulation (OES), 232, 279
  
- Partial kinetic energy, 52
- Phase-average, 29
- Phase-Averaged Navier Stokes (PANS), 29, 30, 229
- Precursor calculation, 295
  
- Quasi-static approximation, 187
  
- Recycling methods, 298
- Reynolds stress tensor, 28
- Reynolds-Averaged Navier–Stokes (RANS), 26, 28, 45
- Scale Adaptive Simulation (SAS), 279
- Scale separation, 24
- Semi-Deterministic Method (SDM), 231, 279
  
- Spectral transfers, 62
- Statistical average, 26
- Steady Reynolds-Averaged Navier–Stokes (SRANS), 228
- Subgrid scales, 32
- Subgrid stress tensor, 33
- Synthetic turbulence, 315
  
- Taylor scale, 11, 253
- Temporal average, 27
- Transient-Reynolds-Averaged Navier–Stokes (TRANS), 229
- Triad, 17
- Turbulence-Resolving Reynolds-Averaged Navier–Stokes (TRRANS), 241, 279
  
- Unsteady Reynolds-Averaged Navier–Stokes (URANS), 27, 229, 279
  
- Velocity estimation model, 128
- Very Large Eddy Simulation (VLES), 243, 244
  
- Wavelet, 196
  
- Zonal DES, 271
- Zonal multigrid methods, 163
- Zonal RANS/LES methods, 283



## Multiscale and Multiresolution Approaches in Turbulence

This unique book gives a general unified presentation of the use of the multiscale/multiresolution approaches in the field of turbulence. The coverage ranges from statistical models developed for engineering purposes to multiresolution algorithms for the direct computation of turbulence. It provides the only available up-to-date reviews dealing with the latest and most advanced turbulence models (including LES, VLES, hybrid RANS/LES, DES) and numerical strategies.

The book aims at providing the reader with a comprehensive description of modern strategies for turbulent flow simulation, ranging from turbulence modeling to the most advanced multilevel numerical methods.

*Cover image: 'La danseuse d'Yr' (four-dimensional fractal Julia set), courtesy of Jean-François Colonna (CMAP/Ecole Polytechnique, FT R&D, <http://www.lactamme.polytechnique.fr>)*

Imperial College Press

[www.icpress.co.uk](http://www.icpress.co.uk)

P447 hc

ISBN 1-86094-650-X



9 781860 946509